Politechnika Warszawska Wydział Inżynierii Materiałowej ul. Wołoska 141 02-507 Warszawa

za pośrednictwem:

Rady Doskonałości Naukowej pl. Defilad 1 00-901 Warszawa (Pałac Kultury i Nauki, p. XXIV, pok. 2401)

Paweł Piotr Michałowski (imię i nazwisko wnioskodawcy)

Sieć Badawcza Łukasiewicz – Instytut Mikroelektroniki i Fotoniki al. Lotników 32/46
02-668 Warszawa
(miejsce pracy/jednostka naukowa)

Wniosek

z dnia17.09.2021

o przeprowadzenie postępowania w sprawie nadania stopnia doktora habilitowanego w dziedzinie nauk inżynieryjno-technicznych w dyscyplinie inżynieria materialowa

Określenie osiągnięcia naukowego będącego podstawą ubiegania się o nadanie stopnia doktora habilitowanego:

Cykl powiązanych tematycznie artykułów naukowych, zgodnie z art. 219 ust. 1. pkt 2b Ustawy "Charakteryzacja struktur półprzewodnikowych z nanometrową i subnanometrową rozdzielczością wgłębną przy użyciu metody Spektrometrii Mas Jonów Wtórnych"

Wnioskuję – na podstawie art. 221 ust. 10 ustawy z dnia 20 lipca 2018 r. Prawo o szkolnictwie wyższym i nauce (Dz. U. z 2018 r. poz. 1668 ze zm.) – aby komisja habilitacyjna podejmowała uchwałę w sprawie nadania stopnia doktora habilitowanego w głosowaniu **jawnym**

Zostałem poinformowany, że:

Administratorem w odniesieniu do danych osobowych pozyskanych w ramach postępowania w sprawie nadania stopnia doktora habilitowanego jest Przewodniczący Rady Doskonałości Naukowej z siedzibą w Warszawie (pl. Defilad 1, XXIV piętro, 00-901 Warszawa).

Kontakt za pośrednictwem e-mail: kancelaria@rdn.gov.pl , tel. 22 656 60 98 lub w siedzibie organu. Dane osobowe będą przetwarzane w oparciu o przesłankę wskazaną w art. 6 ust. 1 lit. c) Rozporządzenia UE 2016/679 z dnia z dnia 27 kwietnia 2016 r. w związku z art. 220 - 221 oraz art. 232 – 240 ustawy z dnia 20 lipca 2018 roku - Prawo o szkolnictwie wyższym i nauce, w celu przeprowadzenie postępowania o nadanie stopnia doktora habilitowanego oraz realizacji praw i obowiązków oraz środków odwoławczych przewidzianych w tym postępowaniu.

Szczegółowa informacja na temat przetwarzania danych osobowych w postępowaniu dostępna jest na stronie www.rdn.gov.pl/klauzula-informacyjna-rodo.html

(podpis wnioskodawcy)

Załączniki:

- 1) Dane wnioskodawcy
- 2) Kopia dokumentu potwierdzającego posiadanie stopnia doktora
- 3) Autoreferat
- 4) Wykaz osiągnięć naukowych
- Publikacje wchodzące w skład cyklu powiązanych tematycznie artykułów naukowych, zgodnie z art. 219 ust. 1. pkt 2b Ustawy
- 6) Oświadczenia współautorów

Dane wnioskodawcy

1. Imiona: Paweł Piotr

2. Nazwisko: Michałowski

3. Data i miejsce urodzenia:

- Miejsce pracy: Sieć Badawcza Łukasiewicz Instytut Mikroelektroniki i Fotoniki al. Lotników 32/46 02-668 Warszawa
- 5. Adres korespondencyjny:
- 6. Nr telefonu:
- 7. Adres e-mail: Pawel.Michalowski@imif.lukasiewicz.gov.pl
- 8. Numer PESEL:

(podpis wnioskodawcy)

UNIWERSYTET IM. ADAMA MICKIEWICZA W POZNANIU Wydział Fizyki

Uchwała

Rady Wydziału Fizyki UAM z IV zwyczajnego posiedzenia z dnia 20 lutego 2015 roku w sprawie nadania stopnia doktora nauk fizycznych w zakresie fizyki dr. Pawłowi Michałowskiemu

Rada Wydziału Fizyki UAM na posiedzeniu w dniu 20 lutego 2015 roku, w głosowaniu tajnym, w którym udział brało 49 członków Rady na 70 uprawnionych do głosowania – 49 głosami "tak", podjęła uchwałę o nadaniu dr. Pawłowi Michałowskiemu stopnia naukowego doktora nauk fizycznych w zakresie fizyki.

Przewodniczący Rady Wydziału Fizyki UAM

Prof. dr hab. Antoni Wójcik

Autoreferat

1 Imię i nazwisko

Paweł Piotr Michałowski

2 Posiadane dyplomy, stopnie naukowe – z podaniem podmiotu nadającego stopień, roku ich uzyskania oraz tytułu rozprawy doktorskiej

- Praca magisterska "Production of Li intercalated C60 films and implementation into electronic devices". Faculty of Physics, Umeå University. Promotor: dr Thomas Wågberg, 01.2007
- Praca magisterska "Badanie wpywu procesu fotopolimeryzacji fulerenów przy użyciu metody SIMS". Wydział Fizyki, Uniwersytet im. Adama Mickiewicza w Poznaniu. Promotor: prof. Józef Barnaś, 06.2008
- Rozprawa doktorska "Diffusion and structural changes in Al1-xSixOy thin films investigated by Time-of-Flight Secondary Ion Mass Spectroscopy". Wydział Fizyki, Uniwersytet im. Adama Mickiewicza w Poznaniu. Promotor: dr hab Maciej Wiesner, 02.2015

3 Informacja o dotychczasowym zatrudnieniu w jednostkach naukowych.

- 03.2007-06.2010 Asystent, Fraunhofer Center Nanoelektronische Technologien, Drezno, Niemcy.
- 04.2015-05.2018 Adiunkt, Zakład Epitaksji i Charakteryzacji, Instytut Technologii Materiałów Elektronicznych, Warszawa, Polska.
- 06.2018-03.2019 Zastępca kierownika Laboratorium Badań Strukturalnych i Charakteryzacji Materiałów, Instytut Technologii Materiałów Elektronicznych, Warszawa, Polska.
- 04.2019-12.2019 Zastępca kierownika Laboratorium Badań Strukturalnych i Charakteryzacji Materiałów, Sieć Badawcza Łukasiewicz - Instytut Technologii Materiałów Elektronicznych, Warszawa, Polska.
- 01.2020-09.2020 Kierownik Laboratorium Badań Strukturalnych i Charakteryzacji Materiałów, Sieć Badawcza Łukasiewicz - Instytut Technologii Materiałów Elektronicznych, Warszawa, Polska.
- 10.2020-05.2021 Kierownik Zakładu Badań Strukturalnych i Charakteryzacji Materiałów, Sieć Badawcza Łukasiewicz - Instytut Mikroelektroniki i Fotoniki, Warszawa, Polska.
- 10.2020- obecnie Lider Grupy Badawczej Charakteryzacja Materiałów i Przyrządów, Sieć Badawcza Łukasiewicz Instytut Mikroelektroniki i Fotoniki, Warszawa, Polska.

Instytut Technologii Materiałów Elektronicznych dołączył do Sieci Badawczej Łukasiewicz w kwietniu 2019 i został skonsolidowany z Instytutem Technologii Elektronowej w październiku 2020. Wspólnie utworzyły Instytut Mikroelektroniki i Fotoniki. Zasadne jest więc uważać, że od 2015 roku nie zmieniłem swojego pracodawcy.

4 Omówienie osiągnięć, o których mowa w art. 219 ust. 1 pkt. 2 ustawy z dnia 20 lipca 2018 r. Prawo o szkolnictwie wyższym i nauce (Dz. U. z 2020 r. poz. 85 z późn. zm.).

4.1 Tytuł osiągnięcia

Charakteryzacja struktur półprzewodnikowych z nanometrową i subnanometrową rozdzielczością wgłębną przy użyciu metody Spektrometrii Mas Jonów Wtórnych.

4.2 Lista artykułów naukowych wchodzących w skład osiągnięca

- [H1] P.P. Michalowski, W. Kaszub, A. Merkulov, W. Strupiński. "Secondary ion mass spectroscopy depth profiling of hydrogen-intercalated graphene on SiC" *Applied Physics Letters*, 109(1):011904, 2016.
- [H2] P.P. Michałowski, W. Kaszub, I. Pasternak, W. Strupinski. "Graphene Enhanced Secondary Ion Mass Spectrometry (GESIMS)" *Scientific Reports*, 7:7479, 2017.
- **[H3] P.P. Michałowski**, P. Gutowski, D. Pierścińska, K. Pierściński, M. Bugajski, W. Strupiński. "Characterization of the superlattice region of a quantum cascade laser by secondary ion mass spectrometry" *Nanoscale*, 9:17571–17575, 2017.
- **[H4] P.P. Michalowski**, I. Pasternak, W. Strupiński. "Contamination-free Ge-based graphene as revealed by graphene enhanced secondary ion mass spectrometry (GESIMS)" *Nanotechnology*, 29(1):015702, 2018.
- **[H5] P.P. Michałowski**, I. Pasternak, P. Ciepielewski, F. Guinea, W. Strupiński. "Formation of a highly doped ultra-thin amorphous carbon layer by ion bombardment of graphene" *Nanotechnology*, 29(30):305302, 2018.
- [H6] P.P. Michalowski, J. Gaca, M. Wójcik, A. Turos. "Oxygen out-diffusion and compositional changes in zinc oxide during ytterbium ions bombardment" *Nanotechnology*, 29(42):425710, 2018.
- [H7] P.P. Michałowski, W. Kaszub, P. Knyps, K. Rosiński, B. Stańczyk, K. Przyborowska, E. Dumiszewska. "A-Crater-within-a-Crater Approach for Secondary Ion Mass Spectrometry Evaluation of the Quality of Interfaces of Multilayer Devices" *ACS Applied Materials & Interfaces*, 10(43):37694–37698, 2018.
- **[H8] P.P. Michałowski**, P. Knyps, P. Ciepielewski, P. Caban, E. Dumiszewska, J. Baranowski. "Destructive role of oxygen in growth of molybdenum disulfide determined by secondary ion mass spectrometry" *Physical Chemistry Chemical Physics*, 21:8837–8842, 2019.
- **[H9] P.P. Michałowski**, P. Knyps, P. Ciepielewski, P.A. Caban, E. Dumiszewska, G. Kowalski, M. Tokarczyk, J.M. Baranowski. "Growth of highly oriented MoS2 via an intercalation process in the graphene/SiC(0001) system" *Physical Chemistry Chemical Physics*, 21:20641–20646, 2019.
- [H10] P.P. Michalowski, P. Caban, J. Baranowski. "Secondary ion mass spectrometry investigation of carbon grain formation in boron nitride epitaxial layers with atomic depth resolution" *Journal of Analytical Atomic Spectrometry*, 34:848–853, 2019.
- [H11] P.P. Michałowski, S. Złotnik, and M. Rudziski. "Three dimensional localization of unintentional oxygen impurities in gallium nitride" *Chemical Communications*, 55:11539–11542, 2019.

- [H12] P.P. Michałowski, E. Grzanka, S. Grzanka, A. Lachowski, G. Staszczak, J. Plesiewicz, M. Leszczyski, A. Turos. "Indium concentration fluctuations in InGaN/GaN quantum wells" *Journal of Analytical Atomic Spectrometry*, 34:1718–1723, 2019.
- **[H13] P.P. Michalowski**. "Probing a chemical state during ultra low impact energy secondary ion mass spectrometry depth profiling" *Journal of Analytical Atomic Spectrometry*, 34:1954–1956, 2019.
- **[H14] P.P. Michałowski**. "Titanium pre-sputtering for an enhanced secondary ion mass spectrometry analysis of atmospheric gas elements" *Journal of Analytical Atomic Spectrometry*, 35:1047–1050, 2020.
- [H15] P.P. Michałowski, S. Zlotnik, I. Jóźwik, A. Chamryga, M. Rudziński. "3D Depth Profile Reconstruction of Segregated Impurities using Secondary Ion Mass Spectrometry" *Journal of Visualized Experiments*, 158:e61065, 2020.
- [H16] P.P. Michałowski, D. Maciążek, Z. Postawa, P.A. Caban, S. Kozdra, A. Wójcik, J.M. Baranowski. "Defect-mediated sputtering process of boron nitride during high incident angle low-energy ion bombardment" *Measurement*, 179:109487, 2021.

4.3 Opis osiągnięcia naukowego

4.3.1 Wstęp

Spektrometria mas jonów wtórnych (skrót SIMS z ang. Secondary Ion Mass Spectrometry) jest główną techniką charakteryzacyjną, którą wykorzystywałem w niniejszym osiągnięciu naukowym. SIMS to bardzo precyzyjna, czuła powierzchniowo technika analityczna. Podczas pomiaru próbka jest bombardowana wiązką jonów pierwotnych, co prowadzi do rozpylania materii z jej powierzchni. Niewielka część rozpylonych cząstek jest naładowana i nazywana jonami wtórnymi. Poddawane są one spektralnej analizie masowej, która dostarcza informacji o ich stosunku masy do ładunku. Właściwa interpretacja pozwala określić skład pierwiastkowy i/lub izotopowy próbki. Kolejne warstwy próbki są usuwane podczas analizy, dzięki czemu można określić, jak zmienia się skład w funkcji głębokości, tworząc tzw. profile wgłębne. Analiza lateralna sygnału pozwala na tworzenie obrazów 3D i przekrojów próbki.

SIMS jest bardzo czuły w wykrywaniu domieszek i zanieczyszczeń.[1–6] Dla większości pierwiastków i materiałów matrycowych (główny skład próbki) granica wykrywalności mieści się w zakresie 10¹⁵-10¹⁶ atomów/cm³,[5] w niektórych przypadkach nawet 10¹² atomów/cm³.[6] Rozdzielczość wgłębna może wynosić poniżej 1 nm, co czyni technikę nieocenioną przy badaniu ultracienkich warstw, takich jak złącza tunelowe, supersieci lub materiały 2D, takie jak grafen lub azotek boru. Tak dobra rozdzielczość wgłębna jest dostępna dla urządzeń CAMECA IMS SC Ultra i CAMECA IMS Wf (ten sam typ spektrometru z różnymi systemami ładowania próbek) dzięki dwóm głównym udoskonaleniom:

- Kwadratowe szablony większość urządzeń SIMS wykorzystuje standardową wiązkę jonów
 o kształcie gaussowskim, co prowadzi do nierównomiernego rozpylania próbki. Wiązka pierwotna w urządzeniu SC Ultra/Wf jest formowana przez dwa szablony zawierające kwadratowe otwory. Pierwszy służy do wybrania najbardziej intensywnej i jednorodnej części wiązki,
 drugi zmienia wielkość plamki. Proces rozpylania jest zatem bardzo równomierny, co znacznie
 poprawia rozdzielczość wgłębną.
- Technologia EXLIE (Extra Low Impact Energy) dla źródła jonów cezowych zastosowano koncepcję tzw. napięcia pływającego. Do kolumny pierwotnej przykładane jest napięcie (w innych urządzeniach kolumna jest uziemiona), dzięki temu jony pierwotne są stopniowo spowalniane. Zachowana natomiast zostaje wysoka jakość i stabilność wiązki. Ta innowacja pozwala

zmniejszyć energię jonów do 90 eV, podczas gdy 500 eV jest najniższą wartością dla większości spektrometrów. W kolumnie tlenowej, zamiast powszechnie stosowanego duoplazmatronu (bardzo trudno obniżyć energię padających jonów poniżej 1 keV), zainstalowano generator plazmy typu radio frequency. Pozwala to obniżyć energię jonów do 60 eV przy zachowaniu wysokiej jakości wiązki pierwotnej. W przypadku obu typów jonów pierwotnych efekt mieszania jest znacznie zmniejszony, a zatem rozdzielczość wgłębna jest znacznie wyższa niż w standardowym spektrometrze.

Niestety, te udoskonalenia nie wystarczą, aby uzyskać wysokiej jakości wyniki pomiarów z subnanometrową rozdzielczością wgłębną. Przy tak niskiej energii padających jonów prawdopodobieństwo ekstrakcji i jonizacji jest znacznie zmniejszone, a zatem granice wykrywalności ulegają pogorszeniu. Mimo że próbka jest rozpylana bardzo jednorodnie i wolno, natężenie sygnałów SIMS nie pozwala na poprawne opisanie zjawisk zachodzących w nanoskali.

4.3.2 Dedykowane procedury pomiarowe

Aby przezwyciężyć ten problem zaproponowałem utworzenie procedur pomiarowych SIMS dedykowanych dla konkretnego materiału. Najważniejsza różnica pomiędzy procedurami standardowymi (dostarczanymi przez producenta wraz z urządzeniem) a dedykowanymi dotyczy parametrów ekstrakcji. W przypadku standardowych procedur są one optymalizowane w ten sam sposób – aby zmaksymalizować całkowitą liczbę zliczeń jonów wtórnych. Zaletą tego podejścia jest prostota formowania wiązki wtórnej, a pomiary można wykonywać na dowolnych materiałach bez czasochłonnej optymalizacji. W swojej pracy wykazałem jednak, że rozkład przestrzenny i energetyczny jonów wtórnych jest odmienny dla różnych materiałów i pierwiastków, a zatem może się zdarzyć, że przy zastosowaniu standardowej procedury intensywność jednego z sygnałów będzie bardzo bardzo niska (lub nawet równa zeru). W takim przypadku należy zwiększyć energię jonów pierwotnych, gęstość wiązki i/lub czas integracji sygnałów. W ten sposób zostanie jednak pogorszona rozdzielczość wgłębna.

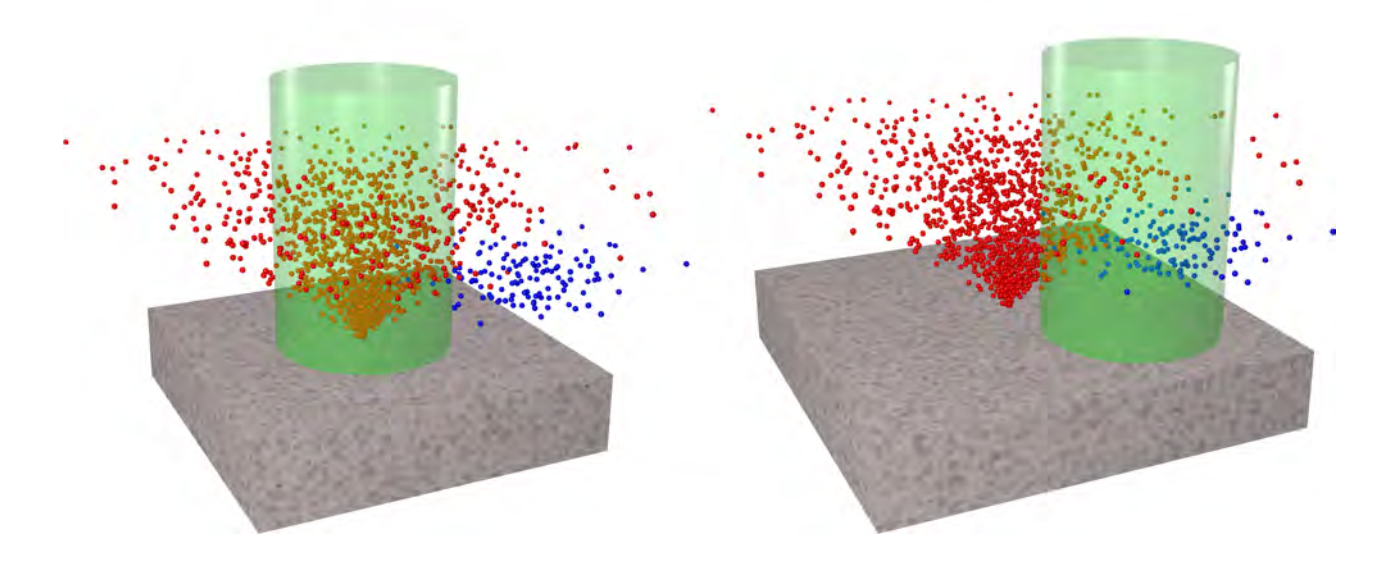
W dedykowanych procedurach problem ten można rozwiązać poprzez ponowną optymalizację parametrów ekstrakcji i skupienie ich na bardziej pożądanych jonach wtórnych, a nie na całkowitej ilości zliczeń. W ten sposób intensywność sygnału matrycy może spaść nawet o więcej niż dwa rzędy wielkości, ale jeśli wartość początkowa była wystarczająco wysoka (na przykład 10^6 zliczeń/s), nie spowoduje to żadnego problemu z interpretacją wyników. Jednocześnie zwiększa się intensywność pożądanego sygnału (np. domieszki lub zanieczyszczenia) i pomiar może być wykonany bez utraty rozdzielczości wgłębnej. Różnica między procedurami standardowymi i dedykowanymi została schematycznie pokazana na rysunku 1. Niewątpliwą wadą jest konieczność przeprowadzenia oddzielnej optymalizacji dla każdego badanego materiału, każdego wybranego jonu wtórnego oraz każdej energii i gęstości wiązki pierwotnej. Ponadto formowanie wiązki wtórnej jest o wiele trudniejsze, a więc cały proces może być bardzo czasochłonny. Na szczęście dla podobnych materiałów i/lub wybranych jonów można dostosować już istniejącą procedurę, a nie opracowywać ją od początku, co pozwala zaoszczędzić czas.

Dzięki zoptymalizowanym parametrom ekstrakcji intensywność sygnałów pochodzących od domieszek i zanieczyszczeń pozostaje wysoka i można korzystać z jonów pierwotnych o ultra niskiej energii bez konieczności wydłużania czasu integracji sygnału. Pomiary prowadzone w ten sposób charakteryzują się subnanometrową rozdzielczością wgłębną.

4.3.3 Opis osiągniecia naukowego zawartego w artykułach [H1] – [H16]

Nadrzędnym celem mojej pracy było rozszerzenie funkcjonalności SIMS i umożliwienie charakteryzacji z nanometrową i subnanometrową rozdzielczością wgłębną oraz wykonanie badań na materiałach, które wymagają takiej rozdzielczości. Aby osiągnąć ten cel, stworzyłem szereg dedykowanych procedur pomiarowych. Żeby uchwycić stopniowy postęp mojej pracy, publikacje będą omawiane w kolejności ich powstawania (z kilkoma drobnymi wyjątkami). W przypadku najstarszych artykułów

Standard Dedicated



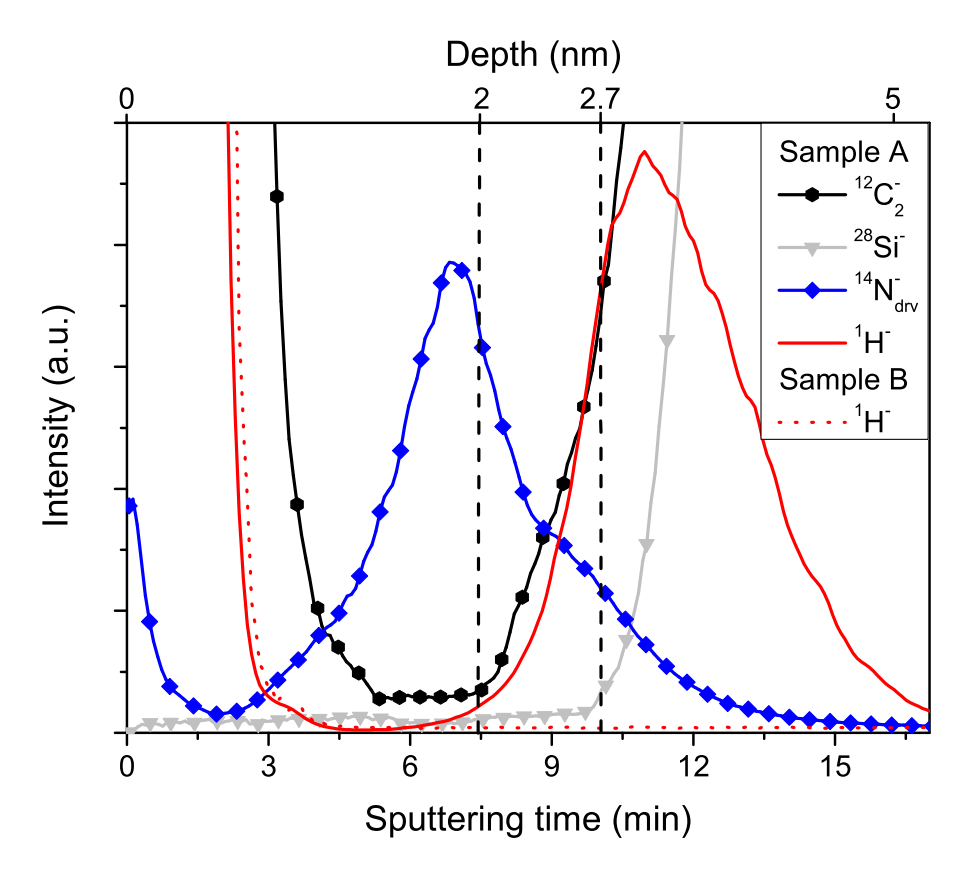
Rysunek 1: W standardowej procedurze pomiarowej parametry ekstrakcji są zoptymalizowane w celu maksymalizacji całkowitej liczby zliczanych jonów wtórnych (zielony walec schematycznie pokazuje, które jony wtórne trafią do detektora). Jednak wykrywanie najistotniejszych atomów (oznaczonych na niebiesko) jest bardzo nieefektywne. W dedykowanej procedurze parametry ekstrakcji są optymalizowane w taki sposób, aby uzyskać najwięcej zliczeń pochodzących od najistotniejszych atomów. Intensywność pozostałych sygnałów maleje, ale jest nadal akceptowalna. Dzięki temu podejściu można uzyskać wyższej klasy wyniki.

modyfikacje procedur uniwersalnych były niewielkie. Z czasem dostosowywałem coraz więcej parametrów, a co za tym idzie jakość uzyskiwanych wyników wzrastała. Należy podkreślić, że wszystkie dedykowane procedury zostały stworzone wyłącznie przeze mnie. Byłem również pierwszym autorem wszystkich artykułów naukowych wchodzących w skład osiągnięcia, zinterpretowałem wyniki SIMS i sformułowałem główne wnioski. Współautorzy byli odpowiedzialni za przygotowanie próbek, przygotowanie opisów technik uzupełniających, omówienie wyników oraz recenzję manuskryptu przed wysyłką do czasopisma naukowego.

Praca [H1] koncentrowała się na charakteryzacji dwuwarstwowego grafenu wzrastanego na podłożu z węglika krzemu i pokrytego cienką warstwą chromu. Główną trudnością w badaniu była utrudniona lokalizacja położenia grafenu. Nie dało się tego zrobić poprzez monitorowaniu sygnału węgla, ponieważ SiC również zawiera ten pierwiastek. Dodatkowo warstwa chromu była lekko zanieczyszczona, przez co sygnał węglowy również w tej warstwie był intensywny. Położenie granicy grafen/SiC określiłem poprzez monitorowanie sygnału krzemu. Punkt, w którym obserwowano znaczny wzrost intensywności sygnału wskazywał na początek podłoża. Oczekiwany zanik sygnału chromu powinien wskazywać koniec warstwy wierzchniej. Jednak przy tak małej energii padających jonów (150 eV) atomy chromu nie były efektywnie rozpylane i tempo zaniku sygnału chromu uniemożliwiała jednoznaczne wskazanie końca warstwy.

Aby rozwiązać ten problem monitorowałem wieloatomowe jony węgla (C₂- i C₃-). Ich intensywność była znacznie wyższa, gdy pochodziły z grafenu niż z cząsteczek organicznych ze względu na obecność silnych wiązań sp² w grafenie: przy tak niskiej energii początkowej, jony pierwotne nie mogły skutecznie zrywać silnych wiązań grafenowych, a zatem intensywność sygnału wieloatomowego była znacznie wyższa niż w warstwie chromu. Dzięki tej modyfikacji udało mi się zidentyfikować granicę między warstwą chromową a grafenem, jak pokazano na rysunku 2.

Metoda została wykorzystana do monitorowania procesu interkalacji, w którym wodór jest używany do pasywacji podłoża SiC i przekształcenia warstwy buforowej w tzw. quasi-free standing grafen.[7] Bardzo wyraźna różnica sygnału wodoru pomiędzy próbkami interkalowanymi i niein-



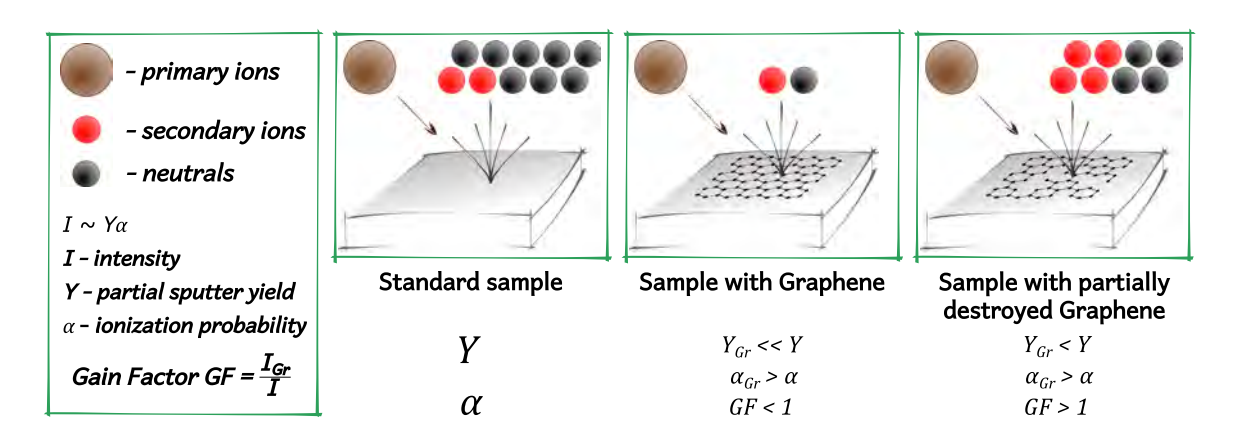
Rysunek 2: Profil wgłębny dwuwarstwowego grafenu wzrastanego na SiC i pokrytego cienką warstwą Cr. Linie przerywane pokazują położenie warstw grafenu. Bardzo silny pik sygnału H^- można zaobserwować na granicy grafenu i podłoża SiC dla próbki interkalowanej, a zatem profilowanie wgłębne SIMS można uznać za odpowiednią technikę monitorowania tego procesu. Stwierdzono, że zanieczyszczenie organiczne (sygnał N_{drv}^- został użyty jako marker) gromadzi się na powierzchni warstwy grafenu, jednak nie penetruje jej. Długość zaniku sygnału spowodowana jest efektem mieszania jonowego. Rysunek zaczerpnięty z artykułu [H1].

terkalowymi (Odpowiednio A i B na rysunku 2) potwierdza jakość opracowanej procedury. Metodę wykorzystano również do monitorowania zanieczyszczenia organicznego (sygnał N_{drv}^- został użyty jako marker) i stwierdzono, że gromadzi się ono na powierzchni grafenu i nie przenika wgłąb.

SIMS był już używany do charakteryzowania grafenu przez inne grupy badawcze[8–10], ale prace te skupiały się na wykrywaniu zanieczyszczeń, a nie ich lokalizacji. Tylko Chou *et al.*[11] zaprezentował profile wgłębne ToF-SIMS z bardzo dobrą rozdzielczością. Należy jednak zauważyć, że profile te zostały uzyskane po skomplikowanych procedurach przetwarzania danych (normalizacja oraz interpolacja funkcjami sklejanymi), podczas gdy modyfikacja procedury pomiarowej, którą zaproponowałem, wykazała wyższą rozdzielczość wgłębną bez jakiejkolwiek obróbki danych.

Podczas eksperymentów SIMS przeprowadzonych na grafenie zauważyłem, że intensywność niektórych sygnałów (szczególnie H⁻ na rysunku 2) była znacznie wyższa niż oczekiwano. Intensywne badania skłoniły mnie do wniosku, że obecność warstwy grafenowej na dowolnym podłożu znacznie zwiększa prawdopodobieństwo jonizacji ujemnej, a jednocześnie blokuje emisję jonów z podłoża. Eksperymentalnie udowodniłem, że jeśli częściowo zniszczy się warstwę grafenu poprzez bombardowanie jonowe to zmniejszony zostanie efekt blokowania, natomiast zachowane zostanie zwiększenie prawdopodobieństwa jonizacji. W ten sposób można badać ultra cienkie materiały z poprawionymi granicami wykrywalności. Nazwałem tę metodę Graphene Enhanced Secondary Ion Mass Spectrometry (GESIMS) [H2], a jej koncepcja została przedstawiona na rysunku 3.

Wykazałem też, że bez wiedzy o tym efekcie wyznaczanie stężenia różnych zanieczyszczeń może zostać mocno przeszacowane. Efekt GESIMS powoduje, że w widmie masowym pojawiają się piki odpowiadające podwójnie zjonizowanym jonom (rzadko obserwowane w standardowym ekspery-



Rysunek 3: Koncepcja metody GESIMS. Grafen blokuje emisję materii z podłoża, ale znacznie zwiększa prawdopodobieństwo jonizacji. Emisja wzrasta po utworzeniu defektów w warstwie grafenu, a zwiększone prawdopodobieństwo jonizacji jest nadal zachowane. Dzięki temu do detektora może dotrzeć więcej jonów, co skutkuje wzmocnieniem sygnału SIMS. Rysunek zaczerpnięty z artykułu [H2].

mencie SIMS) i mogą zostać błędnie zinterpretowane. Należy podkreślić, że metoda SIMS nie wykrywa masy jonu wtórnego, ale stosunek jego masy do ładunku. Jon podwójnie zjonizowany może zatem powodować interferencję masową z pojedynczo zjonizowanym jonem, który jest dwa razy lżejszy. Udowodniłem, że taka interferencja masowa może prowadzić do fałszywego wniosku, że grafen jest silnie zanieczyszczony miedzią [H4].

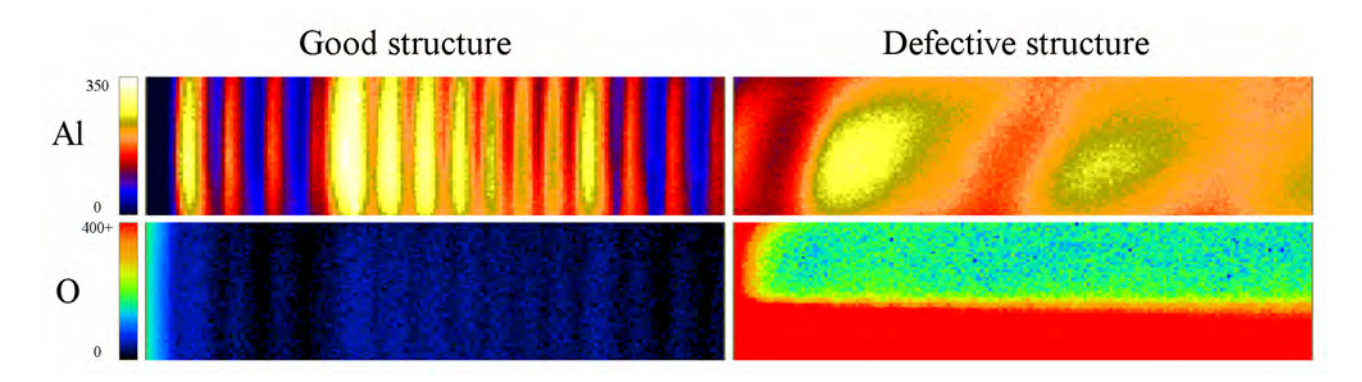
Przedstawiłem również wyjaśnienie efektu GESIMS [H5]: zerwane wiązania sp² grafenu oddziałują z padającymi jonami pierwotnymi i więżą je blisko powierzchni próbki. W przypadku eksperymentów, w którym jonami pierwotnymi jest cez, prowadzi to do tworzenie cienkiej warstwy powierzchniowej bogatej w ten pierwiastek. Ponieważ, jak wykazno w literaturze, cez znacząco obniża pracę wyjścia elektronów[12–15] dlatego podczas eksperymentu dochodzi do ich znacznej emisji, co przekłada się na zwiększenie prawdopodobieństwa jonizacji ujemnej.

Opracowana procedura jest nieoceniona przy charakteryzacji materiałów 2D, ponieważ pozwala osiągnąć granice wykrywalności poniżej 1 ppm dla większości zanieczyszczeń. Taka precyzja nie jest dostępna dla standardowego pomiaru SIMS. Regularnie używam metody GESIMS do oceny czystości materiałów 2D, które są używane przez różnych międzynarodowych partnerów w ramach projektu Graphene Flagship i jego trzech rozszerzeń Core 1, Core 2 i Core 3.

Profilowanie wgłębne z subnanometrowa rozdzielczościa zastosowałem również do badania supersieci AlInAs / InGaAs w kwantowym laserze kaskadowym [H3]. Podczas gdy w poprzednich przykładach konieczne było stosunkowo płytkie profilowanie (do 10 nm), pojedynczy okres wspomnianej supersieci wynosił około 60 nm, a celem pracy było zmierzenie co najmniej trzech z nich w celu potwierdzenia jednorodności struktury. Wyzwaniem w tej pracy było utrzymanie rozdzielczości wgłębnej wymaganej do rozróżnienia nawet najcieńszej warstwy (0.7 nm) i jednoczesne monitorowanie poziomu zanieczyszczenia tlenem. To ostatnie zadanie zwykle wymaga dłuższych czasów integracji sygnału w celu poprawienia stosunku sygnału do szumu. Niestety, w ten sposób pogarsza się rozdzielczość pomiaru. Dlatego zamiast zwiększać czas integracji, opracowałem procedurę o znacznie większym obszarze analizy (200 µm x 200 µm podczas gdy zwykle bada się 50 µm x 50µm lub nawet mniejszy obszar). Dzięki precyzyjnemu dobraniu innych parametrów (przede wszystkim gęstości wiązki pierwotnej i czasu integracji sygnałów) udało mi się jednocześnie zachować doskonałą rozdzielczość wgłębną i zadowalające granice wykrywalności. Analiza wykazała, że tlen jest zlokalizowany głównie w warstwach AlInAs, ale nie był rozłożony jednorodnie: więcej tlenu zostało wbudowane w pierwszym etapie wzrostu tej warstwy. Można to wytłumaczyć mechaniką procesu wzrostu epitaksji z wiązek molekularnych: efekt wyrzutu wywołany otwarciem komórki efuzyjnej spowodował nieco większą zawartość Al na początku wzrostu bariery AlInAs, co skutkowało absorbcją większej ilości tlenu z komory urządzenia.

Dodatkowo zoptymalizowałem tę procedurę aby umożliwić obrazowanie 3D (detektor rejestrował

nie tylko głębokość, z którego pochodzi jon wtórny, ale także pozycje x i y). Było to szczególnie przydatne do analizy usterek. Procedura została przetestowana na dobrej i wadliwej strukturze, co przedstawiono na rysunku 4. Dla poprawienia czytelności wynik został przedstawiony jako przekrój 2D.



Rysunek 4: Przekrój YZ sygnałów Al i O dla dobrej i wadliwej struktury. W poprawnej strukturze obserwuje się dużą jednorodność warstw. Analiza wadliwej struktury wykazuje, że proces wzrostu nie przebiegał w dobrych warunkach: warstwy są rozmyte, pochylone w stosunku do powierzchni próbki oraz silnie utlenione. Intensywność sygnałów podawana jest w zliczeniach na sekundę, skale Y i Z są ograniczone odpowiednio do 200 µm i 75 min czasu rozpylania. Skala tlenowa została ograniczona do 400 zliczeń na sekundę, aby poprawić widoczność sygnału dla dobrej struktury. Rysunek zaczerpnięty z artykułu [H3].

VIGO System, polska firma i wiodący na świecie producent niechłodzonych detektorów podczerwieni, zainteresowała się unikalną możliwością charakteryzowania struktur urządzeń półprzewodnikowych z subnanometrową rozdzielczością wgłębną, którą zaprezentowałem w tym artykule. Rozpoczęliśmy więc bardzo ścisłą współpracę, która trwa do dziś.

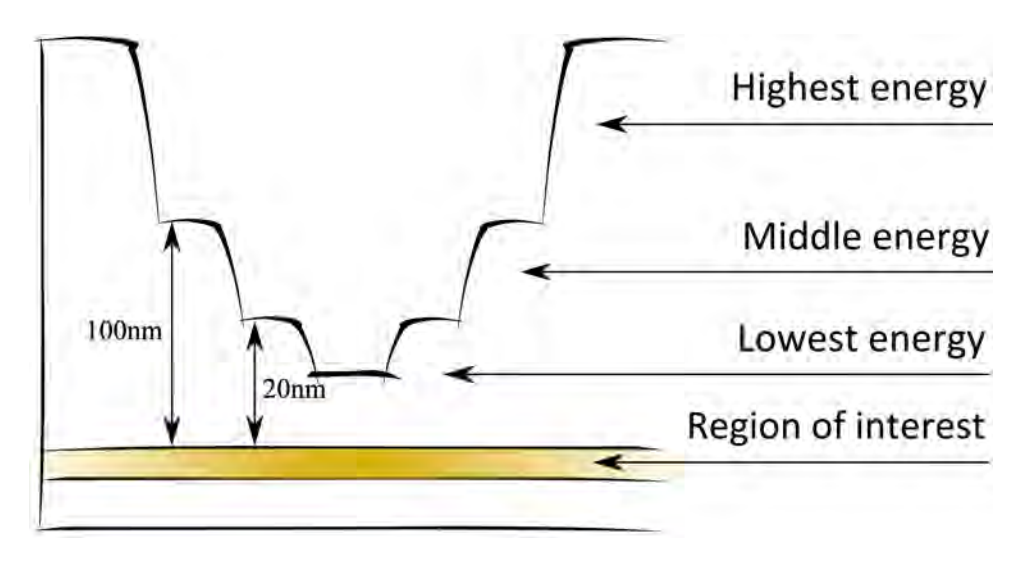
Wyniki pomiarów wysokorozdzielczej dyfrakcji rentgenowskiej (skrót HRXRD, z ang. Highresolution X-ray diffraction) kryształów tlenku cynku implantowanych jonami iterbu [H6] okazały się dość nietypowe: główny pik w profilu HRXRD zlokalizowany przy 34.5° był wywołany rozpraszaniem przez niezaimplantowaną część kryształu. Oscylacje małokątowe odzwierciedlały typowe narastanie naprężeń w warstwie implantowanej.[16] Zagadką była wysokokątowa część profilu. Wskazywała rozpraszania promieniowania rentgenowskiego z części kryształu o mniejszej stałej sieciowej niż ZnO. Ponieważ stała sieciowa metalicznego Zn wynosi 0.49468 nm i jest znacznie niższa niż dla ZnO, która wynosi 0.52069 nm, zaproponowaliśmy wyjaśnienie, że obserwowany efekt jest spowodowany uwalnianiem tlenu z warstwy zaimplantowanej.

SIMS był idealnym kandydatem do weryfikacji tej hipotezy. Jednak rzeczywiste pomiary okazały się nietrywialne. Region z niedoborem tlenu miał istotny wpływ na sam eksperyment SIMS: powodował większą retencję atomów cezu, co zmieniało intensywność wszystkich sygnałów i uniemożliwiało bezpośrednią interpretację danych. Aby rozwiązać ten problem, zaproponowałem normalizację wszystkich sygnałów, punkt po punkcie do sygnału cezu. Trafność tego podejścia została potwierdzona przez monitorowanie sygnału iterbu – dopiero po normalizacji rozkład tego sygnału odtworzył symulowany profil wyznaczony w programie SRIM. Potwierdziłem więc hipotezę, że podczas bombardowania jonami Yb część tlenu została uwolniona i dyfundowała w kierunku powierzchni.

W tym momencie zdałem sobie sprawę, że moje procedury mają jedną poważną wadę: można je stosować tylko do próbek, w których interesujący obszar znajdował się relatywnie blisko powierzchni (maksymalnie około 250 nm). Problem polegał na tym, że szybkość trawienia materiałów wynosiła około 1 nm na minutę lub nawet mniej, więc praktycznie niemożliwe było scharakteryzowanie struktur o grubości kilku mikronów. Takie pomiary byłyby nie tylko czasochłonne, ale co ważniejsze, jednorodność wiązki pierwotnej uległaby pogorszeniu, co negatywnie odbiłoby się na jakości otrzymywanych wyników.

W wielu przyrządach półprzewodnikowych najcieńsze warstwy, takie jak studnie kwantowe lub

złącza tunelowe, są zwykle zakopane kilka mikronów pod powierzchnią. Nie ulegało wątpliwości, że przydatne byłoby umożliwienie charakteryzacji tych cienkich warstw z rozdzielczością subnanometrową. Dlatego też opracowałem bardzo innowacyjne podejście, które nazwałem a-crater-withina-crater (krater-w-kraterze) [H7]: wysokoenergetyczna wiązka jonów pierwotnych została wykorzystana do szybkiego usunięcia większości materiału tworzącego duży krater. Następnie energia została znacznie zmniejszona i na dnie poprzedniego powstał nowy, mniejszy krater. W pobliżu interesującego obszaru energia padających jonów została zmniejszona do 150 eV, a zatem najbardziej istotna część próbki mogła być analizowany ze zminimalizowanym efekcie mieszania. Koncepcję podejścia przedstawiono na rysunku 5.



Rysunek 5: Podejście a-crater-within-a-crater: wysokoenergetyczna wiązka jest używana do szybkiego usunięcia górnej części próbki. Bliżej interesującego obszaru energia jonów i rozmiar krateru ulegają zmniejszeniu i eksperyment jest kontynuowany. W ostatnim kroku stosuje się najniższą wartość energii i wielkość krateru. W ten sposób efekt mieszania jest praktycznie wyeliminowany i możliwe jest scharakteryzowanie warstwy zakopanej głęboko pod powierzchnią z subnanometrową rozdzielczością wgłębną. Rysunek zaczerpnięty z artykułu [H7].

Przetestowałem przydatność tego podejścia na epitaksjalnej strukturze trójzłączowego ogniwa słonecznego. Uzyskałem wiarygodne informacje o niedoskonałości struktury: domieszki typu p i n w złączu tunelowym nakładały się, co pogarszało pracę urządzenia. Na podstawie tego wyniku zoptymalizowano procedurę wzrostu epitaksjalnego, a wydajność urządzenia wzrosła z 0.7% do 24%.

Ta unikalna metoda badania przyrządów stała się podstawą do nawiązania współpracy z krajowymi (TopGaN Lasers, Unipress) i międzynarodowymi (Tyndall National Institute, PVcomB Helmholtz-Zentrum Berlin, Fraunhofer Institute for Integrated Systems and Device Technology) instytucjami.

W tym momencie zauważyłem kolejną wadę mojej metodologii: urządzenie CAMECA IMS SC Ultra może mierzyć tylko jeden jon na raz, więc jeśli konieczne jest monitorowanie większej ilości sygnałów, to mierzone są one sekwencyjnie, od najlżejszego do najcięższego (czas integracji wszystkich sygnałów może być ustalany indywidualnie). Pojedyncze zarejestrowanie wszystkich sygnałów nazywane jest cyklem, a rzeczywisty pomiar składa się zwykle z kilkunastu aż do kliku tysięcy cykli. Problem w tym, że pierwszy i ostatni sygnał cyklu będzie mierzony ze stosunkowo dużą różnicą czasu i, biorąc pod uwagę stałe rozpylanie materiału, będzie zbierany z różnych głębokości.

Aby zminimalizować ten efekt wypracowałem podejście, które później nazwałem supercyklem: dla każdego rejestrowanego sygnału używałem bardzo krótkiego czasu integracji (zwykle 0.2-0.3 s) i dlatego wszystkie były mierzone bez dużych przesunięć czasowych, a cykl był bardzo krótki. Aby uniknąć słabego stosunku sygnału do szumu, zintegrowałem kilka cykli (zwykle 5-100) i zdefiniowałem to jako jeden supercykl. W ten sposób natężenie sygnałów pozostało wysokie, a problem zbierania danych z różnych głębokości został praktycznie wyeliminowany.

Było to szczególnie ważne dla lateralnego obrazowania materiałów 2D, co pokazałem dla warstw siarczku molibdenu [H8]. Zarówno sygnały siarki, jak i molibdenu wymagały co najmniej 15 sekund czasu integracji, aby uzyskać dobrej jakości wynik. Zastosowanie prostego cyklu oznaczałoby znaczne przesunięcie w czasie pomiędzy rejestracją sygnałów, a więc dane byłyby zbierane z różnych głębokości. W związku z tym ustawiłem czas integracji na 0.3 s dla obu sygnałów i zsumowałem 50 standardowych cykli, aby utworzyć pojedynczy supercykl. Całkowity czas rejestracji pojedynczego sygnału pozostał taki sam $(0.3s \times 50 = 15s)$, a zatem stosunek sygnału do szumu nie został pogorszony.

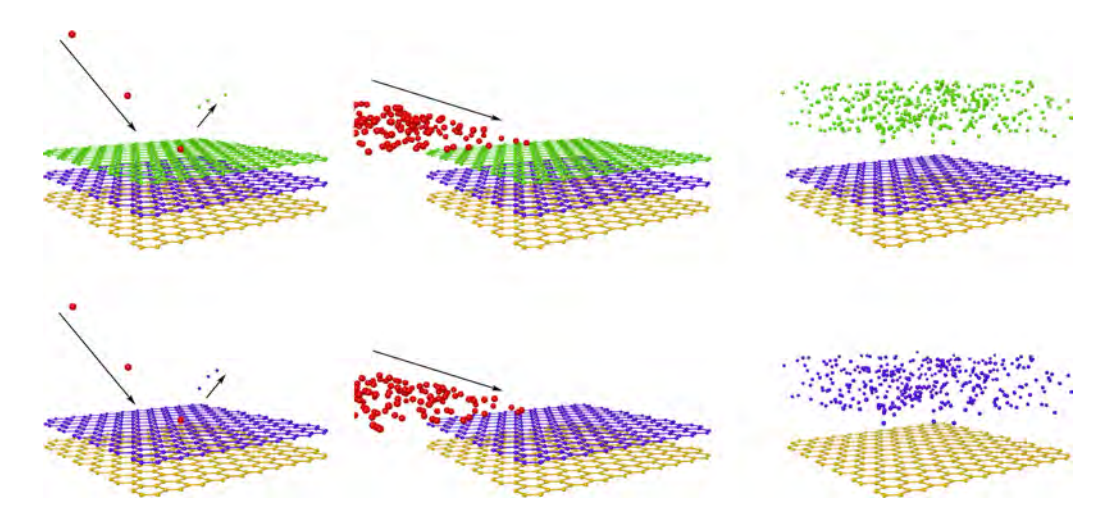
Badania te wykazały, że rodzaj podłoża miał duży wpływ na jakość wzrastanych warstw MoS₂. Pokazałem, że w przypadku podłoży zawierających tlen (tlenek krzemu lub szafir) był on uwalniany z podłoża i przenikał do warstwy podczas wysokotemperaturowego procesu siarkowania. W ten sposób zaobserwowałem tworzenie się trójkątnych domen wysokiej jakości MoS₂ otoczonych amorficznym, silnie utlenionym materiałem. Efekt był szczególnie wyraźny w przypadku tlenku krzemu, co nie było zaskakujące, ponieważ szafir jest materiałem stabilniejszym niż tlenek krzemu. W przypadku podłoża niezawierającego tlenu (azotek boru) wykazałem, że wysokiej jakości warstwa pokrywa całą powierzchnię próbki.

Najbardziej zaskakujący efekt zaobserwowałem, gdy zaplanowaliśmy wzrost MoS₂ na próbce grafen/węglik krzemu [H9]. Moja analiza wykazała, że siarczek molibdenu powstaje pomiędzy warstwą grafenu a podłożem z węglika krzemu, mimo że osadziliśmy prekursory na powierzchni grafenu. Prowadząc dalsze eksperymenty SIMS wykazałem, że wysokotemperaturowy proces siarkowania doprowadził do interkalacji prekursorów pod grafen. Dyfrakcja rentgenowska ujawniła, że warstwy MoS₂ są silnie zorientowane i równoległe do leżącej pod nimi powierzchni podłoża SiC.

Do analizy warstw heksagonalnego azotku boru utworzyłem procedurę pomiarową, którą charakteryzuje atomowa rozdzielczość wgłębna [H10]. Aby to osiągnąć, wykorzystałem tzw. statyczne pomiary SIMS (gęstość wiązki pierwotnej jest bardzo mała i mniej niż 1% powierzchni zostaje zbombardowana) do charakteryzacji wierzchniej warstwy. Następnie wygenerowałem krótki impuls jonów pierwotnych o znacznej gęstości i bardzo dużym kącie padania (69°). Impuls ten preferencyjnie zrywał słabe wiązania van der Waalsa między dwiema warstwami i usunął warstwę wierzchnią, nie powodując żadnych uszkodzeń warstw leżących poniżej. Odsłonięta została więc druga warstwa, którą ponownie scharakteryzowałem przy użyciu statycznych pomiarów SIMS. Powtarzając te kroki, jak schematycznie przedstawiono na rysunku 6, można było scharakteryzować każdą warstwę oddzielnie. Grafika promocyjna przedstawiająca ideę tego eksperymentu znalazł się na okładce czasopisma Journal of Analytical Atomic Spectrometry. [17]

Choć ogólna idea procedury może wydawać się prosta, należy podkreślić, że z technicznego punktu widzenia jest ona bardzo skomplikowana i wymaga jednoczesnej optymalizacji ponad dwudziestu parametrów (napięcie przykładane do różnych soczewek i deflektorów itp.). Co więcej, parametry te nie są niezależne i nawet niewielka zmiana jednego może potencjalnie skutkować rozkalibrowaniem innych. Procedura została wytworzona w sposób iteracyjny: zaczynając od standardowego kąta padania (35°) optymalizowałem parametry aby otrzymać wiązkę wysokiej jakości. Następnie zacząłem stopniowo zwiększać kąt (co jeden stopień) i równocześnie kompensować utratę jednorodności wiązki. Proces był bardzo czasochłonny i zajął mi cały miesiąc (nie wykonywałem w tym czasie żadnych innych pomiarów).

Taka precyzja pozwoliła na zbadanie formowania się wytrąceń węglowych w warstwach azotku boru wzrastanych w różnych trybach wzrostu, a mianowicie wzrostach 3D i tzw. self-terminated. Różne grupy badawcze wykazały, że to przede wszystkim ciśnienie w reaktorze determinuje tryb wzrostu.[18–21] Moje eksperymenty udowodniły, że formacja wytrąceń węglowych również zależy od tego parametru: dla niskiego ciśnienia (tryb wzrostu 3D) wytrącenia węglowe ułożone były w sposób zorganizowany: wytrącenie w jednej warstwie BN zarodkowało formację skupiska węglowego w kolejnej warstwie, tworząc w ten sposób długie ziarna wytrąceń węglowych o kształcie kolumnowym. Przy wysokim ciśnieniu w reaktorze (tryb wzrostu self-terminated) rozkład węgla w warstwach był chaotyczny i nie było żadnej korelacji pomiędzy położeniem skupisk węglowych w sąsiadujących warstwach. Zaobserwowane różnice łatwo było wyjaśnić uwzględniając średnią drogę dyfuzji produktów reakcji. W przypadku niskiego ciśnienia (duża średnia droga dyfuzji) zarówno węgiel jak i



Rysunek 6: Metoda wykorzystania spektrometrii mas jonów wtórnych z atomową rozdzielczością wgłębną do charakteryzacji dwuwymiarowych materiałów van der Waalsa. Warstwa wierzchnia jest analizowana w statycznym reżimie SIMS (bombardowane jest mniej niż 1% powierzchni), następnie krótki impuls jonów pierwotnych o ekstremalnie niskiej energii i dużym kącie padania usuwa całkowicie pierwszą warstwę, nie powodując żadnych znaczących uszkodzeń drugiej warstwy. Dzięki takiemu podejściu każdą warstwę można charakteryzować oddzielnie, a następnie usunąć aby odsłonić kolejną warstwę. Rysunek zaczerpnięty z artykułu [H10].

bor i azot mogły wbudować się w preferowane miejsce i dlatego węgiel dołączał się do istniejących już ziaren węglowych. Z powodu obniżenia średniej drogi dyfuzji przy wysokim ciśnieniu, pierwiastki dołączały się do wzrastanego materiału w miejscu gdzie nastąpiła reakcja. Dlatego rozkład atomów węgla był chaotyczny.

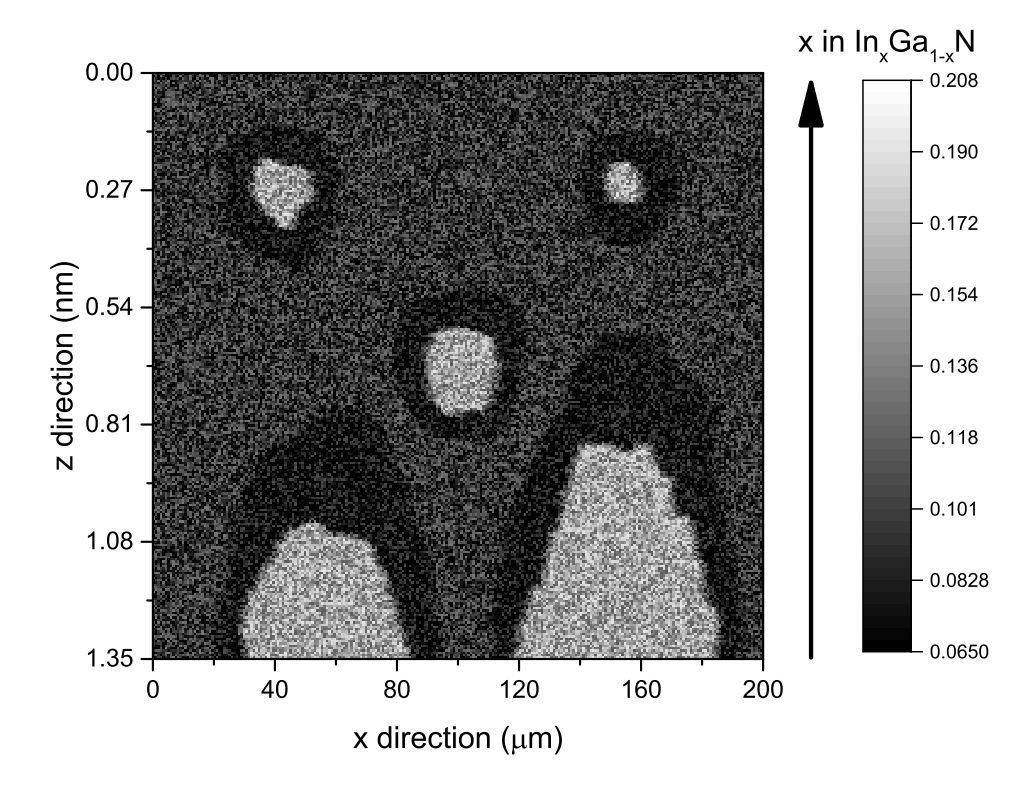
Dwa lata później, wspólnie z grupą badawczą prof. Zbigniewa Postawy z Uniwersytetu Jagiellońskiego, przedstawiliśmy dogłębne wyjaśnienie procesu rozpylania pod dużym kątem padania [H16]. Symulacje komputerowe wykazały, że próbka bez żadnych defektów nie mogła zostać rozpylona w takich warunkach - wszystkie jony odbijały się od powierzchni. Jedynie defekty, zwłaszcza luki, mogą zapoczątkować erozję materiału. Po długotrwałym bombardowaniu liczba defektów i ich rozmiary były na tyle duże, że można było zaobserwować szybkie usunięcie wierzchniej warstwy BN. Symulacje komputerowe i dodatkowe eksperymenty wykazały, że proces rozpylania jest zależny od defektów i anizotropowy - znacznie bardziej intensywny wzdłuż kierunku padania jonów.

SIMS był idealnym kandydatem do badania trójwymiarowego rozkładu tlenu nieintencjonalnie wprowadzonego do warstwy azotku galu podczas wzrostu epitaksjalnego [H11]. Biorąc pod uwagę, że stężenie tlenu było stosunkowo niskie (w granicach 1-10 ppm), głównym wyzwaniem było odjęcie udziału tła komory pomiarowej (zliczenia pochodzące z gazów resztkowych, które były obecne w komorze SIMS). Oszacowałem, że tylko około 5-10% wszystkich zarejestrowanych zliczeń związanych było z faktyczną obecnością tlenu w materiale GaN, a zatem pozostałe zliczenia skutecznie uniemożliwiały ocenę rozkładu przestrzennego tlenu w próbce. Zaproponowałem podejście statystyczne i wykazałem, że losowa eliminacja 90-95% zarejestrowanych zliczeń skutecznie oczyściła uzyskany obraz. Okazało się, że tlen nie był rozłożony jednorodnie, ale gromadził się wzdłuż pionowych struktur. Analiza korelacyjna przy użyciu skaningowej mikroskopii elektronowej wykazała, że struktury te są w rzeczywistości otwartymi rdzeniami dyslokacji śrubowych lub mieszanych. Należy podkreślić, że procedura pomiarowa SIMS wymagała wielu modyfikacji, takich jak flat-field correction dla płytki mikrokanalikowej oraz zadbanie aby wszystkie eksperymenty zostały przeprowadzone w okresie stabilnego działania źródła jonów pierwotnych. Szczegółowy protokół opisujący ten eksperyment został opublikowany w Journal of Visualized Experiments (JoVE) [H15]. Niestety, wideo związane z protokołem nie zostało jeszcze nagrane ze względu na obecną sytuację pandemiczną COVID-19. Jednak animacja pokazująca, jak działa procedura redukcji została już przesłana na stronę JoVE:

https://www.jove.com/t/61065/3d-depth-profile-reconstruction-segregated-impurities-using-secondary (Figure 7). Animacja ta bardzo dobrze oddaje możliwości opracowanej

procedury SIMS.

Obrazowanie trójwymiarowe wykorzystano również do monitorowania fluktuacji koncentracji indu w studniach kwantowych InGaN [H12]. Korzystałem wtedy jeszcze z nieudoskonalonej procedury i studnie kwantowe były rejestrowane jako piki o kształcie gaussowskim i dlatego aby zwizualizować potencjalne wahania koncentracji indu musiałem ustalić definicję początku i końca studni kwantowej. Wybrałem ekstrema lokalne pochodnej sygnału indu, co pozwoliło mi znormalizować sygnał indu i odtworzyć prostokątny kształt studni kwantowej. Dzięki temu możliwe było przedstawienie danych w postaci przekroju poprzecznego, jak pokazano na rysunku 7. Analiza ta wykazała, że średnie stężenie indu wynosiło 10%, co było zgodne z HRXRD. Jednak wykonany przeze mnie pomiar SIMS ujawnił obecność regionów bogatych (koncentracja rzędu 17-20 %) i zubożonych w ind (6-8 %), których nie można było wykryć ani zlokalizować metodą HRXRD.



Rysunek 7: Przekrój koncentracji In w studni kwantowej InGaN. Technika SIMS umożliwia obserwacje wahań stężenia indu. Regiony wzbogacone są otoczone przez regiony zubożone w In, co sugeruje segregację indu podczas wzrostu. Proces ten zachodzi głównie w kierunkach lateralnych, ponieważ całkowita skala z wynosi około 1.35 nm, podczas gdy skala x wynosi 200 μm. Strzałka wskazuje kierunek wzrostu. Rysunek zaczerpnięty z artykułu [H12].

Podczas pracy z jonami o ultra niskiej energii dokonałem ważnej obserwacji. Dla energii standardowych (1 keV i więcej) widmo masowe składało się głównie z pików jednoatomowych: zazwyczaj 80 - 95% wszystkich zarejestrowanych zliczeń, a tylko 5-20% było związanych z sygnałami wieloatomowymi. Dla ultraniskich energii (150 eV i poniżej) sygnały wieloatomowe stanowiły 40-60% wszystkich zarejestrowanych zliczeń. Nie było to zaskakujące, ponieważ energia niesiona przez jony pierwotne była zbyt niska, aby skutecznie zrywać wiązania chemiczne, co prowadziło do zwiększonej emisji cząstek wieloatomowych. Obserwacja ta pozwoliła mi na opracowanie procedury umożliwiającej sondowanie stanu chemicznego badanej próbki [H13]. Udowodniłem również, że w przypadku eksperymentów z tak niską energią padających jonów prawdopodobieństwo połączenia dwóch rozpylonych cząstek było bardzo niskie. Można zatem wnioskować, że rejestracja sygnału wieloatomowego AB oznaczała istnienie wiązania kowalencyjnego między atomami A i B przed eksperymentem SIMS. Procedura ta znacznie rozszerzyła funkcjonalność techniki SIMS i pozwoliła na ogólną identyfikację stanu chemicznego. Przetestowałem tę procedurę na warstwie tytanu nałożonej na tlenek krzemu. Zgodnie z oczekiwaniami udało mi się wykryć zarówno krzemki jak i tlenki tytanu, i udowodniłem, że krzemki tworzą się blisko granicy faz, a tlenki nieco dalej. Ten sam efekt zachodzący w znacznie

większej skali został potwierdzone przez spektroskopię elektronów Augera.[22] Zaletą mojej procedury było zachowanie typowej dla eksperymentów z ultraniską energią subnanometrowej rozdzielczość wgłębnej. W celu walidacji proponowanej metody przetestowałem ją również na warstwie indu osadzonej na tlenku krzemu. W tym przypadku, zgodnie z oczekiwaniami, wykryłem tylko tlenek indu, ponieważ ind nie reaguje z krzemem.

Jak wynika z poprzednich artykułów, często używałem SIMS do wykrywania pierwiastków obecnych w powietrzu (wodór, węgiel, azot i tlen). Jak wcześniej omówiłem, głównym problemem w wykrywaniu tych pierwiastków jest obecność gazów resztkowych w komorze pomiarowej i ich pasożytniczy udział w rejestrowanych zliczeniach. Aby zminimalizować ten problem, Miwa *et al.*[23] zaproponował dodatkowe ulepszenie - rozpylanie wstępne. W tej procedurze, przed właściwym pomiarem, próbka o wysokiej czystości była rozpylana przez długi czas gęstą i wysokoenergetyczną wiązką pierwotną. Atomy rozpylone z tej próbki osadzają się na soczewce immersyjnej i powierzchni próbki właściwej, co zmniejsza proces reimplantacji lekkich pierwiastków, a w konsekwencji poprawia granice wykrywalności. Z biegiem lat krzem otrzymany metodą topienia strefowego stał się najczęściej wykorzystywanym materiałem do rozpylania wstępnego.

Zauważyłem, że podczas eksperymentów z ultraniską energią ta przewaga nie była już wystarczająca. Zaproponowałem więc ulepszenie metody Miwa *et al.* Zamiast krzemu skorzystałem z metalicznego tytanu o wysokiej czystości [H14]. Udowodniłem, że właściwości pochłaniające tytanu pozwoliły osiągnąć lepsze granice wykrywalności wodoru i tlenu. Nie zaobserwowano bezpośredniej poprawy w pomiarach węgla i azotu, jednak należy zauważyć, że w celu osiągnięcia optymalnych warunków krzem musiał być wstępnie rozpylany przez około pięćdziesiąt godzin, a tytan redukował ten czas do około dwudziestu. Zastosowanie tytanu do rozpylania wstępnego jest szczególnie ważne do pomiarów z rozdzielczością subnanometrową, gdy granice wykrywalności lekkich pierwiastków ulegają znacznemu pogorszeniu. Tabela 1 przedstawia porównanie poziomów tła dla eksperymentów bez rozpylania wstępnego oraz z użyciem krzemu i tytanu.

Element / Target	Without	Si	Ti
Hydrogen	$(9.22 \pm 0.84) \times 10^{18}$	$(4.04 \pm 0.63) \times 10^{18}$	$(9.04 \pm 5.42) \times 10^{17}$
Carbon	$(2.04 \pm 0.13) \times 10^{18}$	$(9.71 \pm 3.36) \times 10^{16}$	$(9.65 \pm 3.60) \times 10^{16}$
Nitrogen	$(2.76 \pm 0.29) \times 10^{17}$	$(1.01 \pm 0.34) \times 10^{16}$	$(1.02 \pm 0.32) \times 10^{16}$
Oxygen	$(3.43 \pm 0.27) \times 10^{18}$	$(4.05 \pm 0.60) \times 10^{17}$	$(8.45 \pm 3.34) \times 10^{16}$

Table 1: Granice wykrywalności pierwiastków przy zastosowaniu niskich energii padających jonów. Wyniki przedstawiono dla pomiarów bez oraz z rozpylaniem wstępnym, zarówno dla krzemu jak i tytanu. Wszystkie wartości podane są w atomach/cm³. Tabela zaczerpnięta z artykułu [H14].

4.4 Podsumowanie

Opisane powyżej modyfikacje procedur pomiarowych pozwoliły mi na przeprowadzenie badań SIMS z nanometrową i subnanometrową rozdzielczością wgłębną. Jakość uzyskanych wyników znacznie przewyższa możliwości aparatu CAMECA IMS SC Ultra przy zastosowaniu standardowych procedur pomiarowych. Istniejące procedury można łatwo dostosować i zoptymalizować dla różnych materiałów, o ile istnieją pewne podobieństwa. Na przykład procedurę wykorzystywaną do wykrywania aglomeracji tlenu w azotku galu [H11,15] można łatwo wykorzystać dla innych materiałów, takich jak na przykład węglik krzemu. Podobnie możliwość charakteryzowania heksagonalnego azotku boru z atomową rozdzielczością wgłębną [H10] może być zaimplementowana do badania innych struktur van der Waalsa, oczywiście po pewnych modyfikacjach. Takie podejście jest znacznie szybsze i zajmuje kilka godzin, podczas gdy opracowanie nowej procedury pomiarowej od podstaw zwykle zajmuje kilka tygodni.

Wyniki przeprowadzonych przeze mnie badań rozwiązały liczne problemy technologiczne związane ze wzrostem materiałów, ich właściwościami, a także działaniem przyrządów wykonanych z tych materiałów. Na szczególną uwagę zasługują pace poświęcone materiałom dwuwymiarowym

([H1-2,4-5,8-10,16]). Minęło zaledwie kilkanaście lat od kiedy Novoselov i Geim po raz pierwszy otrzymali pojedynczą warstwę grafenu, a już powstają pierwsze przyrządy elektroniczne i optoelektroniczne, których technologia oparta jest na grafenie i innych materiałach 2D. Integracja tych innowacyjnych materiałów z istniejącymi liniami produkcyjnymi wymusza aby procesy ich wzrostu i obróbki spełniały rygorystyczne wymagania czystości. Dlatego też badania nad zanieczyszczeniami obecnymi w materiałach dwuwymiarowych są niezwykle istotne. Istnieje oczywiście wiele technik, które pozwalają na wykrywanie zanieczyszczeń, np. Rentgenowska analiza fluorescencyjna z całkowitym odbiciem wiązki padającej,[8], Rentgenowska spektroskopia energodyspersyjna,[24] spektroskopia strat energii elektronów, [25] czy technika atomowej spektrometrii emisyjnej ze wzbudzeniem w plazmie indukowanej[26]. Dzięki nim możliwe jest wykrycie zanieczyszczeń, jednak nie ich lokalizacja. Z kolei metody, które charakteryzują się bardzo dobrą rozdzielczością przestrzenną (np. transmisyjna mikroskopia elektronowa) zwykle nie posiadają dostatecznej czułości, żeby wykryć zanieczyszczenia. Udoskonalona przeze mnie technika SIMS umożliwia natomiast zarówno wykrywanie, jak i lokalizację zanieczyszczeń. Co więcej, SIMS daje bezpośrednią możliwość wykrywania wodoru, co jest rzadkością wśród wszystkich metod analitycznych. Opracowane przeze mnie rozwiązania są więc bardzo przydatne w dalszej optymalizacji procesów wzrostu materiałów dwuwymiarowych, które już w najbliższej przyszłości mogą zrewolucjonizować szeroko rozumianą elektronikę i optoelektronikę użytkową.

Badałem również półprzewodniki szerokoprzerwowe ([H6,11,15]), które również stają się coraz ważniejszymi materiałami we współczesnej elektronice. Badania nad azotkiem galu ([H11,15]) ponownie koncentrują się na ocenie czystości procesu wzrostu oraz roli defektów w nieintencjonalnym wbudowywaniu się tlenu w strukturę GaN. Tylko dzięki korelacji wyników SIMS z położeniem dyslokacji można było wykazać silną tendencję tlenu do wbudowywania się w materiał wzdłuż rdzeni dyslokacji śrubowych i mieszanych. Okazuje się więc, że skuteczną metodą na redukcję poziomu zanieczyszczeń jest nie tylko dbałość o szczelność reaktora, ale również opracowanie technologii wzrostu, która obniży gęstość dyslokacji. W przypadku innego półprzewodnika szerokoprzerwowego - tlenku cynku - niezwykle istotnym zagadnieniem technologicznym jest domieszkowanie, wykonywane zazwyczaj w procesie implantacji jonami metali ziem rzadkich. Moje badania [H6] udowodniły, że podczas tego procesu dochodzi do powstania warstwy zubożonej w tlen. Wyniki badań rentgenowskich sugerowały wystąpowanie takiego zjawiska, jednak dopiero dzięki technice SIMS można było bezpośrednio zaobserwować dyfuzję tlenu ku powierzchni oraz określić grubość warstwy zubożonej.

Prowadziłem również badania nad wielowarstwowymi strukturami przyrządów półprzewodnikowych ([H3,7,12]), które powszechnie wykorzystywane są w optoelektronice. Oczywiście SIMS od dawna stosowany był do badania takich próbek, jednak przede wszystkim do określenia poziomu domieszek w grubych warstwach. Opracowane przeze mnie procedury umożliwiły również analizę najcieńszych warstw przyrządów, takich jak studnie kwantowe, złącza tunelowe czy supersieci, dzięki czemu możliwe jest wykonywanie analizy usterek tych warstw. Prace te zaowocowały nawiązaniem współpracy z licznymi ośrodkami przemysłowymi i badawczymi.

Opracowałem również rozwiązania, które zmieniają sposób prowadzania eksperymentów SIMS, a dzięki temu poprawiają granice wykrywalności, pozwalają na badanie bardzo grubych struktur oraz umożliwiają jakościową analizę stanu chemicznego badanej próbki ([H2,7,11,13-15]).

Pracowałem więc nad bardzo ważnymi materiałami, a rozwiązania istotnych problemów technologicznych, które dostarczyłem są w większości przypadków unikatowe - bardzo trudno byłoby dojść do analogicznych wniosków wykorzystując inne techniki badawcze. Wykonywanie badań SIMS z nanometrową i subnanometrową rozdzielczością wgłębną jest bardzo wymagające, jednak w wielu przypadkach nie ma alternatyw. Dlatego należy podkreślić, że dorobek mojej pracy to nie tylko rozwiązywanie konkretnych problemów i pozyskiwanie cennych informacji o właściwościach konkretnych materiałów. Moim celem było zapewnienie, aby charakteryzacja z subnanometrową rozdzielczością wgłębną była dostępna dla bardzo szerokiej grupy różnych materiałów. Aby to osiągnąć, stworzyłem dużą bazę danych dedykowanych procedur - obecnie jest ich ponad 10000 i ciągle tworzę nowe. Każdą z nich zapisuję i kataloguję do dalszego wykorzystania, stworzyłem również skrypt do wyszukiwania procedur. Jak wspomniałem omawiając procedurę dedykowaną heksagonalnemu

azotkowi boru, utworzyłem 43 procedury, które zapewniały wysoką jakość wiązki o różnym kącie padania w zakresie 35 - 77°, różniące się o jeden stopień (te procedury nazywane są "procedurami częściowymi" i zawierają tylko parametry związane z wiązką pierwotną). Wszystkie zostały zoptymalizowane pod kątem badania azotku boru (są to tak zwane "procedury materiałowe" i poza parametrami wiązki pierwotnej są zoptymalizowane pod kątem detekcji boru i azotu). Wszystkie zostały zoptymalizowane pod kątem wykrywania węgla w azotku boru ("specyficzne procedury" - stosowane do jednego zadania). Stworzyłem również 21 specyficznych procedur do wykrywania tlenu i 19 specyficznych procedur do wykrywania chloru. Aby udowodnić, że moje podejście jest słuszne, użyłem 43 procedur cząstkowych i opracowałem 43 procedury materiałowe do charakteryzacji grafenu i rzeczywiście było to znacznie szybsze niż opracowanie ich od podstaw. Podobnie zoptymalizowałem 21 i 19 specyficznych procedur wykrywania tlenu i chloru. Niektóre procedury grafenowe zostały dodatkowo zmienione, aby uwzględnić wpływ podłoża na analizę SIMS (tzw. "procedury specyficzne dla podłoża"), ponieważ wykonywałem pomiary grafenu na krzemie, tlenku krzemu, przewodzącym i izolującym węgliku krzemu, azotku galu, germanie, niklu i złocie. W tym momencie miałem w sumie ponad 300 procedur do materiałów 2D (nie licząc procedur częściowych). Tak więc, jeśli miałbym za zadanie wykryć tlen w dwuwymiarowym selenku platyny (nigdy nie mierzyłem takiej próbki), najprawdopodobniej rozpocząłbym optymalizację jednej z procedur wykrywania tlenu w azotku boru. Ta procedura jest lepszym kandydatem niż metoda dedykowana do grafenu, ponieważ azotek boru, podobnie jak selenek platyny, składa się z dwóch różnych atomów, a grafen tylko z jednego. Jeśli jednak warstwa selenku platyny zostałaby umieszczona na podłożu silnie izolującym (może to spowodować ładowanie podczas eksperymentu SIMS) zacząłbym od procedury specyficznej dla podłoża: detekcja tlenu w grafenie na izolującym węgliku krzemu. Okazuje się bowiem, że optymalizacja działa elektronowego (stosowanego do kompensacji efektu ładowania) jest bardziej czasochłonna niż dołączenie dodatkowego sygnału potrzebnego do analizy składu selenku platyny.

Jak pokazuje ten przykład, moja praca była bardzo systematyczna i nie powinna być postrzegana jako seria studium przypadków. Tworząc dużą bazę danych dedykowanych procedur, znacznie skróciłem czas potrzebny do uzyskania wysokiej jakości pomiaru nieznanej próbki, dla której nie mam żadnego doświadczenia. Można zatem stwierdzić, że osiągnąłem nową funkcjonalność techniki SIMS: charakteryzację z nanometrową i subnanometrową rozdzielczością wgłębną, która jest dostępna dla bardzo szerokiej gamy materiałów, a nie tylko kilku wybranych próbek.

Co więcej, ta nowa funkcjonalność została doceniona przez społeczność naukową. W latach 2016-2018 miałem wiele problemów z publikacją wyników badań i większość moich artykułów była wielokrotnie odrzucana przez edytorów i recenzentów czasopism branżowych. Recenzenci często twierdzili, że taka dokładność jest niemożliwa do osiągnięcia. Po opublikowaniu kilku artykułów stało się to łatwiejsze, ponieważ umieszczałem odniesienia do poprzednich prac (jako efekt uboczny mam stosunkowo dużą liczbę autocytowań), które przekonały recenzentów o wypracowanych przeze mnie możliwościach pomiarowych. Obecnie nie otrzymuję już tego typu uwag, a SIMS z subnanometrową rozdzielczością wgłębną został powszechnie uznany. W jednej z ostatnich recenzji jeden z recenzentów napisał: "I must admit that it was hard for me to believe that SIMS measurements with such precisions are possible. However, I have checked a couple of articles by P.P. Michalowski and seen that he already made many SIMS measurements on 2D materials with atomic depth resolution. I am in awe, congratulations!" ("Muszę przyznać, że trudno mi było uwierzyć, że pomiary SIMS z taką dokładnością są możliwe. Sprawdziłem jednak kilka artykułów P.P. Michałowskiego i zobaczyłem, że wykonał już wiele pomiarów SIMS na materiałach 2D z atomową rozdzielczością wgłębną. Jestem pod wrażeniem, gratulacje!")

4.5 Bibliografia

- [1] K. Wittmaack. High-sensitivity depth profiling of arsenic and phosphorus in silicon by means of SIMS. *Appl. Phys. Lett.*, 29:552, 1976.
- [2] B. Y. Ber, Y. A. Kudriavtsev, A. V. Merkulov, S. V. Novikov, D. E. Lacklison, J. W. Orton, T. S. Cheng, and C. T. Foxon. Secondary ion mass spectroscopy investigations of magnesium and

- carbon doped gallium nitride films grown by molecular beam epitaxy. *Semicond. Sci. Technol.*, 13:71–74, 1998.
- [3] C. Y. Chiou, C. C. Wang, Y. C. Ling, and C. I. Chiang. Secondary ion mass spectrometry analysis of In-doped p-type GaN films. *Appl. Surf. Sci.*, 203-204:482–485, 2003.
- [4] M. Emziane, K. Durose, D. P. Halliday, A. Bosio, and N. Romeo. In situ oxygen incorporation and related issues in CdTe/CdS photovoltaic devices. *J. Appl. Phys.*, 100:013513, 2006.
- [5] T. Matsunaga, S. Yoshikawa, and K. Tsukamoto. Secondary ion yields of C, Si, Ge and Cs surface density and concentration in SIMS. *Surf. Sci.*, 515:390–402, 2002.
- [6] H. Gnaser. SIMS Detection in the 10^{12} atoms cm^{-3} Range. Surf. Interface Anal., 25:737–740, 1997.
- [7] W. Strupinski, K. Grodecki, P. Caban, P. Ciepielewski, I. Jozwik-Biala, and J.M. Baranowski. Formation mechanism of graphene buffer layer on SiC(0001). *Carbon*, 81:63–72, 2015.
- [8] Grzegorz Lupina, Julia Kitzmann, Ioan Costina, Mindaugas Lukosius, Christian Wenger, Andre Wolff, Sam Vaziri, Mikael Östling, Iwona Pasternak, Aleksandra Krajewska, Wlodek Strupinski, Satender Kataria, Amit Gahoi, Max C. Lemme, Guenther Ruhl, Guenther Zoth, Oliver Luxenhofer, and Wolfgang Mehr. Residual Metallic Contamination of Transferred Chemical Vapor Deposited Graphene. ACS Nano, 9(5):4776–4785, 2015.
- [9] Wenjing Xie, Lu-Tao Weng, Kai Mo Ng, Chak K. Chan, and Chi-Ming Chan. Clean graphene surface through high temperature annealing. *Carbon*, 94:740 748, 2015.
- [10] Philipp Braeuninger-Weimer, Barry Brennan, Andrew J. Pollard, and Stephan Hofmann. Understanding and Controlling Cu-Catalyzed Graphene Nucleation: The Role of Impurities, Roughness, and Oxygen Scavenging. *Chem. Mater.*, 28(24):8905–8915, 2016.
- [11] Harry Chou, Ariel Ismach, Rudresh Ghosh, Rodney S. Ruoff, and Andrei Dolocan. Revealing the planar chemistry of two-dimensional heterostructures at the atomic level. *Nature Communications*, 6(1):7482, 2015.
- [12] G. Slodzian, J. C. Lorin, and A. Havette. Isotopic effect on the ionization probabilities in secondary ion emission. *Journal de Physique Lettres*, 41:555–558, 1980.
- [13] Y. Taga. Sputtering and secondary ion emission from metals and alloys subjected to oxygen ion bombardment. *Secondary Ion Mass Spectrometry SIMS*, V:32–37, 1986.
- [14] H. Gnaser and I. D. Hutcheon. Significance of isotope effects for secondary-ion emission models. *Physical Review B*, 38:11112–11117, 1988.
- [15] F. A. Stevie, P. M. Kahora, D. S. Simons, and P. Chi. Secondary ion yield changes in si and gaas due to topography changes during o+2 or cs+ ion bombardment. *Journal of Vacuum Science & Technology A*, 6:76, 1988.
- [16] A. Turos, P. Jozwik, M. Wojcik, J. Gaca, R. Ratajczak, and A. Stonert. Mechanism of damage buildup in ion bombarded zno. *Acta Materialia*, 134:249–256, 2017.
- [17] Front cover http://dx.doi.org/10.1039/c9ja90024a. *Journal of Analytical Atomic Spectrometry*, 34:791–791, 2019.
- [18] Qing S Paduano, Michael Snure, James Bondy, and Timothy WC Zens. Self-terminating growth in hexagonal boron nitride by metal organic chemical vapor deposition. *Appl. Phys. Express*, 7(7):071004, 2014.
- [19] Michael Snure, Qing Paduano, Merle Hamilton, Jodie Shoaf, and J Matthew Mann. Optical characterization of nanocrystalline boron nitride thin films grown by atomic layer deposition. *Thin Solid Films*, 571:51–55, 2014.
- [20] Michael Snure, Qing Paduano, and Arnold Kiefer. Effect of surface nitridation on the epitaxial growth of few-layer sp2 bn. *J. Cryst. Growth*, 436:16–22, 2016.
- [21] Qing Paduano, Michael Snure, David Weyburne, Arnold Kiefer, Gene Siegel, and Jianjun Hu. Metalorganic chemical vapor deposition of few-layer sp2 bonded boron nitride films. *J. Cryst. Growth*, 449:148 155, 2016.
- [22] L. J. Brillson, M. L. Slade, H. W. Richter, H. VanderPlas, and R. T. Fulks. Titanium–silicon and silicon dioxide reactions controlled by low temperature rapid thermal annealing. *J. Vac. Sci. Technol. A*, 4(3):993–997, 1986.

- [23] Shiro Miwa, Ichiro Nomachi, and Hideo Kitajima. High sensitivity analysis of atmospheric gas elements. *Appl. Surf. Sci.*, 252(19):7247 7251, 2006.
- [24] Adriano Ambrosi and Martin Pumera. The CVD graphene transfer procedure introduces metallic impurities which alter the graphene electrochemical properties. *Nanoscale*, 6:472–476, 2014.
- [25] Benjamín Alemán, William Regan, Shaul Aloni, Virginia Altoe, Nasim Alem, Cağlar Girit, Baisong Geng, Lorenzo Maserati, Michael Crommie, Feng Wang, and A. Zettl. Transfer-Free Batch Fabrication of Large-Area Suspended Graphene Membranes. *ACS Nano*, 4(8):4762–4768, 2010.
- [26] Airui Zhang, Hai Wang, Pengfei Zha, Meiling Wang, Haifeng Wang, Bingqi Fan, Danhua Ren, Yanxiang Han, and Sitian Gao. Microwave-induced combustion of graphene for further determination of elemental impurities using ICP-OES and TXRF. *J. Anal. At. Spectrom.*, 33:1910–1916, 2018.
- 5 Informacja o wykazywaniu się istotną aktywnością naukową albo artystyczną realizowaną w więcej niż jednej uczelni, instytucji naukowej lub instytucji kultury, w szczególności zagranicznej.

5.1 Artykuły naukowe

• A. Inaba, Y. Miyazaki, **P.P. Michałowski**, E. Gracia-Espino, B. Sundqvist, T. Wågberg. "Calorimetric measurements on Li4C60 and Na4C60" *The Journal of Chemical Physics*, 142(16):164706, 2015.

Współpraca zagraniczna: Osaka University, Osaka, Japonia; Jilin University, Changchun, Chiny

• **[H1] P.P. Michalowski**, W. Kaszub, A. Merkulov, W. Strupiński. "Secondary ion mass spectroscopy depth profiling of hydrogen-intercalated graphene on SiC" *Applied Physics Letters*, 109(1):011904, 2016.

Współpraca zagraniczna: CAMECA, Gennevilliers, Francja

• **[H3] P.P. Michałowski**, P. Gutowski, D. Pierciska, K. Pierciski, M. Bugajski, W. Strupiski. "Characterization of the superlattice region of a quantum cascade laser by secondary ion mass spectrometry" *Nanoscale*, 9:17571–17575, 2017.

Współpraca krajowa: Instytut Technologii Elektronowej, Warszawa, Polska

• J. Wróbel, K. Grodecki, D. Benyahia, K. Murawski, K. Michalczewski, J. Grzonka, J. Boguski, K. Gorczyca, G.A. Umana-Membreno, Ł. Kubiszyn, A. Kębłowski, **P.P. Michałowski**, E. Gomółka, P. Martyniuk, J. Piotrowski, A. Rogalski. "Structural and optical characterization of the high quality Be-doped InAs epitaxial layer grown on GaAs substrate" *Proceedings of SPIE - The International Society for Optical Engineering*, 10830:176 – 181, 2018.

Współpraca krajowa: Wojskowa Akadamia Techniczna, Warszawa, Polska; VIGO System, Ożarów Mazowiecki, Polska

Współpraca zagraniczna: University of Western Australia, Crawley, Australia

• K.J. Sankaran, M. Ficek, S. Kunuku, K. Panda, C.-J. Yeh, J.Y. Park, M. Sawczak, **P.P. Michałowski**, K.-C. Leou, R. Bogdanowicz, I-N. Lin, K. Haenen. "Self organized multi-layered graphene boron-doped diamond hybrid nanowalls for high performance electron emission devices" *Nanoscale*, 10:1345–1355, 2018.

Współpraca krajowa: Politechnika Gdańska, Gdańsk, Polska; Instytut Maszyn Przepływowych Polskiej Akademii Nauk, Gdańsk, Polska

Współpraca zagraniczna: Hasselt University, Diepenbeek, Belgia; IMOMEC, IMEC Vzw, Diepenbeek, Belgia; National Tsing Hua University, Hsinchu, Tajwan; Institute for Basic Science, Daejeon, Korea Południowa; Korea Advanced Institute of Science and Technology, Daejeon, Korea Południowa; Tamkang University, Tamsui, Tajwan

• **[H5] P.P. Michalowski**, I. Pasternak, P. Ciepielewski, F. Guinea, W. Strupiński. "Formation of a highly doped ultra-thin amorphous carbon layer by ion bombardment of graphene" *Nanotechnology*, 29(30):305302, 2018.

Współpraca zagraniczna: Imdea Nanoscience, Madryt, Hiszpania; University of Manchester, Manchester, Wielka Brytania

J. Grzonka, I. Pasternak, P.P. Michalowski, V. Kolkovsky, W. Strupinski. "Influence of hydrogen intercalation on graphene/Ge(001)/Si(001) interface" *Applied Surface Science*, 447:582 – 586, 2018.

Współpraca krajowa: Politechnika Warszawska, Warszawa, Polska; Instytut Fizyki Polskiej Akademii Nauk, Warszawa, Polska

Współpraca zagraniczna: Technische Universitat Dresden, Drezno, Niemcy

• **[H9] P.P. Michałowski**, P. Knyps, P. Ciepielewski, P.A. Caban, E. Dumiszewska, G. Kowalski, M. Tokarczyk, J.M. Baranowski. "Growth of highly oriented MoS2 via an intercalation process in the graphene/SiC(0001) system" *Physical Chemistry Chemical Physics*, 21:20641–20646, 2019.

Współpraca krajowa: Uniwersytet Warszawski, Warszawa, Polska

R. Muydinov, A. Steigert, M. Wollgarten, P.P. Michałowski, U. Bloeck, A. Pflug, D. Erfurt, R. Klenk, S. Körner, I. Lauermann, B. Szyszka. "Crystallisation Phenomena of In2O3:H Films" *Materials*, 12(2), 2019.

Współpraca zagraniczna: Technical University Berlin, Berlin, Niemcy; Helmholtz-Zentrum Berlin fur Materialien und Energie GmbH, Berlin, Niemcy; Fraunhofer Institute for Surface Engineering and Thin Films IST, Brunszwik, Niemcy;

• [H12] P.P. Michalowski, E. Grzanka, S. Grzanka, A. Lachowski, G. Staszczak, J. Plesiewicz, M. Leszczyski, A. Turos. "Indium concentration fluctuations in InGaN/GaN quantum wells" *Journal of Analytical Atomic Spectrometry*, 34:1718–1723, 2019.

Współpraca krajowa: Instytut Fizyki Wysokich Ciśnień, Warszawa, Polska; TopGaN, Warszawa, Polska

• I. Jówik, A. Barcz, E. Dąbrowska, E. Dumiszewska, **P.P. Michałowski**. "Damage induced voltage alteration (DIVA) contrast in SEM images of ion-irradiated semiconductors" *Ultramicroscopy*, 204:6 – 9, 2019.

Współpraca krajowa: Sieć Badawcza Łukasiewicz - Instytut Technologii Elektronowej, Warszawa, Polska; Instytut Fizyki Polskiej Akademii Nauk, Warszawa, Polska

• Ł. Frąckowiak, P. Kuświk, G.Da. Chaves-O'Flynn, M. Urbaniak, M. Matczak, **P.P. Michałowski**, A. Maziewski, M. Reginka, A. Ehresmann, F. Stobiecki. "Magnetic Domains without Domain Walls: A Unique Effect of He+ Ion Bombardment in Ferrimagnetic Tb/Co Films" *Physical Review Letters*, 124:047203, 2020.

Współpraca krajowa: Instytut Fizyki Molekularne Polskiej Akademii Nauk, Poznań, Polska; Uniwersytet w Białymstoku, Białystok, Polska

Współpraca zagraniczna: University of Kassel, Kassel, Niemcy

• A. Cruz, F. Ruske, A. Eljarrat, **P.P. Michałowski**, A.B. Morales-Vilches, S. Neubert, E. Wang, C. T. Koch, B. Szyszka, R. Schlatmann, B. Stannowski. "Influence of Silicon Layers on the Growth of ITO and AZO in Silicon Heterojunction Solar Cells" *IEEE Journal of Photovoltaics*, 10(2):703–709, 2020.

Współpraca zagraniczna: Helmholtz-Zentrum Berlin fur Materialien und Energie, Berlin, Niemcy; Humboldt-Universitat Berlin, Berlin, Niemcy; Technische Universitat Berlin, Berlin, Niemcy

A. Gocalinska, A. Pescaglini, E. Secco, E.E. Mura, K. Thomas, A. Curran, F. Gity, R. Nagle, M. Schmidt, P.P. Michalowski, P.K. Hurley, I. Povey, E. Pelucchi. "Next generation low temperature polycrystalline materials for above IC electronics. High mobility n- and p-type III–V metalorganic vapour phase epitaxy thin films on amorphous substrates" *Journal of Physics: Photonics*, 2(2):025003, 2020.

Współpraca zagraniczna: Tyndall National Institute, Cork, Irlandia

• V.N. Popok, P.A. Caban, **P.P. Michałowski**, R. Thorpe, L.C. Feldman, K. Pedersen. "Two-dimensional electron gas at the AlGaN/GaN interface: Layer thickness dependence" *Journal of Applied Physics*, 127(11):115703, 2020.

Współpraca zagraniczna: Aalborg University, Aalborg, Dania; State University of New Jersey, Piscataway, USA

• J. Wróbel, G.A. Umana-Membreno, J. Boguski, D. Sztenkiel, **P.P. Michałowski**, P. Martyniuk, L. Faraone, J. Wróbel, A. Rogalski. "Locally-Strain-Induced Heavy-Hole-Band Splitting Observed in Mobility Spectrum of p-Type InAs Grown on GaAs" *Physica Status Solidi Rapid Research Letters*, 14(4):1900604, 2020.

Współpraca krajowa: Wojskowa Akadamia Techniczna, Warszawa, Polska; Instytut Fizyki Polskiej Akademii Nauk, Warszawa, Polska

Współpraca zagraniczna: University of Western Australia, Crawley, Australia

• A. Wójcik, W. Kolkowski, I. Pasternak, W. Strupiski, S. Kozdra, **P.P. Michałowski**. "Electrically active and hydrogen passivated Zn in GaAs/AlGaAs specifically distinguished during secondary ion mass spectrometry depth profiling" *Journal of Analytical Atomic Spectrometry*, 36:178–184, 2021.

Współpraca krajowa: Uniwersytet Warszawski, Warszawa, Polska; VIGO System, Ożarów Mazowiecki, Polska; Politechnika Warszawska, Warszawa, Polska

• A. Taube, M. Kamiński, M. Ekielski, R Kruszka, J. Jankowska-Śliwiska, **P.P. Michałowski**, J. Zdunek, A. Szerling. "Selective etching of p-GaN over A0.25Ga0.75N in Cl2/Ar/O2 ICP plasma for fabrication of normally-off GaN HEMTs" *Materials Science in Semiconductor Processing*, 122:105450, 2021.

Współpraca krajowa: Sieć Badawcza Łukasiewicz - Instytut Technologii Elektronowej, Warszawa, Polska; Politechnika Warszawska, Warszawa, Polska;

 P. Ciechanowicz, S. Gorantla, P.P. Michałowski, E. Zdanowicz, J.-G. Rousset, D. Hlushchenko, K. Adamczyk, D. Majchrzak, R. Kudrawiec, D. Hommel. "Arsenic-Induced Growth of Dodecagonal GaN Microrods with Stable a-Plane Walls" *Advanced Optical Materials*, 9(5):2001348, 2021.

Współpraca krajowa: Sieć Badawcza Łukasiewicz - PORT Polski Ośrodek Rozwoju Technologii, Wrocław, Polska; Uniwersytet Wrocławski, Wrocław, Polska; Politechnika Wrocławska, Wrocław, Polska; Instytut Niskich Temperatur i Badań Strukturalnych Polskiej Akademii Nauk, Wrocław, Polska

• P. Kamiski, R. Budzich, J. Gaca, **P.P. Michałowski**, R. Kozłowski, A. Harmasz, T. Ciuk, and J. Płocharski. "Effect of oxidation temperature on the inhomogeneity of chemical composition and density in nanometric SiO2 films grown on 4H-SiC" *Journal of Materials Chemistry C*, 9:4393–4404, 2021.

Współpraca krajowa: Politechnika Warszawska, Warszawa, Polska

M. Jacquet, M. Izzo, S. Osella, S. Kozdra, P.P. Michałowski, D. Gołowicz, K. Kazimierczuk, M.T. Gorzkowski, A. Lewera, M. Teodorczyk, B. Trzaskowski, R. Jurczakowski, D.T. Gryko, and J. Kargul. "Development of a universal conductive platform for anchoring photo- and electroactive proteins using organometallic terpyridine molecular wires" *Nanoscale*, 13:9773–9787, 2021.

Współpraca krajowa: Uniwersytet Warszawski, Warszawa, Polska; Instytut Chemii Organicznej Polskiej Akademii Nauk, Warszawa, Polska

• T. Ciuk, W. Kaszub, K. Kosciewicz, A. Dobrowolski, J. Jagiello, A. Chamryga, J. Gaca, M. Wojcik, D. Czolak, B. Stanczyk, K.a Przyborowska, R. Kozlowski, M. Kozubal, **P.P. Michalowski**, M.J. Szary, P. Kaminski. "Highly-doped p-type few-layer graphene on uid off-axis homoepitaxial 4H-SiC" *Current Applied Physics*, 27:17–24, 2021.

Współpraca krajowa: Uniwersytet Warszawski, Warszawa, Polska; Politechnika Poznańska, Poznań, Polska

• [H16] P.P. Michałowski, D. Maciążek, Z. Postawa, P.A. Caban, S. Kozdra, A. Wójcik, J.M. Baranowski. "Defect-mediated sputtering process of boron nitride during high incident angle low-energy ion bombardment" *Measurement*, 179:109487, 2021.

Współpraca krajowa: Uniwersytet Warszawski, Warszawa, Polska; Uniwersytet Jagieloński, Kraków, Polska

5.2 Projekty

• 2015-2016 Graphene-Based Revolutions in ICT And Beyond, Seventh Framework Programme, EU, wykonawca (zakończony).

Współpraca zagraniczna: 155 instytucji z 24 krajów

• 2015-2018 Graphene for Integrated Circuit Applications (GRAPHICA), M-ERA.NET, EU, wykonawca (zakończony).

Współpraca krajowa: Nano-Carbon, Warszawa, Polska Współpraca zagraniczna: IHP, Frankfurt Oder, Niemcy; AIXTRON, Aachen, Niemcy

- 2016-2018 Graphene Flagship Core Project 1, Horizon 2020, EU, wykonawca (zakończony).
 Współpraca zagraniczna: 155 instytucji z 24 krajów
- 2018-2020 Graphene Flagship Core Project 2, Horizon 2020, EU, wykonawca (zakończony).
 Współpraca zagraniczna: 187 instytucji z 21 krajów
- 2017-2020 Semiconductor materials technologies for high power and frequency electronics (WidePOWER), NCBR, Polska, wykonawca (zakończony).

Współpraca krajowa: Politechnika Warszawska, Warszawa, Polska; Sieć Badawcza Łukasiewicz - Instytut Technologii Elektronowej, Warszawa, Polska; Nano-Carbon, Warszawa, Polska

- 2020-2023 Graphene Flagship Core Project 3, Horizon 2020, EU, wykonawca (trwający).
 Współpraca zagraniczna: 177 instytucji z 21 krajów
- 2020-2022 Modeling Unconventional Nanoscaled Device FABrication (MUNDFAB), Horizon 2020, EU, przedstawiciel partnera w konsorcjum i kierownik projektu (trwający).
 Współpraca zagraniczna: Fraunhofer Institute for Integrated Systems and Device Technology IISB, Erlangen, Niemcy; CEA-Leti, Grenoble, Francja; Institute for Microelectronics and Microsystems, Katania, Włochy; LAAS-CNRS, Tuluza, Francja; STMicroelectronics, Crolles, Francja; Technische Universitat Wien, Wiedeń, Austria

5.3 Inna współpraca

- Applied Materials, Gloucester, USA (uprzywilejowany partner projektu MUNDFAB) jakościowa analiza SIMS procesu implantacji jonów do gorącego podłoża w technologii krzemowej i germanowej
- II-VI Incorporated, Warren, USA badania SIMS struktur VCSEL
- AMS, Premstaetten, Austria poufne
- Infineon Austria, Villach, Austria jakościowa analiza SIMS procesu implantacji jonów do gorącego podłoża w technologii węglika krzemu
- Oslo University badania SIMS materiałów ALD
- Drexel University badania SIMS materiałów MAX i MXene (współpraca z prof. Yury Gogotsi, potencjalnym laureatem Nagrody Nobla w dziedzinie chemii za wynalezienie rodziny materiałów dwuwymiarowych MXenes)

6 Informacja o osiągnięciach dydaktycznych, organizacyjnych oraz popularyzujących naukę lub sztukę.

6.1 Opieka nad studentami

- Promotor pomocniczy pracy magisterskiej Adrianny Wójcik "Laser induced structural changes and filtering properties of epitaxial boron nitride", Uniwersytet Warszawski, Warszawa, Polska (07.2021)
- Planowany promotor pomocniczy studiów doktoranckich Adrianny Wójcik na Politechnice Warszawskiej, Warszawa, Polska (rozpoczęcie 10.2021)
- Opiekun praktyk studenckich Aleksandra Senderowskiego, które odbywały się w Sieci Badawczej Łukasiewicz Instytucie Mikroelektroniki i Fotoniki (07-08.2021)
- Planowany promotor pomocniczy pracy inżynierskiej Aleksandra Senderowskiego na Politechnice Warszawskiej, Warszawa, Polska (10.2021)
- Planowany opiekun praktyk podyplomowych Aleksandra Senderowskiego, które odbędą się w Sieci Badawczej Łukasiewicz - Instytucie Mikroelektroniki i Fotoniki (10-11.2021)

6.2 Wykłady dla studentów i doktorantów

- 11.2018 "Podstawy oraz możliwości Spektrometrii Mas Jonów Wtórnych (SIMS)" wykład dla studentów Inżynierii Materiałowej Politechniki Warszawskiej, Warszawa, Polska
- 12.2019 "Podstawy oraz możliwości Spektrometrii Mas Jonów Wtórnych (SIMS)" wykład dla studentów Inżynierii Materiałowej Politechniki Warszawskiej, Warszawa, Polska
- 04.2021 "Podstawy oraz możliwości Spektrometrii Mas Jonów Wtórnych (SIMS)" wykład dla studentów Inżynierii Materiałowej Politechniki Warszawskiej, Warszawa, Polska
- 04.2021 "Secondary Ion Mass Spectrometry characterization of thin films with nanometer and subnanometer depth resolution" Courses on Advanced Topics 7, CEITEC, Brno, Czechy

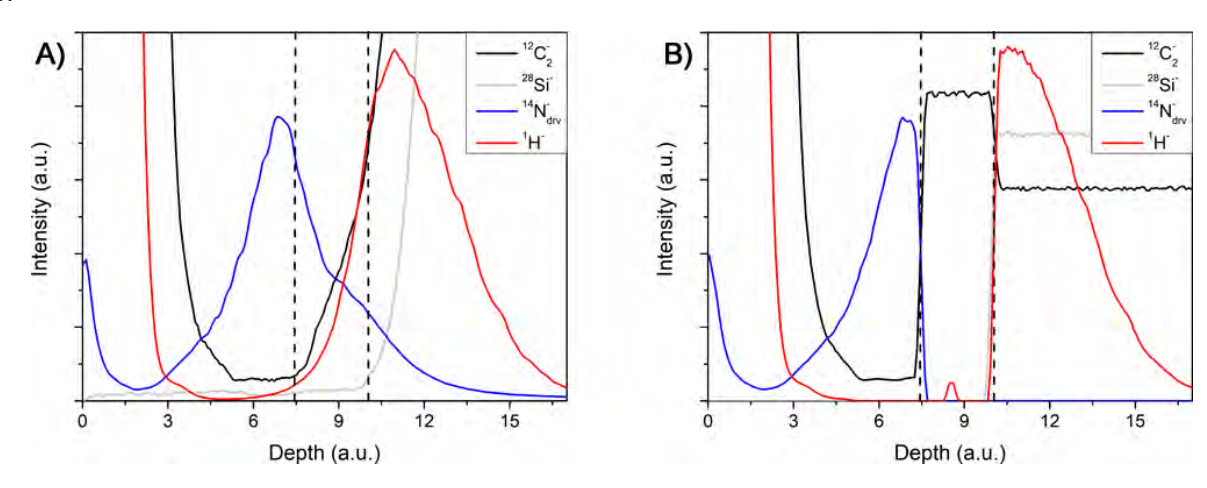
6.3 Wykłady zaproszone popularyzujące technikę SIMS

- 05.2016 Wydział Fizyki, Uniwersytet im. Adama Mickiewicza, Poznań, Polska
- 10.2016 Wydział Fizyki, Uniwersytet Warszawski, Warszawa, Polska
- 06.2017 Wydział Nowych Technologii i Chemii, Wojskowa Akademia Techniczna, Warszawa, Polska
- 10.2017 VIGO System, Ożarów Mazowiecki, Polska
- 03.2018 Akademickie Centrum Materiałów i Nanotechnologii, Akademia Górniczo-Hutnicza im. Stanisława Staszica w Krakowie, Kraków, Polska
- 03.2018 Wydział Elektroniki, Telekomunikacji i Informatyki, Politechnika Gdańska, Gdańsk, Polska
- 04.2018 Wydział Fizyki, Universytet Łódzki, Łódź, Polska
- 05.2018 Instytut Fizyki Wysokich Ciśnień Polskiej Akademii Nauk, Warszawa, Polska
- 09.2018 Fraunhofer Institute for Integrated Systems and Device Technology IISB, Erlangen, Niemcy
- 02.2019 PVcomB Helmholtz-Zentrum Berlin, Berlin, Niemcy
- 03.2019 Wydział Fizyki, Uniwersytet Warszawski, Warszawa, Polska
- 05.2019 Sieć Badawcza Łukasiewicz PORT Polski Ośrodek Rozwoju Technologii, Wrocław, Polska
- 06.2019 Instytut Fizyki Wysokich Ciśnień Polskiej Akademii Nauk, Warszawa, Polska
- 11.2019 Sieć Badawcza Łukasiewicz Instytut Technologii Elektronowej, Warszawa, Polska
- 11.2019 Instytut Fizyki Molekularnej Polskiej Akademii Nauk, Poznań, Polska
- 01.2020 Instytut Podstawowych Problemów Techniki Polskiej Akademii Nauk, Warszawa, Polska
- 06.2020 IMEC, Leuven, Belgia
- 10.2020 Tyndall National Institute, Cork, Irlandia
- 01.2021 Modeling and Exploration of Materials Laboratory CEA, Grenoble, Francja
- 07.2021 Daegu Gyeongbuk Institute of Science and Technology, Daegu, Korea Południowa
- 09.2021 Materials Research Society, OnDemand Webinar Series "Dynamic SIMS for Semiconductors - From compositional analysis of optoelectronics and 2D devices to implant depthprofiling of advanced Si-based structures"

7 Dodatkowe informacje

7.1 Dalszy rozwój dedykowanych procedur pomiarowych

Należy podkreślić, że moje dążenie do poprawy jakości pomiarów SIMS jeszcze się nie skończyło. Staram się ciągle doskonalić dedykowane procedury i wierzę, że staję się w tym coraz lepszy. Opracowałem już wiele procedur, które przewyższają te opisane w artykułach [H1] - [H16]. Doskonałym przykładem jest moje zaangażowanie w bardziej szczegółową charakteryzaję grafenu. Niedawno przesłałem artykuł "Precise localization of contaminants in graphene with secondary ion mass spectrometry" do czasopisma *Measurement*, w którym pokazuję, jak bardzo poprawiłem swoją procedurę pomiarową w porównaniu z pierwszym opublikowanym artykułem przy użyciu urządzenia CAMECA IMS SC Ultra [H1]. Zmierzyłem nawet ponownie tę samą próbkę: dwuwarstwowy grafen na węgliku krzemu pokryty cienką warstwą chromu. Rysunek 8 porównuje wynik pierwotnej procedury (część A, tożsame z rysunkiem 2) z niedawno opracowaną (część B). Łatwo zaobserwować znaczącą poprawę jakości. Co ciekawe, udoskonalony wynik został wykonany dokładnie pięć lat po pierwszym pomiarze.



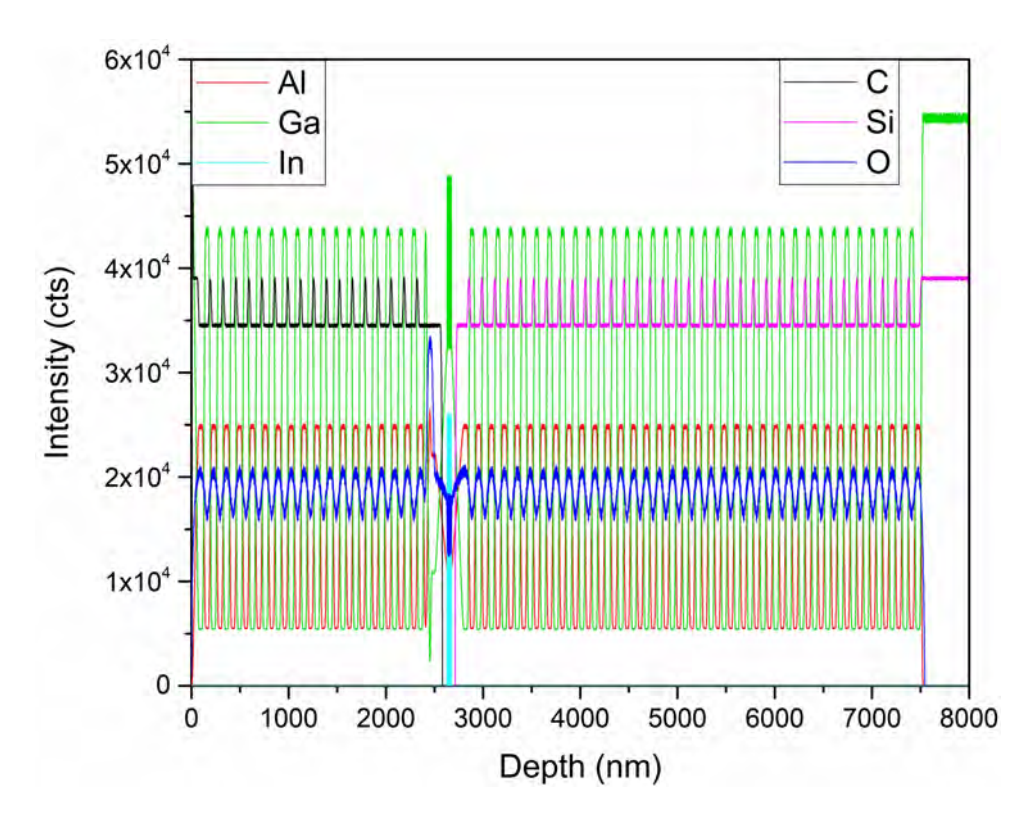
Rysunek 8: Profil wgłębny dwuwarstwowego grafenu wzrastanego na SiC i pokrytego cienką warstwą Cr. Linie przerywane pokazują położenie warstw grafenu. Procedura pierwotna (część A) nie pozwala na jednoznaczną lokalizację zanieczyszczeń. Dla zoptymalizowanej procedury (część B) osiągnięta została atomowa rozdzielczość wgłębna, która pozwala na sformułowanie ważnych wniosków: zanieczyszczenia organiczne (azot użyty jako marker) nie dyfundują przez grafen; Węglik krzemu jest pasywowany wodorem, ale zaobserwować można także resztki wodoru uwięzione między dwiema warstwami grafenowymi.

Podobnie znacznie poprawiłem swoje możliwości charakteryzacji pełnych struktur przyrządów. Dzięki zoptymalizowanej procedurze możliwe jest uzyskanie profilu wgłębnego bardzo grubej struktury (do 20 μm) składającej się z setek pojedynczych warstw. Najlepszym przykładem jest struktura lasera z pionową wnęką rezonansową (Vertical-cavity surface-emitting laser - VCSEL) pokazana na rysunku 9.

Rozdzielczość wgłębna pomiaru nie ulega pogorszeniu nawet w przypadku tak grubej próbki. W tym celu opracowałem koncepcję modulacji energii padających jonów: podczas pomiaru energia jest zmieniana, a szybkość trawienia jest regulowana dynamicznie i dostosowana do grubości mierzonych warstw. Przezwyciężyłem również ograniczenia charakteryzacji studni kwantowych pokazane w artykule [H12] - obecnie potrafię odwzorować nawet bardzo cienkie studnie kwantowe jako prostokątne sygnały, a nie piki gaussowskie, jak pokazano na rysunku 10.

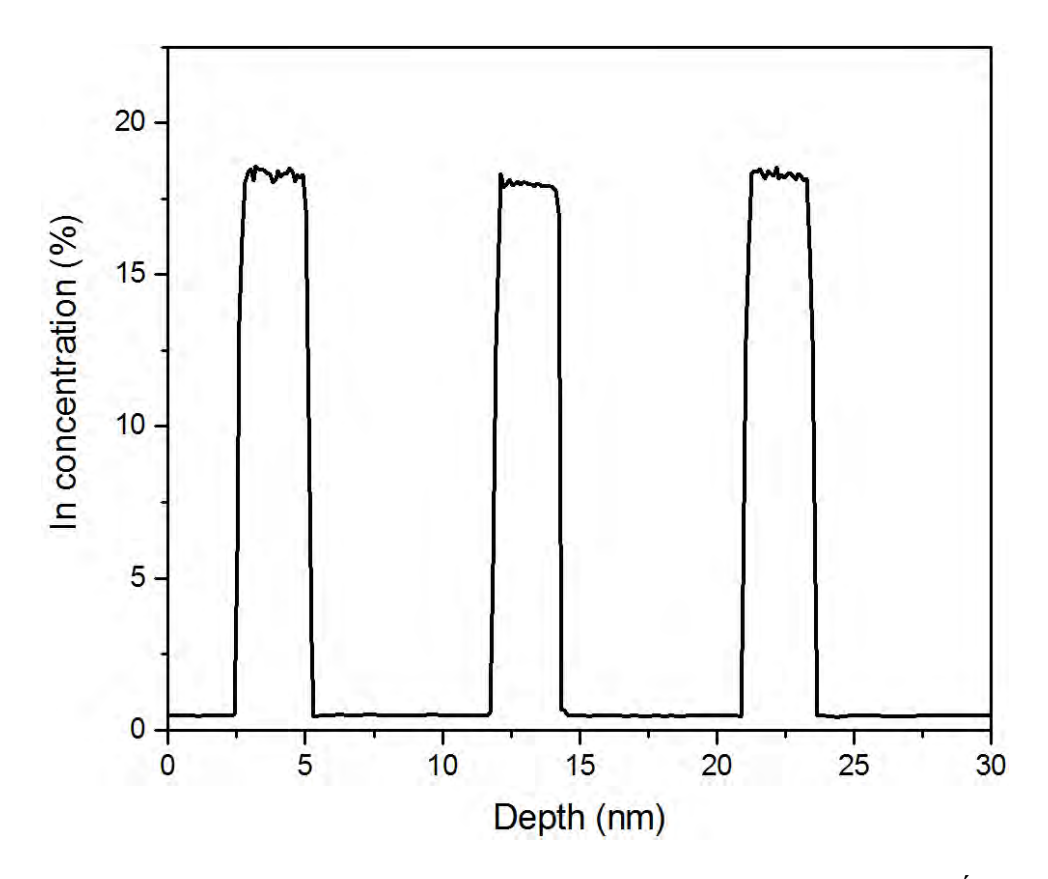
Po osiągnięciu takiej precyzji możliwe jest również o wiele bardziej precyzyjne badanie fluktuacji rozkładu koncentracji indu, a nawet, jak pokazano na rysunku 11, termicznego rozkładu studni kwantowych.

Wszystkie te wyniki nie zostały jeszcze opublikowane, ale artykuły omawiające znaczenie tych odkryć są w przygotowaniu / zostały niedawno przesłane do czasopism naukowych. Uważam jednak,

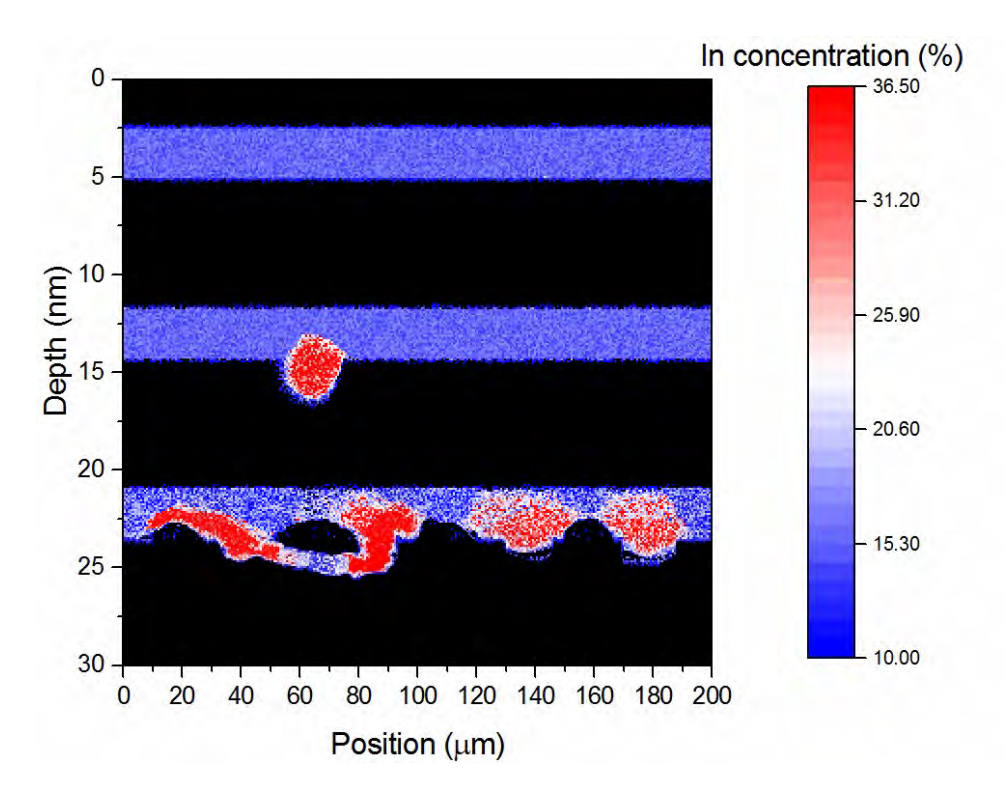


Rysunek 9: Profil wgłębny struktury VCSEL z rozdzielczością, która pozwala rozróżnić studnie kwantowe o grubości 3 nm.

że warto je tutaj przedstawić, ponieważ pokazują dalszy postęp mojej pracy z urządzeniem CAMECA IMS SC Ultra i moje dążenie do rozwijania możliwości SIMS poza jego powszechnie przyjęte granice.



Rysunek 10: Profil wgłębny trzech studni kwantowych InGaN o grubości 2.5 nm. Średnia koncentracja indu w studniach wynosi 18% i 0.5% w barierach. Dzięki osiągniętej rozdzielczości wgłębnej możliwe jest odwzorowanie studni jako prostokątnych sygnałów.



Rysunek 11: Przekrój poprzeczny studni kwantowych InGaN. Wynik SIMS pokazuje rozpad termiczny studni kwantowych - najniższa uległa silnemu rozkładowi, środkowa jest we wczesnej fazie rozkładu, natomiast najwyższa pozostała nienaruszona.

7.2 Nagrody

- 06.2020 stypendium Ministra Nauki i Szkolnictwa Wyższego dla wybitnych młodych naukowców
- 10.2020 laureat Polskiej Nagrody Inteligentnego Rozwoju w kategorii Naukowiec Przyszłości

Wykaz osiągnięć naukowych stanowiących znaczny wkład w rozwój określonej dyscypliny

I INFORMACJA O OSIĄGNIĘCIACH NAUKOWYCH, O KTÓ-RYCH MOWA W ART. 219 UST. 1. PKT 2 USTAWY

- I.2 Cykl powiązanych tematycznie artykułów naukowych, zgodnie z art. 219 ust. 1. pkt 2b Ustawy
- **[H1] P.P. Michałowski**, W. Kaszub, A. Merkulov, W. Strupiński. "Secondary ion mass spectroscopy depth profiling of hydrogen-intercalated graphene on SiC" *Applied Physics Letters*, 109:011904, 2016.

Mój wkład merytoryczny: Sformułowałem hipotezę, że można uzyskać subnanometrową rozdzielczość wgłębną podczas pomiarów SIMS, co umożliwi jakościowe porównanie próbek interkalowanych i nieinterkalowanych wodorem. Aby potwierdzić wysoką jakość próbek wykonałem pomiar metodą spektroskopii Ramana. Stworzyłem dedykowaną procedurę SIMS, która pozwoliła na dokładną lokalizację grafenu. Przeprowadziłem pomiary SIMS, potwierdziłem swoją hipotezę i dodatkowo zauważyłem, że zanieczyszczenia organiczne zgromadziły się na powierzchni warstwy grafenu i nie wnikały w głąb. Byłem autorem treści artykułu (zarówno wersji pierwotnej jak i korekty).

Mój wkład procentowy: 80%

[H2] P.P. Michałowski, W. Kaszub, I. Pasternak, W. Strupinski. "Graphene Enhanced Secondary Ion Mass Spectrometry (GESIMS)" *Scientific Reports*, 7:7479, 2017.

Mój wkład merytoryczny: Sformułowałem hipotezę, że grafen można wykorzystać do polepszenia granic wykrywalności pomiarów SIMS. Udowodniłem, że warstwa grafenowa blokowała emisję atomów z warstw leżących poniżej, ale zwiększała prawdopodobieństwo jonizacji ujemnej. Podczas długotrwałego bombardowania jonowego grafen uległ częściowemu zniszczeniu, co ograniczyło efekt blokowania, podczas gdy wzmocnienie jonizacji nadal było silne. W ten sposób opracowałem podejście GESIMS w celu zwiększenia granic wykrywalności i eksperymentalnie pokazałem, jak osiągnąć optymalne warunki. Byłem autorem treści artykułu (zarówno wersji pierwotnej jak i korekty).

Mój wkład procentowy: 80%

[H3] P.P. Michałowski, P. Gutowski, D. Pierścińska, K. Pierściński, M. Bugajski, W. Strupiński. "Characterization of the superlattice region of a quantum cascade laser by secondary ion mass spectrometry" *Nanoscale*, 9:17571–17575, 2017.

Mój wkład merytoryczny: Sformułowałem hipotezę, że przy profilowaniu stosunkowo grubej próbki (około 200 nm) można zachować subnanometrową rozdzielczość wgłębną. Opracowałem dedykowaną procedurę SIMS: zwiększyłem obszar analizy aby uniknąć konieczności zwiększania czasu integracji wszystkich sygnałów. Przetestowałem to podejście na supersieci AlInAs/InGaAs kwantowego lasera kaskadowego i pokazałem, że wbudowanie tlenu w warstwach AlInAs była bardziej intensywne podczas pierwszego etapu wzrostu, a zatem tlen nie był równomiernie rozłożony w tych warstwach. Rozdzielczość wgłębna była wystarczająca, aby pokazać to nawet dla najcieńszych warstw (0.7 nm). Wykazałem również, że procedura może być wykorzystana do trójwymiarowej analizy usterek. Byłem autorem treści artykułu (zarówno wersji pierwotnej jak i korekty).

Mój wkład procentowy: 80%

[H4] P.P. Michałowski, I. Pasternak, W. Strupiński. "Contamination-free Ge-based graphene as revealed by graphene enhanced secondary ion mass spectrometry (GESIMS)" *Nanotechnology*, 29(1):015702, 2018.

Mój wkład merytoryczny: Sformułowałem hipotezę, że wbrew obiegowej opinii, proces wzrostu grafenu na różnych podłożach nie prowadzi do silnego zanieczyszczenia miedzią. Opracowałem dedykowaną procedurę SIMS i udowodniłem, że efekt GESIMS powoduje pojawienie się podwójnie zjonizowanych pików w widmie masowym. Te piki można błędnie zinterpretować jako dowód obecności miedzi. Wykazałem, jak je poprawnie zidentyfikować i udowodniłem swoją hipotezę, że w zdecydowanej większości wzrastanych warstw grafenowych nie ma miedzi. Byłem autorem treści artykułu (zarówno wersji pierwotnej jak i korekty). Mój wkład procentowy: 80%

[H5] P.P. Michałowski, I. Pasternak, P. Ciepielewski, F. Guinea, W. Strupiński. "Formation of a highly doped ultra-thin amorphous carbon layer by ion bombardment of graphene" *Nanotechnology*, 29(30):305302, 2018.

Mój wkład merytoryczny: Sformułowałem hipotezę, że wyjaśnienie efektu GESIMS opisane w [H2] (grafen pełniący rolę żarnika) było błędne. Prof. Francisco Guinea, teoretyk z IMDEA Nanoscience i University of Manchester zasugerował, że zerwane wiązania sp² grafenu mogły wychwytywać jony cezu i uwięzić je blisko powierzchni. Opracowałem dedykowaną procedurę SIMS i udowodniłem słuszność jego teorii. W ten sposób udało mi się wyjaśnić efekt GES-IMS: duża retencja Cs na powierzchni zmniejszyła pracę wyjścia i więcej elektronów zostało wyemitowanych podczas bombardowania jonami, co zwiększyło prawdopodobieństwo jonizacji ujemnej. Byłem autorem treści artykułu (zarówno wersji pierwotnej jak i korekty). Mój wkład procentowy: 60%

[H6] P.P. Michałowski, J. Gaca, M. Wójcik, A. Turos. "Oxygen out-diffusion and compositional changes in zinc oxide during ytterbium ions bombardment" *Nanotechnology*, 29(42):425710, 2018.

Mój wkład merytoryczny: Sformułowałem hipotezę, że SIMS może ujawnić potencjalne zubożenie tlenu w kryształkach tlenku cynku po bombardowaniu jonami iterbu. Zauważyłem, że obszar zubożony miał duży wpływ na eksperyment SIMS i powodował większą retencję cezu, co zmieniało kształt rejestrowanych sygnałów. Opracowałem dedykowaną procedurę SIMS, znormalizowałem wszystkie sygnały do sygnału Cs i odtworzyłem prawidłowy profil implantacji. W ten sposób udowodniłem dyfuzję tlenu w kierunku powierzchni próbki i uformowanie warstwy zubożonej w ten pierwiastek. Byłem autorem treści artykułu (zarówno wersji pierwotnej jak i korekty).

Mój wkład procentowy: 80%

[H7] P.P. Michałowski, W. Kaszub, P. Knyps, K. Rosiński, B. Stańczyk, K. Przyborowska, E. Dumiszewska. "A-Crater-within-a-Crater Approach for Secondary Ion Mass Spectrometry Evaluation of the Quality of Interfaces of Multilayer Devices" *ACS Applied Materials & Interfaces*, 10(43):37694–37698, 2018.

Mój wkład merytoryczny: Zainicjowałem te badania i sformułowałem hipotezę, że subnanometrowa rozdzielczość wgłębna może być zachowana nawet dla bardzo grubych (kilka mikronów) struktur wielowarstwowych. Opracowałem innowacyjne podejście, które nazwałem a-craterwithin-a-crater (krater w kraterze): wysokoenergetyczna wiązka jonów pierwotnych została wykorzystana do szybkiego usunięcia większości materiału tworzącego duży krater. Następnie energia została znacznie zmniejszona i na dnie poprzedniego powstał nowy, mniejszy krater. W pobliżu interesującego obszaru energia uderzenia została zmniejszona do 150 eV, dzięki czemu rejon ten mógł być analizowany z subnanometrową rozdzielczością wgłębną. Przetestowałem to podejście na epitaksjalnej strukturze trójzłączowego ogniwa słonecznego. Informacje dostarczone przez moją analizę pomogły zoptymalizować procedurę wzrostu. Byłem autorem treści

artykułu (zarówno wersji pierwotnej jak i korekty). Mój wkład procentowy: 80%

[H8] P.P. Michałowski, P. Knyps, P. Ciepielewski, P. Caban, E. Dumiszewska, J. Baranowski. "Destructive role of oxygen in growth of molybdenum disulfide determined by secondary ion mass spectrometry" *Physical Chemistry Chemical Physics*, 21:8837–8842, 2019.

Mój wkład merytoryczny: Zainicjowałem te badania i sformułowałem hipotezę, że rodzaj podłoża ma duży wpływ na jakość wzrastanych warstw MoS₂. Opracowałem dedykowaną procedurę SIMS i wykazałem, że w przypadku podłoży zawierających tlen (tlenek krzemu, szafir) wysokotemperaturowy proces siarkowania powoduje uwalnianie tlenu z podłoża. Dlatego mogłem zaobserwować domeny siarczku molibdenu o wysokiej jakości (większe dla szafiru) otoczone amorficznym, silnie utlenionym materiałem. Wykazałem też, że na podłożu bez tlenu (np. azotku boru) można wytworzyć jednorodną, wysokiej jakości warstwę MoS₂. Byłem autorem treści artykułu (zarówno wersji pierwotnej jak i korekty).

Mój wkład procentowy: 80%

[H9] P.P. Michałowski, P. Knyps, P. Ciepielewski, P.A. Caban, E. Dumiszewska, G. Kowalski, M. Tokarczyk, J.M. Baranowski. "Growth of highly oriented MoS2 via an intercalation process in the graphene/SiC(0001) system" *Physical Chemistry Chemical Physics*, 21:20641–20646, 2019.

Mój wkład merytoryczny: Zainicjowałem te badania i sformułowałem hipotezę, że warstwy MoS₂ tworzą się pomiędzy grafenem i węglikiem krzemu, gdy podjęto próbę ich wzrastania na powierzchni próbki grafen/SiC. Opracowałem dedykowaną procedurę SIMS i wykazałem, że wysokotemperaturowy proces prowadził do interkalacji prekursorów pod warstwę grafenu. Byłem autorem treści artykułu (zarówno wersji pierwotnej jak i korekty). Mój wkład procentowy: 80%

[H10] P.P. Michałowski, P. Caban, J. Baranowski. "Secondary ion mass spectrometry investigation of carbon grain formation in boron nitride epitaxial layers with atomic depth resolution" *Journal of Analytical Atomic Spectrometry*, 34:848–853, 2019.

Mój wkład merytoryczny: Zainicjowałem te badania i sformułowałem hipotezę, że można uzyskać atomową rozdzielczość wgłębną dla struktur van der Waalsa. Opracowałem dedykowaną procedurę SIMS, która pozwoliła mi na analizę wyłącznie wierzchniej warstwy. Następnie wygenerowałem krótki impuls wiązki jonów o dużym kącie padania, który preferencyjnie zerwał słabe wiązania van der Waalsa i usunął górną warstwę, nie powodując żadnych uszkodzeń warstw leżących poniżej. W ten sposób druga warstwa została odsłonięta i przeanalizowana jak poprzednio, a następnie usunięta. Poprzez kilka iteracji procedury mogłem scharakteryzować oddzielnie każdą warstwę azotku boru i wykazać różnicę formacji wytrąceń węglowych w różnych trybach wzrostu. Byłem autorem treści artykułu (zarówno wersji pierwotnej jak i korekty).

Mój wkład procentowy: 80%

[H11] P.P. Michałowski, S. Złotnik, and M. Rudziski. "Three dimensional localization of unintentional oxygen impurities in gallium nitride" *Chemical Communications*, 55:11539–11542, 2019.

Mój wkład merytoryczny: Sformułowałem hipotezę, że pomimo niepożądanego udziału gazów resztkowych w komorze pomiarowej, możliwe jest uzyskanie wiarygodnej informacji o trójwymiarowym rozkładzie tlenu w azotku galu. Opracowałem dedykowaną procedurę SIMS, odjąłem poziom tła komory, rozwiązałem problem niejednorodnej czułości detektora i zoptymalizowałem procedurę w taki sposób, aby pomiar był wykonywany w czasie, w którym źródło jonów pierwotnych jest stabilne. W ten sposób wykazałam, że tlen jest zgromadzony wzdłuż podłużnych struktur, a analiza korelacyjna wykazała, że są to otwarte rdzenie dyslokacji śrubowych i mieszanych. Byłem autorem treści artykułu (zarówno wersji pierwotnej jak i korekty).

Mój wkład procentowy: 60%

[H12] P.P. Michałowski, E. Grzanka, S. Grzanka, A. Lachowski, G. Staszczak, J. Plesiewicz, M. Leszczyski, A. Turos. "Indium concentration fluctuations in InGaN/GaN quantum wells" *Journal of Analytical Atomic Spectrometry*, 34:1718–1723, 2019.

Mój wkład merytoryczny: Zainicjowałem te badania i sformułowałem hipotezę, że ind nie jest rozłożony równomiernie w studniach kwantowych, a SIMS może być odpowiednią techniką do ujawnienia makroskopowych fluktuacji koncentracji indu. Stworzyłem dedykowaną procedurę SIMS, która pozwoliła mi przezwyciężyć wady metodyki (cienkie studnie kwantowe zostały zarejestrowane jako piki o kształcie gaussowskim) i uzyskać obraz przekroju próbki. Dzięki temu mogłem jakościowo i ilościowo opisać fluktuacje koncentracji indu. Byłem autorem treści artykułu (zarówno wersji pierwotnej jak i korekty).

Mój wkład procentowy: 80%

[H13] P.P. Michałowski. "Probing a chemical state during ultra low impact energy secondary ion mass spectrometry depth profiling" *Journal of Analytical Atomic Spectrometry*, 34:1954–1956, 2019.

Mój wkład merytoryczny: wykonałem całą pracę zawartą w artykule.

Mój wkład procentowy: 100%

[H14] P.P. Michałowski. "Titanium pre-sputtering for an enhanced secondary ion mass spectrometry analysis of atmospheric gas elements" *Journal of Analytical Atomic Spectrometry*, 35:1047–1050, 2020.

Mój wkład merytoryczny: wykonałem całą pracę zawartą w artykule.

Mój wkład procentowy: 100%

[H15] P.P. Michałowski, S. Zlotnik, I. Jóźwik, A. Chamryga, M. Rudziński. "3D Depth Profile Reconstruction of Segregated Impurities using Secondary Ion Mass Spectrometry" *Journal of Visualized Experiments*, 158:e61065, 2020.

Mój wkład merytoryczny: wideo-artykuł naukowy prezentujący opis metody pomiarowej zastosowanej w [H11]. Mój wkład naukowy jest taki sam jak w tamtym artykule. Dodatkowo przygotowałem opis metody i stworzyłem animacje.

Mój wkład procentowy: 60%

[H16] P.P. Michałowski, D. Maciążek, Z. Postawa, P.A. Caban, S. Kozdra, A. Wójcik, J.M. Baranowski. "Defect-mediated sputtering process of boron nitride during high incident angle low-energy ion bombardment" *Measurement*, 179:109487, 2021.

Mój wkład merytoryczny: Zainicjowałem te badania i sformułowałem hipotezę, że możliwość osiągnięcia atomowej rozdzielczości wgłębnej jest związana ze specyficzną interakcją jonów pierwotnych padających pod wysokim kątem z materiałem. Symulacje komputerowe (wykonane przez grupę prof. Zbigniewa Postawy z Uniwersytetu Jagiellońskiego) ujawniły, że tylko defekty mogą zainicjować proces rozpylania materiału. Opracowałem dedykowaną procedurę SIMS, która pozytywnie zweryfikowała kolejny wniosek z symulacji komputerowych: proces rozpylania był asymetryczny - bardziej intensywny wzdłuż kierunku padania jonów pierwotnych. Byłem autorem treści artykułu (zarówno wersji pierwotnej jak i korekty).

Mój wkład procentowy: 60%

II INFORMACJA O AKTYWNOŚCI NAUKOWEJ

II.1 Wykaz opublikowanych monografii naukowych.

Nie dotyczy

II.2 Wykaz opublikowanych rozdziałów w monografiach naukowych.

Miałem wkład w powstanie książki "VCSEL Industry: Communication and Sensing" Babu Padullaparthi Dayal, Jim Tatum, Kenichi Iga. Wiley-IEEE Press; 1st edition (data wydania: 28.09.2021). Dostarczyłem profil wgłębny struktury VCSEL, bardzo podobny do rysunku 9 z Autoreferatu.

Informacja o członkostwie w redakcjach naukowych monografii.

Nie dotyczy

Wykaz opublikowanych artykułów w czasopismach naukowych (z zaznaczeniem pozycji niewymienionych w pkt I.2).

Poniższa lista podzielona jest na dwie części, artykuły opublikowane przed uzyskaniem stopnia naukowego doktora ([A1]-[A6]) i po ([B1]-[B41]). Artykuły wchodzące w skład cyklu artykułów naukowych powiązanych tematycznie (wymienionych w punkcie I.2) dodatkowo oznaczone są odpowiednimi etykietami [H1]-[H16].

Dla każdego artykułu podane są dodatkowe informacje:

- Liczba cytowań bez autocytowań według baz danych Web of Science, Scopus i Google Scholar;
- Impact Factor zgodny z rokiem publikacji;
- Punkty przyznawane przez Ministerstwo Edukacji i Nauki. W czasie, gdy aktywnie publikowałem, dwukrotnie zmieniły się zasady przyznawania punktów ministerialnych, a artykuły z lat 2009-2011, 2015-2018 i 2019-2021 byłyby traktowane inaczej. Ponieważ jest to szczególnie istotne w przypadku artykułów wchodzących w skład cyklu artykułów naukowych powiązanych tematycznie (opublikowanych w latach 2016-2021) postanowiłem przedstawić jedynie punkty z najnowszego zestawienia, opublikowanego 18.02.2021;
- Ogólny opis mojego wkładu. Bardziej szczegółowe informacje podano w punkcie I.2 dla artykułów wchodzących w skład cyklu artykułów naukowych powiązanych tematycznie.

II.4.1 Przed uzyskaniem stopnia naukowego doktora

[A1] J. Paul, V. Beyer, P.P. Michałowski, M.F. Beug, L. Bach, M. Ackermann, S. Wege, A. Tilke, N. Chan, T. Mikolajick, U. Bewersdorff-Sarlette, R. Knöfler, M. Czernohorsky, C. Ludwig. "TaN metal gate damage during high-k (Al2O3) high temperature etch" Microelectronic Engineering, 86(4):949 - 952, 2009.

Cytowania bez autocytowań: 9/13/14 (Web of Science/Scopus/Google Scholar)

Impact Factor (2009): 1.488

Punkty przyznawane przez Ministerstwo Edukacji i Nauki (2021): 70

Mój wkład merytoryczny: Wykonałem pomiary ToF-SIMS i zinterpretowałem wyniki, uczestniczyłem w dyskusji dotyczącej istoty tych wyników w kontekście całego artykułu.

[A2] M. Lanza, M. Porti, M. Nafria, X. Aymerich, G. Benstetter, E. Lodermeier, H. Ranzinger, G. Jaschke, S. Teichert, L. Wilde, P.P. Michałowski. "Crystallization and silicon diffusion nanoscale effects on the electrical properties of Al2O3 based devices" Microelectronic Engineering, 86(7):1921 – 1924, 2009.

Cytowania bez autocytowań: 21/23/26 (Web of Science/Scopus/Google Scholar)

Impact Factor (2009): 1.488

Punkty przyznawane przez Ministerstwo Edukacji i Nauki (2021): 70

Mój wkład merytoryczny: Wykonałem pomiary ToF-SIMS i zinterpretowałem wyniki, uczestniczyłem w dyskusji dotyczącej istoty tych wyników w kontekście całego artykułu.

[A3] M. Rose, J. Niinistö, **P.P. Michałowski**, L. Gerlich, L. Wilde, I. Endler, J.W. Bartha. "Atomic Layer Deposition of Titanium Dioxide Thin Films from Cp*Ti(OMe)3 and Ozone" *The Journal of Physical Chemistry C*, 113(52):21825–21830, 2009.

Cytowania bez autocytowań: 42/44/53 (Web of Science/Scopus/Google Scholar)

Impact Factor (2009): 4.224

Punkty przyznawane przez Ministerstwo Edukacji i Nauki (2021): 140

Mój wkład merytoryczny: Wykonałem pomiary ToF-SIMS i zinterpretowałem wyniki, uczestniczyłem w dyskusji dotyczącej istoty tych wyników w kontekście całego artykułu.

[A4] J. Paul, V. Beyer, M. Czernohorsky, M.F. Beug, K. Biedermann, M. Mildner, **P.P. Michałowski**, E. Schütze, T. Melde, S. Wege, R. Knöfler, T. Mikolajick. "Improved high-temperature etch processing of high-k metal gate stacks in scaled TANOS memory devices" *Microelectronic Engineering*, 87(5):1629 – 1633, 2010.

Cytowania bez autocytowań: 2/4/4 (Web of Science/Scopus/Google Scholar)

Impact Factor (2010): 1.575

Punkty przyznawane przez Ministerstwo Edukacji i Nauki (2021): 70

Mój wkład merytoryczny: Wykonałem pomiary ToF-SIMS i zinterpretowałem wyniki, uczestniczyłem w dyskusji dotyczącej istoty tych wyników w kontekście całego artykułu

[A5] P.P. Michałowski, V. Beyer, M. Czernohorsky, P. Kücher, S. Teichert, G. Jaschke, W. Möller. "Formation of an interface layer between All-xSixOy thin films and the Si substrate during rapid thermal annealing" *Physica Status Solidi C*, 7(2):284–287, 2010.

Cytowania bez autocytowań: 0/0/0 (Web of Science/Scopus/Google Scholar)

Impact Factor (2010): -

Punkty przyznawane przez Ministerstwo Edukacji i Nauki (2021): 40

Mój wkład merytoryczny: byłem autorem hipotezy badawczej, Wykonałem pomiary ToF-SIMS i zinterpretowałem wyniki, wykonałem analizę wyników, byłem autorem treści artykułu (zarówno wersji pierwotnej jak i korekty)

[A6] M. Lanza, M. Porti, M. Nafría, X. Aymerich, G. Benstetter, E. Lodermeier, H. Ranzinger, G. Jaschke, S. Teichert, L. Wilde, **P.P. Michałowski**. "Conductivity and charge trapping after electrical stress in amorphous and polycrystalline Al2O3-Based devices studied with afm-related techniques" *IEEE Transactions on Nanotechnology*, 10(2):344–351, 2011.

Cytowania bez autocytowań: 26/29/34 (Web of Science/Scopus/Google Scholar)

Impact Factor (2011): 2.292

Punkty przyznawane przez Ministerstwo Edukacji i Nauki (2021): 100

Mój wkład merytoryczny: Wykonałem pomiary ToF-SIMS i zinterpretowałem wyniki, uczestniczyłem w dyskusji dotyczącej istoty tych wyników w kontekście całego artykułu.

II.4.2 Po uzyskaniu stopnia naukowego doktora

[B1] A. Inaba, Y. Miyazaki, P.P. Michałowski, E. Gracia-Espino, B. Sundqvist, T. Wågberg. "Calorimetric measurements on Li4C60 and Na4C60" *The Journal of Chemical Physics*, 142(16):164706, 2015.

Cytowania bez autocytowań: 1/1/2 (Web of Science/Scopus/Google Scholar)

Impact Factor (2015): 2.894

Punkty przyznawane przez Ministerstwo Edukacji i Nauki (2021): 100

Mój wkład merytoryczny: wykonałem próbki do badań.

[B2] / [H1] P.P. Michałowski, W. Kaszub, A. Merkulov, W. Strupiński. "Secondary ion mass spectroscopy depth profiling of hydrogen-intercalated graphene on SiC" *Applied Physics Letters*, 109(1):011904, 2016.

Cytowania bez autocytowań: 4/4/5 (Web of Science/Scopus/Google Scholar)

Impact Factor (2016): 3.411

Punkty przyznawane przez Ministerstwo Edukacji i Nauki (2021): 100

Mój wkład merytoryczny: byłem autorem hipotezy badawczej, opracowałem procedurę SIMS i wykonałem pomiary, wykonałem pomiary ramanowskie, wykonałem analizę wyników, byłem autorem treści artykułu (zarówno wersji pierwotnej jak i korekty)

[B3] / [H2] P.P. Michałowski, W. Kaszub, I. Pasternak, W. Strupinski. "Graphene Enhanced Secondary Ion Mass Spectrometry (GESIMS)" *Scientific Reports*, 7:7479, 2017.

Cytowania bez autocytowań: 6/6/6 (Web of Science/Scopus/Google Scholar)

Impact Factor (2017): 4.122

Punkty przyznawane przez Ministerstwo Edukacji i Nauki (2021): 140

Mój wkład merytoryczny: byłem autorem hipotezy badawczej, opracowałem procedurę SIMS i wykonałem pomiary, wykonałem analizę wyników, byłem autorem treści artykułu (zarówno wersji pierwotnej jak i korekty)

[B4] / **[H3] P.P. Michałowski**, P. Gutowski, D. Pierciska, K. Pierciski, M. Bugajski, W. Strupiski. "Characterization of the superlattice region of a quantum cascade laser by secondary ion mass spectrometry" *Nanoscale*, 9:17571–17575, 2017.

Cytowania bez autocytowań: 2/1/2 (Web of Science/Scopus/Google Scholar)

Impact Factor (2017): 7.233

Punkty przyznawane przez Ministerstwo Edukacji i Nauki (2021): 140

Mój wkład merytoryczny: byłem autorem hipotezy badawczej, opracowałem procedurę SIMS i wykonałem pomiary, wykonałem analizę wyników, byłem autorem treści artykułu (zarówno wersji pierwotnej jak i korekty)

[B5] J. Wróbel, K. Grodecki, D. Benyahia, K. Murawski, K. Michalczewski, J. Grzonka, J. Boguski, K. Gorczyca, G.A. Umana-Membreno, ł. Kubiszyn, A. Kębłowski, P.P. Michałowski, E. Gomółka, P. Martyniuk, J. Piotrowski, A. Rogalski. "Structural and optical characterization of the high quality Be-doped InAs epitaxial layer grown on GaAs substrate" *Proceedings of SPIE - The International Society for Optical Engineering*, 10830:176 – 181, 2018.

Cytowania bez autocytowań: 0/1/1 (Web of Science/Scopus/Google Scholar)

Impact Factor (2018): -

Punkty przyznawane przez Ministerstwo Edukacji i Nauki (2021): 5

Mój wkład merytoryczny: wykonałem pomiary SIMS i zinterpretowałem wyniki, uczestniczyłem w dyskusji dotyczącej istoty tych wyników w kontekście całego artykułu.

[B6] P.P. Michałowski, S. Złotnik, J. Sitek, K. Rosiński, M. Rudziński. "Oxygen induced high diffusion rate of magnesium dopants in GaN/AlGaN based UV LED heterostructures" *Physical Chemistry Chemical Physics*, 20:13890–13895, 2018.

Cytowania bez autocytowań: 6/6/7 (Web of Science/Scopus/Google Scholar)

Impact Factor (2018): 3.567

Punkty przyznawane przez Ministerstwo Edukacji i Nauki (2021): 100

Mój wkład merytoryczny: byłem autorem hipotezy badawczej, opracowałem procedurę SIMS i wykonałem pomiary, wykonałem analizę wyników, byłem autorem treści artykułu (zarówno wersji pierwotnej jak i korekty)

[B7] / [H4] P.P. Michałowski, I. Pasternak, W. Strupiński. "Contamination-free Ge-based graphene as revealed by graphene enhanced secondary ion mass spectrometry (GESIMS)" *Nanotechnology*, 29(1):015702, 2018.

Cytowania bez autocytowań: 0/0/0 (Web of Science/Scopus/Google Scholar)

Impact Factor (2018): 3.399

Punkty przyznawane przez Ministerstwo Edukacji i Nauki (2021): 100

Mój wkład merytoryczny: byłem autorem hipotezy badawczej, opracowałem procedurę SIMS i wykonałem pomiary, wykonałem analizę wyników, byłem autorem treści artykułu (zarówno wersji pierwotnej jak i korekty)

[B8] K.J. Sankaran, M. Ficek, S. Kunuku, K. Panda, C.-J. Yeh, J.Y. Park, M. Sawczak, P.P. Michalowski, K.-C. Leou, R. Bogdanowicz, I-N. Lin, K. Haenen. "Self organized multi-layered graphene boron-doped diamond hybrid nanowalls for high performance electron emission devices" *Nanoscale*, 10:1345–1355, 2018.

Cytowania bez autocytowań: 28/28/32 (Web of Science/Scopus/Google Scholar)

Impact Factor (2018): 6.970

Punkty przyznawane przez Ministerstwo Edukacji i Nauki (2021): 140

Mój wkład merytoryczny: wykonałem pomiary SIMS i zinterpretowałem wyniki, uczestniczyłem w dyskusji dotyczącej istoty tych wyników w kontekście całego artykułu.

[B9] / [H5] P.P. Michalowski, I. Pasternak, P. Ciepielewski, F. Guinea, W. Strupiński. "Formation of a highly doped ultra-thin amorphous carbon layer by ion bombardment of graphene" *Nanotechnology*, 29(30):305302, 2018.

Cytowania bez autocytowań: 1/1/1 (Web of Science/Scopus/Google Scholar)

Impact Factor (2018): 3.399

Punkty przyznawane przez Ministerstwo Edukacji i Nauki (2021): 100

Mój wkład merytoryczny: byłem autorem hipotezy badawczej, opracowałem procedurę SIMS i wykonałem pomiary, wykonałem analizę wyników, byłem autorem treści artykułu (zarówno wersji pierwotnej jak i korekty)

[B10] J. Grzonka, I. Pasternak, P.P. Michałowski, V. Kolkovsky, W. Strupinski. "Influence of hydrogen intercalation on graphene/Ge(001)/Si(001) interface" *Applied Surface Science*, 447:582 – 586, 2018.

Cytowania bez autocytowań: 12/12/12 (Web of Science/Scopus/Google Scholar)

Impact Factor (2018): 5.155

Punkty przyznawane przez Ministerstwo Edukacji i Nauki (2021): 140

Mój wkład merytoryczny: wykonałem pomiary SIMS i zinterpretowałem wyniki, uczestniczyłem w dyskusji dotyczącej istoty tych wyników w kontekście całego artykułu.

[B11] / [H6] P.P. Michałowski, J. Gaca, M. Wójcik, A. Turos. "Oxygen out-diffusion and compositional changes in zinc oxide during ytterbium ions bombardment" *Nanotechnology*, 29(42):425710,

Cytowania bez autocytowań: 3/3/3 (Web of Science/Scopus/Google Scholar)

Impact Factor (2018): 3.399

Punkty przyznawane przez Ministerstwo Edukacji i Nauki (2021): 100

Mój wkład merytoryczny: byłem autorem hipotezy badawczej, opracowałem procedurę SIMS i wykonałem pomiary, wykonałem analizę wyników, byłem autorem treści artykułu (zarówno wersji pierwotnej jak i korekty)

[B12] P.A. Caban, D. Teklinska, P.P. Michałowski, J. Gaca, M. Wojcik, J. Grzonka, P. Ciepielewski, M. Mozdzonek, J.M. Baranowski. "The role of hydrogen in carbon incorporation and surface roughness of MOCVD-grown thin boron nitride" *Journal of Crystal Growth*, 498:71 – 76, 2018.

Cytowania bez autocytowań: 5/4/6 (Web of Science/Scopus/Google Scholar)

Impact Factor (2018): 1.573

Punkty przyznawane przez Ministerstwo Edukacji i Nauki (2021): 70

Mój wkład merytoryczny: wykonałem pomiary SIMS i zinterpretowałem wyniki, uczestniczyłem w dyskusji dotyczącej istoty tych wyników w kontekście całego artykułu.

[B13] / **[H7] P.P. Michałowski**, W. Kaszub, P. Knyps, K. Rosiski, B. Staczyk, K. Przyborowska, E. Dumiszewska. "A-Crater-within-a-Crater Approach for Secondary Ion Mass Spectrometry Evaluation of the Quality of Interfaces of Multilayer Devices" *ACS Applied Materials & Interfaces*, 10(43):37694–37698, 2018.

Cytowania bez autocytowań: 1/0/1 (Web of Science/Scopus/Google Scholar)

Impact Factor (2018): 8.456

Punkty przyznawane przez Ministerstwo Edukacji i Nauki (2021): 200

Mój wkład merytoryczny: byłem pomysłodawcą badań, byłem autorem hipotezy badawczej, opracowałem procedurę SIMS i wykonałem pomiary, wykonałem analizę wyników, byłem autorem treści artykułu (zarówno wersji pierwotnej jak i korekty)

[B14] T. Ciuk, A. Kozlowski, P.P. Michałowski, W. Kaszub, M. Kozubal, Z. Rekuc, J. Podgorski, Be. Stanczyk, K. Przyborowska, I. Jozwik, A. Kowalik, P. Kaminski. "Thermally activated double-carrier transport in epitaxial graphene on vanadium compensated 6H-SiC as revealed by Hall effect measurements" *Carbon*, 139:776 – 781, 2018.

Cytowania bez autocytowań: 5/6/6 (Web of Science/Scopus/Google Scholar)

Impact Factor (2018): 7.466

Punkty przyznawane przez Ministerstwo Edukacji i Nauki (2021): 140

Mój wkład merytoryczny: wykonałem pomiary SIMS i zinterpretowałem wyniki, uczestniczyłem w dyskusji dotyczącej istoty tych wyników w kontekście całego artykułu.

[B15] T. Ciuk, W. Kaszub, K. Kociewicz, D. Czołak, A. Dobrowolski, J. Jagiełło, A. Chamryga, R. Budzich, B. Staczyk, K. Przyborowska, A. Harmasz, K. Góra, A. Kozłowski, P.P. Michalowski, P. Ciepielewski, I. Jówik, D. Tekliska, E. Tymicki, R. Kozłowski, M. Kozubal, P. Kamiński. "Silicon Carbide Homoepitaxy for Power Devices at Lukasiewicz Research Network - ITME" Przegląd Elektrotechniczny, 9:122092, 2019.

Cytowania bez autocytowań: 0/0/0 (Web of Science/Scopus/Google Scholar)

Impact Factor (2019): 0

Punkty przyznawane przez Ministerstwo Edukacji i Nauki (2021): 20

Mój wkład merytoryczny: wykonałem pomiary SIMS i zinterpretowałem wyniki, uczestniczyłem w dyskusji dotyczącej istoty tych wyników w kontekście całego artykułu.

[B16] / [H8] P.P. Michałowski, P. Knyps, P. Ciepielewski, P. Caban, E. Dumiszewska, J. Baranowski. "Destructive role of oxygen in growth of molybdenum disulfide determined by secondary ion mass spectrometry" *Physical Chemistry Chemical Physics*, 21:8837–8842, 2019.

Cytowania bez autocytowań: 0/0/0 (Web of Science/Scopus/Google Scholar)

Impact Factor (2019): 3.430

Punkty przyznawane przez Ministerstwo Edukacji i Nauki (2021): 100

Mój wkład merytoryczny: byłem pomysłodawcą badań, byłem autorem hipotezy badawczej, opracowałem procedurę SIMS i wykonałem pomiary, wykonałem analizę wyników, byłem autorem treści artykułu (zarówno wersji pierwotnej jak i korekty)

[B17] / [H9] P.P. Michałowski, P. Knyps, P. Ciepielewski, P.A. Caban, E. Dumiszewska, G. Kowalski, M. Tokarczyk, J.M. Baranowski. "Growth of highly oriented MoS2 via an intercalation process in the graphene/SiC(0001) system" *Physical Chemistry Chemical Physics*, 21:20641–20646, 2019.

Cytowania bez autocytowań: 1/1/1 (Web of Science/Scopus/Google Scholar)

Impact Factor (2019): 3.430

Punkty przyznawane przez Ministerstwo Edukacji i Nauki (2021): 100

Mój wkład merytoryczny: byłem pomysłodawcą badań, byłem autorem hipotezy badawczej, opracowałem procedurę SIMS i wykonałem pomiary, wykonałem analizę wyników, byłem autorem treści artykułu (zarówno wersji pierwotnej jak i korekty)

[B18] P. Knyps, P. A. Caban, P. Ciepielewski, **P.P. Michałowski**, E. Dumiszewska, J.M. Baranowski. "Towards increasing of lateral dimension of Molybdenum disulphide MoS2" *Proceedings of SPIE - The International Society for Optical Engineering*, 11176:1361 – 1366, 2019.

Cytowania bez autocytowań: 0/0/0 (Web of Science/Scopus/Google Scholar)

Impact Factor (2019): 0

Punkty przyznawane przez Ministerstwo Edukacji i Nauki (2021): 5

Mój wkład merytoryczny: wykonałem pomiary SIMS i zinterpretowałem wyniki, uczestniczyłem w dyskusji dotyczącej istoty tych wyników w kontekście całego artykułu.

[B19] / [H10] P.P. Michałowski, P. Caban, J. Baranowski. "Secondary ion mass spectrometry investigation of carbon grain formation in boron nitride epitaxial layers with atomic depth resolution" *Journal of Analytical Atomic Spectrometry*, 34:848–853, 2019.

Cytowania bez autocytowań: 1/1/1 (Web of Science/Scopus/Google Scholar)

Impact Factor (2019): 3.498

Punkty przyznawane przez Ministerstwo Edukacji i Nauki (2021): 100

Mój wkład merytoryczny: byłem pomysłodawcą badań, byłem autorem hipotezy badawczej, opracowałem procedurę SIMS i wykonałem pomiary, wykonałem analizę wyników, byłem autorem treści artykułu (zarówno wersji pierwotnej jak i korekty)

[B20] / [H11] P.P. Michałowski, S. Złotnik, and M. Rudziski. "Three dimensional localization of unintentional oxygen impurities in gallium nitride" *Chemical Communications*, 55:11539–11542, 2019.

Cytowania bez autocytowań: 4/5/5 (Web of Science/Scopus/Google Scholar)

Impact Factor (2019): 5.996

Punkty przyznawane przez Ministerstwo Edukacji i Nauki (2021): 200

Mój wkład merytoryczny: byłem autorem hipotezy badawczej, opracowałem procedurę SIMS i wykonałem pomiary, wykonałem analizę wyników, byłem autorem treści artykułu (zarówno wersji pierwotnej jak i korekty)

[B21] R. Muydinov, A. Steigert, M. Wollgarten, P.P. Michałowski, U. Bloeck, A. Pflug, D. Erfurt, R. Klenk, S. Körner, I. Lauermann, B. Szyszka. "Crystallisation Phenomena of In2O3:H Films" *Materials*, 12(2), 2019.

Cytowania bez autocytowań: 8/8/9 (Web of Science/Scopus/Google Scholar)

Impact Factor (2019): 3.260

Punkty przyznawane przez Ministerstwo Edukacji i Nauki (2021): 140

Mój wkład merytoryczny: wykonałem pomiary SIMS i zinterpretowałem wyniki, uczestniczyłem w dyskusji dotyczącej istoty tych wyników w kontekście całego artykułu.

[B22] / [H12] P.P. Michałowski, E. Grzanka, S. Grzanka, A. Lachowski, G. Staszczak, J. Plesiewicz, M. Leszczyski, A. Turos. "Indium concentration fluctuations in InGaN/GaN quantum wells" *Journal of Analytical Atomic Spectrometry*, 34:1718–1723, 2019.

Cytowania bez autocytowań: 2/2/4 (Web of Science/Scopus/Google Scholar)

Impact Factor (2019): 3.498

Punkty przyznawane przez Ministerstwo Edukacji i Nauki (2021): 100

Mój wkład merytoryczny: byłem pomysłodawcą badań, byłem autorem hipotezy badawczej, opracowałem procedurę SIMS i wykonałem pomiary, wykonałem analizę wyników, byłem autorem treści artykułu (zarówno wersji pierwotnej jak i korekty)

[B23] I. Jówik, A. Barcz, E. Dąbrowska, E. Dumiszewska, P.P. Michałowski. "Damage induced voltage alteration (DIVA) contrast in SEM images of ion-irradiated semiconductors" *Ultramicroscopy*, 204:6–9, 2019.

Cytowania bez autocytowań: 1/1/1 (Web of Science/Scopus/Google Scholar)

Impact Factor (2019): 2.452

Punkty przyznawane przez Ministerstwo Edukacji i Nauki (2021): 140

Mój wkład merytoryczny: wykonałem pomiary SIMS i zinterpretowałem wyniki, uczestniczyłem w dyskusji dotyczącej istoty tych wyników w kontekście całego artykułu.

[B24] S. Zlotnik, J. Sitek, K. Rosiński, P.P. Michałowski, J. Gaca, M. Wójcik, M. Rudziński. "Growth and thermal annealing for acceptor activation of p-type (Al)GaN epitaxial structures: Technological challenges and risks" *Applied Surface Science*, 488:688 – 695, 2019.

Cytowania bez autocytowań: 2/2/2 (Web of Science/Scopus/Google Scholar)

Impact Factor (2019): 6.182

Punkty przyznawane przez Ministerstwo Edukacji i Nauki (2021): 140

Mój wkład merytoryczny: wykonałem pomiary SIMS i zinterpretowałem wyniki, uczestniczyłem w dyskusji dotyczącej istoty tych wyników w kontekście całego artykułu.

[B25] / [H13] P.P. Michałowski. "Probing a chemical state during ultra low impact energy secondary ion mass spectrometry depth profiling" *Journal of Analytical Atomic Spectrometry*, 34:1954–1956, 2019.

Cytowania bez autocytowań: 1/1/1 (Web of Science/Scopus/Google Scholar)

Impact Factor (2019): 3.498

Punkty przyznawane przez Ministerstwo Edukacji i Nauki (2021): 100 Mój wkład merytoryczny: wykonałem całą pracę zawartą w artykule

[B26] Ł. Frąckowiak, P. Kuświk, G.Da. Chaves-O'Flynn, M. Urbaniak, M. Matczak, P.P. Michalowski, A. Maziewski, M. Reginka, A. Ehresmann, F. Stobiecki. "Magnetic Domains without Domain Walls: A Unique Effect of He+ Ion Bombardment in Ferrimagnetic Tb/Co Films" *Physical Review Letters*, 124:047203, 2020.

Cytowania bez autocytowań: 4/3/4 (Web of Science/Scopus/Google Scholar)

Impact Factor (2020): 9.161

Punkty przyznawane przez Ministerstwo Edukacji i Nauki (2021): 200

Mój wkład merytoryczny: wykonałem pomiary SIMS i zinterpretowałem wyniki, uczestniczyłem w dyskusji dotyczącej istoty tych wyników w kontekście całego artykułu.

[B27] P.A. Caban, P.P. Michalowski, I. Wlasny, J. Gaca, M. Wojcik, P. Ciepielewski, D. Teklinska, J.M. Baranowski. "Carbon incorporation in boron nitride grown by MOCVD under N2 flow" *Journal of Alloys and Compounds*, 815:152364, 2020.

Cytowania bez autocytowań: 1/0/1 (Web of Science/Scopus/Google Scholar)

Impact Factor (2020): 5.316

Punkty przyznawane przez Ministerstwo Edukacji i Nauki (2021): 100

Mój wkład merytoryczny: wykonałem pomiary SIMS i zinterpretowałem wyniki, uczestniczyłem w dyskusji dotyczącej istoty tych wyników w kontekście całego artykułu.

[B28] A. Cruz, F. Ruske, A. Eljarrat, P.P. Michałowski, A.B. Morales-Vilches, S. Neubert, E. Wang, C. T. Koch, B. Szyszka, R. Schlatmann, B. Stannowski. "Influence of Silicon Layers on the Growth of ITO and AZO in Silicon Heterojunction Solar Cells" *IEEE Journal of Photovoltaics*, 10(2):703–709, 2020.

Cytowania bez autocytowań: 6/6/10 (Web of Science/Scopus/Google Scholar)

Impact Factor (2020): 3.887

Punkty przyznawane przez Ministerstwo Edukacji i Nauki (2021): 100

Mój wkład merytoryczny: wykonałem pomiary SIMS i zinterpretowałem wyniki, uczestniczyłem w dyskusji dotyczącej istoty tych wyników w kontekście całego artykułu.

[B29] A. Gocalinska, A. Pescaglini, E. Secco, E.E. Mura, K. Thomas, A. Curran, F. Gity, R. Nagle, M. Schmidt, P.P. Michałowski, P.K. Hurley, I. Povey, E. Pelucchi. "Next generation low temperature polycrystalline materials for above IC electronics. High mobility n- and p-type III–V metalorganic vapour phase epitaxy thin films on amorphous substrates" *Journal of Physics: Photonics*, 2(2):025003, 2020.

Cytowania bez autocytowań: 1/1/1 (Web of Science/Scopus/Google Scholar)

Impact Factor (2020): 0

Punkty przyznawane przez Ministerstwo Edukacji i Nauki (2021): 20

Mój wkład merytoryczny: wykonałem pomiary SIMS i zinterpretowałem wyniki, uczestniczyłem w dyskusji dotyczacej istoty tych wyników w kontekście całego artykułu.

[B30] V.N. Popok, P.A. Caban, P.P. Michałowski, R. Thorpe, L.C. Feldman, K. Pedersen. "Two-dimensional electron gas at the AlGaN/GaN interface: Layer thickness dependence" *Journal of Applied Physics*, 127(11):115703, 2020.

Cytowania bez autocytowań: 1/1/2 (Web of Science/Scopus/Google Scholar)

Impact Factor (2020): 2.389

Punkty przyznawane przez Ministerstwo Edukacji i Nauki (2021): 70 Mój wkład merytoryczny: wykonałem pomiary SIMS i zinterpretowałem wyniki, uczestniczyłem w dyskusji dotyczącej istoty tych wyników w kontekście całego artykułu.

[B31] J. Wróbel, G.A. Umana-Membreno, J. Boguski, D. Sztenkiel, P.P. Michalowski, P. Martyniuk, L. Faraone, J. Wróbel, A. Rogalski. "Locally-Strain-Induced Heavy-Hole-Band Splitting Observed in Mobility Spectrum of p-Type InAs Grown on GaAs" *Physica Status Solidi Rapid Research Letters*, 14(4):1900604, 2020.

Cytowania bez autocytowań: 1/3/4 (Web of Science/Scopus/Google Scholar)

Impact Factor (2020): 2.821

Punkty przyznawane przez Ministerstwo Edukacji i Nauki (2021): 100

Mój wkład merytoryczny: wykonałem pomiary SIMS i zinterpretowałem wyniki, uczestniczyłem w dyskusji dotyczącej istoty tych wyników w kontekście całego artykułu.

[B32] / [H14] P.P. Michałowski. "Titanium pre-sputtering for an enhanced secondary ion mass spectrometry analysis of atmospheric gas elements" *Journal of Analytical Atomic Spectrometry*, 35:1047–1050, 2020.

Cytowania bez autocytowań: 0/0/0 (Web of Science/Scopus/Google Scholar)

Impact Factor (2020): 4.023

Punkty przyznawane przez Ministerstwo Edukacji i Nauki (2021): 100

Mój wkład merytoryczny: wykonałem całą pracę zawartą w artykule

[B33] / [H15] P.P. Michałowski, S. Zlotnik, I. Jóźwik, A. Chamryga, M. Rudziński. "3D Depth Profile Reconstruction of Segregated Impurities using Secondary Ion Mass Spectrometry" *Journal of Visualized Experiments*, 158:e61065, 2020.

Cytowania bez autocytowań: 0/0/0 (Web of Science/Scopus/Google Scholar)

Impact Factor (2020): 1.355

Punkty przyznawane przez Ministerstwo Edukacji i Nauki (2021): 70

Mój wkład merytoryczny: byłem pomysłodawcą badań, byłem autorem hipotezy badawczej, opracowałem procedurę SIMS i wykonałem pomiary, wykonałem analizę wyników, byłem autorem treści artykułu (zarówno wersji pierwotnej jak i korekty)

[B34] K. Piętak, S. Złotnik, E. Rozbiegała, P.P. Michalowski, M. Wójcik, J. Gaca, M. Rudziński. "Phosphorus implantation of Mg-doped (Al)GaN heterostructures: structural examination and depth profiling" *Journal of Materials Science: Materials in Electronics*, (31):1789217902, 2020.

Cytowania bez autocytowań: 0/0/0 (Web of Science/Scopus/Google Scholar)

Impact Factor (2020): 2.478

Punkty przyznawane przez Ministerstwo Edukacji i Nauki (2021): 70

Mój wkład merytoryczny: wykonałem pomiary SIMS i zinterpretowałem wyniki, uczestniczyłem w dyskusji dotyczącej istoty tych wyników w kontekście całego artykułu.

[B35] A. Wójcik, W. Kolkowski, I. Pasternak, W. Strupiski, S. Kozdra, P.P. Michałowski. "Electrically active and hydrogen passivated Zn in GaAs/AlGaAs specifically distinguished during secondary ion mass spectrometry depth profiling" *Journal of Analytical Atomic Spectrometry*, 36:178–184, 2021.

Cytowania bez autocytowań: 0/0/0 (Web of Science/Scopus/Google Scholar)

Impact Factor (2020): 4.023

Punkty przyznawane przez Ministerstwo Edukacji i Nauki (2021): 100

Mój wkład merytoryczny: byłem pomysłodawcą badań, byłem autorem hipotezy badawczej, wykonałem pomiary SIMS i zinterpretowałem wyniki, uczestniczyłem w dyskusji dotyczącej istoty tych wyników w kontekście całego artykułu, byłem opiekunem autorki treści artykułu (zarówno wersji pierwotnej jak i korekty)

[B36] A. Taube, M. Kamiński, M. Ekielski, R Kruszka, J. Jankowska-Śliwiska, P.P. Michałowski, J. Zdunek, A. Szerling. "Selective etching of p-GaN over A0.25Ga0.75N in Cl2/Ar/O2 ICP plasma for fabrication of normally-off GaN HEMTs" *Materials Science in Semiconductor Processing*, 122:105450, 2021.

Cytowania bez autocytowań: 0/0/0 (Web of Science/Scopus/Google Scholar)

Impact Factor (2020): 3.927

Punkty przyznawane przez Ministerstwo Edukacji i Nauki (2021): 70

Mój wkład merytoryczny: wykonałem pomiary SIMS i zinterpretowałem wyniki, uczestniczyłem w dyskusji dotyczącej istoty tych wyników w kontekście całego artykułu.

[B37] P. Ciechanowicz, S. Gorantla, P.P. Michalowski, E. Zdanowicz, J.-G. Rousset, D. Hlushchenko, K. Adamczyk, D. Majchrzak, R. Kudrawiec, D. Hommel. "Arsenic-Induced Growth of Dodecagonal GaN Microrods with Stable a-Plane Walls" *Advanced Optical Materials*, 9(5):2001348, 2021.

Cytowania bez autocytowań: 1/1/1 (Web of Science/Scopus/Google Scholar)

Impact Factor (2020): 9.926

Punkty przyznawane przez Ministerstwo Edukacji i Nauki (2021): 140

Mój wkład merytoryczny: wykonałem pomiary SIMS i zinterpretowałem wyniki, uczestniczyłem w dyskusji dotyczącej istoty tych wyników w kontekście całego artykułu.

[B38] P. Kamiski, R. Budzich, J. Gaca, P.P. Michałowski, R. Kozłowski, A. Harmasz, T. Ciuk, and J. Płocharski. "Effect of oxidation temperature on the inhomogeneity of chemical composition and density in nanometric SiO2 films grown on 4H-SiC" *Journal of Materials Chemistry C*, 9:4393–4404, 2021.

Cytowania bez autocytowań: 0/0/0 (Web of Science/Scopus/Google Scholar)

Impact Factor (2020): 7.393

Punkty przyznawane przez Ministerstwo Edukacji i Nauki (2021): 140

Mój wkład merytoryczny: wykonałem pomiary SIMS i zinterpretowałem wyniki, uczestniczyłem w dyskusji dotyczącej istoty tych wyników w kontekście całego artykułu.

[B39] M. Jacquet, M. Izzo, S. Osella, S. Kozdra, P.P. Michałowski, D. Gołowicz, K. Kazimierczuk, M.T. Gorzkowski, A. Lewera, M. Teodorczyk, B. Trzaskowski, R. Jurczakowski, D.T. Gryko, and J. Kargul. "Development of a universal conductive platform for anchoring photo- and electroactive proteins using organometallic terpyridine molecular wires" *Nanoscale*, 13:9773–9787, 2021.

Cytowania bez autocytowań: 0/1/1 (Web of Science/Scopus/Google Scholar)

Impact Factor (2020): 7.790

Punkty przyznawane przez Ministerstwo Edukacji i Nauki (2021): 140

Mój wkład merytoryczny: wykonałem pomiary SIMS i zinterpretowałem wyniki, uczestniczyłem w dyskusji dotyczącej istoty tych wyników w kontekście całego artykułu.

[B40] T. Ciuk, W. Kaszub, K. Kosciewicz, A. Dobrowolski, J. Jagiello, A. Chamryga, J. Gaca, M. Wojcik, D. Czolak, B. Stanczyk, K.a Przyborowska, R. Kozlowski, M. Kozubal, P.P. Michalowski,

M.J. Szary, P. Kaminski. "Highly-doped p-type few-layer graphene on uid off-axis homoepitaxial 4H-SiC" *Current Applied Physics*, 27:17–24, 2021.

Cytowania bez autocytowań: 1/1/1 (Web of Science/Scopus/Google Scholar)

Impact Factor (2020): 2.480

Punkty przyznawane przez Ministerstwo Edukacji i Nauki (2021): 70

Mój wkład merytoryczny: wykonałem pomiary SIMS i zinterpretowałem wyniki, uczestniczyłem w dyskusji dotyczącej istoty tych wyników w kontekście całego artykułu.

[B41] / [H16] P.P. Michalowski, D. Maciążek, Z. Postawa, P.A. Caban, S. Kozdra, A. Wójcik, J.M. Baranowski. "Defect-mediated sputtering process of boron nitride during high incident angle low-energy ion bombardment" *Measurement*, 179:109487, 2021.

Cytowania bez autocytowań: 0/0/0 (Web of Science/Scopus/Google Scholar)

Impact Factor (2020): 3.927

Punkty przyznawane przez Ministerstwo Edukacji i Nauki (2021): 200

Mój wkład merytoryczny: byłem pomysłodawcą badań, byłem autorem hipotezy badawczej, opracowałem procedurę SIMS i wykonałem pomiary, wykonałem analizę wyników, byłem autorem treści artykułu (zarówno wersji pierwotnej jak i korekty)

II.5 Wykaz osiągnieć projektowych, konstrukcyjnych, technologicznych

Nie dotyczy

II.6 Wykaz publicznych realizacji dzieł artystycznych

Nie dotyczy

II.7 Informacja o wystąpieniach na krajowych lub międzynarodowych konferencjach naukowych lub artystycznych, z wyszczególnieniem przedstawionych wykładów na zaproszenie i wykładów plenarnych.

Uwzględnione zostały wyłącznie te wystąpienia, które prezentowałem osobiście.

II.7.1 Przed uzyskaniem stopnia naukowego doktora

- 03.2008 ToF-SIMS analysis of thin Al1-xSixOy layers, DPG Spring Meeting, Berlin, Niemcy, prezentacja ustna.
- 03.2009 Characterization of the diffusion process in Al2O3 thin films based on ToF-SIMS measurements, DPG Spring Meeting, Drezno, Niemcy, prezentacja ustna.
- 07.2009 Formation of an interface layer between Al1-xSixOy thin films and the Si substrate during rapid thermal annealing, ICFSI-12, Weimar, Niemcy, prezentacja ustna.

II.7.2 Po uzyskaniu stopnia naukowego doktora

- 06.2016 Secondary Ion Mass Spectroscopy depth profiling of hydrogen-intercalated graphene on SiC, Graphene Week, Warszawa, Polska, prezentacja ustna.
- 09.2016 Secondary Ion Mass Spectroscopy depth profiling of hydrogen-intercalated graphene on SiC, SIMS Europe, Münster, Niemcy, prezentacja ustna.
- 09.2016 Secondary Ion Mass Spectroscopy depth profiling of hydrogen-intercalated graphene on SiC, ELTE16, Wisła, Polska, prezentacja ustna.

- 10.2016 Graphene-Enhanced Secondary Ion Mass Spectroscopy for analysis of surface, 2D materials and ultra-thin films, 2D Materials, Heterostructures and Devices, Manchester, Wielka Brytania, plakat.
- 09.2017 Graphene Enhanced Secondary Ion Mass Spectrometry (GESIMS), SIMS21, Kraków, Polska, prezentacja ustna.
- 09.2017 Copper-free graphene growth process evaluated by Graphene Enhanced Secondary Ion Mass Spectrometry (GESIMS), Graphene Week, Ateny, Grecja, prezentacja ustna.
- 07.2018 Oxygen-induced high diffusion rate of magnesium dopant in GaNie dotyczylGaN based UV LED heterostructures, ISGN-7, Warszawa, Polska, prezentacja ustna.
- 09.2018 3D imagining of boron nitride films with atomic depth resolution, SIMS Europe, Münster, Niemcy, prezentacja ustna.
- 03.2019 Secondary Ion Mass Spectrometry Characterization of 2D Materials, 1PMG, Poznań, Polska, prezentacja ustna.
- 10.2019 Influence of a substrate on a growth process of 2D molybdenum disulfide layers determined by secondary ion mass spectrometry, SIMS22, Kyoto, Japonia, plakat.
- 10.2019 Indium concentration fluctuations in InGaN quantum wells, SIMS22, Kyoto, Japonia, prezentacja ustna.
- 04.2021 Precise localization of contaminants in graphene with secondary ion mass spectrometry, 2021 Rice SIMS workshop, online, plakat.
- 04.2021 Depth profiling of VCSEL structure with modulated impact energy, incident angle and extraction parameters, 2021 Rice SIMS workshop, online, prezentacja ustna.
- 09.2021 Atomic depth-resolution characterization of MAX and MXenes using ultra-low energy secondary ion mass spectrometry, DIAM2021, online, prezentacja ustna.

II.7.3 Nadchodzace wykłady zaproszone

- 12.2021 Secondary ion mass spectrometry with subnanometer depth resolution characterization of smart materials, ESMAC-2021, online, keynote speaker
- 03.2022 Ultra low energy SIMS depth profiling of 2D materials, FCMN 2022, Monterey, CA, USA, wykład zaproszony

II.8 Informacja o udziale w komitetach organizacyjnych i naukowych konferencji krajowych lub międzynarodowych, z podaniem pełnionej funkcji.

II.8.1 Przed uzyskaniem stopnia naukowego doktora

• 07.2009 ICFSI-12, Weimar, Niemcy - pomoc w ustaleniu harmonogramu

II.8.2 Po uzyskaniu stopnia naukowego doktora

• 06.2016 Graphene Week, Warszawa, Polska - pomoc w ustaleniu harmonogramu

II.9 Informacja o uczestnictwie w pracach zespołów badawczych realizujących projekty finansowane w drodze konkursów krajowych lub zagranicznych, z podziałem na projekty zrealizowane i będące w toku realizacji, oraz z uwzględnieniem informacji o pełnionej funkcji w ramach prac zespołów.

II.9.1 Przed uzyskaniem stopnia naukowego doktora

• 2008-2010 Gigascale Oriented Solid State flAsh Memory for EuRope (GOSSAMER), Seventh Framework Programme, EU, wykonawca (zakończony).

II.9.2 Po uzyskaniu stopnia naukowego doktora

- 2015-2016 Graphene-Based Revolutions in ICT And Beyond, Seventh Framework Programme, EU, wykonawca (zakończony).
- 2015-2017 Production engineering technology of UV diode based on aluminum nitride and sapphire substrates, NCBR, Polska, wykonawca (zakończony).
- 2015-2018 Graphene for Integrated Circuit Applications (GRAPHICA), M-ERA.NET, EU, wy-konawca (zakończony).
- 2016-2018 Graphene Flagship Core Project 1, Horizon 2020, EU, wykonawca (zakończony).
- 2018-2020 Graphene Flagship Core Project 2, Horizon 2020, EU, wykonawca (zakończony).
- 2017-2020 Semiconductor materials technologies for high power and frequency electronics (WidePOWER), NCBR, Polska, wykonawca (zakończony).
- 2020-2023 Graphene Flagship Core Project 3, Horizon 2020, EU, wykonawca (trwający).
- 2019-2022 Secondary Ion Mass Spectrometry characterization of thin films with nanometer and subnanometer depth resolution, NCN, Polska, kierownik projektu (trwający).
- 2020-2022 Modeling Unconventional Nanoscaled Device FABrication (MUNDFAB), Horizon 2020, EU, przedstawiciel partnera w konsorcjum i kierownik projektu (trwający).
- II.10 Członkostwo w międzynarodowych lub krajowych organizacjach i towarzystwach naukowych wraz z informacja o pełnionych funkcjach.

Nie dotyczy

II.11 Informacja o odbytych stażach w instytucjach naukowych lub artystycznych, w tym zagranicznych, z podaniem miejsca, terminu, czasu trwania stażu i jego charakteru.

Nie dotyczy

II.12 Członkostwo w komitetach redakcyjnych i radach naukowych czasopism wraz z informacją o pełnionych funkcjach (np. redaktora naczelnego, przewodniczącego rady naukowej, itp.).

Nie dotyczy

- II.13 Informacja o recenzowanych pracach naukowych lub artystycznych, w szczególności publikowanych w czasopismach międzynarodowych.
- II.13.1 Przed uzyskaniem stopnia naukowego doktora

Nie dotyczy

II.13.2 Po uzyskaniu stopnia naukowego doktora

- ACS Applied Materials & Interfaces x2
- ACS Nano x2
- IOP books x1
- Journal of Physics Condensed Matter x2
- Journal of Physics D Applied Physics x1
- Journal of Vacuum Science and Technology B Nanotechnology and Microelectronics x5
- Materials Research Express x2
- Nanotechnology x2
- Semiconductor Science and Technology x2
- Surface and Interface Analysis x4

Suma: 23

II.14 Informacja o uczestnictwie w programach europejskich lub innych programach międzynarodowych.

Nie dotyczy

II.15 Informacja o udziale w zespołach badawczych, realizujących projekty inne niż określone w pkt. II.9.

Nie dotyczy

II.16 Informacja o uczestnictwie w zespołach oceniających wnioski o finansowanie badań, wnioski o przyznanie nagród naukowych, wnioski w innych konkursach mających charakter naukowy lub dydaktyczny.

Nie dotyczy

III INFORMACJA O WSPÓŁPRACY Z OTOCZENIEM SPOŁECZNYM I GOSPODARCZYM

III.1 Wykaz dorobku technologicznego.

Nie dotyczy

- III.2 Informacja o współpracy z sektorem gospodarczym.
- III.2.1 Przed uzyskaniem stopnia naukowego doktora
 - Qimonda, Drezno, Niemcy
 - Infineon, Drezno, Niemcy
 - AMD, Drezno, Niemcy
 - Global foundries, Drezno, Niemcy

III.2.2 Po uzyskaniu stopnia naukowego doktora

- · VIGO System, Ożarów Mazowiecki, Polska
- TopGaN, Warszawa, Polska
- STMicroelectronics, Crolles, Francja
- Applied Materials, Gloucester, USA
- II-VI Incorporated, Warren, USA
- AMS, Premstaetten, Austria
- Infineon Austria, Villach, Austria

III.3 Uzyskane prawa własności przemysłowej, w tym uzyskane patenty, krajowe lub międzynarodowe.

Nie dotyczy

III.4 Informacja o wdrożonych technologiach.

III.4.1 Przed uzyskaniem stopnia naukowego doktora

Nie dotyczy

III.4.2 Po uzyskaniu stopnia naukowego doktora

Opracowałem wiele dedykowanych procedur SIMS dla partnerów przemysłowych, które były wykorzystane w następujących celach:

- VIGO System badanie detektorów podczerwieni oraz struktur VCSEL
- TopGaN badanie struktur diody laserowej
- STMicroelectronics badanie tranzystorów typu gate-all-around
- Applied Materials jakościowa analiza procesu implantacji jonów do gorącego podłoża w technologii krzemowej i germanowej
- II-VI Incorporated badania struktur VCSEL
- AMS poufne
- Infineon Austria jakościowa analiza procesu implantacji jonów do gorącego podłoża w technologii węglika krzemu

III.5 Informacja o wykonanych ekspertyzach lub innych opracowaniach wykonanych na zamówienie instytucji publicznych lub przedsiębiorców.

Nie dotyczy

III.6 Informacja o udziale w zespołach eksperckich lub konkursowych.

Nie dotyczy

III.7 Informacja o projektach artystycznych realizowanych ze środowiskami pozaartystycznymi.

Nie dotyczy

IV INFORMACJE NAUKOMETRYCZNE

Informacja o punktacji Impact Factor (w dziedzinach i dyscyplinach, w których parametr ten jest powszechnie używany jako wskaźnik naukometryczny).

Impact Factor dla poszczególnych artykułów podany jest w punkcie II.4

Całkowity Impact Factor przed uzyskaniem stopnia naukowego doktora: 11.067

Całkowity Impact Factor po uzyskaniu stopnia naukowego doktora: 167.184

Całkowity Impact Factor dla artykułów, które wchodzą w skład cyklu powiązanych tematycznie

artykułów naukowych (wymienionych w punkcie I.2): 66.074

Całkowity Impact Factor podczas całej kariery naukowej: 178.251

IV.2 Informacja o liczbie cytowań publikacji wnioskodawcy, z oddzielnym uwzględnieniem autocytowań.

Liczba cytowania bez autocytowań dla poszczególnych artykułów podana jest w punkcie II.4

Całkowita liczba cytowania bez autocytowań przed uzyskaniem stopnia naukowego doktora: 100/113/131 (Web of Science/Scopus/Google Scholar)

Całkowita liczba cytowania bez autocytowań po uzyskaniu stopnia naukowego doktora: 110/111/133 (Web of Science/Scopus/Google Scholar)

Całkowita liczba cytowania bez autocytowań dla artykułów, które wchodzą w skład cyklu powiązanych tematycznie artykułów naukowych (wymienionych w punkcie I.2): 26/25/30 (Web of Science/Scopus/ Google Scholar)

Całkowita liczba cytowania bez autocytowań podczas całej kariery naukowej: 210/224/264 (Web of Science/Scopus/Google Scholar)

Całkowita liczba autocytowań: 100/100/100 (Web of Science/Scopus/Google Scholar)

IV.3 Informacja o posiadanym indeksie Hirscha.

h-index: 7/7/8 (Web of Science/Scopus/Google Scholar)

h-index z uwzględnieniem autocytowań: 10/10/10 (Web of Science/Scopus/Google Scholar)

Informacja o liczbie punktów MEiN.

W czasie, gdy aktywnie publikowałem, dwukrotnie zmieniły się zasady przyznawania punktów ministerialnych, a artykuły z lat 2009-2011, 2015-2018 i 2019-2021 byłyby traktowane inaczej. Ponieważ jest to szczególnie istotne w przypadku artykułów wchodzących w skład cyklu artykułów naukowych powiązanych tematycznie (opublikowanych w latach 2016-2021) postanowiłem przedstawić jedynie punkty z najnowszego zestawienia, opublikowanego 18.02.2021. Punkty dla poszczególnych artykułów podana jest w punkcie II.4

Całkowita liczba punktów przed uzyskaniem stopnia naukowego doktora: 490

Całkowita liczba punktów po uzyskaniu stopnia naukowego doktora: 4410

Całkowita liczba punktów dla artykułów, które wchodzą w skład cyklu powiązanych tematycznie artykułów naukowych (wymienionych w punkcie I.2): 1950

Całkowita liczba punktów podczas całej kariery naukowej: 4900

Secondary ion mass spectroscopy depth profiling of hydrogen-intercalated graphene on SiC

Paweł Piotr Michałowski, Wawrzyniec Kaszub, Alexandre Merkulov, and Włodek Strupiński

Citation: Appl. Phys. Lett. **109**, 011904 (2016); View online: https://doi.org/10.1063/1.4958144

View Table of Contents: http://aip.scitation.org/toc/apl/109/1

Published by the American Institute of Physics

Articles you may be interested in

SIMS depth profiling and topography studies of repetitive III–V trenches under low energy oxygen ion beam sputtering

Journal of Vacuum Science & Technology B, Nanotechnology and Microelectronics: Materials, Processing, Measurement, and Phenomena **34**, 03H131 (2016); 10.1116/1.4944632

Structural consequences of hydrogen intercalation of epitaxial graphene on SiC(0001)

Applied Physics Letters 105, 161602 (2014); 10.1063/1.4899142

The quasi-free-standing nature of graphene on H-saturated SiC(0001)

Applied Physics Letters 99, 122106 (2011); 10.1063/1.3643034

Fabrication and applications of multi-layer graphene stack on transparent polymer

Applied Physics Letters 110, 041901 (2017); 10.1063/1.4974457

Large area quasi-free standing monolayer graphene on 3C-SiC(111)

Applied Physics Letters 99, 081904 (2011); 10.1063/1.3618674

Time-of-flight secondary ion mass spectrometry as a tool for evaluating the plasma-induced hydrogenation of graphene

Journal of Vacuum Science & Technology B, Nanotechnology and Microelectronics: Materials, Processing, Measurement, and Phenomena **34**, 03H113 (2016); 10.1116/1.4942086





Secondary ion mass spectroscopy depth profiling of hydrogen-intercalated graphene on SiC

Paweł Piotr Michałowski, ^{1,a)} Wawrzyniec Kaszub, ¹ Alexandre Merkulov, ² and Włodek Strupiński ¹

¹Institute of Electronic Materials Technology, Wólczyńska 133, 01-919 Warsaw, Poland ²CAMECA, 29 quai des Grésillons, 92622 Gennevilliers Cedex, France

(Received 20 January 2016; accepted 28 June 2016; published online 7 July 2016)

For a better comprehension of hydrogen intercalation of graphene grown on a silicon carbide substrate, an advanced analytical technique is required. We report that with a carefully established measurement procedure it is possible to obtain a reliable and reproducible depth profile of bi-layer graphene (theoretical thickness of 0.69 nm) grown on the silicon carbide substrate by the Chemical Vapor Deposition method. Furthermore, we show that with depth resolution as good as 0.2 nm/decade, both hydrogen coming from the intercalation process and organic contamination can be precisely localized. As expected, hydrogen was found at the interface between graphene and the SiC substrate, while organic contamination was accumulated on the surface of graphene and did not penetrate into it. Such a precise measurement may prove to be invaluable for further characterization of 2D materials. *Published by AIP Publishing*. [http://dx.doi.org/10.1063/1.4958144]

Further optimization of epitaxial Chemical Vapor Deposition (CVD) growth and processing of graphene on silicon carbide requires the application of advanced characterization techniques. Particularly, the formation of a graphene buffer layer (a graphene-like lattice covalently bonded to the underlying silicon atoms of the SiC substrate)¹⁻⁶ and its subsequent conversion to quasi-free standing graphene by hydrogen intercalation^{7–12} have been the subject of intensive worldwide research. Many analytical techniques have been already applied and changes of structural and electronic properties during the hydrogen intercalation have been adequately described. The diffusion of hydrogen in graphene, however, has not been directly monitored since detection of hydrogen in solid state samples is not possible for many techniques. One of the most sensitive analytical techniques for advanced material research that can also detect hydrogen is Secondary Ion Mass Spectroscopy (SIMS). Several SIMS measurements on graphene have already been reported¹³⁻¹⁹ but no attempt to localize hydrogen and organic contamination in the graphene layer grown on SiC has been made thus far. This is indeed a very challenging task because the best depth resolution of most tools is in the range of 1-2 nm. This was not a problem in those aforementioned experiments because SIMS was used to map the surface of the graphene layer, 13,14 analyze mass spectra of grapheme, 15,16 or create a depth profile of single-layer graphene grown on substrates that do not contain carbon ^{17,18} (and thus the carbon signal that originates from graphene can be easily distinguished from the substrate even though the thickness of the graphene layer is smaller than the nominal depth resolution of the tool). In the case of silicon carbide it is very difficult to identify the interface between graphene and the substrate as both materials contain carbon atoms. It has been achieved for multilayer graphene (with thickness exceeding 3 nm)¹⁹ but the intercalation process is performed for samples with one or two layers of graphene (thickness of less than 1 nm) and thus much better depth resolution is required. One of the possible approaches is to use the influence of ion bombardment on the chemical state of carbon. Such approach is already proposed for high fraction of carbon in a diamond like (sp^3) hybrid state.^{20,21} The difference in ion yield of carbon containing molecular ions might provide the information on chemical state of carbon in layers. In case of graphene the approach must be defined to establish the interface between graphene and carbon contained in the substrate.

Epitaxial graphene was grown at 1600 °C by the CVD technique²² on (10×10) mm² nominally on-axis 4H-SiC (0001), Si-face chemo-mechanically polished substrates. Graphene layers were grown under an argon laminar flow in a hot-wall Aixtron VP508 reactor. The process relies critically on the creation of dynamic flow conditions in the reactor that control the Si sublimation rate and enable the mass transport of hydrocarbon to the SiC substrate. The laminar gas flow over the SiC surface consists of layers moving at different velocities due to the shear stress between adjacent gas layers. Reynolds number Re is a measure of the ratio of inertial forces to viscous forces and consequently quantifies the relative importance of these two forces in a given gas flow. Tuning the value of the Re number enables the formation of an Ar boundary layer (BL) thick enough to prevent Si sublimation, allowing the diffusion of hydrocarbon to the SiC surface and, in consequence, epitaxial CVD of graphene on the SiC surface. Reactor pressure applied in the case of CVD was 30 mbar. The intercalation of hydrogen was achieved in the same process during the sample's cooling down which prevented H_2 escape from graphene. Argon was switched to hydrogen at the temperature of 1100 °C and reactor pressure of 900 mbar. The samples were covered with a 2 nm thick layer of chromium (99.99%) deposited in an electron-beam physical vapor deposition process. Prior to

a) Author to whom correspondence should be addressed. Electronic mail: pawel.michalowski@itme.edu.pl

deposition samples were refreshed in a hot acetone and ethanol bath and annealed at 150 °C and pressure of 10⁻⁶ mbar. Two different samples were prepared for the following experiments: Sample A: bi-layer graphene CVD grown on SiC, hydrogen intercalated. Sample B: mono-layer graphene + a buffer layer CVD grown on SiC, both with a 2 nm thick Cr capping layer. For reliability tests, an additional monolayer graphene sample covered with the same Cr capping layer was prepared.

Raman spectroscopy measurements were performed in back-scattering geometry, using a Renishaw inVia Raman Microscope, with a $\times 100$ objective and a 532 nm Nd:YAG laser as an excitation source. After the CVD process the graphene samples were inspected under an optical microscope and then characterized by Hall effect measurements in van der Pauw geometry (0.55T Ecopia HMS-3000 setup) with four golden probes placed in the corners of the 10 mm \times 10 mm substrates. ^{23,24}

In this work all SIMS depth profiles were performed employing the CAMECA SC Ultra instrument under ultrahigh vacuum (UHV), usually of 4×10^{-10} mbar. Sufficient depth resolution was obtained by using a low impact energy of 150 eV for a Cs^+ primary beam rastered over (100 × 100) μm^2 . The analysis area was limited to $(33 \times 33) \, \mu \text{m}^2$. Mass interferences were verified prior of analysis and mass resolving power $\frac{m}{\Delta m} = 4000$ was used for most experiments. The intensity of the primary beam was 13-15 nA in the majority of experiments. For the most precise measurement it was reduced to 10 nA with the "beam blanking" option enabled (the sample was not sputtered when the detector was switching between various masses). The SC Ultra tool is able to achieve such low impact energies due to the EXLIE (EXtra Low Impact Energy) technology, in the case of which a primary floating column concept is used.²⁵ In this notion, contrary to standard SIMS tools, the primary column has the "floating voltage" instead of the grounded voltage level between the space at any two lenses inside the column and thus primary ions are slowed down at the end of the column maintaining favorable conditions for ion acceleration and beam stability. Ion beam on the sample in the SC Ultra tool has a square shape and due to the "variable rectangular shape concept" forms a homogenous spot. Primary beam at a working point in the SC Ultra is formed by two stencils well-shaped apertures. These innovations allow one to use the low impact energy of primary ions with high sensitivity for all measured elements, high depth resolution (below 1 nm), and high dynamic range with a low sputter rate (lower than 0.5 nm/min).^{26,27}

Prior to the deposition of the Cr cap the layer structure of graphene samples was investigated by Raman spectroscopy. We used the same procedure as already reported 12 and confirmed that Sample A consisted of two graphene layers whereas Sample B was a mono-layer of graphene with a buffer layer (see Fig. 1). We did not consider differences between terraces and edges since the analysis area of the SIMS technique was too large to distinguish them. Furthermore, both samples were measured using Hall effect and, similarly to the aforementioned report, holes were dominant carriers for Sample A (the carrier concentration and electron mobility were determined as $n_h \approx 1.4 \times 10^{13}$ cm⁻²

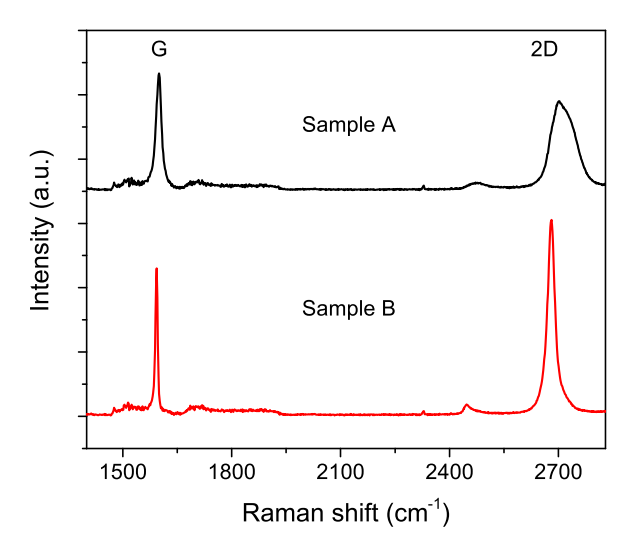


FIG. 1. Typical Raman spectra of graphene for both samples. The contribution from the SiC substrate was subtracted. The position, FWHM, and shape of the 2D peak confirm that Sample A is bi-layer graphene, while sample B is mono-layer graphene with a buffer layer.

and $\mu_h \approx 4420 \, {\rm cm}^2 \, {\rm V}^{-1} \, {\rm s}^{-1}$, respectively) and electrons for Sample B ($n_e \approx 1.7 \times 10^{12} {\rm cm}^{-2}$ and $\mu_e \approx 1320 {\rm cm}^2 \, {\rm V}^{-1} \, {\rm s}^{-1}$).

To obtain a good depth profile of graphene one cannot rely only on the excellent depth resolution of the tool. Dynamic SIMS is used to determine the elemental composition of a sample but in general does not bear information about its chemical state and thus graphene can only be analyzed as signals of carbon mono- or polyatomic ions. A clear and reproducible measurement procedure has to be established to distinguish graphene from organic contamination and the SiC substrate, both of which contain a lot of carbon atoms. In the case of the substrate the solution is relatively easy—an interface between graphene and the SiC substrate can be defined as a point where the ²⁸Si⁻ signal increases rapidly (the intensity is two times higher than the background) as this element is not present in the graphene material. The problem with organic contamination is, however, more serious. On the surface of every sample exposed to air one can expect a lot of organic contamination which can be observed as intense peaks of various signals (most prominently H, C, N, and O) in a SIMS depth profile with a considerable decaying length which is caused by the ion mixing effect. In the case of the hydrogen signal, the range of mixing exceeded the thickness of graphene layers and thus it was not possible to analyze hydrogen coming from the intercalation process. Furthermore, it was reported that during the initial stages of sputtering the secondary ion yield can be significantly different than for the rest of the experiment.²⁸ The thickness of this transition layer was expected to be comparable with the thickness of graphene. To overcome these problems, a thin metal layer was deposited on the sample prior to the SIMS measurements. Fig. 2 shows a typical depth profile of a CVD grown graphene bi-layer on a SiC substrate with a 2 nm thick Cr capping layer. The interface between graphene and the substrate can be easily distinguished but it is not the case for the interface between the chromium capping layer and graphene. The ${}^{54}Cr^{-}$ signal has a long decay length (it reaches half of its maximum intensity in a SiC substrate!) due to ion mixing and thus it is not possible to determine precisely

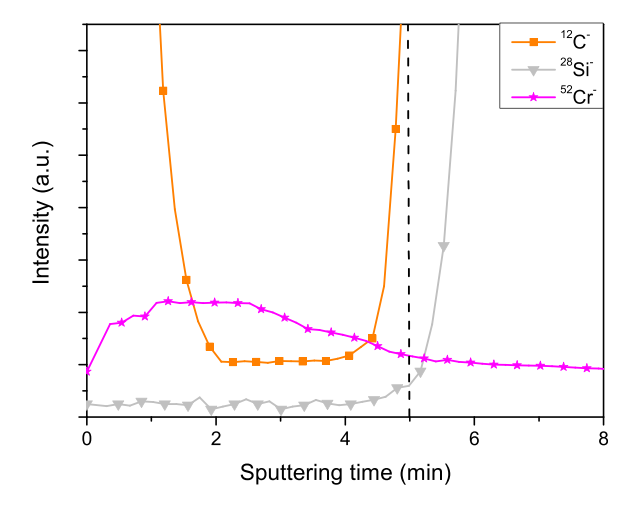


FIG. 2. A depth profile of graphene on SiC with a Cr capping layer (sample A). The interface between graphene and the SiC substrate can be identified (a dashed line) at the point where the $^{28}Si^-$ signal increases rapidly. Due to a strong ion mixing effect, the $^{54}Cr^-$ signal has a very long decay length and thus it is not possible to clearly distinguish the beginning of the graphene layer. All signals were scaled for a better visibility.

where the graphene layer starts (similar effect was observed for other capping materials, namely, Au and Ti). It is possible to define an interface as a point where the intensity of the $^{54}Cr^-$ signal starts to decrease. Further experiments, however, proved that this definition is unreliable: the sputter rate of graphene was found to be 0.18 ± 0.01 nm/min and 0.13 ± 0.01 nm/min for bi- and monolayer graphene samples, respectively, whereas it should have been similar for both cases. Nor did other attempts to define graphene on the depth profile, including the change of the definition of the graphene/SiC interface, give satisfying results.

It was noted that the intensity of the $^{12}C^-$ signal in the graphene layer is low and for the most part of the profile undifferentiated from organic contamination present in the Cr capping layer; therefore, other species, namely, $^{12}C_2^-$ and $^{12}C_3^-$, were proposed as more suitable signals for monitoring the carbon content as it was already suggested by other reports. 13,18 As can be seen in Fig. 3, the intensity of both polyatomic signals starts to increase simultaneously and

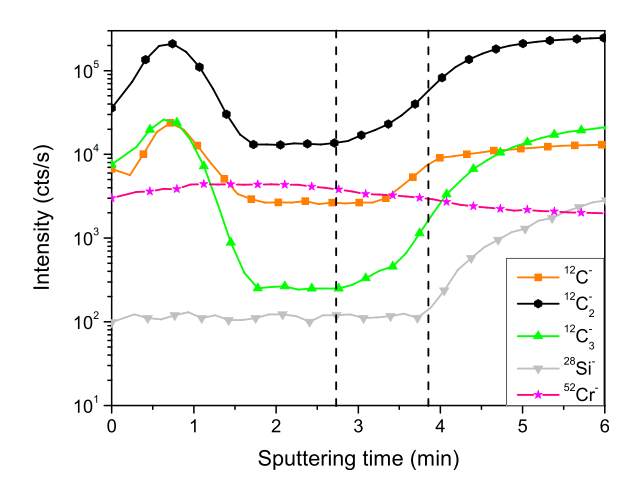


FIG. 3. Sample A depth profile with signals of mono- and polyatomic ions. The $^{12}C_2^-$ and $^{12}C_3^-$ signals start to increase simultaneously and much earlier than the $^{12}C^-$ signal as graphene enhances the formation of polyatomic ions. Both interfaces can be precisely identified (dashed lines).

much earlier than in the case of the $^{12}C^{-}$ signal and thus the beginning of the graphene layer can be precisely distinguished. The same effect was observed for other carbon isotope and larger ions: the ${}^{13}C^{-}$ signal was undifferentiated from organic contamination, whereas every polyatomic signal (every possible di-, tri-, and tetra-atomic ions composed of ${}^{12}C$ and ${}^{13}C$ atoms, if the intensity was high enough to be detected) started to increase earlier and at the very same time as the rest of them. This behavior can be attributed to strong sp^2 bonds present in graphene, which increase a secondary ion yield (the number of generated secondary ions per incident primary ion) of multiatom species when compared with monoatomic species. Measurements on bi- and monolayer graphene samples were repeated, and the sputter rate of graphene was found to be 0.27 ± 0.02 nm/min in both cases, which can be treated as a proof that both interfaces were precisely localized.

With an established procedure for graphene depth profiling, a precise measurement of samples A and B was performed (see Fig. 4). The H^- signal from sample B is the only one which was significantly different from sample A and therefore other signals from sample B were omitted. A straightforward conclusion can be made: a strong hydrogen peak can be observed, as expected, at the interface between graphene and the SiC substrate for sample A, whereas for sample B the signal drops to the background level relatively fast. This is not surprising as it was widely reported $^{7-12}$ that during hydrogen intercalation of graphene grown on SiC hydrogen can penetrate graphene and the buffer layer and transform the latter into a second graphene layer by its bonding to Si atoms at the interface. This effect can be precisely seen in the presented depth profile. Measurements were

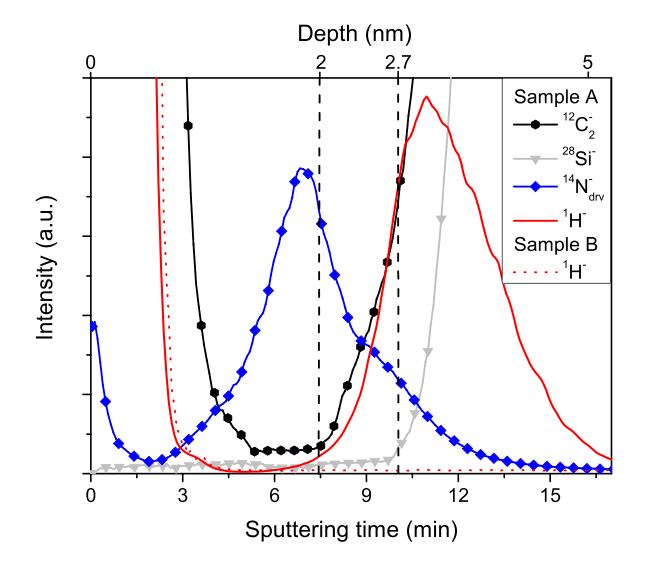


FIG. 4. A precise depth profile of samples A and B. Dashed lines show the location of the graphene layer. A very strong peak of the H^- signal can be observed at the interface between graphene and the SiC substrate for the intercalated sample and thus SIMS depth profiling can be recognized as an appropriate technique for monitoring of this process. Organic contamination (the N_{drv}^- signal was used as a marker) was found to be accumulated at the top of the graphene layer—it did not penetrate it and a long decay length could be attributed to the ion mixing effect. A decay length of the H^- signal in the Cr layer was found to be 0.2 nm/decade. All signals were scaled for a better visibility. The depth scale is nonlinear because the sputter rate differs significantly for all materials.

performed more than ten times for each sample and subsequently repeated on two different sample sets (grown at different times) and perfect reproducibility was confirmed.

Furthermore, we aimed at monitoring organic contamination that can be introduced onto the graphene surface before the deposition of a Cr capping layer. We chose the nitrogen signal as a factor responsible for organic contamination. Due to a very low secondary ion yield of N^- we measured the C_2N^- signal and performed point-to-point normalization to C_2^- , thus obtaining a derived N_{drv}^- signal. As seen in Fig. 4 organic contamination is located above the graphene layer but does not penetrate it (a relatively long decay length can be attributed to the ion mixing effect and preferential sputtering, known to be elemental dependent and more present in case of nitrogen²⁹).

In summary, we have developed a reliable measurement procedure for graphene depth profiling. It can be used for a better comprehension of the intercalation process and to precisely locate contaminations and diffusants that are present in a sample, which may be invaluable for further optimization of both growing and processing procedures of graphene samples. The proposed measurement procedure can be easily applied to graphene grown/transferred onto other substrates and with appropriate modifications onto other two-dimensional structures.

- ¹K. Emtsev, F. Speck, T. Seyller, and L. Ley, Phys. Rev. B 77, 155303 (2008).
- ²S. Kim, J. Ihm, H. Choi, and Y.-W. Son, Phys. Rev. Lett. **100**, 176802 (2008).
- ³F. Varchon, P. Mallet, J.-Y. Veuillen, and L. Magaud, Phys. Rev. B 77, 235412 (2008).
- ⁴Y. Qi, S. Rhim, G. Sun, M. Weinert, and L. Li, Phys. Rev. Lett. **105**, 085502 (2010).
- S. Goler, C. Coletti, V. Piazza, P. Pingue, F. Colangelo, V. Pellegrini, K. V. Emtsev, S. Forti, U. Starke, F. Beltram, and S. Heun, Carbon 51, 249 (2013).
 W. Strupinski, K. Grodecki, P. Caban, P. Ciepielewski, I. Jozwik-Biala, and J. M. Baranowski, Carbon 81, 63 (2015).

- ⁷C. Riedl, C. Coletti, T. Iwasaki, A. A. Zakharov, and U. Starke, *Phys. Rev. Lett.* **103**, 246804 (2009).
- ⁸F. Speck, J. Jobst, F. Fromm, M. Ostler, D. Waldmann, M. Hundhausen, H. B. Weber, and T. Seyller, Appl. Phys. Lett. **99**, 122106 (2011).
- ⁹S. Watcharinyanon, C. Virojanadara, J. Osiecki, A. Zakharov, R. Yakimova, R. Uhrberg, and L. Johansson, Surf. Sci. 605, 1662 (2011).
- ¹⁰M. Tokarczyk, G. Kowalski, M. Mozdzonek, J. Borysiuk, R. Stepniewski, W. Strupinski, and J. M. Baranowski, Appl. Phys. Lett. **103**, 241915 (2013).
- ¹¹Y.-P. Lin, Y. Ksari, and J.-M. Themlin, Nano Res. **8**, 839 (2015).
- ¹²C. Melios, V. Panchal, C. E. Giusca, S. R. P. S. W. Strupinski, and O. Kazakova, Sci. Rep. 5, 10505 (2015).
- ¹³Z. Luo, S. Lim, Z. Tian, J. Shang, L. Lai, B. MacDonald, C. Fu, Z. Shen, T. Yu, and J. Lin, J. Mater. Chem. 21, 8038 (2011).
- ¹⁴G. Lupina, J. Kitzmann, I. Costina, M. Lukosius, C. Wenger, A. Wolff, S. Vaziri, M. Oestling, I. Pasternak, A. Krajewska, W. Strupinski, S. Kataria, A. Gahoi, M. C. Lemme, G. Ruhl, G. Zoth, O. Luxenhofer, and W. Mehr, ACS Nano 9(5), 4776 (2015).
- ¹⁵N. Dwivedi, N. Satyanarayana, R. Yeo, H. Xu, K. Loh, S. Tripathy, and C. Bhatia, Sci. Rep. 5, 11607 (2015).
- ¹⁶W. Xie, L.-T. Weng, K. Ng, C. Chan, and C.-M. Chan, Carbon 94, 740 (2015).
- ¹⁷Q. Li, H. Chou, J.-H. Zhong, J.-Y. Liu, A. Dolocan, J. Zhang, Y. Zhou, R. Ruoff, S. Chen, and W. Cai, Nano Lett. 13(2), 486 (2013).
- ¹⁸H. Chou, A. Ismach, R. Ghosh, R. Ruoff, and A. Dolocan, Nat. Commun. 6, 7482 (2015).
- ¹⁹S. Yannopoulos, A. Siokou, N. Nasikas, V. Dracopoulos, F. Ravani, and G. Papatheodorou, Adv. Funct. Mater. 22, 113 (2012).
- ²⁰P. Sander, U. Kaiser, O. Gainshow, and A. Benninghoven, in *Proceeding of the 5th International SIMS Conference, Washington, DC, 30 September–4 October* (1985), pp. 295–298.
- ²¹J. Robertson, Surf. Coat. Technol. **50**, 185 (1992).
- ²²W. Strupinski, K. Grodecki, A. Wysmolek, R. Stepniewski, T. Szkopek, P. E. Gaskell, A. Grueneis, D. Haberer, R. Bozek, J. Krupka, and J. M. Baranowski, Nano Lett. 11(4), 1786 (2011).
- ²³T. Ciuk, S. Cakmakyapan, E. Ozbay, P. Caban, K. Grodecki, A. Krajewska, I. Pasternak, J. Szmidt, and W. Strupinski, J. Appl. Phys. 116, 123708 (2014).
- ²⁴L. J. van der Pauw, Philips Res. Rep. **13**, 1 (1958).
- ²⁵CAMECA SC-Ultra, User's Guide, CAMECA, Genneviliers, 2005.
- ²⁶D. Kouzminov, A. Merkulov, E. Arevalo, and H. J. Grossmann, Surf. Interface Anal. 45, 345 (2013).
- ²⁷A. Merkulov, Surf. Interface Anal. **45**, 90 (2013).
- ²⁸K. Witmaack, Surf. Interface Anal. **24**(6), 389 (1996).
- ²⁹K. Witmaack, Nucl. Instrum. Methods **209–210**, 191 (1983).



OPEN Graphene Enhanced Secondary Ion Mass Spectrometry (GESIMS)

Paweł Piotr Michałowski, Wawrzyniec Kaszub, Iwona Pasternak & Włodek Strupiński

Received: 16 March 2017 Accepted: 3 July 2017

Published online: 07 August 2017

The following invention - Graphene Enhanced Secondary Ion Mass Spectrometry - (pending European patent application no. EP 16461554.4) is related to a method of analysing a solid substrate by means of Secondary Ion Mass Spectrometry (SIMS). It comprises the steps of providing a graphene layer over the substrate surface and analysing ejected secondary anions through mass spectrometry analysis. The graphene layer acts as a kind of filament that emits a lot of secondary electrons during the experiment which significantly increases the negative ionization probability and thus the intensity of the SIMS signal can be more than two orders of magnitude higher than that of a similar sample without graphene. The method is particularly useful for the analysis of surfaces, 2D materials and ultra-thin films. The intensity of dopants and contamination signals can be enhanced up to 35 times, which approaches the detection limit of $\sim 10^{15} \alpha toms/cm^3$, otherwise unreachable in a standard static SIMS analysis.

SIMS is a very precise analytical technique for determining the elemental composition of a sample $^{1-6}$. The sample is bombarded with a primary ion beam that leads to the sputtering of the surface. Small parts of the sputtered particles are ionized (secondary ions) and the sample composition can be determined by means of mass spectral analysis. During the sputtering subsequent layers of the sample are removed and thus it is possible to obtain information about changes in the composition as a function of depth, thus creating a depth profile.

SIMS is well known for its excellent detection limits of trace elements⁷⁻¹². For most materials it is reported to be in the range of $10^{15}-10^{16}$ atoms/cm³¹¹, sometimes even as good as 10^{12} atoms/cm³¹². These optimum detection limits, however, are achieved during the dynamic SIMS (dSIMS) mode. In this mode a very dense ion beam is used and a substantial amount of material is sputtered simultaneously, allowing more ions to be detected. Drawbacks include very poor depth resolution and limitation to thick materials.

Surfaces, 2D materials and ultra-thin films are analysed ideally in a special mode called static SIMS (sSIMS)^{13–15}, in which a low density ion beam ensures that ions are emitted only from monolayers 1 to 3. This mode, however, has physical limitations. Because a relatively small amount of matter is sputtered, and even less ionized, there are not enough secondary ions extracted from the sample to achieve as optimum detection limit as the dynamic mode does. In most cases it is difficult to exceed a limit of 1 ppm (5 * 10¹⁶ atoms/cm³ or 10⁹ atoms/cm²).

There are many ways to enhance the ionization probability and thus the detection limit. It has been noted that using oxygen as primary ions significantly enhances the formation of positive ions^{16–19}, whereas cesium enhances the formation of negative ions¹⁷⁻²⁰. For some elements the difference can be up to four orders of magnitude. Although most elements can be detected as both positive and negative ions, each element usually gives better results in terms of detection limit in either positive or negative mode. In some experiments, oxygen flooding can further enhance the secondary ion yields of some negative ions^{21–23}. Using these techniques yields acceptable results, but in the cases of surfaces, 2D materials and ultra-thin films, it is often not enough to reach the desired detection limit, particularly in the case of trace elements.

Several SIMS measurements on graphene (Gr) have already been reported²⁴⁻³¹. More specifically, SIMS has been used to map the surface of the graphene layer^{24, 25}, to analyse the mass spectra of graphene^{26, 27}, and to create a depth profile of single-layer graphene grown on substrates that do not contain carbon 28, 29. Furthermore, SIMS has been used for the depth profiling of multilayer graphene of a thickness of more than 3 nm on SiC³⁰ and, recently, of hydrogen-intercalated graphene on SiC having a theoretical thickness of 0.69 nm³¹. All these methods employed SIMS for characterising the graphene layer, while the composition of support material underneath was not analysed.

In this work we present Graphene Enhanced Secondary Ion Mass Spectrometry (GESIMS) - a new technique for enhancing the detection limit in the analysis of thin materials. It has been found that providing a graphene

Institute of Electronic Materials Technology, Wólczyńska 133, 01-919, Warsaw, Poland. Correspondence and requests for materials should be addressed to P.P.M. (email: pawel.michalowski@itme.edu.pl)

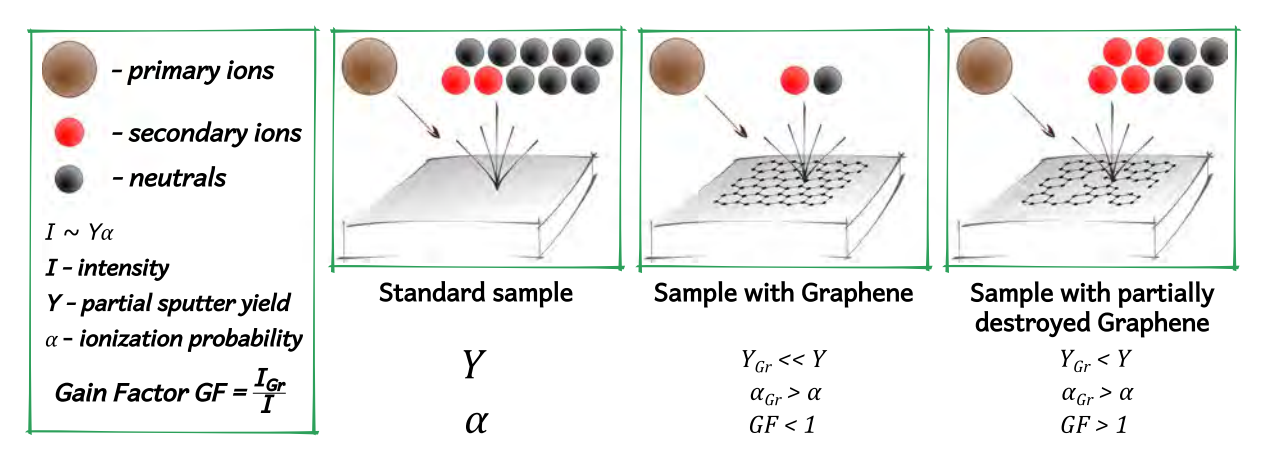


Figure 1. The basic concept of GESIMS analysis. Graphene blocks the emission of the matter from the substrate but significantly increases the ionization probability. By creating some defects in graphene layer the emission increases while the ionization ability is preserved and thus more ions can reach the detector, resulting in enhanced SIMS signal.

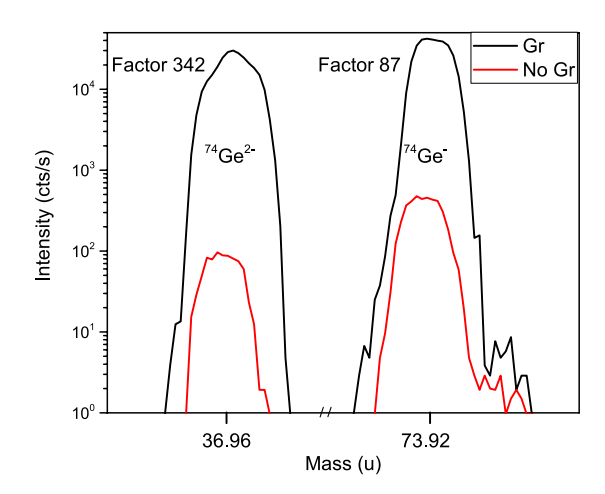


Figure 2. A comparison of mass spectra of the germanium substrate with and without graphene layer for optimal GESIMS conditions. The intensity of the SIMS signal can be enhanced more than two orders of magnitude.

layer on a substrate significantly reduces the emission of matter from the substrate but at the same time increases the negative ionization probability. Destruction of a small part of the graphene layer in a dynamic SIMS mode significantly reduces the initial strong blocking effect of graphene, while the enhancement of the ionization probability of the sputtered material is still observed. Under these conditions the ionization probability greatly prevails, resulting in an SIMS signal with an intensity that is unexpectedly high compared with a sample without graphene and thus able to to reach better detection limits.

Results

The basic concept of GESIMS method is presented on Fig. 1. To understand the process correctly it is necessary to remember that the intensity of SIMS signals depends on the secondary ion yield, which is defined as the number of emitted ions A^-/A^+ (multiple ionization is also possible) per incident ion. In turn, secondary ion yield is defined as the product of the partial sputter yield (number of emitted species A per incident ion) and ionization probability. The presence of graphene on a substrate surface clearly reduces the partial sputter yield of a material from the substrate, since for given conditions it is expected that sputtered species are emitted from the \sim 3 top monolayers of material and graphene acts as a barrier to emission. If despite this fact a significant increase in the SIMS signal intensity is still observed, the only possible explanation is that the presence of graphene drastically increases the negative ionization probability. Fig. 2 presents a comparison of mass spectra for the Ge substrate with and without a graphene layer for optimal GESIMS conditions (the graphene layer was partially destroyed prior to the analysis). From this, it is possible to conclude that graphene can enhance the intensity of peaks by two orders of magnitude.

To quantify the effect, a gain factor can be defined as follows:

Substrate	Dopant	Concentration (atoms/cm³)	Maximal gain factor	Standard detection limit (atoms/cm³)	Enhanced detection limit (atoms/cm³)
GaAs	Te	1 * 1018	35.7	7.04 * 10 ¹⁶	1.97 * 10 ¹⁵
Si	Sb	1*1018	15.1	4.86 * 10 ¹⁶	3.02 * 1015
AlGaAs	Si	2*1018	13.8	6.06 * 10 ¹⁶	4.39 * 10 ¹⁵
Si	As	5 * 10 ¹⁸	7.1	1.35 * 10 ¹⁶	1.90 * 10 ¹⁵

Table 1. Summary of Graphene Enhanced Secondary Ion Mass Spectrometry measurements performed on various materials and dopants.

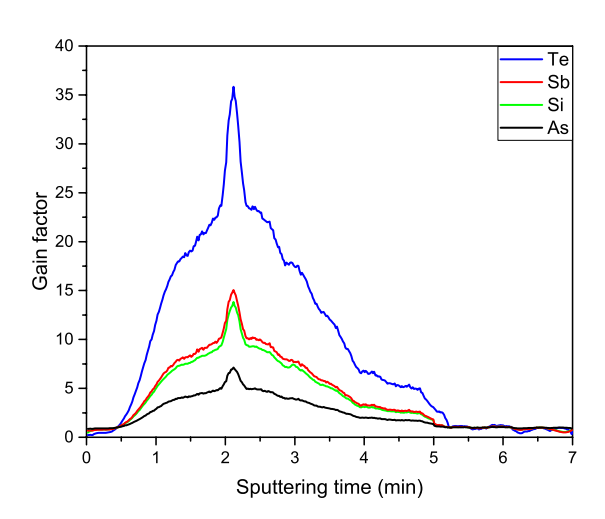


Figure 3. The gain change during sputtering in dSIMS mode for different dopant types in various substrates. At the beginning the blocking effect is very strong but after the partial destruction of graphene it is reduced and the enhanced ionization probability is dominant. Thus the gain is much larger than a factor of 1. After the complete destruction of the graphene layer, no difference between the two samples is observed (GF = 1). The shape of all curves and the position of the maximum depends on the partial destruction of the graphene layer and thus are similar for all samples.

$$GF = \frac{Y_{Gr}\alpha_{Gr}}{Y\alpha} \tag{1}$$

wherein GF is the gain factor, Y_{Gr} and Y denote partial sputter yield for a sample with and without graphene, respectively, while α_{Gr} and α denote ionization probabilities (again, a sample with and without graphene, respectively). Under optimum conditions $Y_{Gr} < Y$ and $\alpha_{Gr} > \alpha$, whereby the latter effect is much stronger, so that GF > 1 and thus the intensity of the SIMS signal can be enhanced.

Although increasing the intensity of the matrix element signal is of interest from a scientific viewpoint, it does not seem to have much practical application in SIMS-based surface analysis. As already mentioned above, the actual benefit is the enhancement of the detection limit of trace elements and thus new sets of samples have been considered and tested. Each of the sets consisted of a pair of samples, one having graphene transferred onto its surface, and the other - without graphene - serving as a reference. Signal enhancement was observed for all of them and the maximum gain that was reached during the experiments has been presented in Table 1 along with standard and enhanced detection limits.

As already mentioned, the effect was not observed at the beginning of the experiment, when a fresh graphene layer was transferred on a sample. This is not surprising since graphene is a strong material and the blocking effect was expected to be high. Thus the reduction in the partial sputter yield was higher than the increase of the ionization probability. To overcome it, the primary beam intensity had to be increased to several hundred pA for a short time. Under such conditions dynamic SIMS mode was achieved and the entire surface was slowly eroded. When only a small part of the graphene sheet was destroyed, the blocking effect was significantly reduced while the enhancement of the ionization probability was still observed. Figure 3 shows the gain change during sputtering in dSIMS mode with the primary beam intensity being set to 200 pA for all samples presented in Table 1. Three regions can be identified: at the beginning of the experiment the blocking effect was too strong and thus the signal for the sample with graphene was reduced (GF < 1). After sputtering off a small part of the graphene, the enhanced ionization probability took the major role and thus the gain was much larger than a factor of 1 (GF \gg 1). If the beam intensity was kept at high values for a longer time, complete destruction of the graphene layer took place, and consequently no difference between the two samples in each set was further observed (GF = 1).

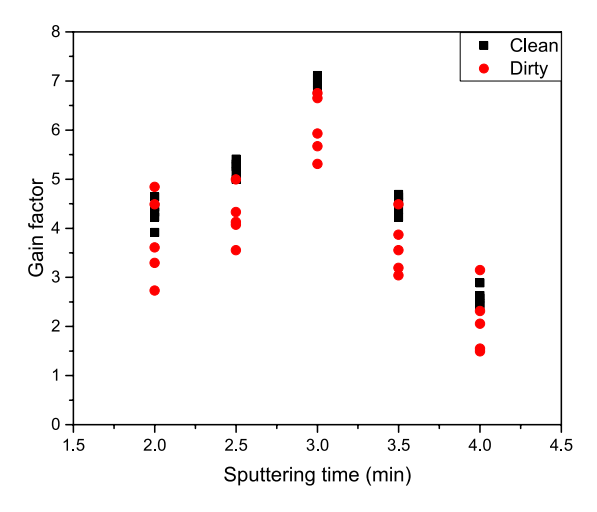


Figure 4. The gain change during sputtering in dSIMS mode for As dopant in Si substrate measured at five different spots for a clean and a dirty sample. For the cleaned sample, the method is reproducible, with small variations only.

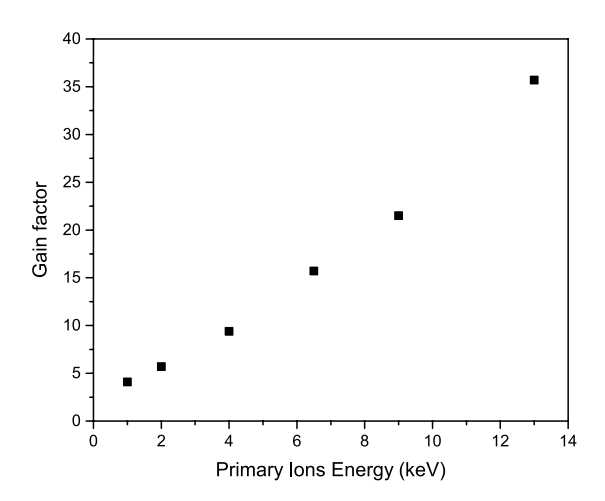


Figure 5. Maximal gain factor as a function of primary ion energy for Te dopant in GaAs substrate. For high-energy ions, a bigger collision cascade is generated and thus it is easier to overcome the graphene blocking effect

It was essential in these experiments for the uniformity and the intensity of the beam to be well defined and reproducible and thus it was not surprising that the shape of all curves and the position of the maximum were similar for all measured samples as they depended on the partial destruction of the graphene layer and not to the type of the dopant and the substrate. Only the actual enhancement was material related (both the substrate and the type of dopant) and thus each sample had a different maximal gain factor.

The result is fully reproducible - Fig. 3 shows the average of 15 measurements performed separately on both types of sample (with and without graphene) for each sample set. We wish to emphasize that to achieve a good reproducibility of the method, samples must be cleaned prior to the measurement by annealing them at elevated temperatures and reduced pressure. In the experiment described above, the samples were subjected to annealing at 200 °C and pressure of 10^{-8} mbar for two hours. Figure 4 shows a suitable comparison of the gain factors measured for As dopant in Si substrate samples with and without cleaning procedures. The intensity of the primary beam was set to 150 pA and the duration of the dSIMS mode was varied between 2 and 4 minutes. Five different measurements were taken at various spots of the sample, leading to a straightforward conclusion that for the cleaned sample the method is reproducible, with only small variations.

The best results, as presented in Table 1, were obtained for higher values of primary ion energy (usually above 10 keV). This is not surprising because as more energy is transferred to the substrate, a larger collision cascade is generated and thus the matter from the substrate has higher energy to overcome the graphene blocking effect. Figure 5 shows a comparison of maximal gain factor versus primary ion energy for Te dopant in GaAs substrate.

When the optimal conditions are reached, the beam intensity should be decreased and sSIMS measurement can be performed. Figure 6 presents a suitable comparison of SIMS measurement for Sb dopant in Si substrate with and without graphene. Two sample sets were analysed: with high $(1*10^{18} atoms/cm^3)$ and low

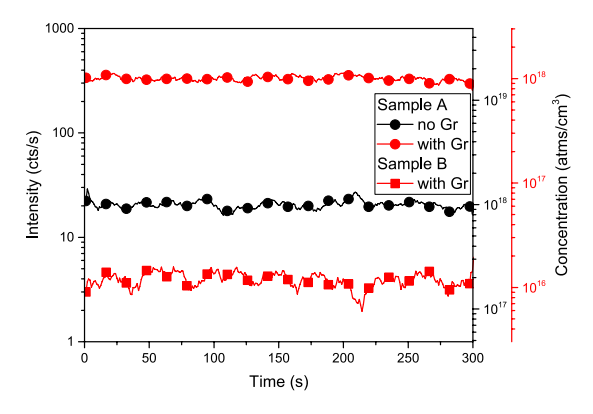


Figure 6. Static SIMS mode measurement for Sb dopant in Si substrate for samples with various dopant concentration: $1*10^{18}$ and $1*10^{16}$ atoms/cm³ for Sample A and B, respectively. The presence of the graphene layer significantly increases the intensity of the SIMS signal, improving the detection limit. The GESIMS method allows the analysis of samples with low concentration, which is not possible using the standard measurement.

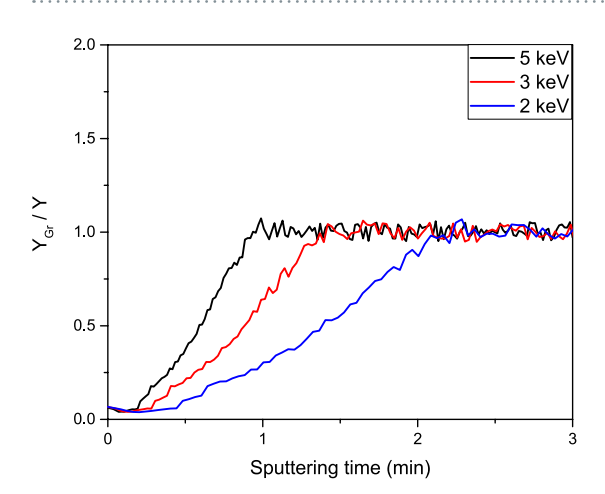


Figure 7. The gain change during sputtering in dSIMS mode for Ga^+ ions in GaAs substrate. In positive ion detection, no enhancement effect is observed, only the blocking effect of graphene. The positive ionization probability remains the same for the whole experiment and thus the Y_{Gr}/Y ratio is being monitored. For smaller impact energies lower sputter rate is observed.

 $(1*10^{16} atoms/cm^3)$ dopant concentration (Sample A and B, respectively). As can be clearly seen for Sample A, the intensity of the SIMS signal was significantly increased and thus a better detection limit was achieved $(3.02*10^{15} instead of 4.86*10^{16} atoms/cm^3)$. In the case of Sample B, the concentration was too low to be measured using a standard sSIMS condition, whereas it was possible for the GESIMS method. As can be seen, the enhancing effect does not depend on the dopant concentration and thus GESIMS method is quantifiable.

The same procedure was used for a ${\rm O_2}^+$ primary beam with positive ion detection. As shown on Fig. 7 only the blocking effect of graphene was observed with no enhancement. Changing the impact energy influenced the sputter rate whereas the general shape of the profile was the same. It was therefore concluded that the positive ionization probability remained the same for the whole experiment and only the sputter yield increased while the graphene layer was being destroyed, therefore the oxygen beam was found suitable to determine the Y_{Gr}/Y ratio.

A new experiment was devised for AlGaAs substrate with Si dopant: the sample was sputtered in dSIMS mode with Cs⁺ ions and the gain factor change was obtained just like it was shown on Fig. 3. Every ten seconds the Cs⁺ beam was switched off and a very brief sSIMS measurement with O_2 ⁺ beam was performed so that the Y_{Gr}/Y ratio could be determined as shown on Fig. 8. We noted that the Y_{Gr}/Y ratio increased rapidly from ~0.27 to ~0.43 close to the optimal condition which apparently led to a significant increase of the gain factor.

It did not, however, explain why the graphene layer increase the negative ionization probability. To better understand the effect we repeated the whole procedure but instead of the graphene layer we deposited a thin layer of amorphous carbon. We tested it in both, negative and positive ion detection mode but no signal enhancement was observed, just the blocking effect and thus the enhancement could not be associated with the presence of carbon atoms only. To gain more insight we studied the electric properties of the graphene layer and amorphous carbon during the SIMS experiment: we transferred/deposited them on insulating materials like SiC, AlN and SiO_2 which normally required an electron flood gun for charge compensation. The intensity of the Cs⁺ primary beam was once again set to 200 pA and it turned out that a thin layer of the amorphous carbon did not alter the

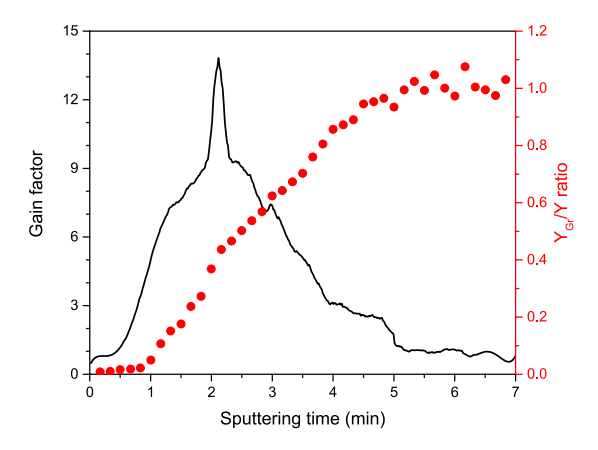


Figure 8. A comparison of the gain change during sputtering in dSIMS mode and the Y_{Gr}/Y ratio for Si dopant in AlGaAs substrate. Close to the optimal condition the Y_{Gr}/Y ratio increases significantly whereas the enhanced ionization probability is still present.

experiment significantly: the charging effect was visible from the very beginning and the flood gun was needed to perform the analysis. However, in case of the graphene layer we were able to sputter the sample without the flood gun up to four an a half minutes before the charging effect occurred. It corresponded well with the time frame of the enhancement effect (see Fig. 3).

From Fig. 8 it could be further deduced that after four and half minutes of sputtering the graphene layer was significantly destroyed (the Y_{Gr}/Y ratio was above 0.8) and yet it was still able to provide enough electrons for charge compensation. We assumed that in a similar way the GESIMS effect could be explained: during the SIMS experiment a high voltage was applied to the sample holder (up to 5 kV) and thus the graphene layer acted as a kind of filament which emitted an excess of electrons during the ion bombardment leading to the enhanced ionization probability.

Discussion

GESIMS is a process for measuring and analysing thin substrates that involves the following steps:

- applying a graphene layer over the substrate surface;
- annealing the graphene-coated substrate at elevated temperature and reduced pressure;
- sputtering of the graphene-coated substrate in dSIMS mode, which leads to the partial destruction of the graphene layer;
- detecting and analysing ejected secondary anions by mass spectrometry analysis in sSIMS mode.

This method cannot be used for depth profiling of thick materials because the graphene layer will be destroyed within the first moments of the measurement and the enhancing property will be lost. Furthermore, the dSIMS analysis itself offers a high detection limit. It cannot be used for a high resolution imagining neither, since the presence of the partially destroyed graphene layer will reduce the spatial resolution. However, in the case of very thin materials, sSIMS reaches its physical limit and any enhancement is beneficial. GESIMS requires more preparation and optimization than the standard sSIMS analysis but improves by one order of magnitude the detection limits of trace elements, which may prove to be invaluable for the further development of 2D materials.

The effect does not take place for samples covered with a thin layer of amorphous carbon. It has been noted that the graphene layer has different electric properties during the SIMS experiment - even a significantly destroyed layer can provide enough electrons to compensate the charging effect which is typically present for insulating materials. This behaviour can suggest the explanation of the GESIMS effect: since a high voltage is applied to the sample holder the graphene layer acts as a kind of filament and emits a lot of secondary electrons during the ion bombardment and thus the negative ionization probability is increased.

Methods

Sample preparation. A pair of samples was created for every experiment described in this work, one having graphene grown or transferred onto its surface, and the other - without graphene - serving as a reference.

In the case of germanium substrate, graphene films were synthesized in a commercially available system by the CVD method as described by Paternak *et al.*^{32,33}. As a substrate, (100)-oriented Ge layers deposited on Si (100) wafers were used. Methane gas in the mixture of Ar and H_2 in the ratio of 200:1 was used as a carbon precursor. Growth was preceded by the substrate's annealing in a pure hydrogen atmosphere in order to reduce native oxides *in-situ*. During the growth process, 800 mbar of pressure were sustained.

In other samples, graphene films were synthesized on 35 μm thick copper foils by the CVD method using a Black Magic Pro system (Aixtron). To grow graphene on copper foils the following procedure was used: copper samples were first pretreated at 960 °C under an Ar gas flow and then a H_2 gas flow at 20 mbar of pressure. The purpose of this step was to improve the quality and enlarge the grain size of Cu substrates as well as to remove oxides from the copper surface. Next, methane was introduced into the reactor at an adequate flow rate for a few

minutes. During this step, the synthesis of graphene was observed. Finally, the copper substrates covering the graphene films were cooled to room temperature in an Ar atmosphere. To transfer graphene onto target substrates, we used the high-speed electrochemical delamination method³⁴.

As described in aforementioned procedures, the presence of the graphene layer was confirmed by Raman spectroscopy measurements performed in back-scattering geometry, using a Renishaw in Via Raman Microscope, with a $\times 100$ objective and a 532 nm Nd:YAG laser as an excitation source.

SIMS measurements. In this work all SIMS measurements were performed employing the CAMECA SC Ultra instrument under ultra-high vacuum (UHV), usually of 4×10^{-10} mbar. A Cs⁺ primary beam with negative ion detection was used for most measurements. Impact energy was varied between 1 keV and 13 keV but the highest energy was used for the most of the experiments. The intensity of the primary beam was 100-2000 pA and 0.5-10 pA for the dynamic and static SIMS mode, respectively. An O_2^+ primary beam with positive ion detection was used for a few experiments to show that graphene do not enhance the positive ionization probability. Impact energy was varied between 2 keV and 5 keV and the intensity of the primary beam was 300-3000 pA and 3-10 pA for the dynamic and static SIMS mode, respectively. Primary beams were rastered over $250\times250~\mu m^2$ and the analysis area was limited to $(200\times200)~\mu m^2$. Mass interferences were verified prior to analysis and adequate mass resolving power was used for each experiment.

Beam on the sample in the SC Ultra tool has a square shape and owning to the "variable rectangular shape concept" forms a homogeneous spot. The primary beam at the working point in the SC Ultra is formed by two stencils - well-shaped apertures. While the first one is used to choose the most intense and homogeneous part of the ion beam, the second one changes the size of the spot. This innovation provides high sensitivity for all measured elements and a high dynamic range with a very low sputter rate^{35–37}.

Secondary ions that are detected in SIMS analysis usually originate from the top three monolayers of the bombarded sample. For static SIMS analysis, very low ion doses are used (typically in range of 10^{12} ions/cm²). This ensures that with a high probability every ion will impact on undamaged surface and not on an area that has already received ion impacts. In this mode, the emission is essentially limited to a few topmost monolayers and thus it is very surface-sensitive. It makes it an ideal mode for the analysis of surfaces, 2D materials and ultra-thin films because there is no interference with the lower layers. In dynamic SIMS mode the emission is theoretically still limited to the topmost monolayers but for higher ion doses it is expected that the whole surface will erode in time and thus the lower layer will be gradually exposed. In this way it is possible to obtain information on the variation of the composition of material below the initial surface, thereby creating so-called depth profiles. In this work, however, the dynamic SIMS mode was used to destroy only partially the graphene layer in order to expose the underlying substrate, which was subjected for further analysis. It was a critical step to ensure good reproducibility of the results and therefore a very homogeneous ion beam was required to perform GESIMS analysis.

References

- 1. Andersen, C. A. & Hinthorne, J. R. Ion microprobe mass analyzer. Science 175, 853-860 (1972).
- 2. Benninghoven, A. Developments in secondary ion mass spectroscopy and applications to surface studies. *Surf. Sci.* **53**, 596–625 (1975)
- 3. Benninghoven, A., Rudenauer, F. G. & Werner, H. W. Secondary ion mass spectrometry: basic concepts, instrumental aspects, applications and trends (John Wiley & Sons, New York, 1987).
- 4. Werner, H. W. The use of secondary ion mass spectrometry in surface analysis. Surf. Sci. 47, 301–323 (1975).
- 5. Liebl, H. Secondary-ion mass spectrometry and its use in depth profiling. J. Vac. Sci. Technol., A 12, 385 (1975).
- 6. Liebl, H. Ion microprobe mass analyzer. J. Appl. Phys. 38, 5277-5283 (1967).
- 7. Wittmaack, K. High-sensitivity depth profiling of arsenic and phosphorus in silicon by means of sims. *Appl. Phys. Lett.* **29**, 552 (1976).
- Ber, B. Y. et al. Secondary ion mass spectroscopy investigations of magnesium and carbon doped gallium nitride films grown by molecular beam epitaxy. Semicond. Sci. Technol. 13, 71–74 (1998).
- 9. Chiou, C. Y., Wang, C. C., Ling, Y. C. & Chiang, C. I. Secondary ion mass spectrometry analysis of in-doped p-type gan films. *Appl. Surf. Sci.* 203–204, 482–485 (2003).
- Emziane, M., Durose, K., Halliday, D. P., Bosio, A. & Romeo, N. In situ oxygen incorporation and related issues in cdte/cds photovoltaic devices. J. Appl. Phys. 100, 013513 (2006).
- 11. Matsunaga, T., Yoshikawa, S. & Tsukamoto, K. Secondary ion yields of c, si, ge and cs surface density and concentration in sims. Surf. Sci. 515, 390–402 (2002).
- 12. Gnaser, H. Sims detection in the 10^{12} atoms cm^{-3} range. Surf. Interface Anal. 25, 737–740 (1997).
- Benninghoven, A. Chemical analysis of inorganic and organic surfaces and thin films by static time-of-flight secondary ion mass spectrometry (tof-sims). Angew. Chem. Int. Ed. 33, 1023–1043 (1994).
- 14. VanVaeck, L., Adriaens, A. & Gijbels, R. Static secondary ion mass spectrometry: (s-sims) part 1. methodology and structural interpretation. *Mass Spectrom. Rev.* 18, 1–47 (1999).
- Adriaens, A., VanVaeck, L. & Adams, F. Static secondary ion mass spectrometry (s-sims) part 2: Material science applications. Mass Spectrom. Rev. 18, 48–81 (1999).
- 16. Novak, S. W. & Wilson, R. G. Systematics of positive secondary ion mass spectrometry relative sensitivity factors for si and sio₂ measured using oxygen and argon ion bombardment. J. Appl. Phys. 69, 463–465 (1991).
- 17. Slodzian, G., Lorin, J. C. & Havette, A. Isotopic effect on the ionization probabilities in secondary ion emission. *J. Phys. Lett. Paris* 41, 555–558 (1980).
- 18. Taga, Y. Sputtering and secondary ion emission from metals and alloys subjected to oxygen ion bombardment. Secondary Ion Mass Spectrometry SIMS V V, 32–37 (1986).
- 19. Gnaser, H. & Hutcheon, I. D. Significance of isotope effects for secondary-ion emission models. *Phys. Rev. B* **38**, 11112–11117 (1998)
- 20. Stevie, F. A., Kahora, P. M., Simons, D. S. & Chi, P. Secondary ion yield changes in si and gaas due to topography changes during o+2 or cs+ ion bombardment. *J. Vac. Sci. Technol.*, A **6**, 76 (1988).
- 21. Lewis, R. K., Morabito, J. M. & Tsa, J. C. Primary oxygen ion implantation effects on depth profiles by secondary ion emission mass spectrometry. *Appl. Phys. Lett.* **23**, 260–262 (1973).
- 22. Vickerman, J. C., Brown, A. & Reed, N. M. Secondary ion mass spectrometry: Principles and applications (Clarendon Press, Oxford, 1989).

- 23. Wilson, R. G., Stevie, F. A. & Magee, C. W. Secondary ion mass spectrometry: A practical handbook for depth profiling and bulk impurity analysis (John Wiley & Sons Inc., New York, 1989).
- 24. Luo, Z. et al. Pyridinic n doped graphene: synthesis, electronic structure, and electrocatalytic property. J. Mater. Chem. 21, 8038 (2011)
- 25. Lupina, G. et al. Residual metallic contamination of transferred chemical vapor deposited graphene. ACS Nano 9(5), 4776 (2015).
- Dwivedi, N. et al. Ultrathin carbon with interspersed graphene/fullerene-like nanostructures: A durable protective overcoat for high density magnetic storage. Sci. Rep. 5, 11607 (2015).
- Xie, W., Weng, L.-T., Ng, K., Chan, C. & Chan, C.-M. Clean graphene surface through high temperature annealing. Carbon 94, 740–748 (2015).
- 28. Li, Q. et al. Growth of adlayer graphene on cu studied by carbon isotope labeling. Nano Lett. 13(2), 486 (2013).
- 29. Chou, H., Ismach, A., Ghosh, R., Ruoff, R. & Dolocan, A. Revealing the planar chemistry of two-dimensional heterostructures at the atomic level. *Nat. Commun.* 6, 7482 (2015).
- 30. Yannopoulos, S. et al. Co2-laser-induced growth of epitaxial graphene on 6h-sic(0001). Adv. Funct. Mater. 22, 113 (2012).
- 31. Michalowski, P. P., Kaszub, W., Merkulov, A. & Strupinski, W. Secondary ion mass spectroscopy depth profiling of hydrogen-intercalated graphene on sic. Appl. Phys. Lett. 109, 011904 (2016).
- 32. Pasternak, I. et al. Graphene growth on ge(100)/si(100) substrates by cvd method. Sci. Rep. 6, 21773 (2016).
- 33. Pasternak, I. et al. Large-area high-quality graphene on ge(001)/si(001) substrates. Nanoscale 8, 11241–11247 (2016).
- 34. Ciuk, T. et al. Properties of chemical vapor deposition graphene transferred by high-speed electrochemical delamination. J. Phys. Chem. C 117, 20833–20837 (2013).
- 35. CAMECA, Genneviliers. CAMECA SC-Ultra, User's Guide (2005).
- 36. Kouzminov, D., Merkulov, A., Arevalo, E. & Grossmann., H. J. Application of extra-low impact energy sims and data reduction algorithm to usj profiling. *Surf. Interface Anal.* 45, 345–347 (2013).
- 37. Merkulov, A. The secondary ions emission from si under low-energy cs bombardment in a presence of oxygen. Surf. Interface Anal. 45, 90–92 (2013).

Acknowledgements

The research leading to these results has received funding from the European Union Seventh Framework Programme under Grant Agreement No. 604391 Graphene Flagship.

Author Contributions

P.P.M. conceived the experiment, P.P.M. and W.K. conducted the SIMS experiments, I.P. and W.S. prepared the samples. All authors reviewed the manuscript.

Additional Information

Competing Interests: The authors declare that they have no competing interests.

Publisher's note: Springer Nature remains neutral with regard to jurisdictional claims in published maps and institutional affiliations.

Open Access This article is licensed under a Creative Commons Attribution 4.0 International License, which permits use, sharing, adaptation, distribution and reproduction in any medium or format, as long as you give appropriate credit to the original author(s) and the source, provide a link to the Creative Commons license, and indicate if changes were made. The images or other third party material in this article are included in the article's Creative Commons license, unless indicated otherwise in a credit line to the material. If material is not included in the article's Creative Commons license and your intended use is not permitted by statutory regulation or exceeds the permitted use, you will need to obtain permission directly from the copyright holder. To view a copy of this license, visit https://creativecommons.org/licenses/by/4.0/.

© The Author(s) 2017

Nanoscale



PAPER



Cite this: Nanoscale, 2017, 9, 17571

Characterization of the superlattice region of a quantum cascade laser by secondary ion mass spectrometry

Paweł Piotr Michałowski, **Derota Pierścińska, **Dorota Pierścińska, **Kamil Pierściński, **Daciej Bugajski** and Włodek Strupiński**.

Secondary ion mass spectrometry is applied to the depth profiling of the superlattice active region of lattice matched (\sim 9.2 μ m) Al_{0.48}In_{0.52}As/In_{0.53}Ga_{0.47}As/InP quantum cascade lasers. The developed measurement procedure is capable of characterizing the quality of each individual layer in the superlattice region, including layers as thin as 0.7 nm. The oxygen level for AllnAs and InGaAs layers is in the range of $1-3\times10^{17}$ atms per cm³ and below the detection limit (\sim 1 \times 10¹⁶ atms per cm³), respectively. Oxygen is not uniformly distributed in the AllnAs layers – more oxygen is embedded into the structure during the very first stage of the growth of the AllnAs layer and thus the corresponding interface is 1.83 \pm 0.31 times more contaminated than the other. The procedure can also be operated in 3D imaging mode which proves to be invaluable for failure analysis.

Received 28th August 2017, Accepted 17th October 2017 DOI: 10.1039/c7nr06401b

rsc.li/nanoscale

1. Introduction

Quantum Cascade Lasers (QCLs) are mid-infrared emitters based on intersubband transitions in multilayer semi-conductor structures. Despite the fact that they were first demonstrated over 20 years ago, ¹ they are still the subject of fundamental studies on the epitaxial growth itself, which represents one of the most challenging tasks for semiconductor material growers. This is mainly because the growth of the QCL's active region demands extreme precision of thickness and composition of individual layers as well as the growth stability over a long time.

In this paper we present the detailed analysis of the superlattice active region of lattice matched (~9.2 μm) $Al_{0.48}In_{0.52}As/In_{0.53}Ga_{0.47}As/InP$ QCLs. Its design follows a 4-well, 2-phonon resonance scheme. The lasers utilize an AlInAs waveguide and were grown exclusively by molecular beam epitaxy (MBE) without metal organic vapor phase epitaxy regrowth. The core structure of the laser consisted of 30 periods (active/injector segments). The conduction band profile and moduli squared wavefunctions in the injector/active/injector segment of the $Al_{0.48}In_{0.52}As/In_{0.53}Ga_{0.47}As/InP$ laser under the applied field of 50 kV cm $^{-1}$ are shown in Fig. 1. The electronic band structure

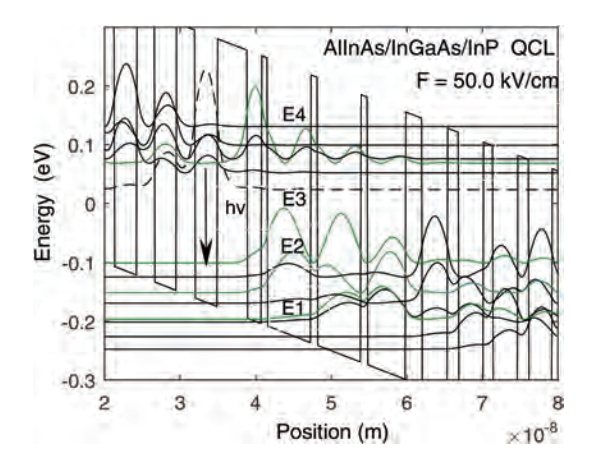


Fig. 1 Conduction band profile and moduli squared wavefunctions in the injector/active/injector segment of the laser under an applied field $F = 50 \text{ kV cm}^{-1}$ (at the threshold). The wavefunctions have been shifted to the energy positions of the respective levels. The E4, E3, E2 and E1 refer to the upper, lower and ground state of lasing transitions. The lowest energy state in the injector couples directly to the upper laser level E4.

of the QCL has been calculated by solving the Schrödinger equation with a position dependent effective mass.

The basic characterization method routinely used for controlling the growth process of QCL structures is High Resolution X-Ray Diffraction (HRXRD), however it gives an average result which is representative for the whole structure but not for particular layers in the active region. Further optimization of the growth process requires the application of

^aInstitute of Electronic Materials Technology, Wólczyńska 133, 01-919 Warsaw, Poland. E-mail: pawel.michalowski@itme.edu.pl

^bInstitute of Electron Technology, al. Lotników 32/46, 02-668 Warsaw, Poland

cENT SA, al. Szucha 8, 00-582 Warsaw, Poland

Paper Nanoscale

advanced characterization techniques capable of monitoring the superlattice region. One of the most sensitive analytical techniques for advanced material research is Secondary Ion Mass Spectrometry (SIMS). This method has already been used for the characterization of quantum cascade lasers.^{3–5} So far it has been used for the determination of Au diffusion into semiconductors³ and the dopant concentration profile.⁴ The active region of the QCL was also monitored⁵ but with a resolution that does not allow individual quantum wells to be distinguished. In our previous work we presented the reproducible procedure for depth profiling of graphene (theoretical thickness of 0.69 nm).⁶ In this work we adapt a procedure for QCL structures and show that it is capable of characterizing the quality of the interfaces of each individual quantum well in the superlattice region.

2. Experimental

2.1. Sample preparation

The growth process of laser structures was performed by solid source MBE on a Riber Compact 21T reactor. The epitaxial system was equipped with in situ diagnostics such as a reflection high-energy electron diffractometer, LayTec EpiCurve reflectometer and optical pyrometer. The growth chamber environment was monitored with a mass spectrometer. For gallium, indium and aluminum ABN80DF type cells were used. The cells were equipped with conical pyrolytic boron nitride crucibles which give good uniformity over the entire 2 inch wafer. The second gallium cell was Veeco SUMO, which offers a much more stable flux than the classical Knudsen like cells. For group V arsenic valved cracker cell VAC500 was used. Diatomic As₂ was used for better growth morphology. The growth rate was $0.7 \mu m h^{-1}$. The arsenic flux ratio to group III materials was equal to 12.5. The growth temperature was 520 °C. The choice of growth temperature represents a tradeoff between the need for low oxygen contamination and smooth surfaces during growth, favored by high growth temperature, and the need for low background shallow impurity concentration and preservation of the interface quality, improved at lower temperatures. The growth details are described by Gutowski et al.7 The structure for SIMS investigation was grown on a highly doped $(2 \times 10^{18} \text{ atms per cm}^3)$ InP wafer. Then a 500 nm undoped In_{0.53}Ga_{0.47}As buffer layer was deposited. After that 20 periods of the active region superlattice were grown. The structure was completed by a 10 nm In_{0.53}Ga_{0.47}As cap layer, to enable SIMS characterization. The layer sequence of one period (active/injector segment) of the structure, in nanometers, starting from the injection barrier is: **4.0**, 1.9, **0.7**, 5.8, **0.9**, 5.7, **0.9**, 5.0, **2.2**, 3.4, **1.4**, 3.3, **1.3**, 3.2, **1.5**, 3.1, 1.9, 3.0, 2.3, 2.9, 2.5 and 2.9 nm. The AlInAs layers are denoted in bold. The total thickness of one period is 59.8 nm.

2.2. SIMS measurements

In this work all SIMS depth profiles were performed by employing the CAMECA SC Ultra instrument under ultra-high

vacuum (UHV), usually of 4×10^{-10} mbar. Sufficient depth resolution was obtained by using a low impact energy of 150 eV for a Cs⁺ primary beam and negative ion detection mode. For some experiments the positive ion detection mode was used with an impact energy of 500 eV. The primary beam was rastered over $(250 \times 250) \text{ } \mu\text{m}^2$ while the analysis area was limited to $(200 \times 200) \mu m^2$. Mass interferences were verified prior to analysis and the mass resolving power $\frac{m}{\Delta m}$ = 4000 was used for most experiments. The intensity of the primary beam was 13 nA in the majority of experiments. The SC Ultra tool is able to achieve such low impact energies due to the EXILE (EXtra Low Impact Energy) technology, in the case of which a primary floating column concept is used.8 In this notion, contrary to standard SIMS tools, the primary column has the "floating voltage" instead of the grounded voltage level between the space at any two lenses inside the column and thus primary ions are slowed down at the end of the column maintaining favorable conditions for ion acceleration and beam stability. Ion beam on the sample in the SC Ultra tool has a square shape and due to the "variable rectangular shape concept" forms a homogeneous spot. The primary beam at a working point in the SC Ultra tool is formed by two stencils well-shaped apertures. While the first one is used to choose the most intense and homogeneous part of the ion beam, the second one changes the size of the spot. These innovations allow one to use the low impact energy of primary ions with high sensitivity for all measured elements, a high depth resolution (below 1 nm), and a high dynamic range with a low etching rate (lower than 0.5 nm per minute). 9,10

Results & discussion

Fig. 2 presents a typical depth profile of the first three periods of the superlattice region of the QCL (due to a relatively big difference in the etching rate for InGaAs and AlInAs – 1.28 and

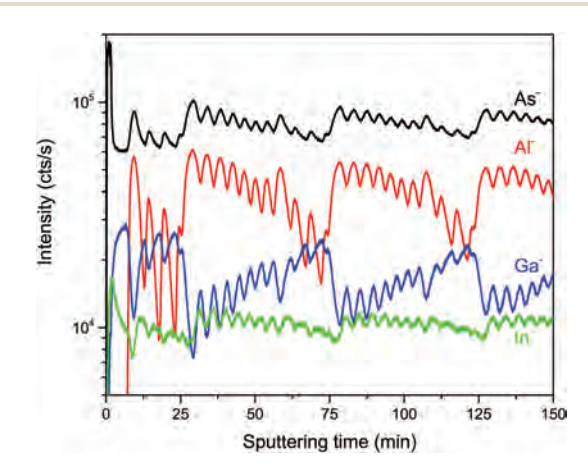


Fig. 2 A depth profile of the superlattice region of the QCL structure in the 150 eV mode. The resolution is good enough to distinguish even the thinnest layers of AllnAs (0.7 nm) – they are located at \sim 25, \sim 75 and \sim 125 min

Nanoscale Paper

0.48 nm min⁻¹ for the 150 eV mode, respectively - all presented profiles are not depth calibrated to avoid stretching and compressing of signals which significantly reduces the clearness of the presented data). Even the thinnest layer of AlInAs (0.7 nm) can be identified at \sim 25, \sim 75 and \sim 125 min as a small shoulder of the Al signal. The feature is also visible for most of the other signals with only slightly worse contrast. Measurements with such a depth resolution can be very useful, however, a proper interpretation of the obtained results is not straightforward: it may seem that consequent InGaAs and AlInAs layers have different compositions because signals have different maxima for each layer. Furthermore, As and In signals fluctuate a lot while the concentration of these elements is expected to be constant (As - 50%) or with small variations only (In - 26.5% and 26% for InGaAs and AlInAs, respectively). These effects are, however, not unexpected: each element is measured for a short period of time (usually below one second) and the number of counts is averaged. For a very thin layer there are just a few measurement points and the signal does not reach its maximum before the whole layer is already sputtered. This is why layers with different thicknesses have different maxima. It has to be also noted that each element may have a significantly different probability to be sputtered and ionized from a different layer (a so called matrix effect). For example, the presence of Al may increase the probability of detecting As ions or it can be related to a higher concentration of oxygen in AlInAs layers. Furthermore, as was discussed, the etching rate is much lower for AlInAs layers and thus the Cs retention concentration is higher which may result in higher ion yield. Even though it is not possible to distinguish which effect plays the dominant role it can be concluded that the differences between the consequent AlInAs and InGaAs layers are most probably not related to the changes of the composition.

This hypothesis, however, should be verified and thus a positive ion detection mode was used to confirm the uniformity of the structure (Fig. 3). In this mode each element is registered as a Cs_2X^+ cluster ion which leads to a significant reduction of the matrix effect. The drawback is that the depth resolution is much worse and due to a large incident angle $(64^{\circ}\ vs.\ 32^{\circ}\ in$ the 150 eV mode) the roughness of the crater's bottom increases rapidly and thus all signals are blurred after ~20 minutes of sputtering.

It is well known that the amount of oxygen contamination may have a crucial impact on the performance of an electronic device 16,17 and thus it is beneficial to monitor the presence of oxygen in the superlattice region of the QCL structure. We performed the measurements using the 150 eV mode because despite some minor measurement artifacts, it offered a superior depth resolution. Concentration calibration was based on a thick AlInAs reference sample with a known oxygen concentration. The measurement (see Fig. 4), however, was prone to the same measurement artifacts as discussed before and thus the concentration calibration should be seen as a rough estimation only. The measurement provides some important conclusions. InGaAs layers are less oxygen contami-

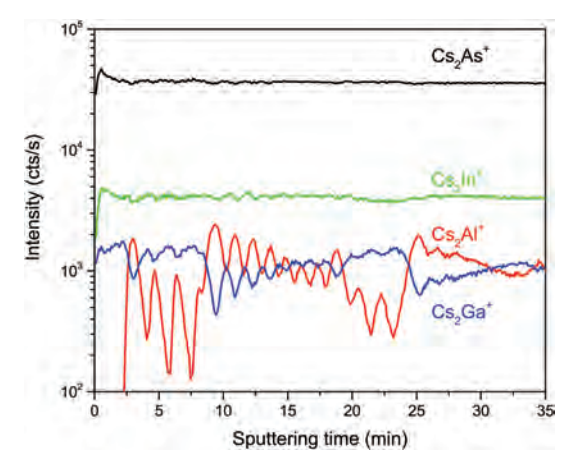


Fig. 3 A depth profile of the superlattice region of the QCL structure in the positive ion detection mode. The matrix effect is reduced and thus the uniformity of the structure is confirmed. The concentration of As is constant and In has only small variations. The resolution is, however, much worse than the 150 eV mode and the roughness of the crater's bottom increases rapidly which further decreases the resolution in time.

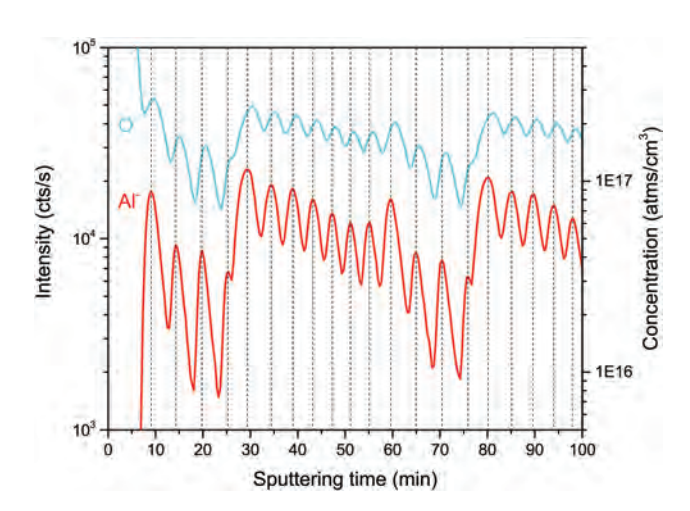


Fig. 4 Oxygen concentration in the superlattice region of the QCL structure. Centres of the AllnAs layers are marked with dashed lines. AllnAs layers are more contaminated with oxygen than the InGaAs layer. The maxima of the oxygen signal are shifted when compared to the aluminium signal and thus it can be concluded that during the first stage of the AllnAs growth process more oxygen is embedded into the structure.

nated than AlInAs layers. Seeing how the oxygen signal decreases rapidly in InGaAs layers we conclude that they are probably much cleaner than the estimation seems to suggest and the elevated oxygen level is caused by the mixing effect only. To verify this we measured a thick InGaAs layer grown using the same procedure and found that the oxygen level is below the detection limit of this mode (\sim 1 × 10¹⁶ atms per cm³).

The case of the AlInAs layers is by far more interesting. As it can be seen the oxygen contamination is not uniformly distributed in these layers: the maxima of the oxygen signal are visibly shifted when compared to the maxima of the aluminium signals (which are marked with dashed lines in

Paper Nanoscale

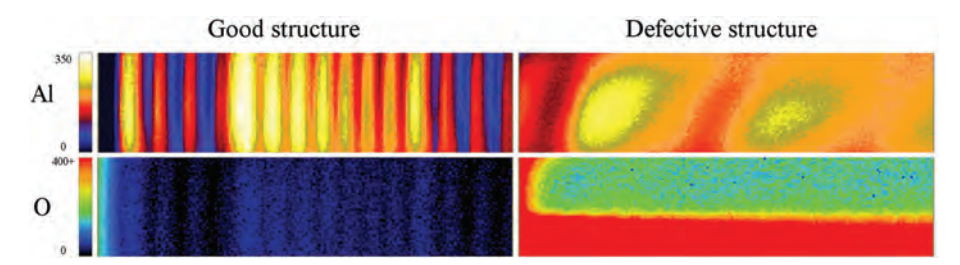


Fig. 5 YZ cross-section of Al and O signals for good and defective structures. A high uniformity of the layers is observed for the former while the growth procedure of the latter clearly went wrong – layers are blurred, tilted and highly contaminated. The intensity is given in counts per second, Y and Z scales are limited to 200 μ m and 75 min of the sputtering time, respectively. The oxygen scale was truncated at 400 counts per second to improve the visibility of the signal for the good structure.

Fig. 4). This effect is even visible (albeit barely) for the thinnest layer. This means that more oxygen is embedded into the structure during the very first stage of the growth of the AlInAs layer. This is not surprising because of the burst effect generated by opening an effusion cell, which yields slightly higher Al content at the beginning of the AlInAs barrier growth, which results in gettering more oxygen. For thicker AlInAs layers (>2 nm) the resolution is good enough so it can be estimated that one interface is 1.83 ± 0.31 times more contaminated than the other (the result is based on ten independent measurements).

The measurement procedure with such a good resolution is useful not only for the characterization of interfaces, but also for failure analysis as well. Fig. 5 compares a YZ cross-section of Al and O signals for good and defective structures. The former confirms the previous result: quantum wells are well defined and uniform. The shift between the Al and O maxima is also visible, especially for layers separated by thick InGaAs layers. Signals presented at the top and the bottom of the cross-sections are collected from the region close to the crater edge and thus some small irregularities are visible there. A series of similar measurements were performed very close to each other and all of them exhibited the same crater edge problem. No irregularities were found in the central part of the cross-section and thus we concluded that quantum wells are of very good quality and the edge problem is a measurement artifact.

The measurement of the defective structure immediately clarifies the problem: the layers are blurred, without a clear AlInAs/InGaAs separation and are not parallel to the surface of the sample. Moreover, the region is highly contaminated with oxygen, especially the bottom part.

4. Conclusions

In summary, we have developed a reliable measurement procedure for the depth profiling and 3D imaging of the superlattice region of the QCL structure, which can evaluate its quality as well as characterize the interfaces for oxygen contamination. It can be used for a better comprehension of the growth process which may be invaluable for further optimization of

quantum cascade lasers. In this case the grown heterostructures were processed into double trench Fabry–Perot lasers using standard processing technology. For the isolation layer $\mathrm{Si_3N_4}$ was used. Low resistivity electrical contacts were alloyed at 370 °C for 60 s. A Ti/Pt/Au alloy was used for the *epi*-side, and AuGe/Ni/Au for the low doped substrate side. The waveguide from the bottom side was formed by a low doped InP substrate and from the top by a 2.5 μ m AlInAs layer covered by a heavily doped InGaAs layer. Devices operated up to 360 K emitting 1 W pulse power per uncoated facet at 300 K. The room temperature threshold current was \sim 4 kA cm $^{-2}$. ^{18,19}

Conflicts of interest

There are no conflicts to declare.

Acknowledgements

P. G., D. P., K. P. and M. B. were supported by Narodowe Centrum Nauki grant UMO-2015/17/B/ST7/04015 (OPUS 9).

References

- J. Faist, F. Capasso, D. Sivco, C. Sirtori, A. Hutchinson and A. Y. Cho, *Science*, 1994, 264, 553–556.
- 2 M. Beck, D. Hofstetter, T. Aellen, J. Faist, U. Oesterle, M. Ilegems, E. Gini and H. Melchior, *Science*, 2002, 295, 301–305.
- 3 P. Karbownik, A. Barańska, A. Szerling, W. Macherzyński, E. Papis, K. Kosiel, M. Bugajski, M. Tłaczała and R. Jakieła, *Opt. Appl.*, 2009, **39**, 655–661.
- 4 R. Dhar and D. Ban, J. Microsc., 2013, 251, 35-44.
- 5 V. Mamutin, V. Ustinov, N. Ilyinskaya, M. Baydakova, B. Ber and D. Kasantsev, *J. Phys.: Conf. Ser.*, 2011, **291**, 012008.
- 6 P. Michałowski, W. Kaszub, A. Merkulov and W. Strupiński, *Appl. Phys. Lett.*, 2016, **109**, 011904.
- P. Gutowski, I. Sankowska, P. Karbownik,
 O. Serebrennikova, M. Morawiec, E. Pruszyńska-Karbownik,
 K. Gołaszewska-Malec, D. Pierścińska, K. Pierściński,

Nanoscale Paper

J. Muszalski and M. Bugajski, J. Cryst. Growth, 2017, 466, 22–29.

- 8 CAMECA, CAMECA SC-Ultra, User's Guide, Genneviliers, 2005.
- 9 D. Kouzminov, A. Merkulov, E. Arevalo and H. J. Grossmann, *Surf. Interface Anal.*, 2013, 45, 345–347.
- 10 A. Merkulov, Surf. Interface Anal., 2013, 45, 90-92.
- 11 H. Storms, K. Brown and J. Stein, *Anal. Chem.*, 1977, **49**, 2023–2030.
- 12 Y. Gao, J. Appl. Phys., 1988, 64, 3760.
- 13 C. Magee, W. Harrington and E. Botnick, *Int. J. Mass Spectrom. Ion Processes*, 1990, **103**, 45–56.
- 14 A. Mikami, Jpn. J. Appl. Phys., 2004, 43, 2745.
- 15 B. Saha and P. Chakraborty, Energy Procedia, 2013, 41, 80–109.

- 16 M. Troccoli, L. Diehl, D. Bour, S. Corzine, N. Yu, C. Wang, M. Belkin, G. Höfler, R. Lewicki, G. Wysocki, F. Tittel and F. Capasso, J. Lightwave Technol., 2008, 26, 3534–3555.
- 17 Y. Huang, J. Ryou, R. Dupuis, C. Pflugl, F. Capasso, K. Sun, A. M. Fischer and F. A. Ponce, *J. Cryst. Growth*, 2011, **316**, 75–80.
- 18 P. Gutowski, P. Karbownik, A. Trajnerowicz, K. Pierściński, D. Pierścińska, I. Sankowska, J. Kubacka-Traczyk, M. Sakowicz and M. Bugajski, *Photonics Lett. Pol.*, 2014, 6, 142–144.
- 19 M. Bugajski, P. Gutowski, P. Karbownik, A. Kolek, G. Hałdaś, K. Pierściński, D. Pierścińska, J. Kubacka-Traczyk, I. Sankowska, A. Trajnerowicz, K. Kosiel, A. Szerling, J. Grzonka, K. Kurzydłowski, T. Slight and W. Meredith, *Phys. Status Solidi B*, 2014, 251, 1144–1157.

PAPER

Contamination-free Ge-based graphene as revealed by graphene enhanced secondary ion mass spectrometry (GESIMS)

To cite this article: P P Michaowski et al 2018 Nanotechnology 29 015702

View the <u>article online</u> for updates and enhancements.

IOP Publishing Nanotechnology

Nanotechnology 29 (2018) 015702 (7pp)

https://doi.org/10.1088/1361-6528/aa98ed

Contamination-free Ge-based graphene as revealed by graphene enhanced secondary ion mass spectrometry (GESIMS)

P P Michałowski , I Pasternak and W Strupiński

Institute of Electronic Materials Technology, Wólczyńska 133, 01-919 Warsaw, Poland

E-mail: pawel.michalowski@itme.edu.pl

Received 7 September 2017, revised 3 November 2017 Accepted for publication 8 November 2017 Published 4 December 2017



Abstract

In this study, we demonstrate that graphene grown on Ge does not contain any copper contamination, and identify some of the errors affecting the accuracy of commonly used measurement methods. Indeed, one of these, the secondary ion mass spectrometry (SIMS) technique, reveals copper contamination in Ge-based graphene but does not take into account the effect of the presence of the graphene layer. We have shown that this layer increases negative ionization significantly, and thus yields false results, but also that the graphene enhances, by an order of two, the magnitude of the intensity of SIMS signals when compared with a similar graphene-free sample, enabling much better detection limits. This forms the basis of a new measurement procedure, graphene enhanced SIMS (GESIMS) (pending European patent application no. EP 16461554.4), which allows for the precise estimation of the realistic distribution of dopants and contamination in graphene. In addition, we present evidence that the GESIMS effect leads to unexpected mass interferences with double-ionized species, and that these interferences are negligible in samples without graphene. The GESIMS method also shows that graphene transferred from Cu results in increased copper contamination.

1

Keywords: graphene, secondary ion mass spectrometry, Cu contamination

(Some figures may appear in colour only in the online journal)

1. Introduction

Graphene (Gr) is widely considered as a good candidate for integration with the existing electronic and photonic devices [1–12]. That means that the growth and processing procedures have to fulfil the requirements of the existing fabrication lines, including high purity standards of the front-end-of-line (FEOL) integration approaches. Copper contamination is considered to be particularly dangerous and thus it has to be carefully monitored.

Secondary ion mass spectrometry is a very precise analytical technique which provides information about the surface and microstructure of a sample [13–19] and allows to determine the elemental composition of a sample, [20–25] it is especially well known for its excellent detection limits of trace elements [26–31]. Therefore SIMS is very good candidate to monitor copper contamination. Several SIMS

measurements on graphene have already been reported, [11, 32–38]. Lupina *et al* [11] have already demonstrated the usefulness of the SIMS technique for monitoring copper contamination.

However, in our recent work [39] we demonstrated that graphene significantly increases the ionization probability during the SIMS measurement. We proposed to use this effect to enhance SIMS measurements of 2D materials, surfaces and ultra thin films—by transferring graphene on top of such samples the intensity of SIMS signals can be increased and better detection limits can be reached. This method is not suitable for thicker layers as graphene will be sputtered quickly and the enhancement effect will vanish.

It has to be taken into account that the very same effect occurs during characterization of graphene itself and the intensity of every signal can be enhanced. It means that a proper interpretation of obtained results is complicated and requires reduction of the enhancement effect. Up to this point the influence of the graphene layer on the SIMS experiment has not been considered and SIMS experiments were performed routinely and therefore it can be concluded that the reported Cu contamination was overestimated. In this work, however, we describe a detailed procedure how to reduce the enhancement effect in order to obtain a realistic distribution of the Cu contamination in a sample. Only then a prove that some of the graphene growth processes are clean can be delivered.

2. Experimental setup

2.1. Sample preparation

All samples described in this work were prepared on (100)-oriented Ge layers deposited on Si (100) wafers. Three types of samples were considered: one having graphene CVD grown directly on the substrate, other transferred from a copper foil and the pure substrate serving as a reference.

In the first case graphene films were synthesized by the CVD method in a commercially available system as described by Paternak *et al* [40, 41]. At the beginning the substrate was annealed in a pure hydrogen atmosphere in order to reduce native oxides *in situ*, then a carbon precursor was introduced (methane gas in the mixture of Ar and H₂ in the ratio of 200:1) and 800 mbar of pressure were sustained.

In other case, graphene films were synthesized on $35 \, \mu m$ thick copper foils by the CVD method using a Black Magic Pro system (Aixtron). At the beginning copper foil was annealed at 960 °C under an Ar gas flow and then a H_2 gas flow at 20 mbar of pressure in order to remove oxides from the surface and improve the quality and enlarge the grain size of Cu substrates. Methane was used as a carbon precursor and graphene were synthesized on the surface of the foil, which was then cooled to room temperature in an Ar atmosphere. As a last step, graphene was transferred onto the Ge substrate by the high-speed electrochemical delamination method [42].

2.2. SIMS measurements

In this work all SIMS measurements were performed employing the CAMECA SC Ultra instrument under ultrahigh vacuum, usually of 4×10^{-10} mbar. A Cs⁺ primary beam rastered over (250 \times 250) μ m² with impact energy of 13 keV and the intensity of 100 pA along with negative ion detection was used for all measurements. The analysis area was limited to (200 \times 200) μ m². A highly uniform beam was required for this work—the beam on the sample in the SC Ultra tool has a square shape and owning to the 'variable rectangular shape concept' forms a homogeneous spot. The primary beam at the working point in the SC Ultra is formed by two stencils—well-shaped apertures. While the first one is used to choose the most intense and homogeneous part of the Gaussian-shaped ion beam, the second one changes the size of the spot. This innovation provides high sensitivity for all measured elements [43–45].

We performed and compared the result obtained in three different modes:

- (i) Low mass resolution (LMR) mode which offers the best sensitivity but due to a low mass resolving power (400) does not allow to distinguish any possible mass interferences.
- (ii) High mass resolution (HMR) mode with higher mass resolving power (3000) which allows the identification of each interfering component in the mass spectrum.
- (iii) Offset voltage mode which filters low energy ions and thus drastically decreases a probability to detect polyatomic ions and thus leaving only monoatomic ions to be detected.

3. Results and discussion

Quantification of SIMS results is based on a measurement of a reference sample with a known distribution of a trace element. In most cases such reference samples are bulk materials with ion implanted impurities [22, 46–50]. In case of graphene, however, such a procedure cannot be applied because for such a thin layer it is not possible to create an ion implanted sample. As a consequence there is no easy way to determine the concentration of impurities and dopants in graphene by SIMS measurements. Usually only a general estimation is possible—for a given dopant or impurity, the intensity of SIMS signal measured on graphene/substrate sample is compared to the measurement performed on a substrate sample without graphene and it is assumed that the relative sensitivity factor is roughly the same.

Usually such routine measurements are performed in a static SIMS mode which is surface sensitive and quasi nondestructive (only $\sim 1\%$ of the surface is damaged during the experiment). Furthermore, they are usually limited to the most abundant isotopes (in this case ⁶³Cu). In this work, however, we used a slightly higher primary ion current (in range of 100 pA) and thus the very beginning of the experiment still fulfilled the static mode limitation (ion dose typically in range of 10^{12} ions cm⁻²) but the continuous ion bombardment led to an erosion of the graphene layer and the Ge substrate was eventually fully exposed. Moreover, we recorded signals for both stable isotopes of copper, namely ⁶³Cu⁻ and ⁶⁵Cu⁻. Since at this point we were not able to rule out possible mass interferences we denoted them as mass 63 u and mass 65 u $(^{63}\mathrm{m}^-$ and $^{65}\mathrm{m}^-$, respectively). Figure 1 shows a typical measurement performed on three different samples: graphene CVD grown on a germanium substrate (black lines), graphene CVD grown on a copper foil and transferred onto a germanium substrate (red lines) and a pure germanium substrate (blue lines) as a reference.

If we follow a routine procedure (static SIMS regime and analysis of the most abundant isotope only) a straightforward conclusions can be made: graphene grown on copper and transferred on Ge substrate is somewhat more contaminated than graphene grown directly on Ge substrate; both graphene samples are about three order of magnitude more contaminated

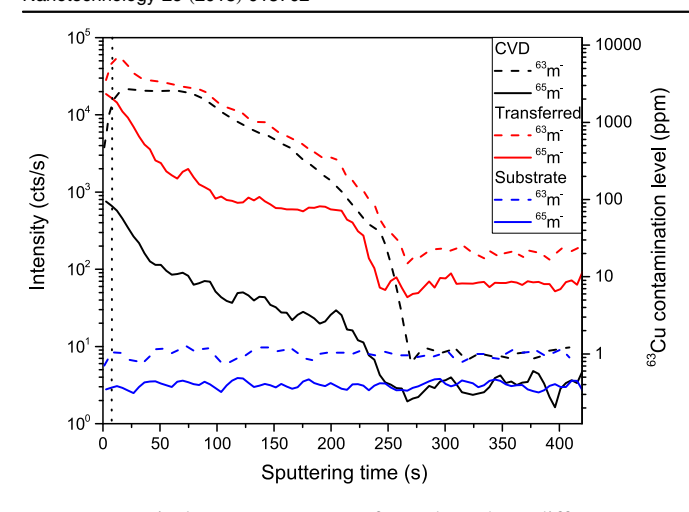


Figure 1. Typical measurements performed on three different samples in LMR mode. Both stables isotopes of copper were recorded but since mass interferences could not be excluded they were denoted as 63 m⁻ and 65 m⁻. Static SIMS regime is marked as a dot line at the beginning of the profile. Cu contamination level is given for the 63 m⁻ signal. A routine measurement procedure (static SIMS, 63 m⁻ signal) seems to suggest that the graphene layer is highly contaminated with Cu, regardless on which substrate it has been grown.

than a pure Ge substrate. It means that contamination level can be as high as parts per thousands regime which is completely unacceptable for the FEOL integration approaches for electronic and photonic devices.

There are, however, a number of issues with this routine procedure:

- For all types of samples the ratio of 63 m $^-$ and 65 m $^-$ signals for the substrate region equals 2.61 ± 0.44 which corresponds to the ratio of the natural abundance of these isotopes (2.24). For the graphene region, however, the ratio is much higher.
- The shape of 63 m⁻ and 65 m⁻ signals for the same sample is significantly different whereas similar from sample to sample (i.e. the shape of both 63 m⁻ signals and both 65 m⁻ signals for graphene samples is similar).
- The ratio of ⁶⁵m⁻ signals for transferred and CVD grown samples is much higher than the ratio of ⁶³m⁻ signals.

Such high discrepancies cannot be neglected and the routine procedure should be treated as untrustworthy. It is, however, essential to determine what has led to such strange results. Besides carbon, germanium and copper the samples could contain silicon (germanium was deposited on Si substrate) and, at the surface, traces of elements coming from water vapour and dust particles like oxygen, nitrogen, hydrogen, fluorine, sodium and perhaps a few others. Unfortunately no credible mass interference was found that would be able to explain such high anomalies.

The idea of the mass interference, however, was not immediately disqualified. CAMECA SC Ultra SIMS has an ability to filter mass interferences even if they are initially unknown. It is a well known fact that a monoatomic ions have a much broader energy distribution than the polyatomic ions [22]. By applying a few tens of volts of decelerating voltage

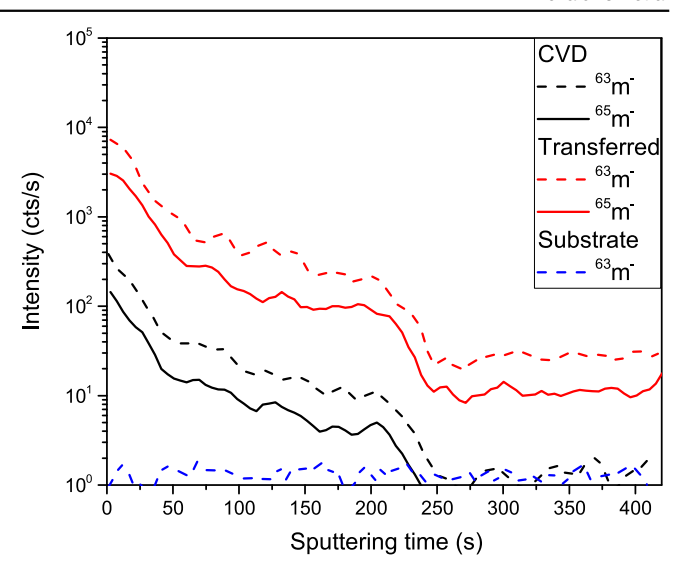


Figure 2. Typical measurements performed on three different samples in offset voltage mode. Graphene grown on a copper foil is about twenty times more contaminated than graphene grown on a germanium substrate but both samples still seems to be highly contaminated.

(a so called offset voltage) polyatomic ions are filtered and cannot reach the detector while a substantial portion of monoatomic ions (those with energies higher than the offset voltage) can still be registered. This way one can be sure that every detected ion of mass 63 u and 65 u can be attributed to ⁶³Cu and ⁶⁵Cu, respectively.

We performed such an experiment with the offset voltage set to 20 V and the results are presented on figure 2. There are a lot of significant differences when compared to the figure 1:

- Comparing to the LMR mode, the overall sensitivity of the experiment has been reduced because low energy ions were filtered out. ⁶⁵m⁻ signal for the pure substrate is below the detection limit.
- For both graphene samples, the shape of ⁶³m⁻ signal has changed significantly and is similar to the shape of ⁶⁵m⁻ signal which has remained the same.
- For both graphene samples, the ratio of $^{63}\text{m}^-$ and $^{65}\text{m}^-$ signals for the same sample is constant for the whole profile and equals 2.59 ± 0.47 which corresponds to the ratio of the natural abundance of these isotopes (2.24).
- The intensity of both 63 m⁻ and 65 m⁻ signals for the transferred sample is 20.7 ± 1.1 times higher when compared to the CVD sample. This ratio is constant for the whole profile as long as the signal is above the detection limit (in case of 65 m⁻).

At this point it becomes clear that graphene grown on a copper foil and transferred on the Ge substrate is about twenty times more contaminated than graphene directly grown on the Ge substrate (a routine measurement suggested only 2–3 times more). One question, however, remains—which ion has caused such a strong mass interference with ⁶³Cu for experiments in LMR mode? A relatively low offset voltage was needed to filter the interfering ion completely which suggested that it consisted

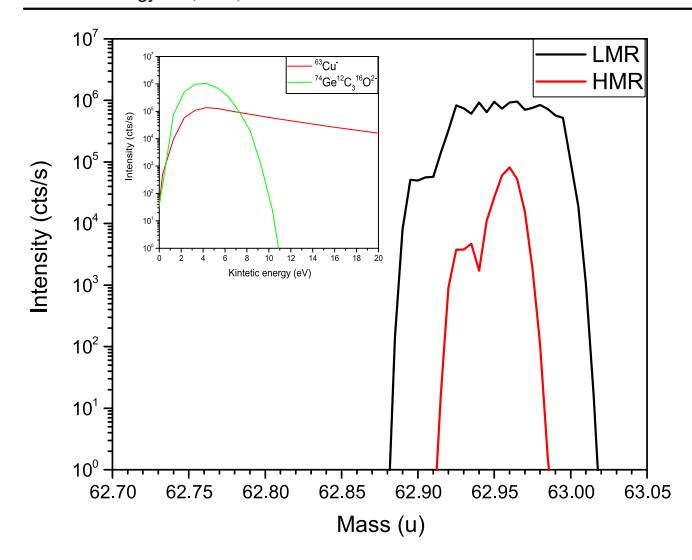


Figure 3. A mass spectrum recorded around mass 63 u in high and low mass resolution modes. In HMR mode it is possible to distinguish two components of $^{63}\text{m}^-$ peak: $^{63}\text{Cu}^-$ and $^{74}\text{Ge}^{12}\text{C}_3^{16}\text{O}^{2-}$. Inset: kinetic energy distribution of these two ions.

more than three atoms. Unfortunately, as it was mentioned before, no suitable candidate could initially be found.

To solve this problem it has to be taken into account that graphene significantly increases the ionization probability during the SIMS measurement, as we described in our previous work [39]. The effect is particularly strong for double ionized species (more then two orders of magnitude). By taking it into account it is indeed possible to explain this problematic mass interference. SIMS actually does not measure a mass of the secondary ions but a mass to charge ratio. So any double ionized specie with mass 2m can interfere with single ionized specie with mass m. In vast majority of SIMS experiments this is not a problem because the probability of double ionization is low and the intensity of double ionized signals is usually below 100 counts per second. But as we proved in our work [39] graphene can significantly increase the double ionization probability and thus such ions can play a significant role in a mass spectrum and thus cause problematic mass interferences.

In this particular case we had to search for a specie with nominal mass 126 u which, as a double ionized ion, could mass interfere with 63 Cu $^-$ signal. After a careful analysis we found that 74 Ge 12 C $_3$ 16 O $^{2-}$ ion was the only one that could explain the whole situation. There was an abundance of each element at the surface of our samples: germanium came from the substrate, carbon from graphene and oxygen is present at the surface of every sample in various forms (water vapour and dust particles). Furthermore, at the very beginning of the experiment germanium was covered by graphene and its extraction was somewhat blocked. After a few seconds graphene was partially destroyed and more Ge atoms could be emitted from the sample. That is why the intensity of the 63 m $^-$ signal in LMR mode reached its maximum after a few seconds.

To confirm this hypothesis we recorded a mass spectrum around mass 63 u in high and LMR modes (figure 3). In HMR

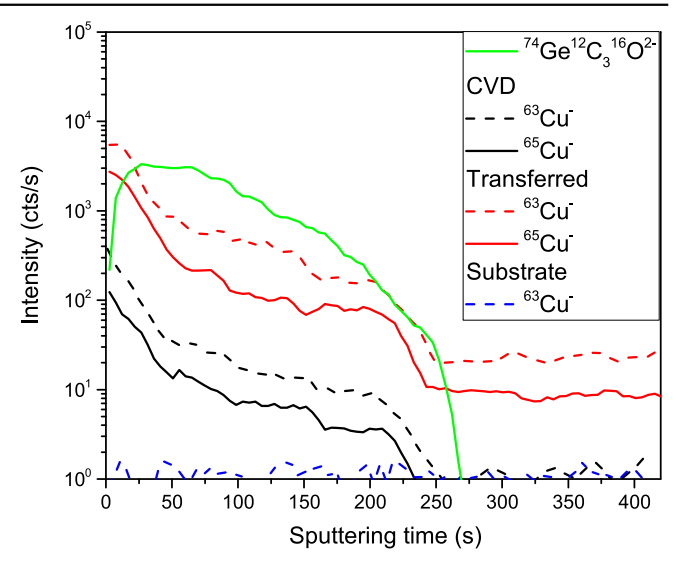


Figure 4. Typical measurements performed on three different samples in HMR mode. The measurements confirm that graphene grown on a copper foil is about twenty times more contaminated than graphene grown on a germanium substrate. Furthermore, ⁷⁴Ge¹²C₃ ¹⁶O²⁻ signal was recorded which was responsible for the mass interference in LMR mode.

mode it is possible to distinguish two components of 63 m⁻ peak. The exact mass to charge ratio of 63 Cu⁻ and 74 Ge 12 C₃ 16 O²⁻ ions is 62.9295975 u/e and 62.95804621 u/e, respectively so the difference between them is 0.02844871 u/e which is exactly what we registered (0.028 u/e). The distribution of kinetic energy (figure 3, inset) further confirms that ions have been identified correctly since the monoatomic ions have much broader distribution. 74 Ge 12 C₃ 16 O²⁻ peak has a much higher intensity so it plays a major role in LMR measurements and thus 63 m⁻ signal on figure 1 cannot be attributed to 63 Cu⁻ ions.

In theory such a HMR measurement could have been performed without any knowledge about possible interfering ions. However, it could have led to a mistake because peak identification is more or less arbitrary and depends on the operator. As it was said before in vast majority of SIMS experiments double ionized species have a very low intensity so in this particular case the most intense peak around mass 63 u would have been attributed to 63 Cu $^-$ ions because no other species would have been expected there.

An additional depth profile in HMR mode was obtained (figure 4) and the result confirms conclusions from the offset voltage mode (figure 2): the overall sensitivity of the experiment is lower than in LMR mode, the ratio of ⁶³Cu⁻ and ⁶⁵Cu⁻ signals corresponds to the ratio of the natural abundance of these isotopes and graphene grown on copper foil is about twenty times more contaminated than graphene grown on germanium substrate. Additionally, ⁷⁴Ge¹²C₃ ¹⁶O²⁻ signal was recorded and was found to be, as expected, the same for both graphene samples and therefore for a better visibility it was presented only once. Moreover, the shape of ⁶³m⁻ signal in LMR mode (figure 1) can be finally explained since a sum of ⁶³Cu⁻ and ⁷⁴Ge¹²C₃ ¹⁶O²⁻ signals has exactly the same shape, no matter which graphene sample is

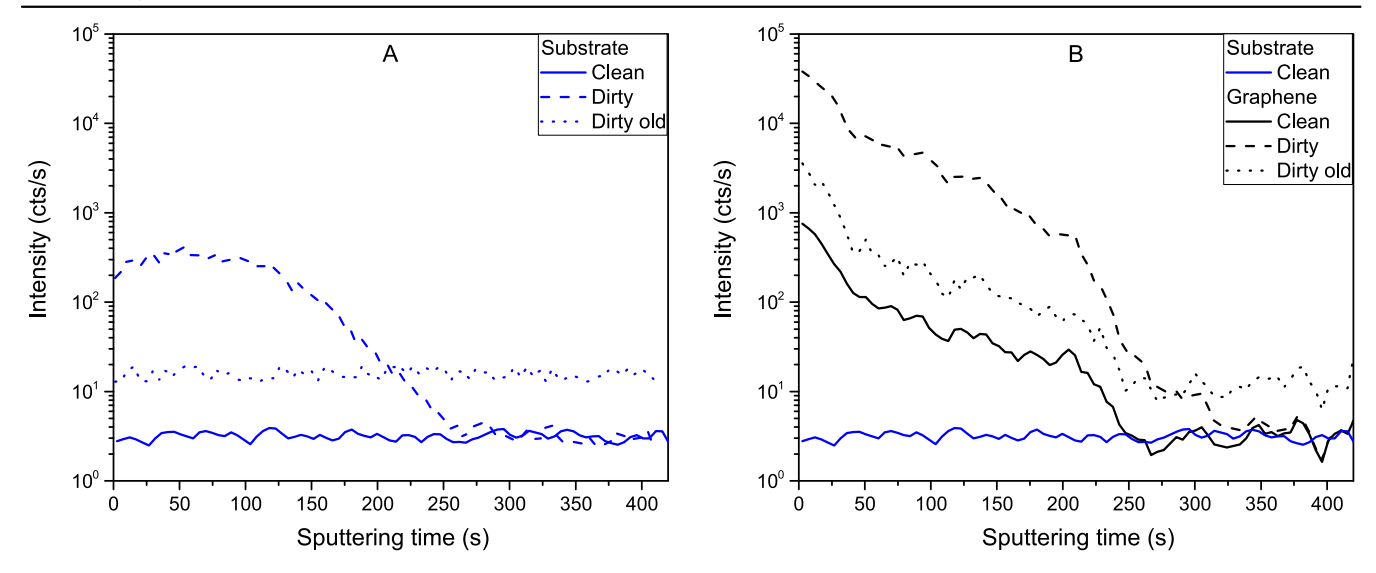


Figure 5. SIMS measurements were performed on clean and intentionally contaminated sample. For the latter two independent measurements were recorder: immediately after the contamination and one month later. Part A: the pure Ge substrate sample. At the beginning the Cu atoms are localized close to the surface but after one month they have diffused and are evenly distributed. Part B: the Ge substrate with the graphene layer. Despite the signal enhancement a similar effect is observed: at the beginning a lot of Cu atoms are localized at the surface and the signal drops to the base level after the destruction of the graphene layer. For the old sample the base level is much higher than that of the clean sample.

considered. It further confirms that every peak in mass spectrum was adequately identified.

At this point it can be concluded that the best sensitivity is obtained for the LMR mode and the ⁶⁵Cu⁻ signal as it does not have any mass interferences. The signal, however, do not correspond to the concentration of the copper contamination in the sample. As we explained in our previous work [39] every signal measured in negative ions detection mode is enhanced by the presence of the graphene layer and thus the effect has to be subtracted if the real distribution of Cu atoms in the samples is to be determined.

We devised a simple experiment to determine how the graphene layer enhances the ⁶⁵Cu⁻ signal: we touched samples with a copper foil and made a SIMS measurement immediately after that and repeated it one month later. Figure 5 presents a typical result for the pure substrate sample (part A) and the graphene grown on Ge substrate (part B). We noted that at the beginning Cu atoms are initially localized at the surface but after one month they diffused into the sample and were evenly distributed. The effect was visible even for the graphene sample, despite the signal enhancement. The most important observation, however, was that for the clean sample and first measurement of the contaminated one the signal dropped to the same level as the pure substrate after a complete destruction of the graphene layer whereas it did not for the old dirty sample. Therefore we concluded that if the growing procedure on Ge substrate introduced any copper contamination the signal would not dropped to the same level as for the pure substrate. As a consequence we concluded that the shape of the 65Cu- signal was related to the enhancement effect only and thus could be used to subtract the GESIMS effect and obtain the real distribution of Cu atoms in the sample.

We performed the subtraction procedure for clean and contaminated samples (figure 6) and reproduced the very same behaviour as it was for the pure substrate (figure 5, part A): shortly after the contamination Cu atoms were localized at the surface and diffused into the sample after some time. It further confirmed that our procedure was correct.

After many experiments we finally established a reliable procedure that could determine the real distribution of Cu atoms in graphene samples without any mass interferences and artificial signals enhancements. We used it more than fifty times on both, graphene CVD grown on Ge and copper foil and transferred on a Ge substrate samples. All of the measurements confirmed that the growth process on Ge substrate was clean and did not introduce any copper and had the same contamination level as a pure substrate (1 ppm). In the case of the fresh transferred graphene we found that some additional copper contamination was always introduced but inhomogeneously: the contamination level varied from 17 to 430 times more than a pure substrate. For the old sample, as expected, copper atoms diffused into the sample and the global contamination level was found to be around 56 times higher than for a pure substrate. A summary of these measurements is presented on figure 7.

4. Conclusions

We have demonstrated that Ge-based graphene is of high quality and does not contain any copper contamination. Furthermore, we proved that routinely used SIMS technique may lead to many errors and overestimation of dopants and contamination distribution because the presence of the graphene layer significantly influences SIMS experiment. For each sample and dopant/contamination atom a separate

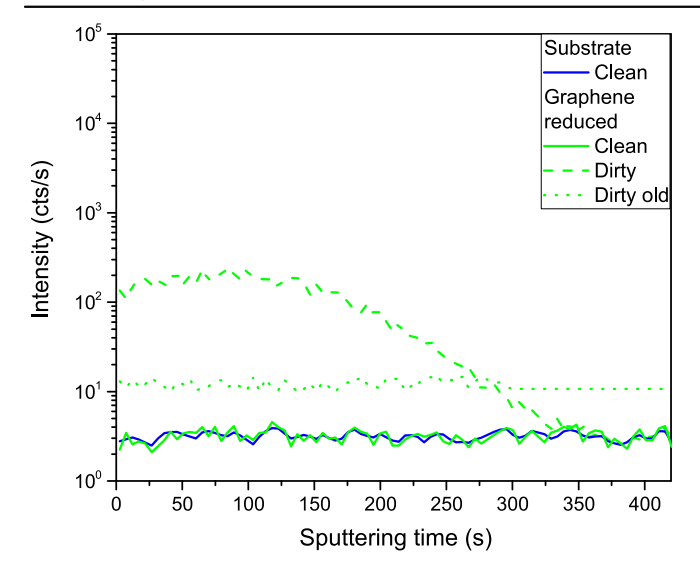


Figure 6. Typical measurements performed on CVD grown sample with reduced GESIMS effect. The clean sample has the same contamination level as the substrate. For the intentionally contaminated sample Cu atoms are initially localized at the surface and diffuse into the sample after some time.

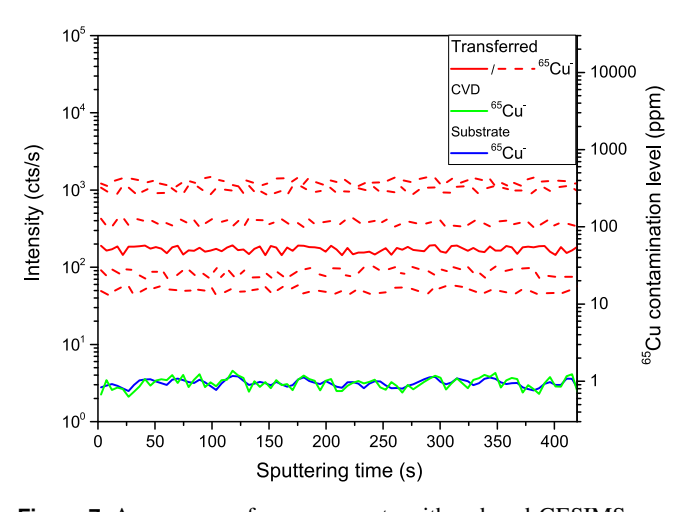


Figure 7. A summary of measurements with reduced GESIMS effect. All measurements performed on CVD graphene confirmed that the contamination level is the same as for a pure Ge substrate (1 ppm). The contamination level for the transferred sample was different from spot to spot (dash red lines presents a few examples). It became homogeneous for the aged sample (solid red line).

reduction procedure has to be established. It consists of the following steps:

- (i) Identification of all possible mass interferences, including those caused by double ionized species.
- (ii) Choosing an isotope and a mode (LMR, HMR, offset voltage) which offers the best sensitivity.
- (iii) Finding a suitable way to subtract the enhancement effect from the raw data.

Despite these complications it is possible to obtain a reliable results from the experiment and the proper interpretation allows for the precise estimation of the realistic distribution of dopants and contamination in graphene. So far we have proved that the graphene growth process on Ge and SiC substrates is clean and does not introduce any copper contamination, whereas transferring procedure and growing graphene on Cu substrate results in increased copper contamination. This information may be invaluable for further development of graphene based electronic devices, especially for the FEOL integration approaches.

Acknowledgments

The research leading to these results has received funding from the European Union Seventh Framework Programme under Grant Agreement No. 604391 Graphene Flagship.

ORCID iDs

P P Michałowski https://orcid.org/0000-0002-3299-4092

References

- [1] Levendorf M P, Ruiz-Vargas C, Garg S and Park J 2009 Nano Lett. 9 4479–83
- [2] Kim K S et al 2009 Nature 457 706-10
- [3] Jobst J, Waldmann D, Emtsev K, Seyller T and Weber H B 2010 Mater. Sci. Forum 645–648 637–41
- [4] Bonaccorso F, Sun Z, Hasan T and Ferrari A 2010 Nat. Photon. 4 611–22
- [5] Jauregui L, Cao H, Wu W, Yu Q and Chen Y 2011 Solid State Commun. 151 1100–4
- [6] Kim K, Choi J Y, Kim T, Cho S H and Chung H J 2011 Nature 479 338–44
- [7] Park J U, Nam S, Lee M S and Lieber C 2012 *Nat. Mater.* 11
- [8] Mehr W, Dabrowski J, Scheytt C, Lippert G, Xie Y, Lemme M, Ostling M and Lupina G 2012 Electron Device Lett. 33 691–3
- [9] Vaziri S, Lupina G, Henkel C, Smith A, Lippert G, Mehr W and Lemme M 2013 Nano Lett. 13 1435–9
- [10] Han S, Valdes Garcia A, Oida S, Jenkins K and Haensch W 2014 Nat. Commun. 5 3086
- [11] Lupina G et al 2015 ACS Nano 9 4776
- [12] Fiori G, Bonaccorso F, Iannaccone G, Palacios T, Neumaier D, Seabaugh A, Banerjee S and Colombo L 2014 Nat. Nanotechnol. 9 768–79
- [13] Paul J et al 2009 Microelectron. Eng. 86 949–52
- [14] Lanza M et al 2009 Microelectron. Eng. 86 1921-4
- [15] Michałowski P, Beyer V, Czernohorsky M, Kuecher P, Teichert S, Jaschke G and Moeller W 2009 Phys. Status Solidi c 7 284–7
- [16] Paul J et al 2010 Microelectron. Eng. 87 1629–33
- [17] Bayan S and Chakraborty P 2014 Appl. Surf. Sci. 303 233-40
- [18] Bayan S, Choudhury B, Satpati B, Chakraborty P and Choudhury A 2015 J. Appl. Phys. 117 095304
- [19] Bayan S, Satpati B and Chakraborty P 2015 Surf. Interface Anal. 47 37–44
- [20] Andersen C A and Hinthorne J R 1972 Science 175 853-60
- [21] Benninghoven A 1975 Surf. Sci. 53 596-625
- [22] Benninghoven A, Rudenauer F G and Werner H W 1987 Secondary Ion Mass Spectrometry: Basic Concepts, Instrumental Aspects, Applications and Trends (New York: Wiley) (https://doi.org/10.1002/sia.740100811)

- [23] Werner H W 1975 Surf. Sci. 47 301-23
- [24] Liebl H 1975 J. Vac. Sci. Technol. A 12 385
- [25] Liebl H 1967 J. Appl. Phys. 38 5277-83
- [26] Wittmaack K 1976 Appl. Phys. Lett. 29 552
- [27] Ber B Y, Kudriavtsev Y A, Merkulov A V, Novikov S V, Lacklison D E, Orton J W, Cheng T S and Foxon C T 1998 Semicond. Sci. Technol. 13 71–4
- [28] Chiou C Y, Wang C C, Ling Y C and Chiang C I 2003 Appl. Surf. Sci. 203–204 482–5
- [29] Emziane M, Durose K, Halliday D P, Bosio A and Romeo N 2006 J. Appl. Phys. 100 013513
- [30] Matsunaga T, Yoshikawa S and Tsukamoto K 2002 Surf. Sci. 515 390–402
- [31] Gnaser H 1997 Surf. Interface Anal. 25 737-40
- [32] Luo Z, Lim S, Tian Z, Shang J, Lai L, MacDonald B, Fu C, Shen Z, Yu T and Lin J 2011 J. Mater. Chem. 21 8038
- [33] Dwivedi N, Satyanarayana N, Yeo R, Xu H, Loh K, Tripathy S and Bhatia C 2015 *Sci. Rep.* **5** 11607
- [34] Xie W, Weng L T, Ng K, Chan C and Chan C M 2015 *Carbon* 94 740–8
- [35] Li Q, Chou H, Zhong J H, Liu J Y, Dolocan A, Zhang J, Zhou Y, Ruoff R, Chen S and Cai W 2013 Nano Lett. 13 486
- [36] Chou H, Ismach A, Ghosh R, Ruoff R and Dolocan A 2015 Nat. Commun. 6 7482

- [37] Yannopoulos S, Siokou A, Nasikas N, Dracopoulos V, Ravani F and Papatheodorou G 2012 Adv. Funct. Mater. 22 113
- [38] Michałowski P P, Kaszub W, Merkulov A and Strupinski W 2016 Appl. Phys. Lett. 109 011904
- [39] Michałowski P P, Kaszub W, Pasternak I and Strupinski W 2017 Sci. Rep. 7 7479
- [40] Pasternak I, Wesolowski M, Jozwik I, Lukosius M, Lupina G, Dabrowski P, Baranowski J M and Strupinski W 2016 Sci. Rep. 6 21773
- [41] Pasternak I, Dabrowski P, Ciepielewski P, Kolkovsky V, Klusek Z, Baranowski J M and Strupinski W 2016 Nanoscale 8 11241-7
- [42] Ciuk T, Pasternak I, Krajewska A, Sobieski J, Caban P, Szmidt J and Strupinski W 2013 J. Phys. Chem. C 117 20833-7
- [43] CAMECA Genneviliers 2005 CAMECA SC-Ultra User's Guide
- [44] Kouzminov D, Merkulov A, Arevalo E and Grossmann H J 2013 Surf. Interface Anal. 45 345–7
- [45] Merkulov A 2013 Surf. Interface Anal. 45 90-2
- [46] Werner H W 1980 Surf. Interface Anal. 2 56
- [47] Leta D P and Morrison G H 1980 Anal. Chem. 52 514
- [48] Galuska A A and Morrison G H 1983 Anal. Chem. 55 2051
- [49] Galuska A A and Morrison G H 1987 Pure Appl. Chem. 59 229
- [50] Hues S M and Colton R J 1989 Surf. Interface Anal. 14 101

PAPER

Formation of a highly doped ultra-thin amorphous carbon layer by ion bombardment of graphene

To cite this article: Pawe Piotr Michaowski et al 2018 Nanotechnology 29 305302

View the <u>article online</u> for updates and enhancements.

IOP Publishing Nanotechnology

Nanotechnology 29 (2018) 305302 (7pp)

https://doi.org/10.1088/1361-6528/aac307

Formation of a highly doped ultra-thin amorphous carbon layer by ion bombardment of graphene

Paweł Piotr Michałowski¹, Iwona Pasternak¹, Paweł Ciepielewski¹, Francisco Guinea^{2,3} and Włodek Strupiński¹

E-mail: pawel.michalowski@itme.edu.pl

Received 22 February 2018, revised 26 April 2018 Accepted for publication 8 May 2018 Published 22 May 2018



Abstract

Ion bombardment of graphene leads to the formation of defects which may be used to tune properties of the graphene based devices. In this work, however, we present that the presence of the graphene layer on a surface of a sample has a significant impact on the ion bombardment process: broken sp² bonds react with the incoming ions and trap them close to the surface of the sample, preventing a standard ion implantation. For an ion bombardment with a low impact energy and significant dose (in the range of 10¹⁴ atoms cm⁻²) an amorphization of the graphene layer is observed but at the same time, most of the incoming ions do not penetrate the sample but stop at the surface, thus forming a highly doped ultra-thin amorphous carbon layer. The effect may be used to create thin layers containing desired atoms if no other technique is available. This approach is particularly useful for secondary ion mass spectrometry where a high concentration of Cs at the surface of a sample significantly enhances the negative ionization probability, allowing it to reach better detection limits.

Keywords: graphene, ion bombardment, secondary ion mass spectrometry, SIMS, Raman spectroscopy

1

(Some figures may appear in colour only in the online journal)

1. Introduction

Pristine graphene is known for its many unique properties, however, the implementation of graphene into the existing fabrication lines of electronic and photonic devices requires a fully reproducible procedure to tune its properties [1–5]. While there are many possible approaches to achieve this goal, ion bombardment is widely considered as a method to functionalize graphene with intense studies being reported worldwide [6–13]. The mechanism of defects formation and their influence on various properties of graphene have been described along with the optimization of this process.

At the same time, ion bombardment is used in secondary ion mass spectrometry (SIMS) measurements to obtain

information about the elemental composition of a sample and several SIMS measurements on graphene have already been reported [14–23].

Notably, in our recent work [22] we showed that graphene can significantly change the outcome of the SIMS experiment as it increases the negative ionization probability and thus enhances the intensity of SIMS signals. We used this effect to introduce a novel measurement procedure—graphene enhanced secondary ion mass spectrometry (GESIMS) for characterization of 2D materials, surfaces and ultra-thin films. Similar approaches to enhance the intensity of SIMS signals have been already reported and are widely used, like matrix-enhanced SIMS [24] or metal-assisted SIMS [25, 26].

¹ Institute of Electronic Materials Technology, Wólczyńska 133, 01-919 Warsaw, Poland

² Imdea Nanoscience, Faraday 9, E-28049 Madrid, Spain

³ School of Physics and Astronomy, University of Manchester, Manchester M13 9PY, United Kingdom

To quantify the effect, we defined a gain factor as follows:

$$GF = \frac{Y_{Gr}\alpha_{Gr}}{Y\alpha},\tag{1}$$

wherein GF was the gain factor, $Y_{\rm Gr}$ and Y denoted partial sputter yield (number of emitted species A per incident ion) for a sample with and without graphene, respectively, while $\alpha_{\rm Gr}$ and α denoted ionization probabilities (again, a sample with and without graphene, respectively). Under optimum conditions $Y_{\rm Gr} < Y$ and $\alpha_{\rm Gr} > \alpha$, whereby the latter effect was much stronger, so that GF > 1 and thus the intensity of the SIMS signal could be enhanced. Partial sputter yield ratio was estimated using the oxygen gun and we showed that the graphene layer had to be considerably damaged to reach the optimum conditions.

We concluded that the effect was most probably related to electric properties of graphene—since a high voltage was applied to the sample, graphene could act as a kind of filament, emitting an excess of electrons during the ion bombardment which led to a higher negative ionization probability.

After many experiments, however, we have to conclude that this mechanism is not dominant: changing the voltage applied to the sample has a little impact on the maximum enhancement we can reach in GESIMS experiment. For example, in case of Te dopant in GaAs substrate maximum enhancement is always around 15.7 for 6.5 keV primary ions impact energy even though the voltage applied to the sample is varied in the range of 0.5–5 kV whereas it should be much lower for smaller values if the graphene layer acted as a filament

In this work, however, we intend to show that the graphene layer distorts a standard ion implantation process and blocks the penetration of the incoming ions trapping them at the surface of a sample. The result not only provides an explanation of the GESIMS effect but offer a general information about the reactivity of sp² bonds in graphene as well.

2. Experimental setup

2.1. Sample preparation

CVD graphene layers were grown on $35 \,\mu\mathrm{m}$ thick copper foils using a Black Magic Pro system (Aixtron) with methane as a hydrocarbon precursor. In order to improve the general quality and remove oxides from the surface of the substrate it was annealed prior to the growth process at $960\,^{\circ}\mathrm{C}$ under an Ar and a H_2 gas flow at 20 mbar of pressure. A high-speed electrochemical delamination method [27] was used to transfer graphene on various substrates, namely Si, SiO₂, Ge and GaAs.

2.2. SIMS measurements

In this work, all SIMS measurements were performed employing the CAMECA SC Ultra instrument under ultra-high vacuum, usually of $4\times10^{-10}\,\text{mbar}$. Cs⁺ and O₂⁺ primary

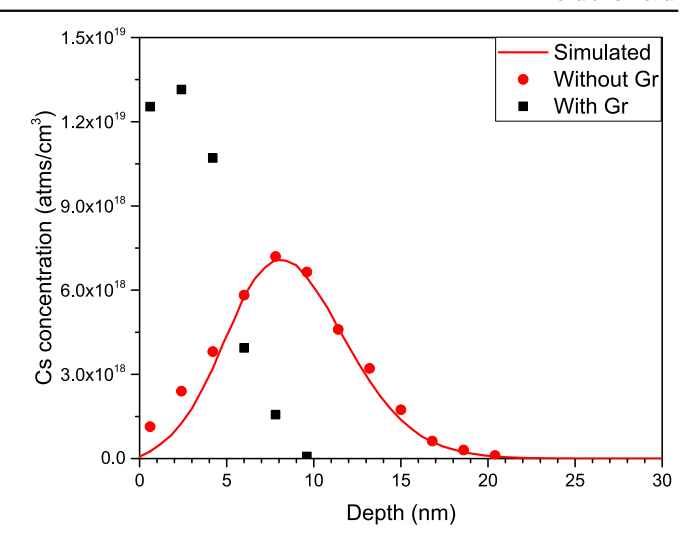


Figure 1. The distribution of cesium atoms in Si substrate with and without graphene. For the sample without graphene a typical ion implantation profile can be observed, whereas for the other sample most cesium atoms are located at the surface. The impact energy and the incident angle were set to 13 keV and 54°, respectively.

beams were used in the experiment. The former was used to detect O^- and $CsAr^+$ ions while the latter for Cs^+ , Si^+ and Ga^+ ions. Beams were rastered over $(250 \times 250) \, \mu m^2$ and the analysis area was limited to $(200 \times 200) \, \mu m^2$. The SIMS accuracy of $< 10^{17} \, atms \, cm^{-3}$ was reached for most experiments. A highly uniform beam was required for this work—the beam on the sample in the SC Ultra tool has a square shape and owning to the 'variable rectangular shape concept' forms a homogeneous spot. The primary beam at the working point in the SC Ultra is formed by two stencils—well-shaped apertures. While the first one is used to choose the most intense and homogeneous part of the Gaussian-shaped ion beam, the second one changes the size of the spot [28]. This innovation provides high sensitivity for all measured elements [29, 30].

2.3. Raman Spectroscopy measurements

Raman spectroscopy measurements were performed in back-scattering geometry, using a Renishaw inVia Raman Microscope, with a $\times 100$ objective and a 532 nm Nd:YAG laser as an excitation source.

2.4. Computer simulations

Simulated ion implantation curves were obtained with transport of ions in matter software using standard ion distribution and the quick calculation of damage option and the total number of ions were set to ten millions.

3. Results and discussion

3.1. Initial experiments

To study the nature of the GESIMS effect we focus on the changes of the surface composition during the GESIMS experiment. During the Cs⁺ ions bombardment a lot of

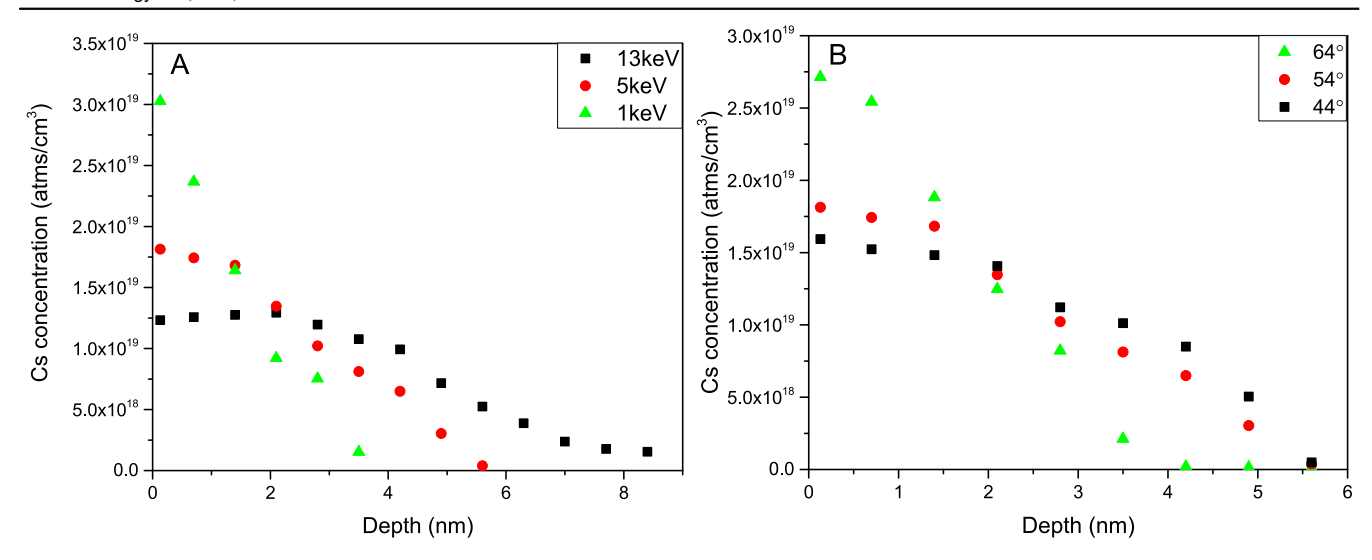


Figure 2. The distribution of cesium atoms for different impact energies for 54° incident angle (Part A) and different incident angles for 5 keV impact energy (Part B). The larger the energy/smaller the angle, the higher the chance for a Cs⁺ ion to overcome the blocking effect of graphene and thus a broader distribution. For lower energies/higher angles cesium atoms are located at the surface of the sample.

carbon atoms from graphene are misplaced and/or sputtered, creating a lot of defects in the graphene layer. These atoms with broken sp² bonds may react with the incoming Cs⁺ ions forming carbon–cesium bonds and thus effectively trapping cesium atoms at the surface, distorting a standard ion implantation process.

We have confirmed this hypothesis for several different substrates: Si, SiO2, Ge and GaAs. For each of them we prepared a sample with and without graphene on the surface and bombarded them with cesium ions keeping the same dose, impact energy and incident angle. Then we made a SIMS depth profile using oxygen gun to measure cesium distribution in the sample. The results are the same for all types of substrates: for samples without graphene a typical ion implantation curve can be observed while for samples with graphene most cesium atoms are located close to the surface and do not penetrate the substrate significantly. Figure 1 presents the result for the Si substrate. A small variation from the simulations, especially at the beginning, was expected because the dose of cesium ions was large (in the range of 10¹⁴ atoms cm⁻²) and thus sputtering of the first few monolayers of Si occurred.

This and the following results are presented for Si substrate because the projected range of cesium ions implantation is the largest and thus it is easier to compare the difference in distribution of implanted atoms. Simulations with and without graphene layer are almost identical (adding an additional layer of 0.345 nm thick carbon does not change the outcome significantly) and thus it will be presented only once.

The impact energy for these experiments was relatively large (13 keV for 54° incident angle), and thus it can be expected that some cesium ions overcome the blocking effect of graphene and penetrate the substrate. For a lower value of the impact energy even more Cs ions are stopped close to the surface, as demonstrated on figure 2(A). The same effect, as expected, can be observed for higher incident angles for a given impact energy—see figure 2(B).

3.2. The mechanism of the GESIMS effect

A high concentration of cesium close to the surface of a sample can finally explain the GESIMS effect as it is widely known that cesium reduces work functions and more secondary electrons are emitted during the experiments leading to an enhanced negative ionization probability [31–34]. In our previous work [22], we showed that the shape of the enhancement profile is universal and depends strongly on a partial sputter yield ratio— Y_{Gr}/Y . Now we can expand this observation further and monitor how the Cs concentration ratio (C_{Gr}/C) where C_{Gr} and C are cesium concentration for a sample with and without graphene, respectively) changes during the GESIMS experiment—see figure 3. Observed GF is a measured value how the GF changes during the sputtering of the graphene layer while the Estimated GF is a product of $Y_{\rm Gr}/Y$ and $C_{\rm Gr}/C$ and a scaling factor (a constant value)—as it can be seen it recreates the shape of the Observed GF. Small discrepancies are expected because the cesium concentration ratio is not the same as the ionization probability ratio and, as previously explained, the partial sputter yield ratio has been estimated with the oxygen gun. Nevertheless, a very similar shape of both plots can be considered as a proof that we have identified the mechanism of the GESIMS enhancements correctly.

3.3. Formation of a highly doped ultra-thin amorphous carbon layer

Having found the mechanism of the enhancement, we focus more on the nature of the newly formed cesium-rich layer at the surface of the sample. The presented empirical results are based on an assumption that broken sp² bonds may react with the incoming Cs⁺ ions. To evaluate this assumption, we have studied the probability to form various ions during the SIMS experiment. In our previous work [22], we showed that no enhancement effect was observed for amorphous carbon and thus, such a sample may serve as a reference. Figure 4 compares

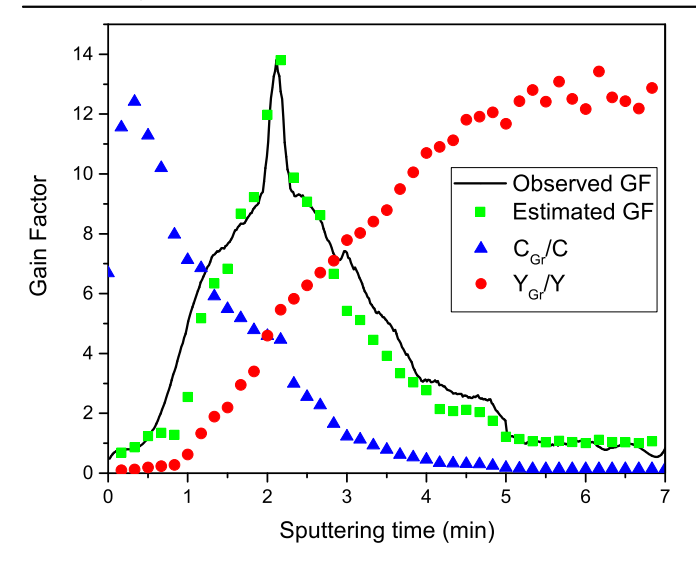


Figure 3. A comparison of the gain change during the graphene enhanced secondary ion mass spectrometry experiment along with the $Y_{\rm Gr}/Y$ and $C_{\rm Gr}/C$ ratios. The product of these ratios (estimated GF) recreates the shape of the observed gain factor profile which serves as proof that the enhancement mechanism was correctly identified. All data points except for the observed gain factor were scaled for a better visibility.

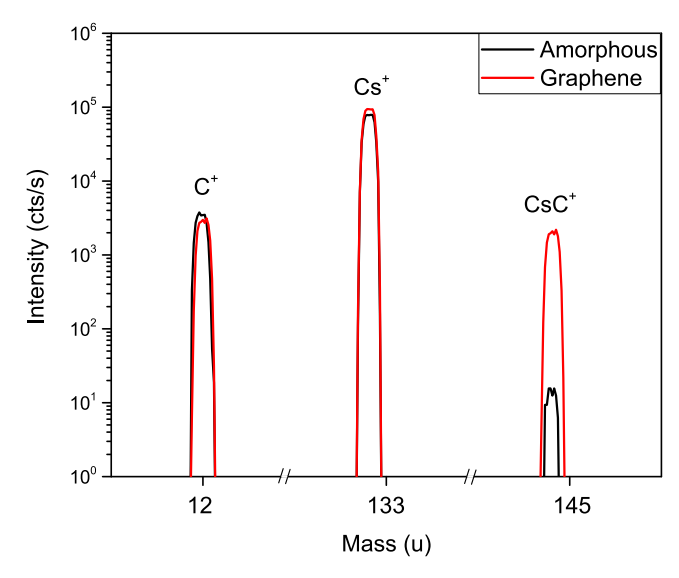


Figure 4. A comparison of a mass spectrum of graphene and amorphous carbon implanted with Cs⁺ ions (13 keV impact energy for 54° incident angle). Both materials have a similar tendency to form C⁺ and Cs⁺ ions, whereas in case of graphene the formation of CCs⁺ ions is more than two orders of magnitude more probable than in the case of amorphous carbon. It can be interpreted that a large quantity of strong bonds between C and Cs atoms are present in the graphene sample.

parts of a mass spectrum of graphene and amorphous carbon implanted with Cs⁺ ions and measured with the oxygen gun. The average intensity of C⁺ and Cs⁺ peaks are very similar for both materials, however the intensity of CsC⁺ peak is more then two orders of magnitude higher for the graphene sample. It means that the probability of sputtering a CCs molecule from the graphene sample is much higher and thus it can be concluded that a much stronger bond between C and Cs atoms exists in

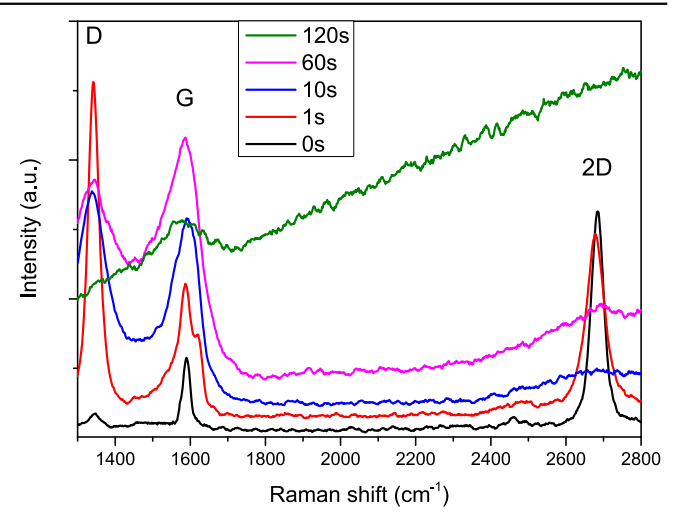


Figure 5. A comparision of Raman spectra for samples bombarded with Cs⁺ ions (13 keV impact energy for 54° incident angle) with different exposure times. The larger the dose, the more defects are created, eventually leading to an amorphization of the graphene layer.

large quantity in this sample. This result is in agreement with our initial assumption that the incoming ions react with broken sp² bonds in the graphene structure.

We have also studied the Raman spectra of graphene before and after bombardment by Cs ions during the SIMS experiment. Four different Cs⁺ ion doses have been used corresponding to times of exposure 1, 10, 60, 120 s with the flux $2 \times 10^{12} \, \mathrm{ions} \, \mathrm{s}^{-1}$. Raman spectra are presented in figure 5. Analyzing the intensities ratios of D and G Raman modes we can estimate the concentration of the defects following the model described in details by Cancado *et al* [6]:

$$\frac{I_{\rm D}}{I_{\rm G}} = C_A \frac{r_A^2 - r_s^2}{r_A^2 - 2r_s^2} [e^{-\pi r_s^2/L_D^2} - e^{-\pi (r_A^2 - r_s^2)/L_D^2}],$$

where $I_{\rm D}$ and $I_{\rm G}$ are the intensities of D and G Raman modes, respectively, C_A is approximately equal to 160EL⁻⁴, where EL is the excitation wavelength, r_A is the distance from the center of the defect, r_s is the lateral radius of the vacancy defect and L_D is the average inter-defect distance.

The efficiency of creation of the defects obtained from Raman data is about 1 defect/Cs ion, as expected from our previous experimental data for such heavy ions as Cs $^+$ [12]. These gives the concentrations of defects about 2 × $10^{12}\,\mathrm{cm}^{-2}$ for 1s bombardment (good graphene structure, distance between defect 7–8 nm) and $2.4\times10^{14}\,\mathrm{cm}^{-2}$ for 120 s where the hexagonal graphene structure is almost completely destroyed (distance between defects less than 1 nm, D mode disappears). It means that during the ion bombardment the graphene layer effectively traps most of the incoming ions close to the surface but becomes more and more amorphous during this process.

3.4. Different ions and number of graphene layers

Eventually we have assumed that broken sp² bonds may react with any incoming ion just as we found it for cesium. We

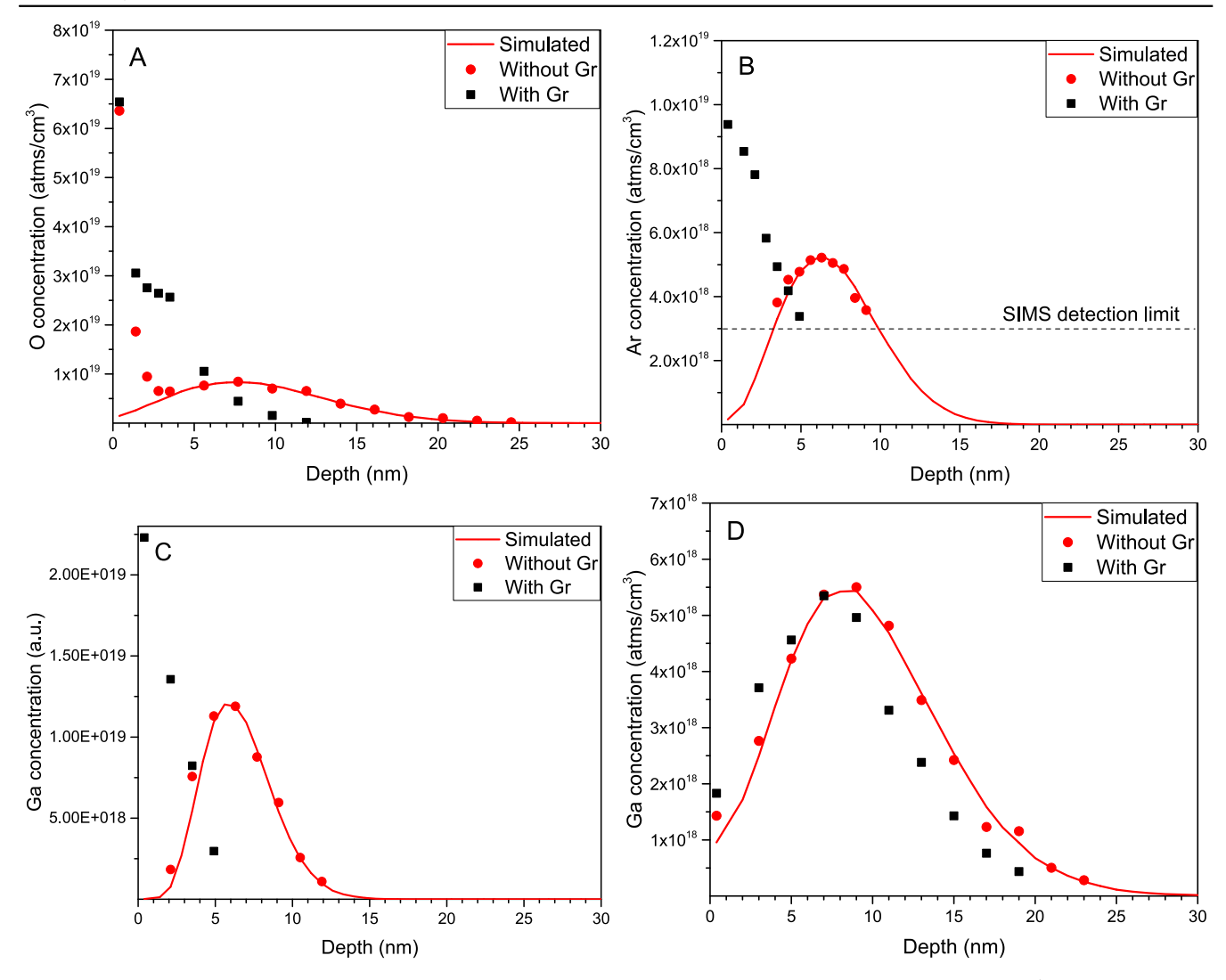


Figure 6. A comparison of depth profiles in Si substrate with and without graphene for various incident ions. Part A: O_2^+ ions, 3 keV impact energy for 36° incident angle. Part B: Ar⁺ ions, 3 keV impact energy for 0° incident angle. Part C: Ga⁺ ions, 3 keV impact energy for 0° incident angle. Part D: Ga⁺ ions, 13 keV impact energy for 54° incident angle.

have tested it for O₂⁺, Ar⁺ and Ga⁺ ions for various impact energies and incident angles and observed the formation of an amorphous layer with most incoming atoms located at the surface of a sample for all of them. These ions, however, are much smaller than Cs⁺, so the impact energy has to be low to see this effect. For higher energies ions perforate the graphene layer and get implanted into the substrate and only a fraction of them get stopped at the surface. In case of Ar⁺ and Ga⁺ ions, we have observed graphene perforation if a normal component of the impact energy was exceeding 5 keV. In case of O_2^+ , 4.5 keV is enough to achieve a similar effect. For very high energies like 13 keV for 54° incident angle (these values were used for initial test with Cs⁺ ions), a very small amount of ions are trapped at the surface. For lower impact energies and higher incident angles most of the ions are trapped very close to the surface, just as it was observed for Cs⁺ ions.

Figure 6 presents a summary of these experiments. For part A, B and C the chosen energy and the incident angle provide the most clear result when comparing samples with

and without graphene. For part D, the impact energy and the incident angle has been set to $13 \, \text{keV}$ and 54° , respectively, in order to match experimental conditions for the initial test with Cs^+ ions, as presented in figure 1. For such a high impact energy gallium ions perforate graphene and are implanted into the substrate. Only a small fraction of atoms are trapped at the surface.

It should also be noted that in the case of O_2^+ (Part A) a strong oxygen concentration at the beginning of the profile comes from organic contamination. Nevertheless both, standard implantation profile (for sample without graphene) and trapping effect (for sample with graphene) are visible. SIMS detection limit is poor for argon and thus only a few data points are available for this element (Part B).

For these implants we have repeated the experiments which revealed a tendency to form a strong bond between carbon and implanted atoms. As it can be seen in figure 7, a similar result was found for all of these implants. The case of gallium is the easiest one as we have used the oxygen gun and positive ion detection mode. C⁺ and Ga⁺ signals have been

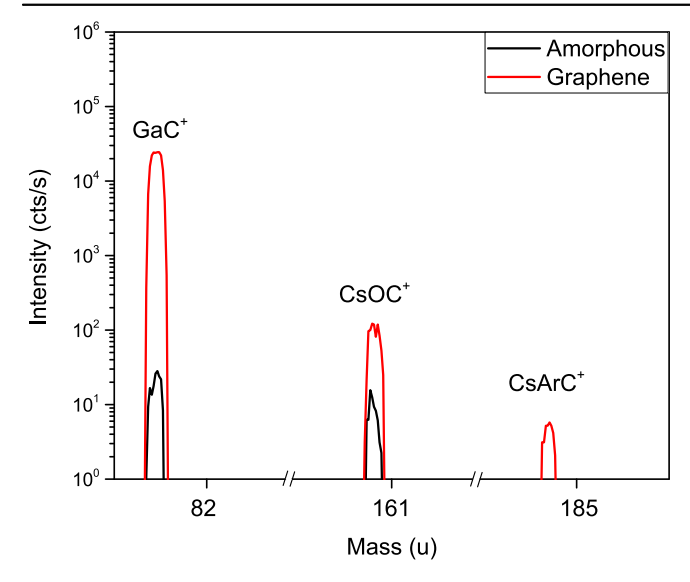


Figure 7. A comparison of a mass spectrum of graphene and amorphous carbon implanted with O_2^+ , Ar^+ and Ga^+ ions. Similarly to the previous result, the formation of cluster ions which contain both, carbon and the implanted species is more probable for the graphene sample. For all samples, signals coming from carbon and implanted atoms are of comparable intensities for both graphene and amourphous carbon samples and thus are not presented in the spectrum to ensure a better visibility of the most important peaks.

found to be of comparable intensity for both, graphene and amorphous carbon samples, whereas the GaC⁺ signal is almost three orders of magnitude higher for the graphene sample. Obviously, in case of oxygen implant it is not possible to use the oxygen gun. Cesium primary beam and negative ion detection mode is not a good choice neither, as we have already acknowledged that graphene may enhance the negative ionization probability. Thus, we have used cesium primary beam and positive ion detection mode. However, in this mode to reach acceptable detection limits cluster ions containing Cs should be measured. Once again, CsC⁺ and CsO⁺ signals are similar for both types of sample, whereas CsOC⁺ signal is more intense for the graphene sample. Argon was measured in the same mode and CsC⁺ and CsAr⁺ signals are similar for both samples. Due to a very poor detection limit of Ar it is not possible to register any signal coming from CsArC⁺ ion for the amorphous carbon sample. In case of graphene, such a peak, albeit of low intensity, is present in the mass spectrum. Even though in some cases it has been more challenging, it is indeed possible to prove that a large quantity of strong bonds between carbon and incoming ions have been formed during the ion bombardment of graphene.

Eventually, we have repeated these experiments for samples covered with several layers of graphene (from two to ten layers) and the results are the same: graphene stops the incoming ions close to the surface and the formation of cluster ions which contain both, carbon and the implanted species is more probable for the graphene sample when compared to amorphous carbon. Naturally, the trapping effect for multilayer graphene is stronger and even high energetic ions cannot perforate several layers of graphene. Using multilayer

graphene, however, has little practical implementation in GESIMS experiments as the surface of the substrate has to partially exposed in order to obtain any meaningful signal for the analysis.

4. Conclusions

We have shown that low energy and high dose ion bombardment of the graphene layer not only results in defects generation in graphene but the ion implantation process is distorted as well. Incoming ions react with broken sp² bonds and thus are stopped close to the surface of the sample. SIMS measurement confirms that instead of a standard ion implantation profile most of the incoming species are trapped and thus the formation of an amorphous layer containing both carbon and implanted atoms is observed. A comparison of graphene and amorphous carbon samples shows that the probability to form carbon and implanted species ions are similar, whereas the formation of a cluster ion containing both carbon and implanted atoms is more probable for the graphene sample. It means that implanted atoms are strongly bonded to carbon which confirms our initial assumption that incoming ions react with broken sp² bonds.

In this way, one can create a very thin layer containing the desired atoms, if no other technique is available. As we have shown, it is especially beneficial in case of the GESIMS technique where a Cs rich layer can be formed *in situ* and used to enhance the intensity of signals allowing it to reach better detection limits.

Acknowledgments

This work was supported by the European Unions Horizon 2020 research and innovation programme under grant agreement No. 696656.

ORCID iDs

Paweł Piotr Michałowski https://orcid.org/0000-0002-3299-4092

References

- [1] Zhang Y, Tang Y Y, Girit C, Hao Z, Martin M C, Zettl A, Crommie M F, Shen Y R and Wang F 2009 Nature 459 820-3
- [2] Yu Y J, Zhao Y, Ryu S, Brus L E, Kim K S and Kim P 2009 Nano Lett. 9 3430–4
- [3] Baitimirova M et al 2016 J. Phys. Chem. C 120 23716–25
- [4] Haque E, Sarkar S, Hassan M, Hossain M S, Minett A I, Dou S X and Gomes V G 2016 J. Power Sources 328 472–81
- [5] Brede J, Slawinska J, Abadia M, Rogero C, Ortega J E, Piquero-Zulaica I, Lobo-Checa J, Arnau A and Cerda J I 2017 2d. Mater. 4 015016

- [6] Cancado L G, Jorio A, Martins Ferreira E H, Stavale F, Achete C A, Capaz R B, Moutinho M V O, Lombardo A, Kulmala T and Ferrari A C 2010 Carbon 48 1592
- [7] Bangert U, Pierce W, Kepaptsoglou D M, Ramasse Q, Zan R, Gass M H, Van den Berg J A, Boothroyd C B, Amani J and Hofsaess H 2013 Nano Lett. 13 4902-7
- [8] Qin X M, Gao T H, Yan W J, Guo X T and Xie Q 2014 J. Mol. Struct. 1065 19–25
- [9] Bai Z, Zhang L and Liu L 2015 J. Phys. Chem. C 119 26793–802
- [10] Bai Z, Zhang L and Liu L 2016 Nanoscale 8 8761-72
- [11] Ahlberg P, Johansson F O L, Zhang Z B, Jansson U, Zhang S L, Lindblad A and Nyberg T 2016 APL Mater. 4 046104
- [12] Herbig C and Michely T 2016 2d. Mater. 3 025032
- [13] Gawlik G, Ciepielewski P, Baranowski J and Jagielski J 2017 Nucl. Instrum. Methods Phys. Res. B 408 228–34
- [14] Lupina G et al 2015 ACS Nano 9 4776
- [15] Luo Z, Lim S, Tian Z, Shang J, Lai L, MacDonald B, Fu C, Shen Z, Yu T and Lin J 2011 J. Mater. Chem. 21 8038
- [16] Dwivedi N, Satyanarayana N, Yeo R, Xu H, Loh Kand Tripathy S and Bhatia C 2015 Sci. Rep. 5 11607
- [17] Xie W, Weng L T, Ng K, Chan C and Chan C M 2015 Carbon 94 740–8
- [18] Li Q, Chou H, Zhong J H, Liu J Y, Dolocan A, Zhang J, Zhou Y, Ruoff R, Chen S and Cai W 2013 Nano Lett. 13 486
- [19] Chou H, Ismach A, Ghosh R, Ruoff R and Dolocan A 2015 Nat. Commun. 6 7482

- [20] Yannopoulos S, Siokou A, Nasikas N, Dracopoulos V, Ravani F and Papatheodorou G 2012 Adv. Funct. Mater. 22 113
- [21] Michałowski P P, Kaszub W, Merkulov A and Strupinski W 2016 Appl. Phys. Lett. 109 011904
- [22] Michałowski P P, Kaszub W, Pasternak I and Strupinski W 2017 Sci. Rep. 7 7479
- [23] Michałowski P P, Pasternak I and Strupinski W 2018 Nanotechnology 29 015702
- [24] Wu K J and Odom R W 1996 Anal. Chem. 68 873–82
- [25] Delcorte A, Medard N and Bertrand P 2002 Anal. Chem. 74 4955–68
- [26] Adriaensen L, Vangaever F and Gijbels R 2004 Anal. Chem. 76 6777–85
- [27] Ciuk T, Pasternak I, Krajewska A, Sobieski J, Caban P, Szmidt J and Strupinski W 2013 J. Phys. Chem. C 117 20833-7
- [28] CAMECA Genneviliers 2005 CAMECA SC-Ultra, User's Guide
- [29] Kouzminov D, Merkulov A, Arevalo E and Grossmann H J 2013 Surf. Interface Anal. 45 345–7
- [30] Merkulov A 2013 Surf. Interface Anal. 45 90-2
- [31] Slodzian G, Lorin J C and Havette A 1980 *J. Phys. Lett.* **41** 555–8
- [32] Taga Y 1986 Secondary Ion Mass Spectrometry SIMS V Proc. 5th Int. Conf. (Washington, DC, 30 September–4 October 1985) (Berlin: Springer) pp 32–7
- [33] Gnaser H and Hutcheon I D 1988 Phys. Rev. B 38 11112-7
- [34] Stevie F A, Kahora P M, Simons D S and Chi P 1988 J. Vac. Sci. Technol. A 6 76

PAPER

Oxygen out-diffusion and compositional changes in zinc oxide during ytterbium ions bombardment

To cite this article: Pawe Piotr Michaowski et al 2018 Nanotechnology 29 425710

View the <u>article online</u> for updates and enhancements.



IOP ebooks™

Bringing you innovative digital publishing with leading voices to create your essential collection of books in STEM research.

Start exploring the collection - download the first chapter of every title for free.

IOP Publishing Nanotechnology

Nanotechnology 29 (2018) 425710 (5pp)

https://doi.org/10.1088/1361-6528/aad881

Oxygen out-diffusion and compositional changes in zinc oxide during ytterbium ions bombardment

1

Paweł Piotr Michałowski¹, Jarosław Gaca¹, Marek Wójcik¹ and Andrzej Turos^{1,2}

E-mail: pawel.michalowski@itme.edu.pl

Received 24 May 2018, revised 30 July 2018 Accepted for publication 7 August 2018 Published 20 August 2018



Abstract

Oxygen release and out-diffusion in zinc oxide crystals during heavy ions bombardment has been suggested by many experimental techniques. In this work we have employed secondary ion mass spectrometry to study ZnO implanted with ytterbium ions. Our measurements confirm formation of an oxygen-depleted layer and oxygen out-diffusion and agglomeration at the surface. Moreover, an average compositional change in a heavily damaged near-surface region can also be monitored. This reproducible measurement procedure with subnanometer depth resolution allows to localize precisely these altered layers at the depth of 14–28 nm (oxygen-depleted layer) and 9 nm (maximum of the amorphized region). Such precise measurements may prove to be valuable for further characterization of ion beam induced defects in wide bandgap compound semiconductors and optimization of optoelectronic devices based on these materials.

Keywords: zinc oxide, ion bombardment, oxygen out-diffusion, secondary ion mass spectrometry, high resolution x-ray diffraction

(Some figures may appear in colour only in the online journal)

1. Introduction

The controlled introduction of rare earth (RE) ions into ZnO is a very promising technique for the production of optoelectronic devices with emission in the visible region. RE doping by ion implantation offers the possibility of controlled doping at required depths and easy lateral pattering. It also enables the doping much above the solid solubility limit which is more difficult using *in situ* doping techniques. However, because of its ballistic nature it does cause considerable structural damage, which must be removed by postimplantation annealing.

In ion implanted compound semiconductors defect agglomeration increases lattice stress eventually causing plastic deformation at sufficiently high fluence. The typical evolution of defects in compound crystals has been discussed in detail for the case of GaN by Turos [1]. Ion implantation in

ZnO has been extensively studied in the last decade by many groups [2–6]. Different analytical techniques have been applied leading to the accumulation of a vast amount of data. Defect accumulation in ion bombarded ZnO is a complicated multistep process. TEM study of Perillat-Merceroz [7] provided important insight into occurring defect transformations, eventually leading to the formation of basal and prismatic dislocation bands. By the complementary use of Rutherford backscattering/channeling (RBS/c) and high resolution x-ray diffraction (HRXRD) Turos et al [8] revealed the driving force for such a transformation. The most important issue is the continuous growth of compressive stress with increasing ion fluence leading to nucleation and growth of dislocation bands. Typical defect depth profile is bimodal composed of a surface peak and a broad bulk peak located at the depth coinciding with implanted atom distribution [9]. However, Kucheyev et al [2] revealed the presence of a third peak,

¹ Institute of Electronic Materials Technology, Wólczyńska 133, 01-919 Warsaw, Poland

² National Centre for Nuclear Research, Soltana 7, 05-400 Otwock, Poland

called intermediate peak (IP) located between of the aforementioned two. High resolution RBS/c study of Azarov *et al* [10] revealed rather peculiar behavior of IP: it starts on the surface and moves to the greater depth with increasing ion fluence. The nature of IP is still under debate. It has been speculated that IP results from the layer of stoichiometric imbalance produced by oxygen release and out-diffusion in the collision cascade. This suggestion is corroborated by XPS [2] and TEM [5] analysis. Our previous study of ZnO bombarded with Ar-ions did not reveal any presence of IP [8].

Secondary ion mass spectrometry (SIMS) is a very precise analytical technique which provides information about the surface and microstructure of a sample [11-17] and allows to determine the elemental composition of a sample [18–25] and therefore SIMS is a very good candidate to monitor any compositional changes that may occur in ZnO during Yb⁺ ions bombardment. However, regions that undergo these changes are very thin and thus an extreme depth resolution is required to describe them properly. In our previous studies we have already established reproducible procedures for depth profiling with subnanometer depth resolution using a low impact energy of 150 eV [26-28] and thus in this work we adapt these procedures to zinc oxide material and study compositional changes that occurs during a Yb⁺ ions implantation. Contrary to other analytical methods, SIMS allows very precise analysis of oxygen release and outdiffusion.

2. Experimental setup

(0001) ZnO single crystals delivered by MaTecK, Germany, were implanted at room temperature with 150 keV Yb⁺ ions to fluences of 5×10^{14} atoms cm⁻², 1×10^{15} atoms cm⁻² and 2×10^{15} atoms cm⁻².

HRXRD measurements were performed using the Rigaku SmartLab diffractometer equipped with a 9 kW rotating Cu anode producing $\text{CuK}_{\alpha 1}$ wavelength = 0.15405 nm. The omega/2theta diffraction profiles were recorded for samples adjusted in such a way that the *c*-axis was parallel to the Φ -axis of the goniometer. This allows to perform radial scans of the (004) reciprocal lattice spot of ZnO single crystals.

SIMS depth profiles were obtained employing the CAMECA SC Ultra instrument under ultra-high vacuum, usually of 4×10^{-10} mbar. Cs⁺ primary beam rastered over $80 \times 80 \,\mu\text{m}^2$ (the analysis area was limited to $20 \times 20 \,\mu\text{m}^2$) and positive ions detection mode was used in the experiments and thus all species were measured as CsX⁺ cluster ions. The intensity of the primary beam was 10 nA and the impact energy was 150 eV. To avoid charging problems the electron gun was used. Mass interferences were verified prior of analysis and mass resolving power $\frac{m}{\Delta m} = 2000$ was used for most experiments. Prior to the analysis samples were annealed at $200 \,^{\circ}\text{C}$ and pressure of 10^{-8} mbar in the airlock of the instrument.

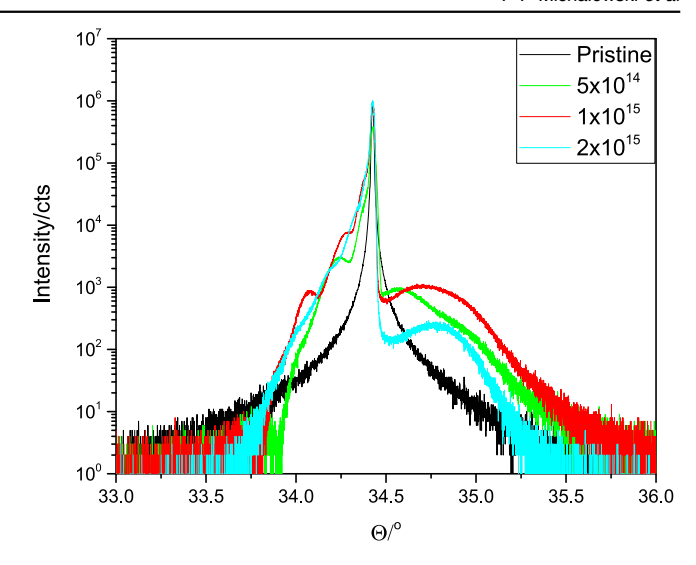


Figure 1. HRXRD profile for ZnO single crystals implanted to different fluences of 150 keV Yb-ions.

3. Results and discussion

HRXRD study of ZnO single crystals implanted with 150 keV Yb-ions provided somewhat peculiar results as shown in figure 1. The main peak in the HRXRD profile located at 34.5° is due to the scattering by the unimplanted part of the crystal. Oscillations on the low-angle side reflect the typical strain buildup in implanted layer [8]. The puzzle is the high-angle part of the profile. It results from the x-ray scattering from the part of the crystal with lower lattice spacing than ZnO. Since the lattice constant of metallic Zn amounts to 0.49468 nm and is significantly lower than that for ZnO, which is 0.52069 nm one can speculate that the observed effect is due to oxygen release from a part of the implanted layer. Furthermore, it can be noted that the position of the peak in the high-angle part of the profile is different for the sample implanted to the lowest fluence whereas similar for other two (lower intensity for the sample implanted to the highest fluence is expected because the quality of the crystal is lower due to bombardment induced defects). It can be therefore assumed that for these two samples a similar amount of oxygen has been released. To prove this assumption the detailed SIMS analysis has been performed.

Figure 2 presents a typical dopant distribution in ZnO implanted with Yb⁺ ions (to fluence 2 × 10¹⁵ atoms cm⁻²). It can be noted that the raw data (CsYb⁺ signal) does not correspond well with the SRIM simulated values. At the depth around 9 nm the result is lower than the simulated whereas between 14–28 nm it is bigger. However, in these regions the intensity of the base Cs⁺ signal also differs significantly from the mean value (no anomalies of the Cs⁺ signal have been observed for the pristine sample). To obtain an actual distribution of Yb atoms in the sample the CsYb⁺ signal should be point-to-point normalized to Cs⁺ signal. This operation (Yb norm. signal) recreates the implantation profile very well. Some minor discrepancies are below 5%.

Even though the implantation profile has been adequately reproduced a question remains what could have caused such a

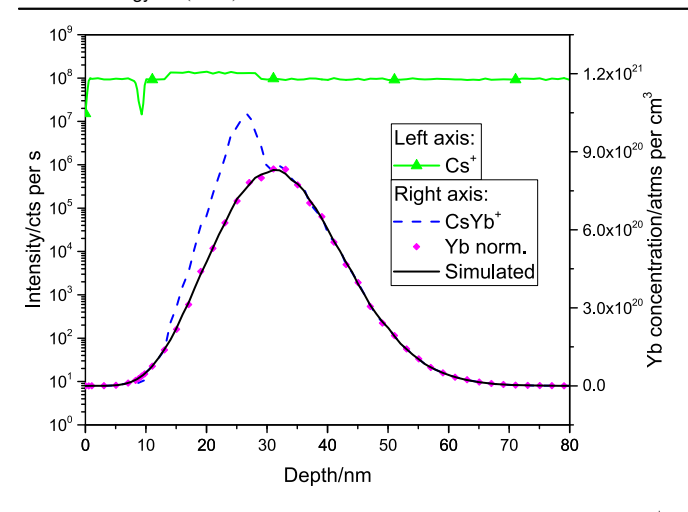


Figure 2. A typical dopant distribution in ZnO implanted with Yb⁺. The raw data (CsYb⁺ signal) does not fit to the simulated distribution of ytterbium. Two regions are problematic: at the depth of about 9 nm and in the range of 14–28 nm. However, cesium retention in these regions are smaller/bigger than the average and thus CsYb⁺ signal is also affected. Point-to-point normalization (Yb norm.) recreates the implantation profile very well.

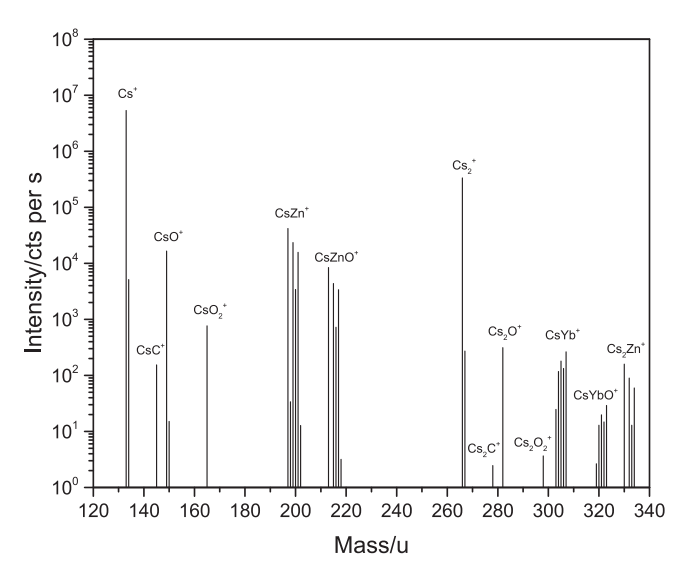


Figure 3. A typical mass spectrum of ZnO implanted with Yb⁺. No significant amount of impurities can be found in the sample, just a minor content of carbon and hydrogen.

significant change of the cesium retention in these two regions. At the beginning it is essential to check whether some other elements have not been implanted along with ytterbium. In theory a large agglomeration of impurities at the specific depth may have change the composition of a material in such a way that cesium accumulation is less/more probable than in the pristine sample. A mass spectrum has been acquired as shown in figure 3, however, no additional impurities have been found in the sample. Just a minor content of carbon (mass 145 and 278u for CsC^+ and Cs_2C^+ ions, respectively) and hydrogen (some of the most intense peaks X has additional peak located at X + 1u which corresponds to XH⁺ ions) but the pristine sample contains them as well. It can also be noted that the intensities of Zn and Yb related

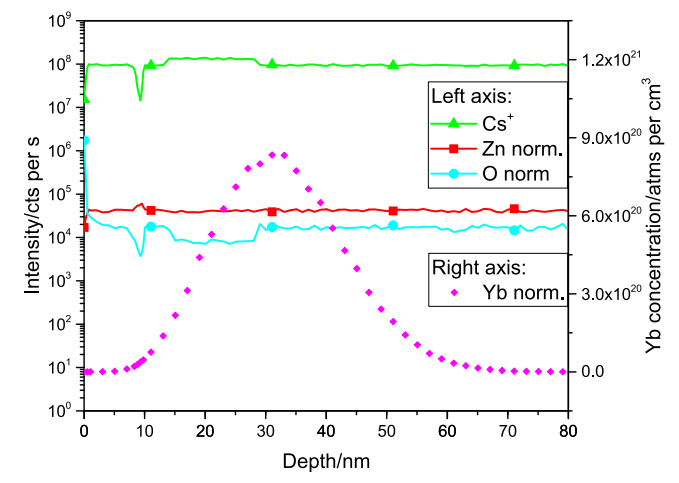


Figure 4. A typical depth profile of ZnO implanted with Yb⁺. SIMS experiments confirm that ion bombardment induces compositional changes in the ZnO sample: at the depth around 9 nm oxygen concentration decreases whereas zinc concentration increases. Oxygen-depleted layer is formed at 14–28 nm depth. For this layer zinc concentration is not affected.

peaks are in agreement with the abundance of various isotopes of these elements. Similar spectra have been acquired for cesium and oxygen primary beams with negative and positive ions detection mode, respectively, as these modes have higher sensitivity for impurities but no contamination of ZnO crystals has been detected.

Having confirmed that no additional impurities are present in the sample we have studied the distribution of zinc and oxygen in the sample. A proper quantification of the obtained results is difficult in SIMS experiment as each element may have a significantly different probability to be sputtered and ionized from a different material, including materials composed of the same elements just with varying concentration (a so called matrix effect). However, the mode which has been used in the experiments (Cs⁺ primary beam, detection of cluster CsX⁺ ions) leads to a significant reduction of the matrix effect [29–33] and thus is particularly desired in this analysis.

Figure 4 presents a typical depth profile of ZnO implanted with Yb $^+$ to the fluence of 2×10^{15} atoms cm $^{-2}$. This time matrix elements, namely Zn and O, have also been measured. All signals have been point-to-point normalized to the base Cs $^+$ signal. A clear change of the composition of the sample can be observed: around 9 nm a very thin layer with lower oxygen and higher zinc content is formed whereas between 14–28 nm oxygen depletion can be observed but without any agglomeration of Zn atoms.

To study these effects in detail we have compared oxygen and zinc signals for three samples implanted to different fluences, namely $5 \times 10^{14}~atoms~cm^{-2}$, $1 \times 10^{15}~atoms~cm^{-2}$ and $2 \times 10^{15}~atoms~cm^{-2}$ and the pristine sample as a reference—see figure 5. This comparison has revealed that three regions of implanted samples are significantly different from the pristine one:

• The surface region—for the pristine sample only a very sharp peak of the oxygen signal can be observed. For

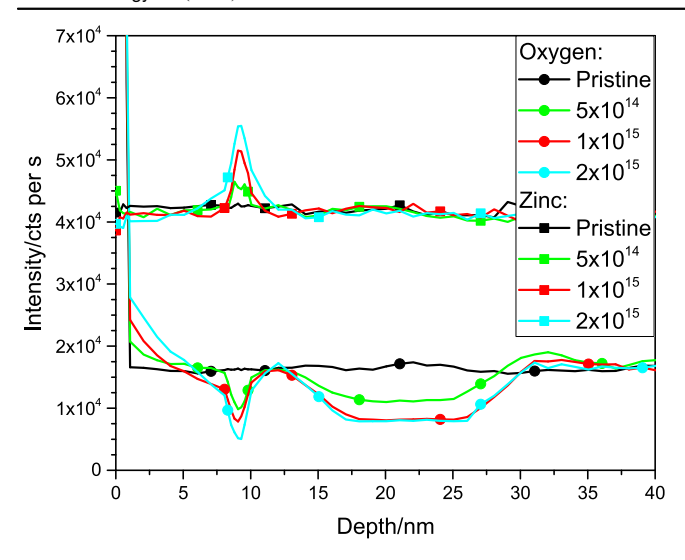


Figure 5. A comparison of samples bombarded to different Yb-ion fluences. Oxygen agglomeration at the surface is revealed when compared to the pristine sample. The change in ZnO composition is scalable with the ion fluence, however in case of the thicker layer (14–28 nm) the effect is saturable. An average of five independent measurements for each sample is presented on the plot.

measurements with such a high depth resolution its width is less than one nanometer and can be attributed to non-steady state conditions at the very beginning of the SIMS experiment and some residual organic contamination that still might be present at the surface of the sample despite long annealing treatment in vacuum conditions. For implanted samples an agglomeration of oxygen and small depletion of zinc close to the surface can be observed and the effect scales with the ion fluence.

- A very thin (1–2 nm) layer around 9 nm—where oxygen depletion and zinc agglomeration is observed. Once again, the effect scales with the ion fluence.
- A thicker layer located between 14–28 nm—where oxygen depletion is observed but zinc concentration is the same as for the pristine sample. Thickness of this layer is independent of the ion fluence and the change of oxygen concentration is smaller for sample implanted with the lowest ion fluence but similar for the other two, which is exactly what has been assumed from HRXRD measurements.

It is essential to emphasize that the total number of counts of oxygen and zinc signals is the same for all samples: oxygen-depleted regions are balanced by the surface agglomeration. It can also be noted that for the first 8 nm the intensity of Zn signal is higher for pristine sample. The difference is enough to balance the thin layer of Zn agglomeration. Similar profiles have been obtained for higher primary ions impact energies (250, 500, 1000 eV) and while the resolution of measurements is lower the total number of counts of oxygen and zinc signals is the same for all samples. It confirms that these depth profiles describe compositional changes of samples and are not caused by measurement artifacts.

SIMS experiment have provided high quality information about compositional changes in zinc oxide during ytterbium ions bombardment. As it has been already reported [2–6, 8] for samples implanted to such a high fluence a lot of defects occurs in the first 10 nm of the sample and about 80% of atoms are misplaced from their original position which means that this layer is effectively amorphous. SIMS experiment reveals an average compositional change in this layer. The case of the thick oxygen-depleted layer is more interesting: XPS [2] and TEM [5] analysis along with the XRXRD measurements (see figure 1) have suggested the presence of such a layer but the results have been ambiguous. SIMS depth profiling allows precise localization of this layer and show oxygen out-diffusion towards the surface.

4. Conclusions

HRXRD measurements have revealed that a region with lower lattice spacing is formed during the Yb-ion implantation of ZnO crystals. However, it is not possible to determine the nature nor the localization of this region from the diffraction technique only and thus we have employed SIMS to resolve these problems. It can be therefore concluded that the high fluence Yb-ion implantation induces the oxygen outdiffusion leading to compositional changes in ZnO crystals. Three non-stoichiometric ZnO regions are formed. At the surface oxygen agglomeration is observed; a very thin layer around 9 nm contains less oxygen and more zinc when compared to the pristine sample; a thicker layer around 14–28 nm is oxygen-depleted but the concentration of zinc is unaffected. The amount of depleted oxygen saturates at the middle fluence. The question whether the observed depleted layer can be assigned to the intermediate damage peak (IP) observed in the RBS/c experiments [2, 4] is still open. The main problem is the continuous shift of IP to the greater depth with increasing ion fluence whereas the position of depleted layer remains constant. It should be noted that SIMS has delivered qualitative information only—a relative change in the composition of the sample can be monitored and affected regions precisely localized. However, it has not been determined how much oxygen has been released and out-diffused during the ion bombardment. In theory such a study is possible but it would require a set of reference samples consisting of ZnO_x crystals with varying x content. The problem is that the x value should be relatively close to 1 for all samples as it is not expected that more than 25% of oxygen out-diffused during the ion bombardment and all samples should be very uniform—otherwise SIMS results would be ambiguous.

Acknowledgments

This work was partially supported by the Polish National Centre for Research and Development (NCBiR) through the project PBS2/A5/34/2013.

ORCID iDs

Paweł Piotr Michałowski https://orcid.org/0000-0002-3299-4092

References

- [1] Turos A 2013 Radiat. Eff. Defects Solids 168 431-41
- [2] Kucheyev S, Williams J, Jagadish C, Zou J, Evans C, Nelson A and Hamza A 2003 Phys. Rev. B 67 094115
- [3] Wendler E, Bilani O, Gartner K, Wesch W, Hayes M, Auret F, Lorenz K and Alves E 2009 Nucl. Instrum. Methods Phys. Res. B 267 2708–11
- [4] Azarov A, Hallen A, Du X, Rauwel P, Kuznetsov A and Svenson B 2014 J. Appl. Phys. 115 073512
- [5] Myers M, Charnvanichborikarn S, Wei C, Luo Z, Aitkaliyeva A, Shao L and Kucheyev S 2012 Acta Mater. 60 6086–90
- [6] Ratajczak R et al 2017 Thin Solid Films 643 24-30
- [7] Perillat-Merceroz G, Gergaud P, Marotel P, Brochen S, Jouneau P and Feuillet G 2011 J. Appl. Phys. 109 023513
- [8] Turos A, Jozwik P, Wojcik M, Gaca J, Ratajczak R and Stonert A 2017 Acta Mater. 134 249–56
- [9] Kucheyev S, Williams J, Jagadish C, Zou J, Li G and Titov A 2001 Phys. Rev. B 64 035202
- [10] Azarov A, Galeckas A, Hallen A, Kuznetsov A, Monakhov E and Svenson B 2015 J. Appl. Phys. 118 125703
- [11] Paul J et al 2009 Microelectron. Eng. 86 949-52
- [12] Lanza M et al 2009 Microelectron. Eng. 86 1921-4

- [13] Michałowski P, Beyer V, Czernohorsky M, Kuecher P, Teichert S, Jaschke G and Moeller W 2009 Phys. Status Solidi c 7 284–7
- [14] Paul J et al 2010 Microelectron. Eng. 87 1629-33
- [15] Bayan S and Chakraborty P 2014 Appl. Surf. Sci. 303 233-40
- [16] Bayan S, Choudhury B, Satpati B, Chakraborty P and Choudhury A 2015 J. Appl. Phys. 117 095304
- [17] Bayan S, Satpati B and Chakraborty P 2015 Surf. Interface Anal. 47 37–44
- [18] Andersen C A and Hinthorne J R 1972 Science 175 853-60
- [19] Benninghoven A 1975 Surf. Sci. 53 596-625
- [20] Benninghoven A, Rudenauer F G and Werner H W 1987 Secondary Ion Mass Spectrometry: Basic Concepts, Instrumental Aspects, Applications and Trends (New York: Wiley)
- [21] Werner H W 1975 Surf. Sci. 47 301-23
- [22] Liebl H 1975 J. Vac. Sci. Technol. A 12 385
- [23] Liebl H 1967 J. Appl. Phys. 38 5277–83
- [24] Michałowski P P, Kaszub W, Pasternak I and Strupinski W 2017 Sci. Rep. 7 7479
- [25] Michałowski P P, Pasternak I and Strupinski W 2018 Nanotechnology 29 015702
- [26] Michałowski P, Kaszub W, Merkulov A and Strupiński W 2016 Appl. Phys. Lett. 109 011904
- [27] Michałowski P, Gutowski P, Pierścińska D, Pierściński K, Bugajski M and Strupiński W 2017 Nanoscale 9 17571–5
- [28] Michałowski P, Złotnik S, Sitek J, Rosiński K and Rudziński M 2018 Phys. Chem. Chem. Phys. 20 13890–5
- [29] Storms H, Brown K and Stein J 1977 Anal. Chem. 49 2023-30
- [30] Gao Y 1988 J. Appl. Phys. 64 3760
- [31] Magee C, Harrington W and Botnick E 1990 *Int. J. Mass Spectrom. Ion Process.* **103** 45–56
- [32] Mikami A 2004 Japan. J. Appl. Phys. 43 2745
- [33] Saha B and Chakraborty P 2013 Energy Procedia 41 80-109

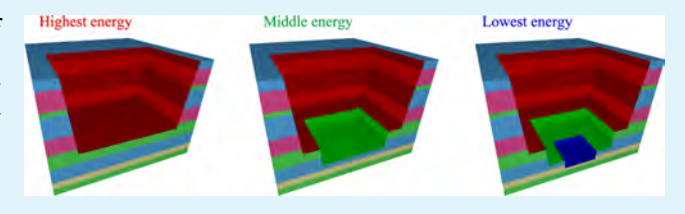


A-Crater-within-a-Crater Approach for Secondary Ion Mass Spectrometry Evaluation of the Quality of Interfaces of Multilayer **Devices**

Paweł Piotr Michałowski,* Wawrzyniec Kaszub, Piotr Knyps, Krzysztof Rosiński, Beata Stańczyk, Krystyna Przyborowska, and Ewa Dumiszewska

Institute of Electronic Materials Technology, Wólczyńska 133, 01-919 Warsaw, Poland

ABSTRACT: Further development and optimization of modern optoelectronic devices requires fast and reliable procedures that may evaluate the quality of interfaces. For thick multilayer devices, mixing effect may significantly prevent proper interpretation of secondary ion mass spectrometry depth profiles especially if a region of interest is located far from the sample surface. In this work, we present



how to overcome this problem with a so-called a-crater-within-a-crater approach. In this notion, a high energetic primary ion beam is used to rapidly remove most of the material forming a large crater. Then, the energy is significantly reduced and a new smaller crater is formed at the bottom of the previous one. Close to the region of interest, the impact energy is decreased to 150 eV and thus an interface can be analyzed with minimal mixing effect and thus its quality can be adequately assessed. Usefulness of this approach is tested on an epitaxial structure of a triple-junction solar cell and reliable information about the structure imperfection has been obtained: p and n dopants in the tunnel junction overlapped, deteriorating the operation of the device.

KEYWORDS: secondary ion mass spectrometry, SIMS, failure analysis, interfaces, solar cells

1. INTRODUCTION

Secondary ion mass spectrometry (SIMS) is a very precise analytical technique for determining the elemental composition of a sample¹⁻⁶ and is especially well known for its excellent detection limits of trace elements⁷⁻¹² and thus is widely used for failure analysis. ¹³⁻¹⁸ However, in most cases, tested structures are relatively simple and thus a proper analysis and interpretation is often straightforward. In the case of several microns thick and complicated structures with layers as thin as tens of nanometers SIMS failure analysis faces a major problem: mixing effect may prevent proper evaluation of interfaces because signals will have long decay length, and thus it will not be possible to assess whether some intermixing or diffusion occurred. The motivation of this work is to present that despite this problem, fast and reliable SIMS failure analysis procedure can be indeed established.

In this work, we test such a procedure on a triple-junction solar cell structure—a device of great importance, as solar energy is considered to be one of the key energy resources with most commonly mentioned benefits like availability, reliability, and cleanliness. Working principle of multijunction solar cells is well discussed in the literature. 19-24 Briefly, they are composed of several different p-n junctions that produce electric current in response to different wavelengths of light. In this way, a broader range of solar spectrum can be absorbed and thus the energy conversion efficiency is increased.

The structure of a multijunction solar cell is complicated, comprising many different elements stacked in layers of varying thickness (from a dozen or so nanometers to several microns),

and thus it is an ideal candidate for testing a high-precision SIMS failure analysis procedure with a-crater-within-a-crater approach.

2. RESULTS AND DISCUSSION

The epitaxial structure of a triple-junction solar cell was processed into a full device, but unfortunately, its efficiency was below 1%. It was not a problem of the processing stage (two different groups created metal contacts and the result was the same) and thus it was concluded that the epitaxial structure itself was defective. SIMS was proposed as a suitable technique to determine which part of the structure is faulty.

Failure analysis of such a complicated structure is challenging and a straight-forward SIMS characterization is not possible. The total thickness of the sample is considerable—around 6 µm—and thus a relatively dense and energetic beam should be used to sputter it effectively. We have obtained a depth profile of the photovoltaic cell using cesium ions with 6.5 keV impact energy—see Figure 1. The proposed measurement procedure has proved to be reproducible and with good resolution—even though the whole structure is about 6 μ m thick, even the thinnest layers (15 nm) can be adequately identified in the profile. The total acquisition time is about one and a half hour, which is reasonable for such a thick and complicated structure. However, the problem with

Received: August 1, 2018 Accepted: October 4, 2018 Published: October 4, 2018



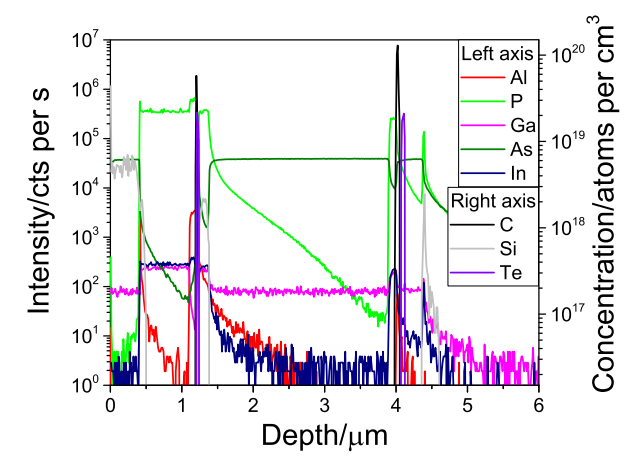


Figure 1. Full-depth profile of the photovoltaic cell. Each layer, even as thin as 15 nm, can be identified and precisely localized.

the mixing effect has remained. It is particularly well visible for P signal in the thickest GaAs layer (~1250-4000 nm). The signal decreases by 2 orders of magnitude faster, but then the decay length is considerable and the average diffusion length is more than 200 nm. The question is whether the observed effect is caused by the SIMS mixing effect (and thus may be treated as a measurement artifact), or is it a real distribution of phosphorous in the sample. If some elements are intermixed into several layers, then the performance of the device may be crippled.

To reduce the mixing effect, the primary ions energy should be significantly decreased, down to 500 eV or even lower. Unfortunately, it is practically impossible to analyze the whole structure in such conditions, as it may take even several dozen hours, which would be very ineffective. Furthermore, the beam stability will be a big issue in this case.

We have therefore developed a so-called a-crater-within-acrater approach (see Figure 2): the first part of the sample has been be removed with a dense and high energetic (16 keV) primary beam. The experiment was stopped around 100 nm from the region of interest and then the energy of primary ions was decreased to 1 keV. A new, smaller crater was formed at the bottom of the first crater. About 20 nm from the region of interest, the energy was further reduced to 150 eV and even a

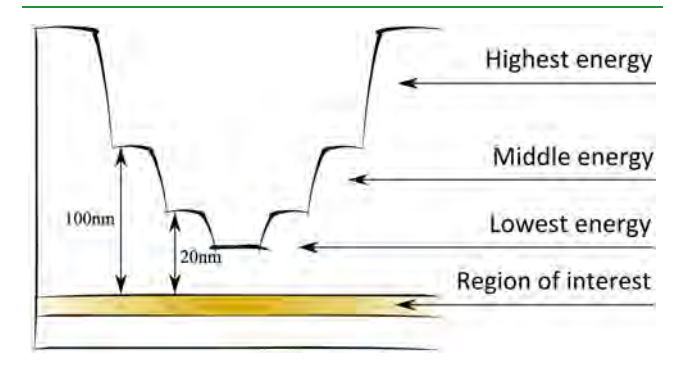


Figure 2. A-crater-within-a-crater approach: high energetic beam is used to rapidly remove the top part of the sample. Closer to the region of interest, the impact energy and the crater size are reduced and the experiment is continued. In the last step, the smallest values of the impact energy and the crater size are used. In this way, the mixing effect is practically negligible and high-quality characterization of each interface is possible.

smaller crater was formed at the bottom of the second one. The choice of these parameters is not random. It has been experimentally noted that sputtering through several different layers with low etching rate increases the roughness of the bottom of the crater. This is not surprising, as sputtering through the interface between two layers may increase the roughness considerably, especially if the bottom layer is sputtered faster than the top layer. As schematically presented in Figure 3, at some point of time, only a small fraction of the bottom layer will be revealed. At this places, the sputtering rate will be much faster and thus roughness will increase. The effect will be amplified at each interface. Sputtering with the most energetic and dense beam minimizes this problem because large chunks of materials are removed rapidly and the whole interface region is removed simultaneously and thus the roughness will not increase. It is therefore essential that most interfaces are sputtered with the most energetic beam. Hence, the proposed values for changing the energy of the beam are 100 and about 20 nm from the region of interest for the highest and middle energies, respectively. They ensure fast characterization and limited crater roughness and are still far enough from the region of interest so that the mixing effect caused by high/middle energetic beams does not influence the final measurement of the interface.

Figure 4 shows the topographic atomic force microscopy (AFM) micrograph of the bottom of the smallest crater after analyzing the last interface. Root-mean-square (RMS) roughness has been found to be 1.2 nm, thus, it can be concluded that a-crater-within-a-crater approach can be applied to evaluate each interface of the device.

The most efficient way to analyze all interfaces is to prepare craters in sequence: at the beginning, the whole structure is sputtered with the most energetic beam so that the etching rate of the most energetic beam can be determined so that the profile can be depth calibrated and in further experiments, the most energetic beam can be stopped precisely at the desired depth. Then, for each interface, a pair of the biggest craters is formed; each crater stopped 100 nm from a particular interface. Then, the beam energy is reduced and the middle craters are formed at the bottom of the bigger ones. The first crater from the pair is used to determine the etching rate of the middle energetic so that the result can be depth calibrated. In the second crater, it is therefore possible to stop the sputtering at the desired depth of 20 nm from the region of interest. Eventually, the energy is decreased down to 150 eV, and each interface is properly characterized because the mixing effect is negligible for the final impact energy.

In this particular case, there are 14 interfaces to analyze, but the first one does not require formation of the biggest crater, as the top layer is 100 nm. The whole procedure requires formation of 27, 28, and 14 biggest, middle, and smallest craters, respectively. The first two steps take less than an hour each, as the etching rate is in the range of 1 μ m/min and 20 nm/min for the most energetic and middle beam, respectively. The last step-the actual analysis-is the most time consuming because the etching rate of the least energetic beam is about 1-5 nm/min (depending on the material), so it takes about 5 h to analyze each interface. Nevertheless, the quality of measurements is superior and can still be considered as very effective, especially considering that a standard profile (Figure 1) takes one and a half hour to acquire.

We have analyzed each and every interface of the solar cell structure and found the quality of most of them to be very **ACS Applied Materials & Interfaces**

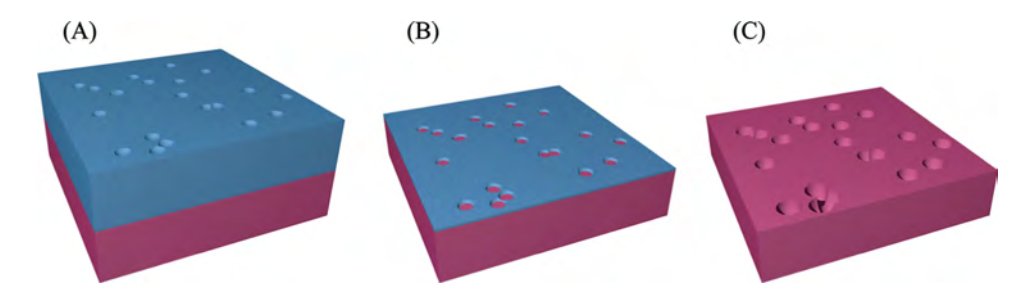


Figure 3. Sputtering with low etching rate may lead to considerable crater roughness, especially if the bottom layer is sputtered faster than the top one. Even small irregularities (A) may lead to a serious problem: at some moment, only a small fraction of layer B will be revealed (B). These points will be sputtered at considerable rate and thus roughness will increase (C). The effect is cumulative at each interface.

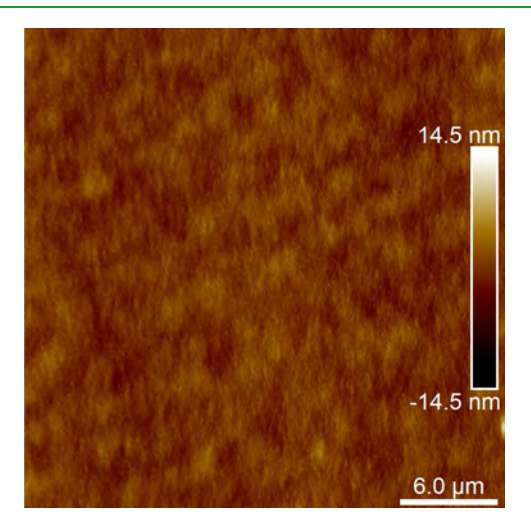


Figure 4. Topographic AFM micrograph of the smallest crater at the depth of about 6 μ m. RMS roughness has been found to be 1.2 nm.

high. For example, we have determined that the average diffusion length of P atoms in the thickest GaAs layer is actually less than 10 nm and not >200 nm, as it can be concluded from Figure 1. It can be therefore concluded that the quality of most interfaces is very high and they could not cause the malfunction of the device.

There is, however, one exception, namely, the tunnel junction between the second and the third junction. A proper interpretation of the results requires focusing on relevant area

and choosing the most important signals—see Figure 5A. The problem with the sub-par operation of the device is immediately clarified: the distribution of p- and n-type dopants (C and Te, respectively) is not as intended—they strongly overlap and thus a charge compensation in that region is expected, which, in turn, deteriorates the operation of the device.

Based on this result, the growth procedure has been slightly corrected—a longer waiting time has been introduced between the introduction of p- and n-type dopants. Additional SIMS measurement performed on a new structure—see Figure 5B confirms that p and n dopants are separated and thus no more problems with the device is expected.

3. CONCLUSIONS

The refined epitaxial structure has been processed into a full device and, indeed, the efficiency has been found to be in the range of 20%. Obviously, it is not close to the record value²⁵ and a lot of optimization of the epitaxial growth process and the processing stage is still required. Nevertheless, a-craterwithin-a-crater approach for the SIMS failure analysis of a full structure has proven to be invaluable to correct the epitaxial process.

The most important achievement of this work is the development of a fully reproducible a-crater-within-a-crater approach for SIMS technique. Two major problems, namely, significant mixing effects and crater roughness have been adequately solved. The proposed procedure, after some minor

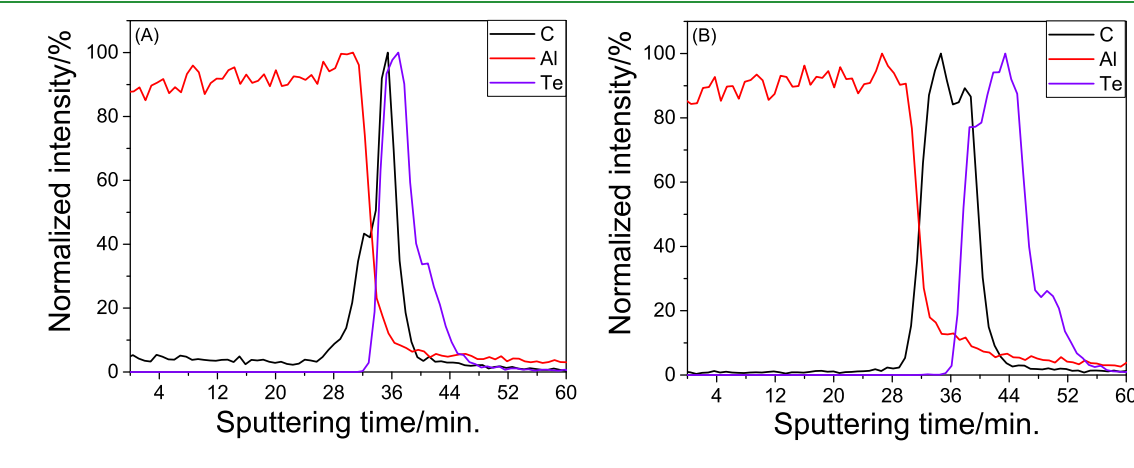


Figure 5. Depth profile focused on the first tunnel junction. (A) The p- and n-type dopants (C and Te, respectively) overlap and thus deteriorate the operation of the device. After the failure analysis, a new device has been fabricated (B). This time p- and n-type dopants are separated and thus an optimal operation of the device is expected. To ensure the best visibility of the problem, signals have been normalized, but calibrated without depth to avoid artificial stretching and compressing of signals, which significantly reduces the clearness of the presented data.

optimization, can be easily applied to other devices not necessarily based on A^{III}-B^V materials. The whole procedure is not very time consuming, it only requires some initial optimization for each device—for some materials, mixing effect may be more/less significant and thus the depth at which the energy of the primary beam is reduced should be readjusted. It offers practically artifact-free characterization of each interface, which is not possible for classical approach, especially if the interface is buried deep under the surface of a thick sample. This approach is therefore effective and resourcesaving option, as the epitaxial growth of a full structure and processing into a device tend to be time-consuming and expensive and thus cannot be performed blindly.

It is important to emphasize that in this work we present how to apply this procedure to analyze every interface of a complicated structure without any additional knowledge about the performance of the device. In this way, the usefulness of acrater-within-a-crater approach can be fully seen. In some cases, it can be applied even if the thickness of each layer is unknown because the mixing effect is negligible for the impact energy as low as 150 eV and thus qualitative information about the stability of the layers may be enough to determine which part of the device is faulty. This is well visible in Figure 5even though profiles are not depth calibrated, it is immediately apparent what is the problem with a faulty device. It can be therefore concluded that the ability to perform a detailed failure analysis on a practically unknown device justifies the total measurement time of a-crater-within-a-crater approach.

In most cases, however, the effectiveness of this approach can be significantly increased if it is complemented with information from other techniques. If it is possible to roughly determine which part of the device is broken, then the procedure can applied to characterize this region only and thus save a lot of time. In the case of multijunction solar cells, there are well-established measurement procedures that allow to analyze each junction separately. 26-29 These measurements may suggest that the problem originates at the tunnel junction between the second and the third junction, and thus a-craterwithin-a-crater approach can be directly applied to characterize this region only. This way, the total measurement time can be reduced to 1 h or even less, and it is the most efficient way to use a-crater-within-a-crater approach.

4. METHODS

4.1. Sample Preparation. InGaP/InGaAs/Ge multijunction solar cells were grown using the MOCVD AIXTRON AIX 200/4 reactor, where the source of elements of group V were phosphine (PH₃) and arsine (AsH₃), whereas the source of elements of group III were trimethylgallium, trimethylaluminum, and trimethylindium. The structure was composed of three p-n junction regions made from A^{III}-B^V compounds: Ge, InGaAs, and InGaP with an energy band gap of 0.65, 1.4, and 1.86 eV respectively. Table 1 presents the structure of the cell along with charge carrier density, thickness of each layer, and

4.2. SIMS Measurements. In this work, all SIMS depth profiles were performed employing the CAMECA SC Ultra instrument under ultrahigh vacuum, usually 4×10^{-10} mbar. A Cs⁺ primary beam with an impact energy of 6.5 keV and intensity of 15 nA was rastered over the area of 150 \times 150 μ m² and the analysis was limited to 50 \times 50 μ m². The choice of primary beam parameters represents a trade-off between the need for sufficient depth resolution favored by low impact energy and beam density and the need for high sputtering rate, which ensures good measurement stability and high dynamic range, improved at higher values of these parameters. Measurements were performed in negative secondary ions detection mode. An offset

Table 1. Structure of a Triple-Junction Solar Cell

material	charge carrier density (cm^{-3})	thickness (nm)	function
InAlP/Si	$p = 7 \times 10^{17}$	100	third junction 1.86 eV
InGaP	$n=2\times 10^{18}$	100	
InGaP	$p=1\times 10^{17}$	450	
InAlP/Zn	$p=2\times 10^{18}$	100	
AlGaAs/C	$p=5\times 10^{19}$	25	tunnel junction
GaAs/Te	$n=2\times 10^{19}$	25	
InGaP/Si	$n=2\times 10^{18}$	100	second junction 1.40 eV
InGaAs/Si	$n=2\times 10^{18}$	350	
InGaAs/Zn	$p = 1 \times 10^{17}$	3500	
InGaP/Zn	$p=2\times 10^{18}$	100	
AlGaAs/C	$p = 5 \times 10^{19}$	15	tunnel junction
GaAs/Te	$n=2\times 10^{19}$	15	
InGaAs	$n=4\times 10^{17}$	500	first junction 0.65 eV
InGaP/Si	$n=9\times10^{18}$	20	
p-type Ge	$p=1-5\times10^{18}$	180 000	

voltage of 15 V was used in majority of experiments to filter out unwanted mass interferences and thus mass resolving power was set at the lowest value of 400.

For a-crater-within-a-crater experiments, the impact energy and intensity of primary beams were set at 16 keV and 80 nA, 1 keV and 12 nA, and 150 eV and 8 nA for the most, middle, and least energetic beams, respectively. The raster size was gradually reduced from 300 \times 300 to 200 \times 200 to 100 \times 100 μ m². The analysis performed with the least energetic beam was limited to $30 \times 30 \ \mu m^2$. Because most of the sample is sputtered with the most energetic beam and the shadowing effect is significantly reduced for such a large raster size, it is possible to analyze devices as thick as $20-30 \mu m$ (depending on the material).

The SC Ultra tool is able to achieve such low impact energies due to the EXtra Low Impact Energy technology, in which case, a primary floating column concept is used. 30 In this notion, contrary to the standard SIMS tools, the primary column has the "floating voltage" instead of the grounded voltage level between the space at any two lenses inside the column and thus primary ions are slowed down at the end of the column, maintaining favorable conditions for ion acceleration and beam stability.

A highly uniform beam was required for this work—the beam on the sample in the SC Ultra tool is square and forms a homogeneous spot owing to the "variable rectangular shape concept". The primary beam at the working point in the SC Ultra is formed by two stencilswell-shaped apertures. Whereas the first one is used to choose the most intense and homogeneous part of the Gaussian-shaped ion beam, the second one changes the size of the spot. This innovation provides high sensitivity for all measured elements.^{30–3}

4.3. Atomic Force Microscopy. Atomic force microscopy (AFM) measurements were performed by a Bruker Dimension FastScan with ScanAsyst using silicon probes (Bruker OTESPA-R3 model) with nominal force constant of 26 N/m and a typical nominal tip radius of 7 nm. The root-mean-square (RMS) roughness of the samples was measured over a scan area of $30 \times 30 \ \mu \text{m}^2$.

AUTHOR INFORMATION

Corresponding Author

*E-mail: pawel.michalowski@itme.edu.pl.

ORCID ®

Paweł Piotr Michałowski: 0000-0002-3299-4092

The authors declare no competing financial interest.

ACKNOWLEDGMENTS

This study was supported by the Applied Research Programme of the National Centre for Research and Development (Project No. PBS3/A5/46/2015).

REFERENCES

- (1) Andersen, C. A.; Hinthorne, J. R. Ion Microprobe Mass Analyzer. Science 1972, 175, 853-860.
- (2) Benninghoven, A. Developments in secondary ion mass spectroscopy and applications to surface studies. *Surf. Sci.* **1975**, *53*, 596–625.
- (3) Benninghoven, A.; Rudenauer, F. G.; Werner, H. W. Secondary Ion Mass Spectrometry: Basic Concepts, Instrumental Aspects, Applications and Trends; John Wiley & Sons: New York, 1987.
- (4) Werner, H. W. The use of secondary ion mass spectrometry in surface analysis. *Surf. Sci.* **1975**, *47*, 301–323.
- (5) Liebl, H. Secondary-ion mass spectrometry and its use in depth profiling. J. Vac. Sci. Technol. 1975, 12, 385.
- (6) Liebl, H. Ion microprobe mass analyzer. J. Appl. Phys. 1967, 38, 5277-5283.
- (7) Wittmaack, K. High-sensitivity depth profiling of arsenic and phosphorus in silicon by means of SIMS. *Appl. Phys. Lett.* **1976**, 29, 552
- (8) Ber, B. Y.; Kudriavtsev, Y. A.; Merkulov, A. V.; Novikov, S. V.; Lacklison, D. E.; Orton, J. W.; Cheng, T. S.; Foxon, C. T. Secondary ion mass spectroscopy investigations of magnesium and carbon doped gallium nitride films grown by molecular beam epitaxy. *Semicond. Sci. Technol.* 1998, 13, 71–74.
- (9) Chiou, C. Y.; Wang, C. C.; Ling, Y. C.; Chiang, C. I. Secondary ion mass spectrometry analysis of In-doped p-type GaN films. *Appl. Surf. Sci.* **2003**, 203–204, 482–485.
- (10) Emziane, M.; Durose, K.; Halliday, D. P.; Bosio, A.; Romeo, N. In situ oxygen incorporation and related issues in CdTe/CdS photovoltaic devices. *J. Appl. Phys.* **2006**, *100*, No. 013513.
- (11) Matsunaga, T.; Yoshikawa, S.; Tsukamoto, K. Secondary ion yields of C, Si, Ge and Cs surface density and concentration in SIMS. *Surf. Sci.* **2002**, *515*, 390–402.
- (12) Gnaser, H. SIMS Detection in the 10¹² atoms cm⁻³ Range. *Surf. Interface Anal.* **1997**, 25, 737–740.
- (13) Banerjee, I.; Tracy, B.; Davies, P.; McDonald, B. In *Use of Advanced Analytical Techniques for VLSI Failure Analysis*, 28th Annual Proceedings on Reliability Physics Symposium, 1990; pp 61–68.
- (14) Gui, D.; Hua, Y. N.; Eng, C. S.; Ooi, S. C.; Goh, A. In *Dynamic SIMS Study on Failure Analysis of Multiple E-Test Failure in Wafer Fabrication*, Proceedings of the 12th International Symposium on the Physical and Failure Analysis of Integrated Circuits, 2005 (IPFA 2005), 2005; pp 205–208.
- (15) Li, Y.; Goyal, D. In 3D Microelectronic Packaging: From Fundamentals to Applications; Li, Y., Goyal, D., Eds.; Springer International Publishing: Cham, 2017; pp 421–459.
- (16) Budri, T.; Sehgal, A.; Arsenault, S.; Klatt, J.; Van Noort, W.; Ruby, S.; Ramdani, J.; Allard, P.; Schnieders, A. D & TOF-SIMS failure analysis of P-buried layer from BiCMOS transistors. *Surf. Interface Anal.* **2011**, *43*, 609–611.
- (17) Yeoh, T. S.; Chaney, J. A.; Leung, M. S.; Ives, N. A.; Feinberg, Z. D.; Ho, J. G.; Wen, J. Three-dimensional failure analysis of high power semiconductor laser diodes operated in vacuum. *J. Appl. Phys.* **2007**, *102*, No. 123104.
- (18) Miyaki, S.; Yoshida, A.; Yamamoto, Y.; Takeuchi, K. Failure analysis of liquid crystal display panel by time-of-flight secondary ion mass spectrometry. *Appl. Surf. Sci.* **2003**, 203–204, 836–841 Secondary ion mass spectrometry SIMS XIII .
- (19) Lee, E. H.; Yeo, J. S.; Lee, J. H.; Cheong, D. I. Temperature-dependent photovoltaic properties of 54-µm-thick InGaP/InGaAs/Ge triple-junction solar cell on flexible substrate. *Curr. Appl. Phys.* **2016**, 16, 1674–1679.
- (20) Lee, J.; Wu, J.; Ryu, J. H.; Liu, Z.; Meitl, M.; Zhang, Y.-W.; Huang, Y.; Rogers, J. A. Stretchable Semiconductor Technologies

- with High Areal Coverages and Strain-Limiting Behavior: Demonstration in High-Efficiency Dual-Junction GaInP/GaAs Photovoltaics. *Small* **2012**, *8*, 1851–1856.
- (21) Gerald, S.; Andreas, W. B. Analysis of temperature coefficients for III-V multi-junction concentrator cells. *Prog. Photovoltaics* **2012**, 22, 515–524.
- (22) Paraskeva, V.; Norton, M.; Hadjipanayi, M.; Pravettoni, M.; Georghiou, G. E. Luminescent emission of multi-junction InGaP/InGaAs/Ge PV cells under high intensity irradiation. *Sol. Energy Mater. Sol. Cells* **2015**, *134*, 175–184.
- (23) Paraskeva, V.; Hadjipanayi, M.; Norton, M.; Pravettoni, M.; Georghiou, G. E. Voltage and light bias dependent quantum efficiency measurements of GalnP/GalnAs/Ge triple junction devices. *Sol. Energy Mater. Sol. Cells* **2013**, *116*, 55–60.
- (24) Shu, G. W.; Lin, J. Y.; Jian, H. T.; Shen, J. L.; Wang, S. C.; Chou, C. L.; Chou, W. C.; Wu, C. H.; Chiu, C. H.; Kuo, H. C. Optical coupling from InGaAs subcell to InGaP subcell in InGaP/InGaAs/Ge multi-junction solar cells. *Opt. Express* **2013**, *21*, A123–A130.
- (25) Green, M. A.; Emery, K.; Hishikawa, Y.; Warta, W.; Dunlop, E. D.; Levi, D. H.; Ho-Baillie, A. W. Y. Solar cell efficiency tables (version 49). *Prog. Photovoltaics* **2017**, *25*, 3–13.
- (26) Heidler, K.; Müller-Bierl, B. In Measurement of Multi-Junction Solar Cells, Tenth E.C. Photovoltaic Solar Energy Conference, Dordrecht, 1991; pp 111–114.
- (27) Kirchartz, T.; Rau, U.; Hermle, M.; Bett, A. W.; Helbig, A.; Werner, J. H. Internal voltages in GaInP/GaInAs/Ge multijunction solar cells determined by electroluminescence measurements. *Appl. Phys. Lett.* **2008**, *92*, No. 123502.
- (28) Siefer, G.; Baur, C.; Bett, A. W. In External Quantum Efficiency Measurements of Germanium Bottom Subcells: Measurement Artifacts and Correction Procedures, 2010 35th IEEE Photovoltaic Specialists Conference, 2010; pp 000704–000707.
- (29) Rutzinger, M.; Nesswetter, H.; Lugli, P.; Bett, A. W.; Zimmermann, C. G. Determination of subcell open circuit voltages and Iph—Voc curves in multijunction solar cells by sequentially pulsed, monochromatic illumination. *Appl. Phys. Lett.* **2016**, *108*, No. 253902.
- (30) CAMECA SC-Ultra, User's Guide; CAMECA: Gennevilliers, 2005.
- (31) Kouzminov, D.; Merkulov, A.; Arevalo, E.; Grossmann, H. J. Application of extra-low impact energy SIMS and data reduction algorithm to USJ profiling. *Surf. Interface Anal.* **2013**, *45*, 345–347.
- (32) Merkulov, A. The secondary ions emission from Si under low-energy Cs bombardment in a presence of oxygen. *Surf. Interface Anal.* **2013**, *45*, 90–92.

PCCP



PAPER



Cite this: Phys. Chem. Chem. Phys., 2019, 21, 8837

Received 31st January 2019, Accepted 3rd April 2019

DOI: 10.1039/c9cp00613c

rsc.li/pccp

Destructive role of oxygen in growth of molybdenum disulfide determined by secondary ion mass spectrometry

Paweł Piotr Michałowski, **D** Piotr Knyps, Paweł Ciepielewski, Piotr Caban, Ewa Dumiszewska and Jacek Baranowski

The application of secondary ion mass spectrometry (SIMS) in investigation and comparison of molybdenum disulfide (MoS₂) films grown on SiO₂, Al₂O₃ and BN substrates is presented. SIMS measurements of the MoS₂/substrate interface reveals oxygen out-diffusion from the substrates containing oxygen and the formation of an amorphous MoOS layer in addition to MoS₂. The total area of MoS₂ domains covering the substrate is directly related to the type of substrate. For SiO₂, small triangular domains of MoS₂ separated by amorphous MoOS material are observed. For Al₂O₃, the sizes of the MoS₂ domains are drastically improved due to the higher stability of sapphire. For a BN substrate, SIMS measurements reveal a uniform MoS₂ coverage over the whole 2-inch wafer. These results show the destructive role of oxygen released from substrates such as SiO₂ or Al₂O₃ during the growth process of MoS₂. The fast and cheap growth process on a non-oxide substrate allows large wafer-scale uniform molybdenum disulfide material to be obtained, which is promising for device fabrication.

1 Introduction

Two-dimensional transition metal dichalcogenides (TMDs), such as MoS₂, MoSe₂, WS₂, WSe₂ *etc.* have received great attention and have emerged as an attractive class of nanomaterials due to their unique structures.^{1–4} Their electronic properties vary with thickness and make them possible candidates for 2D nano-electronic and optoelectronic applications such as solar cells, photodetectors, field effect transistors, and sensors.

Among TMD materials, molybdenum disulfide has been extensively studied. $^{5-13}$ MoS $_2$ is a two-dimensional crystal with strong in-plane covalent bonding and weak out of plane van der Waals interactions. In the monolayer form, MoS $_2$ has a direct energy gap.

The most common way to obtain MoS₂ monolayers is by mechanical exfoliation of bulk material. However, this method is not promising for obtaining large wafer-scale uniform areas of 2D material suitable for device fabrication. There have been several attempts to produce MoS₂ layers *via* chemical vapour deposition (CVD) on insulating substrates. ¹⁴⁻¹⁶ Among CVD methods, the direct growth of 2D materials with the use of thin metal film deposition connected with controlled sulfurization

Institute of Electronic Materials Technology, Wólczyńska 133, 01-919 Warsaw, Poland. E-mail: pawel.michalowski@itme.edu.pl

has become one of the promising ways to synthesize large area 2D materials. ^{17,18} In the present work, we report successful sulfurization of molybdenum film deposited on different substrates such as SiO_2 , Al_2O_3 and BN.

Various experimental techniques such as Raman spectroscopy, transmission electron microscopy, scanning probe microscopy, scanning tunnelling microscopy, atomic force microscopy, X-ray diffraction, and X-ray photoelectron spectroscopy have been used to investigate 2D materials. 19-30 Each of these methods has its own strengths and limitations, and the information they provide is complementary. In this work, secondary ion mass spectrometry (SIMS) is introduced as a suitable method for characterization of MoS₂ layers. The technique is widely used to determine the elemental composition of a sample, 31-36 however in the case of 2D materials sub-nanometer depth resolution is required. In our previous works we have already established reliable procedures to characterize such samples, namely graphene³⁷⁻⁴¹ and boron nitride. 42,43 These results have inspired us to methodically develop our measurement procedures and adjust them for a wide range of 2D materials, including MoS2.

The main motivation of this work is to investigate the role of substrates such as SiO_2 , Al_2O_3 and BN on the quality and size of the grown MoS_2 domains. The SIMS measurements play an essential role in this investigation. It is shown that the choice of substrate has a dramatic influence on the size of the grown MoS_2 domains.

Paper PCCP

2 Experimental

2.1 Sample preparation

Three kinds of substrate were used for the growth of MoS₂ layers:

- 1. Sample A: SiO_2/Si (thermal oxide of 200 nm of SiO_2 on a Si substrate)
 - 2. Sample B: sapphire (Al₂O₃)
 - 3. Sample C: BN grown on Al₂O₃

The sizes of all substrates were 2 inches. Boron nitride was grown at 1050 °C in the self-terminated growth mode, which corresponds to a thickness of 2 nm by the CVD process described by us previously.42 All samples were cleaned in alcohol and DI water. Thin Mo film deposition was done by an e-beam PVD deposition process. Deposition of Mo metal was done under 5×10^{-7} Torr pressure with a rate of 0.05 Å s⁻¹. The evaporated Mo film had from 0.4 to 1.0 nm thickness. The Mo sputtered samples were placed in the high temperature zone of a chemical vapour deposition (CVD) reactor for sulfurization to form MoS₂ film. H₂S was used as the source of sulfur and H₂ as the carrier gas. The furnace was heated up to a temperature of 750 °C and held for 15 minutes. Afterwards, the growth furnace was naturally cooled to 150 $^{\circ}\mathrm{C}$ for evaporation of excess sulfur from the surface of the samples. A monolayer of MoS2 exfoliated from a bulk material and transferred on to SiO2 was used as a reference sample.

2.2 SIMS measurements

In this work, all SIMS measurements were performed employing a CAMECA SC Ultra instrument under ultra-high vacuum (UHV), usually of 4×10^{-10} mbar. The Cs⁺ primary beam was rastered over $80 \times 80 \ \mu\text{m}^2$ (the analysis area was limited to $50 \times 50 \ \mu\text{m}^2$) and positive ions detection mode was used in the experiments and thus all species were measured as CsX⁺ cluster ions. The intensity of the primary beam was 4 nA and the impact energy was 150 eV. For precise oxygen detection measurements, secondary ions detection mode was switched to negative but the rest of the parameters remained the same. To avoid charging problems the electron gun was used. A highly uniform beam was required for this work - the beam on the sample in the SC Ultra tool has a square shape and owning to the "variable rectangular shape concept" forms a homogeneous spot. The primary beam at the working point in the SC Ultra is formed by two stencils - wellshaped apertures. While the first one is used to choose the most intense and homogeneous part of the Gaussian-shaped ion beam, the second one changes the size of the spot. This innovation provides high sensitivity for all measured elements. 44-46

The lateral imaging mode was very important in these experiments. This task was, however, very challenging. The intensity of SIMS signals in the CsX⁺ mode depended predominantly on cesium deposition at the surface of the sample. In the depth profiling mode, ions were collected from a large area and thus the average intensity was very stable. For the imaging mode each point was measured individually and thus some significant fluctuations might decrease the quality of measurements. Indeed, we performed standard imaging measurements

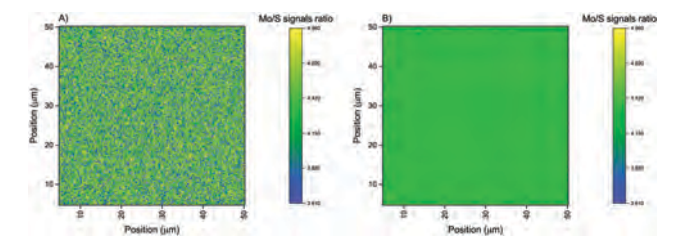


Fig. 1 SIMS distribution maps for the reference sample. (A) The standard imaging procedure showed significant fluctuations; (B) the refined procedure increases the quality of measurements and is suitable for identification of the MoS_2 phase.

on the reference sample – see Fig. 1A – and found that while the average ratio of the Mo and S signals was 4.313 (just like it was in the depth profiling mode), the fluctuations were as high as 30%. It was concluded that a proper identification of the MoS_2 phase would be impossible for this kind of experiment.

To solve this issue, the source of these fluctuations was identified. The primary beam was very uniform and thus a lateral distribution of cesium at the surface of a sample should have inherited this characteristic. The problem was that the magnetic sector SIMS can only measure one ion at a time. In the depth profiling mode, it was not an important issue as the integration time for each signal was about one second, so each cycle was as follows: integration of the S signal, adjusting the electromagnet for different ion mass (during this phase the primary beam was blanked and the sample was not sputtered), integration of the Mo signal and once again adjusting the electromagnet. It meant that there was only one second of sputtering time difference between the integration of the S and Mo signals, and thus it was not expected that the cesium deposition changed significantly within that time. Such a short integration time could be used because ions were collected from a relatively large area. Lateral imaging, however, required much longer integration time to achieve similar sensitivity - in this particular case each signal was integrated for fifteen seconds to form a distribution map. During that time the cesium deposition might have changed a lot and thus the Mo/S ratio fluctuated a lot. To solve this problem we changed the measurement procedure: each signal was sequentially integrated for about 0.3 seconds and fifty cycles were summed to form a distribution map so that the total integration time of each signal was fifteen seconds. Such a procedure is significantly more time consuming as it introduced fifty times more electromagnet adjusting phases (each of them lasted for about two seconds) during which the sample was not sputtered, but it increased the quality of measurements. Indeed, measurements on the reference sample with this refined procedure - see Fig. 1B - showed that the fluctuations were reduced to about 6% which was acceptable for identification of molybdenum disulfide. Based on these results, we assumed that the ratio Mo/S = 4.313 \pm 3% was a marker of the MoS₂ phase.

2.3 Raman spectroscopy measurements

Room temperature Raman measurements were performed with a Renishaw inVia Raman microscope using a 532 nm wavelength

PCCP Paper

obtained from a Nd:YAG laser. The size of a laser spot was about 0.5 μm and the power was below 0.1 mW to avoid the destruction of MoS₂ layers. The laser was focused on the sample using a $\times 100$ objective and numerical aperture NA = 0.9 in a backscattering geometry.

3 Results & discussion

When a new growth procedure is being established and optimized it is usually advisable to test it on a cheap, easily accessible substrate. The growth of MoS₂ films on SiO₂ substrates meets this criterion and provides the additional advantage of possible direct integration of a novel 2D material with the existing silicon-based fabrication lines. However, the influence of the substrate on the growth process is often omitted. The SIMS imaging mode shows that the quality of the obtained film is poor - Fig. 2A and B presents lateral distributions of the Mo/S ratio close to the surface and the substrate, respectively. As was determined on a reference sample, the ratio of Mo/S signals equals 4.313 for MoS₂ material. It can be immediately noted that the proposed measurement procedure is effective as triangles of molybdenum disulfide can be identified, and this material is particularly known for formation of such triangular domains. $^{47-50}$ Experiments performed on several different spots confirmed that for layers closer to the surface the size of the MoS2 domains is bigger.

Outside of these triangular domains, the ratio of Mo/S signals is chaotic but the average value is below 4.313. Some points are close to this value, but it should be noted that the lateral resolution of the experiment is about one micron and thus these points should not be treated as very small domains of MoS_2 . The only valid conclusion is that these regions contain more sulfur than molybdenum disulfide. To gather more information we have checked whether some other elements are present in this region. Our analysis – see Fig. 2C and D – reveals that these regions are oxidized. It should be noted

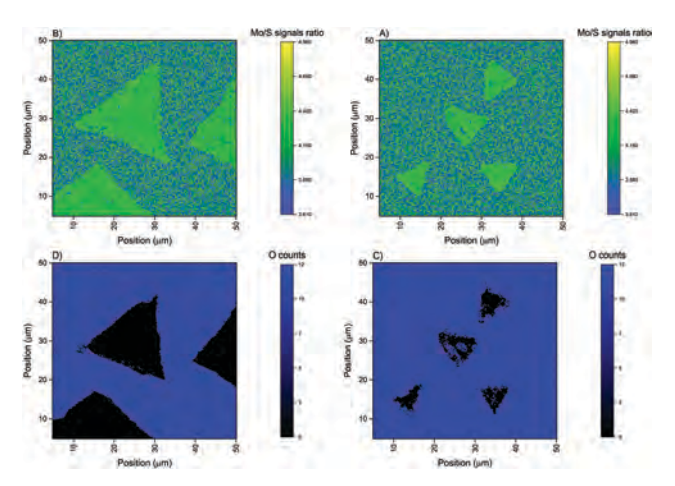


Fig. 2 SIMS distribution maps for sample A. Maps (A) and (B) show the Mo/S distribution close to the surface and the substrate, respectively (counting from the surface) while (C) and (D) show oxygen distribution for the same layers. Bigger domains are formed close to the surface.

that the CsX⁺ mode is not sensitive for oxygen contamination – when some oxygen counts are registered it can be concluded that these regions contain at least several atomic percent of this element. The lateral resolution of this element is worse than in the case of Mo and S, as oxygen ions are lighter and thus have a broader energy distribution and it is more difficult to effectively filter ions coming from neighboring regions. Nevertheless, the quality is good enough to show that no/little oxygen is found in the triangular MoS₂ domains, which is particularly well visible for bigger triangles.

At this point, we were not able to determine what the source of oxygen that has oxidized the sample was. In theory, the film could have oxidized during the time it was transferred from the reactor to the SIMS tool. Thus, we decided to compare the quality of MoS₂ film grown under the same growth conditions but on a different substrate. For that, we chose another easily accessible substrate, namely sapphire, and found that the quality of MoS2 films significantly increased. Fig. 3A shows the distribution of the Mo/S ratio for sample B. There is no difference between the region close to the surface and to the substrate - they look exactly the same. Even though the film is not perfectly uniform, the domains of MoS2 cover more than 90% of the sample. Boundaries between these domains contain more sulfur and are oxidized - see Fig. 3B. However, it should be noted that the width of these boundaries is artificially stretched, since when the primary beam is located partially on a MoS2 region and partially on the boundary the registered Mo/S ratio will be lower, and the whole region will be marked as molybdenum sulfide with unknown stoichiometry. Given that the average width of these boundaries is about 2-2.5 micron and the size of a primary beam is about 0.9 micron, it can be concluded that the actual width of the boundaries is in the range of 200-700 nm.

Another possibility is that residual water present at the surface of the samples is responsible for oxidation of the molybdenum sulfide film. We have prepared several samples grown on both types of substrate but with varying vacuum annealing conditions (temperature, time) but no differences have been found. It is important to emphasize that the only difference between samples A and B is the type of substrate. The growth conditions and transfer time from the reactor to the SIMS tool have been as similar as possible. Therefore, this result reveals that the substrate itself has a crucial impact on the quality of the molybdenum sulfide film. It is not surprising

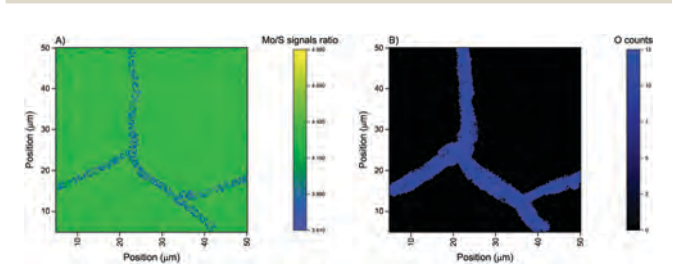


Fig. 3 SIMS distribution maps for sample B. Map (A) shows Mo/S and (B) shows oxygen distribution.

Paper PCCP

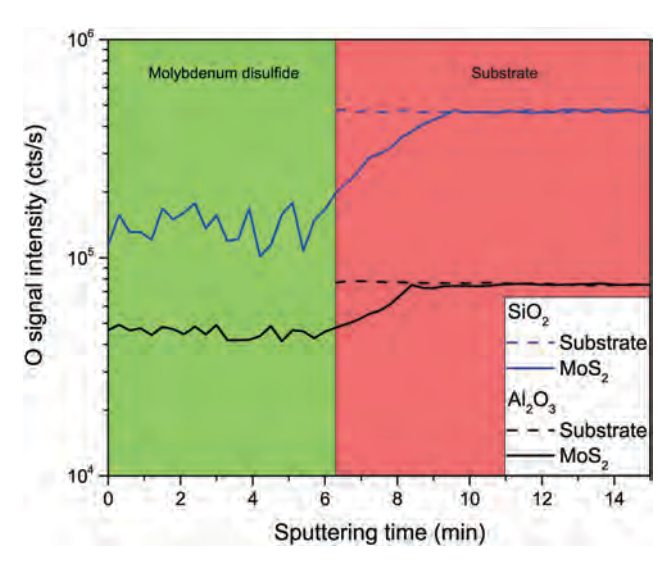


Fig. 4 Oxygen profiles for MoS_2 films grown on SiO_2 and Al_2O_3 . The oxygen profiles are similar for both substrates: a clear oxygen depletion from the interface region inside of the substrates is observed. The location of the interface between MoS_2 and the substrates has been identified at the point where Si or Al signals increase rapidly (these SIMS signals are not presented in the figure to achieve a better visibility).

that the quality of MoS₂ film is much better for sapphire, as this oxide is more stable. The only remaining question is at which point of the growth procedure is oxygen from the substrate incorporated into the molybdenum sulfide film. To answer this question, we have performed additional depth profiling experiments in the negative mode which is more suitable for oxygen detection. For each type of substrate we have compared three different samples: pure substrate, Mo film before the sulfurization process and molybdenum sulfide film. Mo film is not interesting - there is some residual oxygen (in the range of ppm) but no impact of the substrate can be detected. Molybdenum sulfide film is by far more interesting. Fig. 4 presents the results of these experiments - as it has been confirmed before, a lot of oxygen can be detected in these samples but the most important finding is the interface region: it can be clearly seen that, after sputtering the whole molybdenum sulfide film, the oxygen signal is still below the level which is typical for the substrate, which means that several nanometers of the substrate is oxygen depleted. It can be therefore concluded that during the sulfurization process at 750 °C some oxygen is released from the substrate and incorporated into the film, decreasing the overall quality of the sample. We have performed additional experiments where Mo film is heated in a CVD reactor but without introduction of H₂S, and oxygen depletion in the substrate has been also found (similarly to what is presented in Fig. 4). This means that at high temperature Mo atoms have a tendency to absorb oxygen from a substrate.

It was therefore deemed beneficial to repeat these experiments for another substrate which does not contain any oxygen, namely boron nitride. Fig. 5 presents a lateral imaging of the Mo/S ratio for a molybdenum sulfide film grown on a BN/Al $_2$ O $_3$ substrate

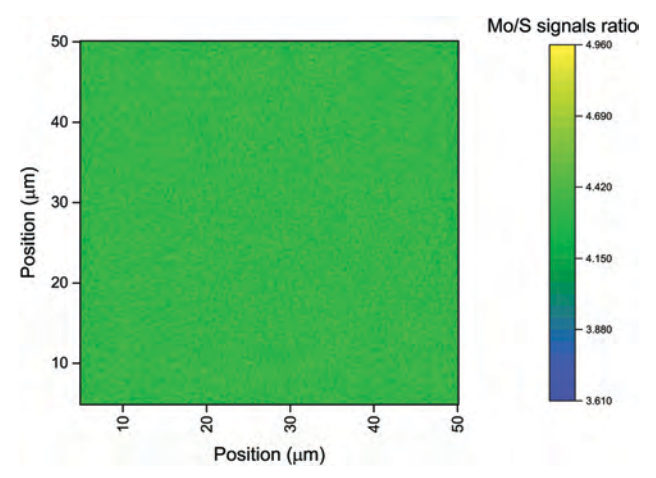


Fig. 5 SIMS distribution map for sample C. The map shows the Mo/S distribution. The sample is very uniform and can be identified as stoichiometric MoS₂

(sample C). It becomes immediately apparent that the film is very uniform and the quality is comparable to the reference sample (see Fig. 1B). Furthermore, no oxygen can be detected in this sample. We have repeated these measurements on 40 spots over the whole 2-inch sample. In all these areas the uniform MoS₂ film has been detected without any exception. Therefore it can be concluded that the whole area of the 2-inch BN/Al₂O₃ substrate is covered by MoS₂ film.

Finally, we confirmed the quality of these samples with Raman spectroscopy, a powerful nondestructive characterization tool which is widely used to characterize 2D materials. Specifically, in the case of ultrathin MoS_2 it is used to identify the number of layers, as it has been demonstrated by Li *et al.*⁵¹ that the frequencies of the Raman E_{2g}^1 and A_{1g} peaks are strongly dependent on the MoS_2 thickness in the range of 1–4 monolayers. The frequency difference of these modes increases from about 19 cm⁻¹ for a monolayer to 25 cm⁻¹ for a bulk material.

Fig. 6 compares the Raman spectra of samples A, B and C. It can be immediately noted that the quality of the sample A is poor – both peaks are broad and of very low intensity (the Raman signal was collected 5 times longer with the same laser power). The frequency difference is about 24 cm⁻¹ which indicates four layers of MoS₂. Sample B is of much better quality.

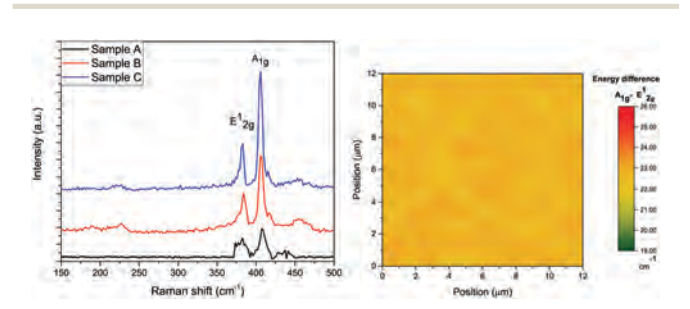


Fig. 6 Raman spectra of samples A, B and C. Changing the substrate from silicon dioxide to sapphire significantly increased the quality of the MoS_2 , but the sample grown on boron nitride was the best one. The Raman map shows the energy difference between the E^1_{2q} and A_{1q} peaks for sample C.

PCCP Paper

Both peaks are sharp and intense. The frequency difference is about $22~{\rm cm^{-1}}$ which indicates two layers of MoS₂. Sample C is confirmed to be of the highest quality, and the frequency difference is about $23~{\rm cm^{-1}}$ which indicates three layers. The map of the frequency difference between E_{2g}^1 and A_{1g} peaks indicates that the average thickness of the MoS₂ film is uniform indeed.

4 Conclusions

The most important result of our investigation is a comparison of the MoS₂ coverage area on different types of substrates. It has been found that the coverage is dramatically influenced by the choice of type of substrate, such as SiO₂, Al₂O₃, or BN. SIMS measurements have revealed the release of oxygen from a substrate such as SiO2 or Al2O3, which has a drastic influence on the size of the grown MoS2 domains. During the sulfurization of Mo, the oxygen out-diffuses from a substrate and reacts with Mo, leading to formation of an amorphous MoOS material of unknown stoichiometry. In the case of growth on a SiO₂ substrate, a relatively large amount of oxygen was released, leading to the formation of a large area of amorphous MoOS covering about 50% of the total area. The presence of MoOS prevented enlargement of the MoS2 triangle domains. On the other hand, sapphire is a much more stable oxide then SiO₂ and, therefore, a smaller amount of oxygen may go into the grown layer, which led to much larger MoS2 domains separated by narrow oxidized boundaries. In this case, about 90% of the whole area was covered by MoS2 domains and only 10% by oxygen-rich amorphous MoOS. Some substrates such as BN do not contain oxygen at all. The BN layer grown on Al₂O₃ separates the sapphire, and apparently blocks oxygen diffusion to the grown MoS₂ film. In this case, 100% of the BN 2-inch wafer was covered by continuous and uniform MoS₂.

Let us emphasize the key role of SIMS measurements in our investigation. SIMS determination of the presence of oxygen at the MoS_2 /substrate interface has disclosed the process of oxygen out-diffusing from oxide substrates. This process is destructive from the perspective of growth of MoS_2 domains, due to the formation of MoOS material which prohibits the formation of a large and continuous MoS_2 film. The BN substrate, being free from oxygen, is the optimal one for obtaining continuous wafer-scale MoS_2 film.

Generalizing, the presented SIMS results show the invalidity of the assumption that a substrate does not react with a grown layer in CVD growth. Such a reaction can go beyond simple contamination and can determine the size of the grown MoS₂ domains. The choice of an oxide-free substrate for the growth of MoS₂, and most likely for other TMDs, is of fundamental importance especially when device fabrication is considered.

Conflicts of interest

There are no conflicts to declare.

Acknowledgements

This work was supported by the European Union's Horizon 2020 research and innovation programme under grant agreement no. 785219.

References

- 1 W. S. Yun, S. W. Han, S. C. Hong, I. G. Kim and J. D. Lee, *Phys. Rev. B: Condens. Matter Mater. Phys.*, 2012, **85**, 033305.
- 2 D. W. Bullett, J. Phys. C: Solid State Phys., 1978, 11, 4501.
- 3 Q. H. Wang, K. Kalantar-Zadeh, A. Kis, J. N. Coleman and M. S. Strano, *Nat. Nanotechnol.*, 2012, 7, 669.
- 4 X. Song, J. Hu and H. Zeng, J. Mater. Chem. C, 2013, 1, 2952.
- 5 S. Ding, D. Zhang, J. S. Chen and X. W. D. Lou, *Nanoscale*, 2012, 4, 95.
- 6 Y. Li, H. Wang, L. Xie, Y. Liang, G. Hong and H. Dai, *J. Am. Chem. Soc.*, 2011, **133**, 7296.
- 7 G. L. Yu, R. Jalil, B. Belle, A. S. Mayorov, P. Blake, F. Schedin, S. V. Morozov, L. A. Ponomarenko, F. Chiappini, S. Wiedmann, U. Zeitler, M. I. Katsnelson, A. K. Geim, K. S. Novoselov and D. C. Elias, *Proc. Natl. Acad. Sci. U. S. A.*, 2013, 110, 3282.
- 8 S. Wi, H. Kim, M. Chen, H. Nam, L. J. Guo, E. Meyhofer and X. Liang, *ACS Nano*, 2014, **8**, 5270.
- 9 A. K. Geim and I. V. Grigorieva, Nature, 2013, 499, 419.
- 10 M. Chhowalla, H. Shin, G. Eda, L.-J. Li, K. Loh and H. Zhang, *Nat. Chem.*, 2013, 5, 263.
- 11 W. Wu, L. Wang, Y. Li, F. Zhang, L. Lin, S. Niu, D. Chenet, X. Zhang, Y. Hao, T. Heinz, J. Hone and Z. Wang, *Nature*, 2014, 514, 470.
- 12 R. Ganatra and Q. Zhang, ACS Nano, 2014, 8, 4074.
- 13 X. Li and H. Zhu, J. Materiomics, 2015, 1, 33.
- 14 X. Wang, H. Feng, Y. Wu and L. Jiao, *J. Am. Chem. Soc.*, 2013, 135, 5304.
- 15 Y.-H. Lee, X.-Q. Zhang, W. Zhang, M.-T. Chang, C.-T. Lin, K.-D. Chang, Y.-C. Yu, J. T.-W. Wang, C.-S. Chang, L.-J. Li and T.-W. Lin, Adv. Mater., 2012, 24, 2320.
- 16 Y. Zhan, Z. Liu, S. Najmaei, P. M. Ajayan and J. Lou, *Small*, 2012, **8**, 966.
- 17 M. H. Heyne, D. Chiappe, J. Meersschaut, T. Nuytten, T. Conard, H. Bender, C. Huyghebaert, I. P. Radu, M. Caymax, J.-F. de Marneffe, E. C. Neyts and S. De Gendt, J. Mater. Chem. C, 2016, 4, 1295.
- 18 A. Stesmans, S. Iacovo, D. Chiappe, I. Radu, C. Huyghebaert, S. De Gendt and V. V. Afanas'ev, *Nanoscale Res. Lett.*, 2017, 12, 283.
- 19 L. Malard, M. Pimenta, G. Dresselhaus and M. Dresselhaus, *Phys. Rep.*, 2009, **473**, 51.
- 20 G. Plechinger, S. Heydrich, J. Eroms, D. Weiss, C. Schüller and T. Korn, Appl. Phys. Lett., 2012, 101, 101906.
- 21 A. Ferrari and D. Basko, Nat. Nanotechnol., 2013, 8, 235.
- 22 X. Ming, Int. J. Spectrosc., 2018, 2018, 4861472.
- 23 M. Paillet, R. Parret, J.-L. Sauvajol and P. Colomban, *J. Raman Spectrosc.*, 2018, **49**, 8.
- 24 S. Zhang, N. Zhang, Y. Zhao, T. Cheng, X. Li, R. Feng, H. Xu, Z. Liu, J. Zhang and L. Tong, Chem. Soc. Rev., 2018, 47, 3217.

Paper PCCP

25 F. Liang, H. Xu, X. Wu, C. Wang, C. Luo and J. Zhang, *Chin. Phys. B*, 2018, 27, 037802.

- 26 C. N. R. Rao and A. Nag, Eur. J. Inorg. Chem., 2015, 4244.
- 27 S. Z. Butler, S. M. Hollen, L. Cao, Y. Cui, J. A. Gupta, H. R. Gutiérrez, T. F. Heinz, S. S. Hong, J. Huang, A. F. Ismach, E. Johnston-Halperin, M. Kuno, V. V. Plashnitsa, R. D. Robinson, R. S. Ruoff, S. Salahuddin, J. Shan, L. Shi, M. G. Spencer, M. Terrones, W. Windl and J. E. Goldberger, ACS Nano, 2013, 7, 2898.
- 28 C. N. R. Rao, H. S. S. Ramakrishna Matte and U. Maitra, *Angew. Chem., Int. Ed.*, 2013, **52**, 13162.
- 29 G. R. Bhimanapati, Z. Lin, V. Meunier, Y. Jung, J. Cha, S. Das, D. Xiao, Y. Son, M. S. Strano, V. R. Cooper, L. Liang, S. G. Louie, E. Ringe, W. Zhou, S. S. Kim, R. R. Naik, B. G. Sumpter, H. Terrones, F. Xia, Y. Wang, J. Zhu, D. Akinwande, N. Alem, J. A. Schuller, R. E. Schaak, M. Terrones and J. A. Robinson, ACS Nano, 2015, 9, 11509.
- 30 C. Rao and U. Maitra, Annu. Rev. Mater. Res., 2015, 45, 29.
- 31 C. A. Andersen and J. R. Hinthorne, Science, 1972, 175, 853.
- 32 A. Benninghoven, Surf. Sci., 1975, 53, 596.
- 33 A. Benninghoven, F. G. Rudenauer and H. W. Werner, Secondary ion mass spectrometry: basic concepts, instrumental aspects, applications and trends, John Wiley & Sons, New York, 1987.
- 34 H. W. Werner, Surf. Sci., 1975, 47, 301.
- 35 H. Liebl, J. Vac. Sci. Technol., A, 1975, 12, 385.
- 36 H. Liebl, J. Appl. Phys., 1967, 38, 5277.
- 37 P. P. Michałowski, W. Kaszub, A. Merkulov and W. Strupinski, *Appl. Phys. Lett.*, 2016, **109**, 011904.
- 38 P. P. Michałowski, W. Kaszub, I. Pasternak and W. Strupinski, *Sci. Rep.*, 2017, 7, 7479.

- 39 P. P. Michałowski, I. Pasternak and W. Strupinski, *Nanotechnology*, 2018, **29**, 015702.
- 40 P. P. Michałowski, I. Pasternak, P. Ciepielewski, F. Guinea and W. Strupinski, *Nanotechnology*, 2018, **29**, 305302.
- 41 J. Grzonka, I. Pasternak, P. P. Michałowski, V. Kolkovsky and W. Strupinski, *Appl. Surf. Sci.*, 2018, 447, 582.
- 42 P. A. Caban, D. Teklinska, P. P. Michalowski, J. Gaca, M. Wojcik, J. Grzonka, P. Ciepielewski, M. Mozdzonek and J. M. Baranowski, J. Cryst. Growth, 2018, 498, 71.
- 43 P. P. Michałowski, P. Caban and J. Baranowski, *J. Anal. At. Spectrom.*, 2019, DOI: 10.1039/C9JA00004F.
- 44 CAMECA, Genneviliers, CAMECA SC-Ultra, User's Guide, 2005.
- 45 D. Kouzminov, A. Merkulov, E. Arevalo and H. J. Grossmann, *Surf. Interface Anal.*, 2013, 45, 345.
- 46 A. Merkulov, Surf. Interface Anal., 2013, 45, 90.
- 47 R. Ionescu, W. Wang, Y. Chai, Z. Mutlu, I. Ruiz, Z. Favors, D. Wickramaratne, M. Neupane, L. Zavala, R. Lake, M. Ozkan and C. S. Ozkan, *IEEE Trans. Nanotechnol.*, 2014, 13, 749.
- 48 Z. Lin, M. T. Thee, A. L. Elías, S. Feng, C. Zhou, K. Fujisawa, N. Perea-López, V. Carozo, H. Terrones and M. Terrones, *APL Mater.*, 2014, 2, 092514.
- 49 W. Chen, J. Zhao, J. Zhang, L. Gu, Z. Yang, X. Li, H. Yu, X. Zhu, R. Yang, D. Shi, X. Lin, J. Guo, X. Bai and G. Zhang, J. Am. Chem. Soc., 2015, 137, 15632.
- 50 Z. Cheng, M. Xia, R. Hu, C. Liang, G. Liang and S. Zhang, *J. Cryst. Growth*, 2017, **480**, 6.
- 51 H. Li, Q. Zhang, C. C. R. Yap, B. K. Tay, T. H. T. Edwin, A. Olivier and D. Baillargeat, *Adv. Funct. Mater.*, 2012, 22, 1385.

PCCP



PAPER



Cite this: Phys. Chem. Chem. Phys., 2019, 21, 20641

Accepted 3rd September 2019

DOI: 10.1039/c9cp03846a

Received 9th July 2019,

rsc.li/pccp

Growth of highly oriented MoS₂ via an intercalation process in the graphene/SiC(0001) system

Paweł Piotr Michałowski, **D** Piotr Knyps, ** Paweł Ciepielewski, **Piotr A. Caban, **Ewa Dumiszewska, **Grzegorz Kowalski, **D Mateusz Tokarczyk ** and Jacek M. Baranowski**

A method of growing highly oriented MoS_2 is presented. First, a Mo film is deposited on a graphene/ SiC(0001) substrate and the subsequent annealing of it at $750\,^{\circ}C$ leads to intercalation of Mo underneath the graphene layer, which is confirmed by secondary ion mass spectrometry (SIMS) measurements. Formation of highly oriented MoS_2 layers is then achieved by sulfurization of the graphene/Mo/SiC system using H_2S gas. X-ray diffraction reveals that the MoS_2 layers are highly oriented and parallel to the underlying SiC substrate surface. Further SIMS experiments reveal that the intercalation process occurs via the atomic step edges of SiC and Mo and S atoms gradually diffuse along SiC atomic terraces leading to the creation of the MoS_2 layer. This observation can be explained by a mechanism of highly oriented growth of MoS_2 : nucleation of the crystalline MoS_2 phase occurs underneath the graphene planes covering the flat parts of SiC steps and Mo and S atoms create crystallization fronts moving along terraces.

1 Introduction

The drive towards miniaturization of electronic devices leads to a tendency to introduce new technologies connected with graphene and other 2D materials such as transition metal dichalcogenides (TMDs). Among TMDs MoS₂ has emerged as the material which has been the most extensively studied.¹⁻⁹ MoS₂ has also been studied for application in future electronic devices.^{10,11}

Early investigations of MoS_2 were based on stacking the layered material using wet or dry transfer methods. ¹² This strategy requires a complicated transfer process which generates defects and leaves residues at the interface, and is not promising for obtaining large wafer scale material suitable for device fabrication.

Chemical Vapour Deposition (CVD) epitaxy seems to be the natural strategy for growth of large area MoS₂ and other TMD layers. There have been several efforts and reports on CVD growth of MoS₂ on insulating substrates. Among epitaxial methods direct growth of MoS₂ with the use of a Mo film deposited on an insulating substrate and controllable sulfurization was also reported. In most cases SiO₂ substrates

have been used on which triangular shape MoS₂ grains have been obtained, for example as shown in recent work.²¹ However, only recently has it been shown that wafer scale large area continuous MoS₂ layers are possible to grow. This was achieved by eliminating substrates containing oxygen. Oxygen released from such substrates plays a disruptive role in the increase of the grain size of MoS₂ during layer growth.²² Therefore, use of substrates without oxygen such as BN/Al₂O₃ epilayers is beneficial. Furthermore, integration of several 2D materials is seen as the best route to fabricate novel heterostructure devices.²³

In this work we have used a new kind of substrate, graphene grown on SiC(0001). Our growth method of MoS2 was connected with evaporation of a Mo film onto graphene covered 6H-SiC(0001) substrates. The process of CVD growth of graphene on SiC(0001) is well known.²⁴ Epitaxial growth of graphene on SiC(0001) is connected with formation of a buffer layer underneath the graphene. 25,26 The buffer layer comprises a carbon layer that is covalently bonded to the underlying SiC substrate and does not show graphitic electronic properties. The electronically inactive reconstructed buffer layer on SiC(0001) may be converted into quasi-free-standing monolayer graphene after hydrogen intercalation.^{27,28} Intercalation of hydrogen decouples the buffer layer from its substrate and forms weakly coupled bilayer graphene. Hydrogen intercalation opened up the possibility to produce quasi-free-standing epitaxial graphene on large SiC wafers. It is known that CVD grown graphene on SiC(0001) after

^a Lukasiewicz Research Network - Institute of Electronic Materials Technology, Wólczyńska 133, 01-919 Warsaw, Poland. E-mail: pawel.michalowski@itme.edu.pl

^b Faculty of Physics, University of Warsaw, Pasteura 5, 02-093 Warsaw, Poland

Paper PCCP

hydrogen intercalation produces p-type layers with higher carrier mobilities than grown on metal substrates.

It is known that the process of intercalation of atoms under a graphene layer is not only limited to hydrogen. It was already reported that intercalation of metals under graphene on SiC(0001) can take place as well. Intercalation of transition metals such as Fe,29 Mn,30 and Co31 was reported. Also, other elements such as Au,³² Ge,³³ and Ca³⁴ were successfully intercalated underneath graphene layers grown on SiC(0001). There is an open question of how atoms of these elements incorporate underneath the graphene layer. Most likely, they go through graphene defects on step edges of the SiC surface. This suggestion is supported by evidence that for ultra-thin Co films magnetic wires are formed at the step edges.³¹ Furthermore, it is believed that graphene on SiC(0001) grows in a contionous fashion over terraces and step edges as well. Indeed TEM measurements show that graphene drapes over steps like a blanket. 35 However, there is evidence of a polycrystalline nature of graphene layers as well. In particular grain boundaries are expected to alter the electronic transport in graphene.³⁶ A theory developed on the formation of grain boundaries in graphene has shown that different orientations of graphene can be joined together into a contionous layer via boundaries with seven-fold and five-fold rings.³⁶ Such seven-fold rings can create openings in the graphene lattice suitable for intercalation of atoms. Therefore, it may be expected that the orientaion of the graphene lattice on terraces and step edges will be different and the presence of seven-fold rings on step edges will create channels for intercalation. Our secondary ion mass spectrometry (SIMS) results directly show that such a mechanism of intercalation in the case of Mo may well happen.

The present work describes formation and investigation of MoS₂ layers grown underneath a graphene layer on 6H-SiC(0001). Successful growth of MoS₂ underneath a graphene layer obtained on 6H-SiC(0001) was created in two steps. The first one was connected with intercalation of a molybdenum layer under the graphene layer. Successful intercalation of Mo was confirmed by SIMS measurements. The next step was sulfurization of the molybdenum and formation of MoS₂ under the graphene layer. Formation of the MoS₂ layer was verified by SIMS, X-ray diffraction and Raman spectroscopy. The SIMS measurements directly showed that the MoS₂ layer was located underneath the graphene layer. The presence and highly oriented character of the grown MoS₂ layer was shown by X-ray diffraction.

2 Experimental

Sample preparation

Graphene layers were grown on 6H-SiC(0001) by Chemical Vapour Deposition (CVD) methods at 1600 $^{\circ}$ C under an argon laminar flow in an Aixtron VP508 hot-wall reactor. Semi-insulating on-axis oriented 6H-SiC (0001) substrates were etched in hydrogen at 1600 $^{\circ}$ C prior to the epitaxy process. The graphene growth was controlled by the Ar pressure, Ar linear flow velocity, and reactor temperature as described previously.²⁴

The intercalation of hydrogen was achieved by the process of changing the gas from argon to hydrogen at a temperature of $1100\,^{\circ}\text{C}$ during the sample cooling.²⁸

Thin Mo film deposition was done by an E-beam PVD deposition process. Deposition of Mo metal was done under a 5×10^{-7} Torr pressure. The evaporated Mo film ranged from 0.4 to 1.0 nm thickness. After this stage, Mo sputtered samples were placed in the high temperature zone of a Chemical Vapour Deposition (CVD) reactor for sulfurization to form the MoS₂ film. H_2S was used as the source of sulphur and H_2 as the carrier gas. The sulfurization process took place at a 750 °C temperature for 15 minutes. After the growth, the furnace was naturally cooled down to 150 °C for evaporation of excess sulphur from the surface of the sample.

Characterization

In this work all SIMS measurements were performed employing a CAMECA SC Ultra instrument under an ultra-high vacuum (UHV), usually of 4×10^{-10} mbar. Sufficient depth resolution was obtained for negative ion detection mode by using a low impact energy of 100 eV for a Cs⁺ primary beam rastered over $250 \times 250 \,\mu\text{m}^2$. The analysis area was limited to $200 \times 200 \,\mu\text{m}^2$. The SC Ultra tool is able to achieve such low impact energies due to the EXLIE (EXtra Low Impact Energy) technology, in the case of which a primary floating column concept is used.³⁷ In this notion, contrary to standard SIMS tools, the primary column has a "floating voltage" instead of a grounded voltage level between the space at any two lenses inside the column and thus primary ions are slowed down at the end of the column, maintaining favourable conditions for ion acceleration and beam stability. The ion beam on the sample in the SC Ultra tool has a square shape and due to the "variable rectangular shape concept" forms a homogeneous spot. The primary beam at a working point in the SC Ultra is formed by two stencils well-shaped apertures. While the first one is used to choose the most intense and homogeneous part of the ion beam, the second one changes the size of the spot. These innovations allow one to use the low impact energy of primary ions with high sensitivity for all elements measured, a high depth resolution (below 1 nm), and a high dynamic range with a low sputter rate. 38,39 All experiments were repeated several times with the primary beam oriented parallel, perpendicular and at several intermediate angles to the steps of SiC but no significant difference was found.

Room temperature Raman measurements were performed on a Renishaw in Via Raman microscope using a 532 nm wavelength obtained from a Nd:YAG laser. The size of the laser spot was about 0.5 μ m and the power was below 0.1 mW to avoid the destruction of MoS₂ layers. The laser was focused on the sample using a $\times 100$ objective and numerical aperture NA = 0.9 in a backscattering geometry.

Investigation of the crystallographic structure and quality of the Gr/MoS₂/SiC heterostructure was done by X-ray diffraction measurements using an X'pert Phillips diffractometer equipped with a standard laboratory X-ray source (Cu K_{α} radiation) and parallel beam Bragg reflection mirror.

PCCP Paper

3 Results and discussion

SIMS is a very precise analytical technique for determining the elemental composition of a sample 40-45 and we have already showed that it can be used to characterize 2D materials like graphene, 46-50 BN thin films 51,52 and MoS2 films. 22 Therefore SIMS was a natural choice to monitor the intercalation process.

As it can be seen in Fig. 1a Mo is evaporated on top of the graphene/SiC(0001) substrate. After annealing (Fig. 1b) a clear indication of intercalation can be seen: a Mo film can be found between the graphene and the SiC(0001) substrate. Subsequent sulfurization of the graphene/Mo/SiC system (Fig. 1c) leads to formation of a molybdenum disulfide film between the graphene and the SiC(0001) substrate. It should be noted that while SIMS provides very accurate and depth-resolved information about the composition of the sample it cannot directly determine the phase nor the quality of the measured layers. Complementary use of the Raman spectroscopy technique can provide this missing information, but without any knowledge of at which depth specific layers are present. Fig. 1d confirms the presence of the MoS₂ layer. There are peaks characteristic of

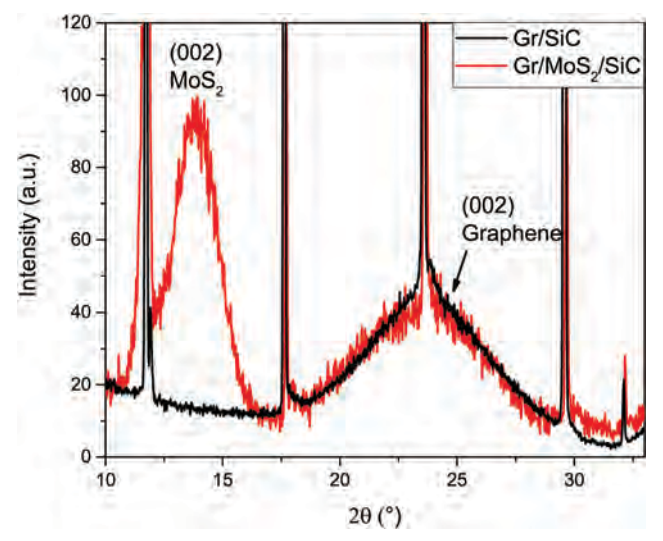


Fig. 2 ω -2 θ scan of the sample Gr/MoS₂/SiC showing well developed MoS₂ and graphene peaks. Same scan for the Gr/SiC substrate showing a similar graphene peak. The position and FWHM of the graphene peak before and after Mo evaporation are almost the same.

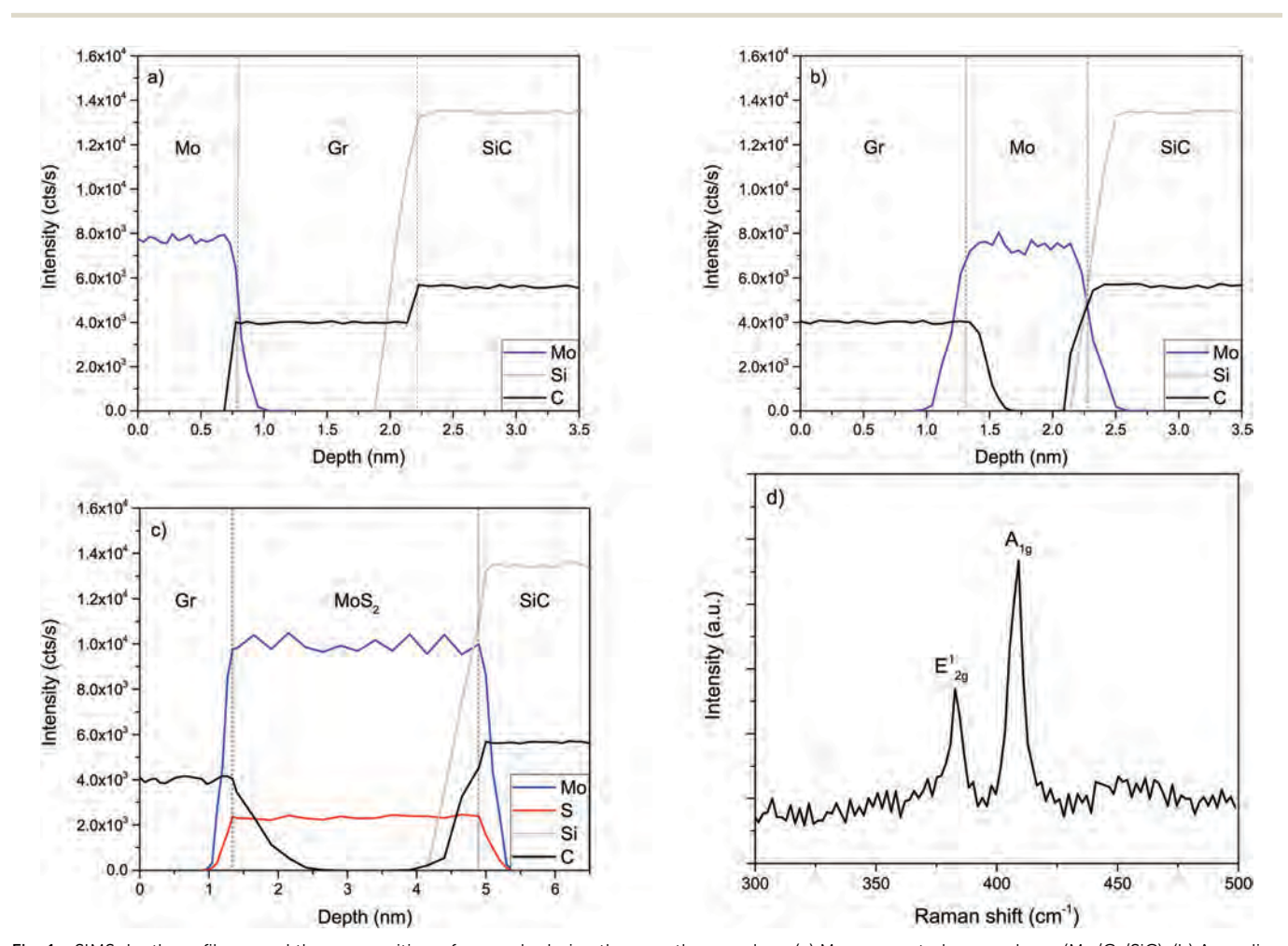


Fig. 1 SIMS depth profiles reveal the composition of a sample during the growth procedure. (a) Mo evaporated on graphene (Mo/Gr/SiC). (b) Annealing leads to intercalation of Mo (Gr/Mo/SiC). (c) Sulfurization leads to formation of MoS₂ under the graphene layer. (d) Raman spectroscopy measurements showing characteristic E_{2q}^1 and A_{1q} peaks connected with MoS₂.

Paper PCCP

the MoS_2 in-plane vibration mode (E_{2g}^1) and out-of-plane vibration mode (A_{1g}) peaks. The wavenumber difference between E_{2g}^1 at 407 cm⁻¹ and the A_{1g} peak at 383 cm⁻¹ is close to 24 cm⁻¹, which indicates that more than three MoS_2 layers are present.

In addition to the MoS_2 peaks the G and 2D graphene peaks have been measured. Their presence proves that the 6H-SiC(0001) surface initially has been covered by a continous layer of graphene. The Raman spectra after graphene growth and after Mo deposition have indicated a negligible D peak. This shows that Mo deposition does not introduce a measurable concentration of defects.

A combination of these two techniques can therefore clearly identify every layer and its location in the sample. Even though the Mo film has been evaporated on top of graphene the formation of MoS_2 occurs between graphene and SiC. To study the crystal structure additional X-ray diffraction (XRD) measurements has been performed on samples without and with evaporated Mo and after formation of MoS_2 (see Fig. 2). A well developed peak around $29 = 14^{\circ}$ (MoS_2 (002)) is clearly seen,

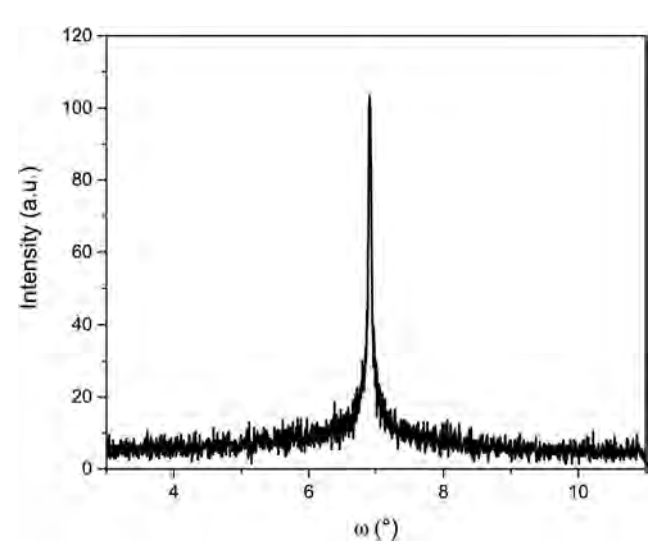


Fig. 3 $\,$ ω -Scan for the Gr/MoS₂/SiC sample indicating a high quality of the MoS₂ layer with FWHM = 0.06°.

which is connected with a well crystallized MoS_2 layer. The estimated thickness of the MoS_2 layer on the basis of the FWHM of the MoS_2 peak = 2.09° indicates a layer thickness around 3.8 nm (5–6 layers) with interlayer distance d_{002} = 0.615 nm. In addition, a broad peak close to $29 = 23^{\circ}$ ((002) graphene) was observed that indicates standard hydrogenated graphene. This graphene peak with FWHM = 6.44° indicates a thickness of around 1.3 nm (3–4 layers). The position and FWHM of the graphene peaks are the same for both samples, which demonstrates that formation of MoS_2 underneath graphene does not influence the graphene layer in a noticeable way for the XRD experiment.

Additionally a ω -scan, with a fixed position of the X-ray detector on the 2 scale, was also employed to verify the quality and positioning of the MoS₂ layer with respect to the underlying SiC substrate (Fig. 3). The ω -scan of the Gr/MoS₂/SiC sample was taken for a fixed position of the X-ray detector corresponding to the 002 reflection from a MoS₂ type structure. The sample itself was set to reflect from crystallographic planes which are parallel to the sample substrate SiC. The measurements were taken along the direction of main atomic surface steps of the 6H-SiC. The FWHM of the ω scan peak is at the level of 0.06°, which means that the MoS₂ layer is highly oriented. We can conclude that the quality of the MoS₂ layer, confirmed by the FWHM of the peak for the ω -scan and very good alignment with the SiC surface, is at very high level.

This is indeed very surprising as growing MoS_2 layers with the same technique on other substrates has led to a polycrystal-line material. To provide a suitable explanation it is necessary to study the intercalation process in more detail. For practical reasons a sample with Mo evaporated on top of the graphene layer has been chosen for this purpose. The SIMS tool allows one to heat a sample holder in the load lock and thus it is possible to study the evolution of the intercalation process as a function of the thermal treatment without removing the sample from a vacuum environment. The sample has been annealed at 250 $^{\circ}$ C for fifteen minutes and transferred to the measurement chamber for the SIMS analysis. This time, however, a lateral imaging mode has been used to study the spatial distribution of Mo at the surface

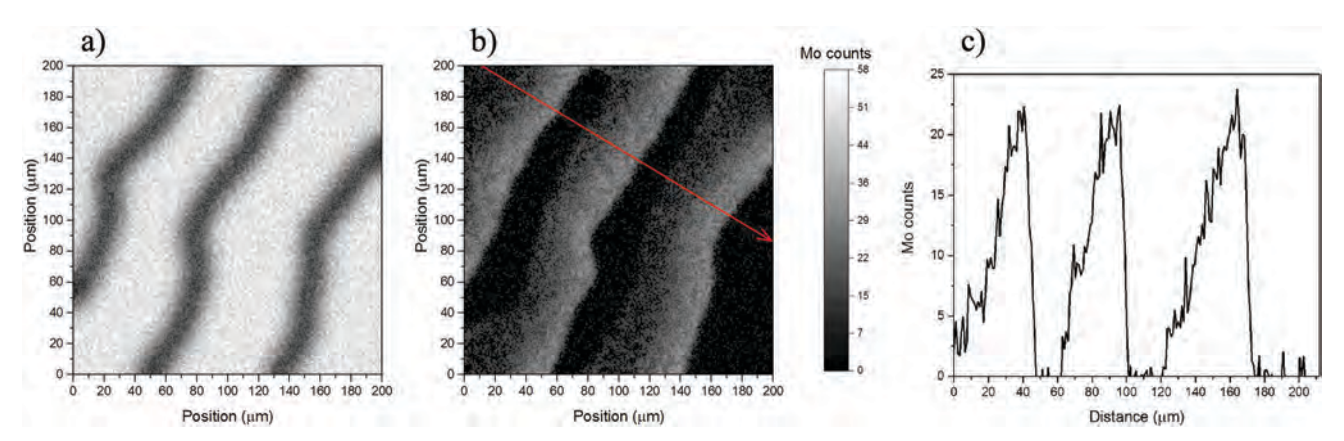


Fig. 4 SIMS lateral imaging showing the distribution of Mo after evaporation and annealing at 250 °C. (a) At the surface of the sample. (b) Close to the SiC substrate. (c) A profile of Mo counts along the red arrow presented in part (b).

PCCP Paper

of the sample and close to the SiC substrate (Fig. 4(a) and (b), respectively). It becomes immediately apparent that the intercalation process indeed occurs at the step edges of the sample: both molybdenum depletion at the surface and agglomeration close to the substrate are directly related to the position of the edges.

There is, however, a significant difference between these two pictures: while the depletion of Mo at the surface is symmetrical the agglomeration and diffusion close to the SiC substrate are clearly occurring only in one direction. It is even better visible in Fig. 4(c), which presents a profile of Mo counts along the red arrow presented in part (b). These results further indicate that the intercalation most likely occurs at the bottom of the step edges of the SiC substrate and thus molybdenum atoms diffuse along the terrace but cannot overcome the barrier of the step. However, it is possible that some textured structure is formed when molybdeum disulfide layers from different terraces are merged together forming a highly oriented but not necessary continuous layer.

4 Conclusions

Complementary use of several advanced characterization techniques has revealed that an attempt to grow MoS₂ layers on a Gr/SiC substrate results in formation of a Gr/MoS₂/SiC heterostructure. The process of intercalation of molybdenum and sulphur atoms under the graphene layer clearly leads to creation of well organized MoS₂ layers. We suggest that the intercalation process takes place almost exclusively *via* the step edges of the SiC substrate and is most probably related to graphene defects present there. Mo and S atoms can only diffuse along the SiC terrace underneath the more perfect graphene plane and thus a single crystallization front ensures high quality and orientation of the MoS₂ layer. These findings may be of the utmost importance for fabrication of future electronic devices based on 2D material heterostructures.

Conflicts of interest

There are no conflicts to declare.

Acknowledgements

This work was supported by the European Union's Horizon 2020 research and innovation programme under grant agreement No 785219. The first author was supported by the National Science Centre within the SONATA14 2018/31/D/ST5/00399 project.

References

- 1 S. Ding, D. Zhang, J. S. Chen and X. W. D. Lou, *Nanoscale*, 2012, 4, 95–98.
- 2 Y. Li, H. Wang, L. Xie, Y. Liang, G. Hong and H. Dai, J. Am. Chem. Soc., 2011, 133, 7296–7299.
- 3 S. Wi, H. Kim, M. Chen, H. Nam, L. J. Guo, E. Meyhofer and X. Liang, *ACS Nano*, 2014, **8**, 5270–5281.
- 4 A. K. Geim and I. V. Grigorieva, *Nature*, 2013, 499, 419-425.

5 M. Chhowalla, H. S. Shin, G. Eda, L.-J. Li, K. P. Loh and H. Zhang, *Nat. Chem.*, 2013, 5, 263–275.

- 6 W. Wu, L. Wang, Y. Li, F. Zhang, L. Lin, S. Niu, D. Chenet, X. Zhang, Y. Hao, T. F. Heinz, J. Hone and Z. L. Wang, *Nature*, 2014, 514, 470-474.
- 7 R. Ganatra and Q. Zhang, ACS Nano, 2014, 8, 4074-4099.
- 8 X. Li and H. Zhu, J. Materiomics, 2015, 1, 33-44.
- 9 Z. Wang, H.-H. Wu, Q. Li, F. Besenbacher, X. C. Zeng and M. Dong, *Nanoscale*, 2018, 10, 18178–18185.
- 10 S. Kim, A. Konar, W.-S. Hwang, J. H. Lee, J. Lee, J. Yang, C. Jung, H. Kim, J.-B. Yoo, J.-Y. Choi, Y. W. Jin, S. Y. Lee, D. Jena, W. Choi and K. Kim, *Nat. Commun.*, 2012, 3, 1011.
- 11 P. Zhang, Z. Wang, L. Liu, L. H. Klausen, Y. Wang, J. Mi and M. Dong, *Appl. Mater. Today*, 2019, **14**, 151–158.
- 12 A. Gurarslan, Y. Yu, L. Su, Y. Yu, F. Suarez, S. Yao, Y. Zhu, M. Ozturk, Y. Zhang and L. Cao, ACS Nano, 2014, 8, 11522–11528.
- 13 X. Wang, H. Feng, Y. Wu and L. Jiao, *J. Am. Chem. Soc.*, 2013, **135**, 5304–5307.
- 14 Y.-H. Lee, X.-Q. Zhang, W. Zhang, M.-T. Chang, C.-T. Lin, K.-D. Chang, Y.-C. Yu, J. T.-W. Wang, C.-S. Chang, L.-J. Li and T.-W. Lin, *Adv. Mater.*, 2012, 24, 2320–2325.
- 15 Y. Zhan, Z. Liu, S. Najmaei, P. M. Ajayan and J. Lou, *Small*, 2012, 8, 966–971.
- 16 Y. Lee, J. Lee, H. Bark, I.-K. Oh, G. H. Ryu, Z. Lee, H. Kim, J. H. Cho, J.-H. Ahn and C. Lee, *Nanoscale*, 2014, 6, 2821–2826.
- 17 Y. Shi, W. Zhou, A.-Y. Lu, W. Fang, Y.-H. Lee, A. L. Hsu, S. M. Kim, K. K. Kim, H. Y. Yang, L.-J. Li, J.-C. Idrobo and J. Kong, *Nano Lett.*, 2012, 12, 2784–2791.
- 18 J. Jeon, S. K. Jang, S. M. Jeon, G. Yoo, Y. H. Jang, J.-H. Park and S. Lee, *Nanoscale*, 2015, 7, 1688–1695.
- 19 M. H. Heyne, D. Chiappe, J. Meersschaut, T. Nuytten, T. Conard, H. Bender, C. Huyghebaert, I. P. Radu, M. Caymax, J.-F. de Marneffe, E. C. Neyts and S. De Gendt, J. Mater. Chem. C, 2016, 4, 1295–1304.
- 20 A. Stesmans, S. Iacovo, D. Chiappe, I. Radu, C. Huyghebaert, S. De Gendt and V. V. Afanas'ev, *Nanoscale Res. Lett.*, 2017, 12, 283.
- 21 K. Lee, R. Gatensby, N. McEvoy, T. Hallam and G. S. Duesberg, *Adv. Mater.*, 2013, **25**, 6699–6702.
- 22 P. P. Michałowski, P. Knyps, P. Ciepielewski, P. Caban, E. Dumiszewska and J. Baranowski, *Phys. Chem. Chem. Phys.*, 2019, **21**, 8837–8842.
- 23 K. S. Novoselov, A. Mishchenko, A. Carvalho and A. H. Castro Neto, *Science*, 2016, 353, aac9439.
- 24 W. Strupinski, K. Grodecki, A. Wysmolek, R. Stepniewski, T. Szkopek, P. E. Gaskell, A. Grüneis, D. Haberer, R. Bozek, J. Krupka and J. M. Baranowski, *Nano Lett.*, 2011, 11, 1786–1791.
- 25 K. V. Emtsev, F. Speck, T. Seyller, L. Ley and J. D. Riley, *Phys. Rev. B: Condens. Matter Mater. Phys.*, 2008, 77, 155303.
- 26 W. Strupinski, K. Grodecki, P. Caban, P. Ciepielewski, I. Jozwik-Biala and J. Baranowski, *Carbon*, 2015, 81, 63–72.
- 27 C. Riedl, C. Coletti, T. Iwasaki, A. A. Zakharov and U. Starke, *Phys. Rev. Lett.*, 2009, **103**, 246804.

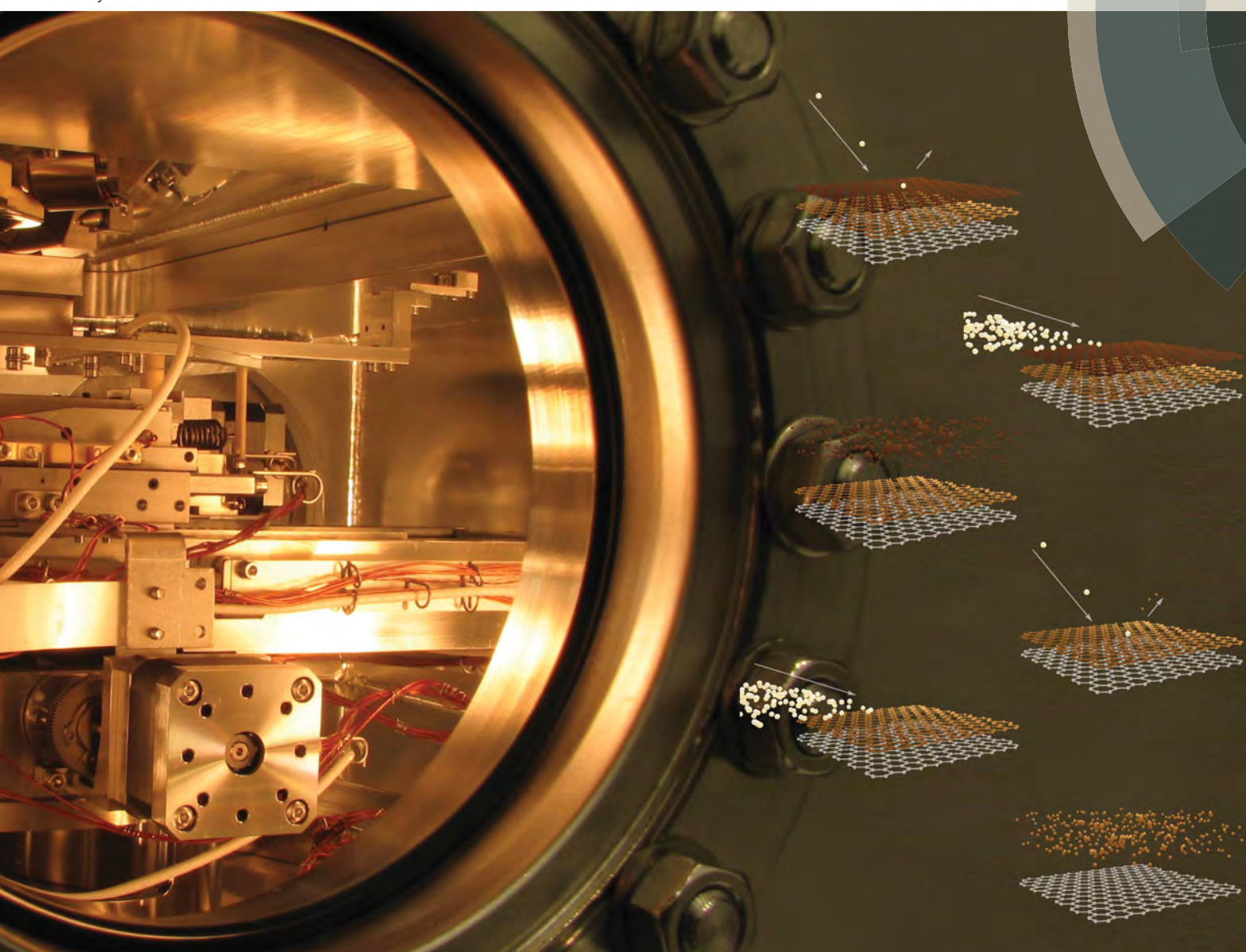
Paper PCCP

- 28 M. Tokarczyk, G. Kowalski, M. Możdżonek, J. Borysiuk, R. Stepniewski, W. Strupiński, P. Ciepielewski and J. M. Baranowski, *Appl. Phys. Lett.*, 2013, **103**, 241915.
- 29 T. Gao, Y. Gao, C. Chang, Y. Chen, M. Liu, S. Xie, K. He, X. Ma, Y. Zhang and Z. Liu, *ACS Nano*, 2012, **6**, 6562–6568.
- 30 M. U. Kahaly, T. Kaloni and U. Schwingenschlögl, *Chem. Phys. Lett.*, 2013, 578, 81-84.
- 31 R. Honig, P. Roese, K. Shamout, U. Berges and C. Westphal, *Nanotechnology*, 2019, **30**, 025702.
- 32 I. Gierz, T. Suzuki, R. T. Weitz, D. S. Lee, B. Krauss, C. Riedl, U. Starke, H. Höchst, J. H. Smet, C. R. Ast and K. Kern, *Phys. Rev. B: Condens. Matter Mater. Phys.*, 2010, **81**, 235408.
- 33 K. V. Emtsev, A. A. Zakharov, C. Coletti, S. Forti and U. Starke, Phys. Rev. B: Condens. Matter Mater. Phys., 2011, 84, 125423.
- 34 K. Li, X. Feng, W. Zhang, Y. Ou, L. Chen, K. He, L.-L. Wang, L. Guo, G. Liu, Q.-K. Xue and X. Ma, *Appl. Phys. Lett.*, 2013, 103, 062601.
- 35 W. Norimatsu and M. Kusunoki, Phys. E, 2010, 42, 691-694.
- 36 O. V. Yazyev and S. G. Louie, Nat. Mater., 2010, 9, 806.
- 37 CAMECA, Genneviliers, CAMECA SC-Ultra, User's Guide, 2005.
- 38 D. Kouzminov, A. Merkulov, E. Arevalo and H. J. Grossmann, *Surf. Interface Anal.*, 2013, **45**, 345–347.
- 39 A. Merkulov, Surf. Interface Anal., 2013, 45, 90-92.

- 40 C. A. Andersen and J. R. Hinthorne, Science, 1972, 175, 853-860.
- 41 A. Benninghoven, Surf. Sci., 1975, 53, 596-625.
- 42 A. Benninghoven, F. G. Rudenauer and H. W. Werner, Secondary ion mass spectrometry: basic concepts, instrumental aspects, applications and trends, John Wiley & Sons, New York, 1987.
- 43 H. W. Werner, Surf. Sci., 1975, 47, 301-323.
- 44 H. Liebl, J. Vac. Sci. Technol., A, 1975, 12, 385.
- 45 H. Liebl, J. Appl. Phys., 1967, 38, 5277-5283.
- 46 P. P. Michałowski, W. Kaszub, A. Merkulov and W. Strupiński, *Appl. Phys. Lett.*, 2016, **109**, 011904.
- 47 P. P. Michałowski, W. Kaszub, I. Pasternak and W. Strupinski, *Sci. Rep.*, 2017, 7, 7479.
- 48 P. P. Michałowski, I. Pasternak and W. Strupinski, *Nanotechnology*, 2018, **29**, 015702.
- 49 I. Grzonka, J. Pasternak, P. P. Michałowski, V. Kolkovsky and W. Strupinski, *Appl. Surf. Sci.*, 2018, 447, 582–586.
- 50 P. P. Michałowski, I. Pasternak, P. Ciepielewski, F. Guinea and W. Strupinski, *Nanotechnology*, 2018, **29**, 305302.
- 51 P. Caban, D. Teklińska, P. Michałowski, J. Gaca, M. Wójcik, J. Grzonka, P. Ciepielewski, M. Możdżonek and J. Baranowski, J. Cryst. Growth, 2018, 498, 71–76.
- 52 P. P. Michałowski, P. Caban and J. Baranowski, *J. Anal. At. Spectrom.*, 2019, 34, 848–853.

JAAS

Journal of Analytical Atomic Spectrometry rsc.li/jaas







PAPER

Paweł Piotr Michałowski *et al.*Secondary ion mass spectrometry investigation of carbon grain formation in boron nitride epitaxial layers with atomic depth resolution

JAAS



PAPER



Cite this: *J. Anal. At. Spectrom.*, 2019, **34**. 848

Received 7th January 2019 Accepted 25th February 2019

DOI: 10.1039/c9ja00004f

rsc.li/jaas

Secondary ion mass spectrometry investigation of carbon grain formation in boron nitride epitaxial layers with atomic depth resolution[†]

Paweł Piotr Michałowski, ** Piotr Caban and Jacek Baranowski

Secondary ion mass spectrometry (SIMS) measurements show that boron nitride (BN) films grown under an argon flow are contaminated with carbon in the form of clusters. SIMS imagining of carbon clusters with atomic depth resolution allows us to show that there are two different growth modes for BN films: 3D growth and self-terminated growth. The choice of the growth mode predominantly depends on reactor pressure. In the 3D growth mode (low pressure) carbon clusters appear in an organized way: the cluster in one BN layer nucleates the one in the successive layer. Eventually, they create three-dimensional carbon grains. In the self-terminated growth mode (high pressure) the distribution of carbon within the volume of the film is chaotic. The differences observed between the growth modes seem to depend on the diffusion length of the carbon and boron species.

1 Introduction

Two-dimensional (2D) materials and their heterostructures have attracted worldwide attention due to their remarkable optical, mechanical and electronic transport properties.¹ Growth of 2D materials on insulating substrates is essential for the production of 2D devices on a commercial scale. Boron nitride (BN) with sp²-hybridized atomic sheets of boron and nitrogen is a particularly promising 2D material. It has a structure similar to that of graphene (1.7% lattice mismatch) but a wide band gap. Not only does BN have high thermal conductivity and high resistivity, but it has possibilities for integration with other 2D materials. Due to its sp²-hybridized bonding and weak van der Waals bonds, BN is an excellent candidate for use as a substrate and dielectric for graphene-based electronics.² A great deal of effort has therefore been devoted to synthesizing BN films.

The Metalorganic Chemical Vapour Deposition (MOCVD) method, well recognized for the epitaxial growth of III–V nitrides, is commonly used for the growth of BN epitaxial films.³ The most common substrate is sapphire – Al₂O₃ and precursors are triethylborane (TEB) for boron and ammonia (NH₃) for nitrogen. There are several publications describing MOCVD growth on sapphire and other substrates.⁴⁻⁹ These earlier studies show a lack of surface uniformity of the BN films grown. A pulsed growth technique was also introduced for the deposition of BN, where the B metalorganics and ammonia are

Institute of Electronic Materials Technology, Wólczyńska 133, 01-919 Warsaw, Poland. E-mail: pawel.michalowski@itme.edu.pl

† Electronic supplementary information (ESI) available. See DOI 10.1039/c9ja00004f

supplied to the reactor alternately. This reduces parasitic gas phase reactions. 10-12 Important progress in the MOCVD growth of uniform BN films was achieved when it was demonstrated that the growth mode could be changed from 3D nucleation to 2D self-terminated nucleation by an increase in the V/III ratio and the use of high reactor pressure. 13-16 The self-terminated growth mode with high reactor pressure resulted in atomically smooth 5-6 monolayer thick BN films. It was also found that substrate nitridation promotes self-terminating growth leading to atomically smooth films.16 Recently, it was reported that selfterminated behaviour is attributed to the fact that a sufficiently high NH₃ partial pressure saturates the BN surface and prevents further absorption of boron precursors.17 However, this proposition does not explain why the growth stops after 5-6 layers. The detailed mechanism of BN growth and its change from 3D mode to self-terminated mode is still not understood.

In our previous work¹⁸ we showed that 3D growth and selfterminated growth under Ar flow lead to very high contamination by unreacted carbon. Secondary ion mass spectrometry (SIMS) measurements supported by several experimental techniques such as Scanning Electron Microscopy, X-Ray Reflectivity, Attenuated Total Reflectivity, Raman spectroscopy and Atomic Force Microscopy (AFM) have shown that the carbon appears predominantly in the form of clusters. Motivation behind the present work is to find how formation of carbon clusters takes place in the two growth modes of boron nitride. Distribution of these carbon clusters within the BN layers may be different under two growth modes. Such distribution was not measured up to now and due to significant improvement of our SIMS method it is now possible to get atomic resolution and thus obtain very precise information about carbon grain formation within BN layers.

Paper JAAS

2 Experimental

2.1 Sample preparation

Boron nitride films were grown on 2-inch double-sided polished (0001)-oriented Al_2O_3 with a maximum off-cut of 0.2° substrates using the MOCVD Aixtron Epigress VP508 system (horizontal, hot wall). A pulsed source injection mode with triethylborane (TEB) and ammonia (NH $_3$) precursors was applied for suppressing gas phase prereactions. A single pulse consisted of the following steps: (1) TEB injection, (2) interruption, (3) NH $_3$ injection, and (4) interruption.

A high V/III ratio during the deposition at a temperature of 1050 °C was used for all the samples investigated. The BN layers were grown using argon as the carrier gas. The number of cycles was 800 for the three-dimensional growth mode (deposition at low pressure – 100 mbar and argon ambient) and 200 for the self-terminated growth mode (high pressure – 400 mbar and either argon or hydrogen ambient). Before the growth a thin, amorphous buffer layer was formed on the Al_2O_3 by a low temperature nitridation step. All growth parameters were kept the same in order to compare the carrier gas influence on the properties of the BN layers grown. Epilayers were cooled by NH $_3$ and carrier gas flow.

2.2 Atomic force microscopy

AFM measurements were performed using a Bruker Dimension FastScan with ScanAsystTM, using silicon probes (Bruker OTESPA-R3 model) with a nominal force constant of 26 N m⁻¹, and a typical nominal tip radius of 7 nm. The root mean square (RMS) roughness of the samples was measured over a scan area of $30 \times 30 \ \mu m$.

2.3 Secondary ion mass spectrometry

In this work, all SIMS measurements were performed employing the CAMECA SC Ultra instrument under ultra-high vacuum (UHV), usually of 4×10^{-10} mbar. Sufficient depth resolution was obtained for the negative ion detection mode by using a low impact energy of 100 eV for a Cs⁺ primary beam rastered over 80 \times 80 μ m². The analysis area was limited to 40 \times 40 μ m². The SC Ultra tool is able to achieve such low impact energies due to the EXLIE (EXtra Low Impact Energy) technology, in the case of which a primary floating column concept is used.19 In this notion, contrary to standard SIMS tools, the primary column has the "floating voltage" instead of the grounded voltage level between the space at any two lenses inside the column and thus primary ions are slowed down at the end of the column maintaining favourable conditions for ion acceleration and beam stability. The ion beam on the sample in the SC Ultra tool has a square shape and due to the "variable rectangular shape concept" forms a homogeneous spot. The primary beam at a working point in the SC Ultra is formed by two stencils - wellshaped apertures. While the first one is used to choose the most intense and homogeneous part of the ion beam, the second one changes the size of the spot. These innovations allow one to use the low impact energy of primary ions with high sensitivity for all elements measured, high depth resolution (below 1 nm), and

a high dynamic range with a low sputter rate. ^{20,21} The electron gun was used to prevent charge build-up.

To analyse each layer individually and reach atomic resolution, measurements were performed in two modes:

- Static SIMS mode. The acquisition time for each element was one minute and the total primary ion dose was limited to 10^{13} ions per cm² and thus less than 1% of the surface was damaged during the analysis. The incident angle was relatively low (40°) .
- Dynamic SIMS mode. A short and relatively dense pulse was used to remove one layer completely without causing any significant damage to the layers beneath. The optimal conditions were reached for the total ion dose in the range of 10^{15} ions per cm² and the pulse duration of 3 s. The incident angle was high (69°) to prevent damaging the lower layers.

Even though the tool did not allow direct control over the incident angle, the desired value had been reached by changing the voltages applied to the accelerator, sample holder and primary column (floating voltage). Even though for the high incident angle the quality of the primary and secondary beam was not optimal, this mode was used to remove subsequent layers only so it was not an issue.

3 Results & discussion

SIMS is a very precise analytical technique for determining the elemental composition of a sample²²⁻²⁷ and it is especially well known for its excellent detection limits of trace elements.²⁸⁻³³ In our previous studies we have already presented the possibility of reaching nanometer and subnanometer depth resolution for the characterization of graphene³⁴⁻³⁸ as well as BN thin films.¹⁸ Therefore SIMS is a very good candidate for expanding this research and gaining some information about formation of carbon grains in boron nitride thin films.

It has been noted experimentally that for a specific type of material - layered structures where the monolayers are held together by van der Waals (vdW) forces - secondary ion mass spectrometry measurements can reach atomic depth resolution as presented schematically in Fig. 1. The first layer is analysed in the static SIMS regime (the density of the beam is sufficiently low that less than 1% of the surface is damaged during the analysis). Then a short, dense pulse of primary ions with an extremely low impact energy (100 eV) and high incident angle removes the first layer completely without causing any significant damage to the second layer. Subsequent layers are similarly analysed in the static SIMS regime and then removed by a dense ion pulse. Such an extreme depth resolution can be reached only for two-dimensional van der Waals materials because the energy of the incoming ions will go to break up some covalent bonds in the first layer along with vdW bonds between the first and the second layer, as they are much weaker than covalent bonds (even up to three orders of magnitude) and are thus preferentially broken up. If the density and duration of the pulse are finely optimized the energy that is transferred to the sample is sufficient to sputter the first layer only. If a material consists of only covalent bonds then no bond will be preferentially broken up. A standard collision cascade will thus be

JAAS Paper

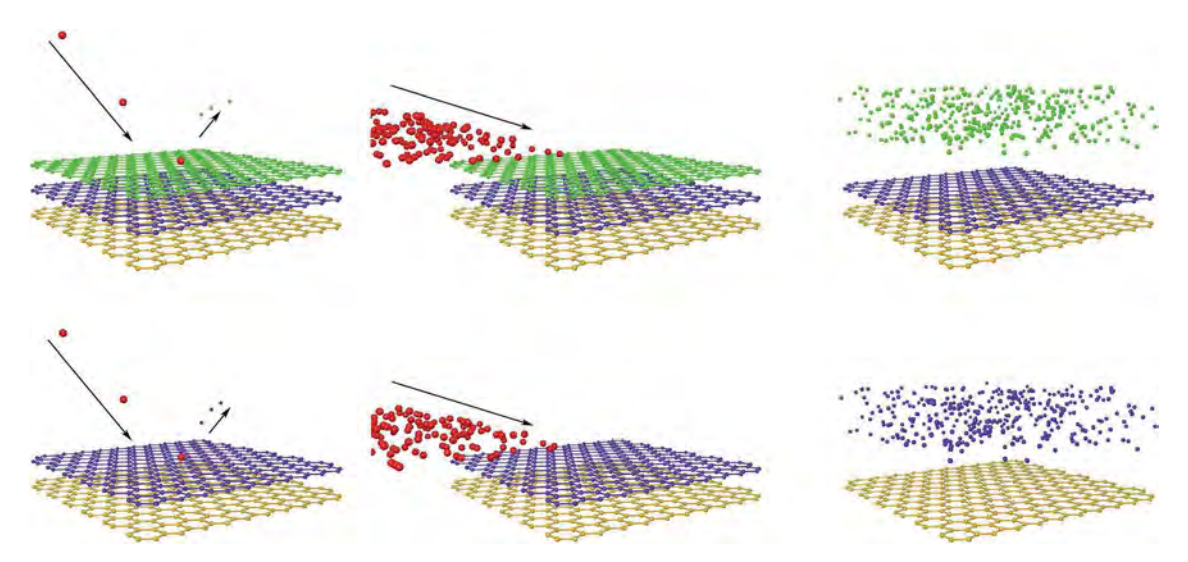


Fig. 1 Secondary ion mass spectrometry with atomic resolution for two-dimensional van der Waals materials. The top layer is analysed in the static SIMS regime (less than 1% of the surface is bombarded) where a short pulse of primary ions with an extremely low impact energy and high incident angle removes the first layer completely without causing any significant damage to the second layer. With this approach each layer can be individually characterized and then removed.

generated and atoms from several monolayers will be sputtered, so the depth resolution will be lower.

The possibility of reaching atomic depth resolution for SIMS measurements has been confirmed for multi-layer graphene and boron nitride thin films. This has been validated by AFM roughness measurements: for multi-layer graphene and boron nitride grown in self-terminated mode, RMS before and after SIMS experiments is the same, namely 0.15 \pm 0.03 nm and 0.50 \pm 0.05 nm, respectively. In the case of boron nitride grown in 3D mode, it has been observed that RMS slightly increases from 1.11 \pm 0.07 nm to 1.20 \pm 0.07 nm but the difference remains within standard deviation. It can be therefore concluded that this kind of SIMS measurement does not introduce any additional roughness and thus atomic depth resolution is indeed possible.

Out of these two materials the case of boron nitride is particularly interesting. Recent SIMS measurements have shown that the BN film grown under argon flow contains a high concentration of carbon, predominantly in the form of carbon clusters.18 It was proposed that the result of the reaction of two TEB molecules with ammonia molecules leads to BN and unreacted carbon. At that time, however, our SIMS procedure was not fully optimized and lateral imaging was not limited to a single layer of BN film. Reaching atomic resolution has allowed us to study carbon precipitates in detail. Fig. 2 presents a lateral distribution of carbon, boron and nitrogen for the third BN layer (counting from the surface) for a spot which was particularly contaminated. It can immediately be noted that the distributions of boron and nitrogen match very well. Analysing the distribution of nitrogen only may lead to the impression that the film is torn in some places. However, the nitrogen detection limit is very poor in this kind of measurement and the average intensity is only about 5 counts, and thus in some places no nitrogen signal has been detected even

though boron has successfully been measured. This is just a measurement artifact and the distribution of boron should be treated as the most trustworthy signal to assess the quality of the BN film.

The most important conclusion is that at the places where a significant amount of carbon has been detected both signals (those coming from B and N) equal zero or are at least very small, which means that no or a negligible amount of boron and nitrogen is present in the carbon precipitates. Similar carbon inclusions have already been analysed by high-resolution transmission electron microscopy.39 It should be emphasized, however, that atomic depth resolution of SIMS measurements is achieved at the expense of lateral resolution, which is in the range of a few microns. This means that the size of the registered carbon precipitates is artificially stretched out and that there may exist much smaller carbon inclusions which we cannot detect. In fact, a high intensity of the carbon signal on the whole area under analysis confirms the presence of many small carbon precipitates. They are not big enough to be directly imaged so the signal coming from them is averaged. Nevertheless the ability to image each BN layer separately, even with poor lateral resolution, may provide a lot of important information about the material.

Carbon precipitates can also be presented in a 3D view. To obtain the best possible image clarity we have followed a simple rule: if at one spot the intensity of the carbon signal is at least 1.5 higher than the average and at the same time the intensity of the boron signal is at least 0.5 smaller than the average then a colour voxel is used to denote high carbon content (the higher the intensity the brighter the voxel). In other cases, the voxel is transparent. Fig. 3a and b present a 3D visualization of carbon clusters within BN layers, which correspond to growth under low and high reactor pressure respectively. Simple inspection of these pictures clearly shows that there are basic differences

JAAS Paper

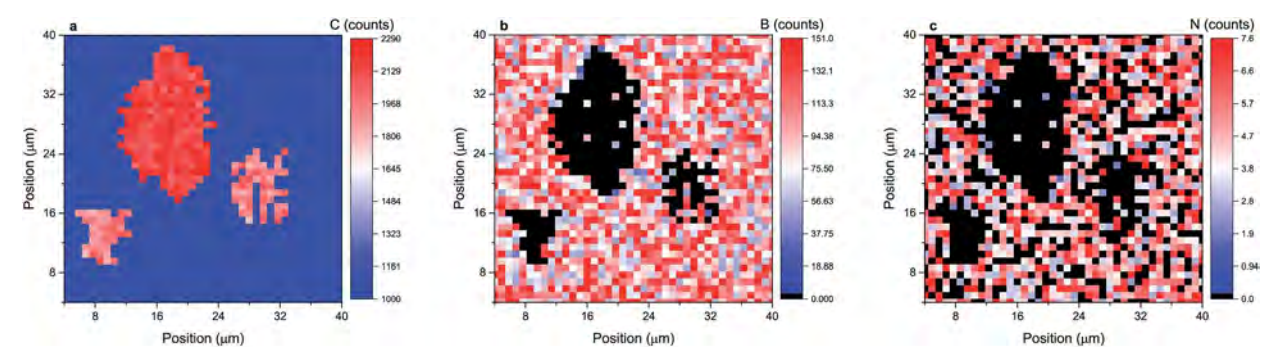


Fig. 2 A lateral distribution of carbon, boron and nitrogen (a, b and c, respectively) for the third BN layer (counting from the surface) for a sample grown under high reactor pressure under Ar flow.

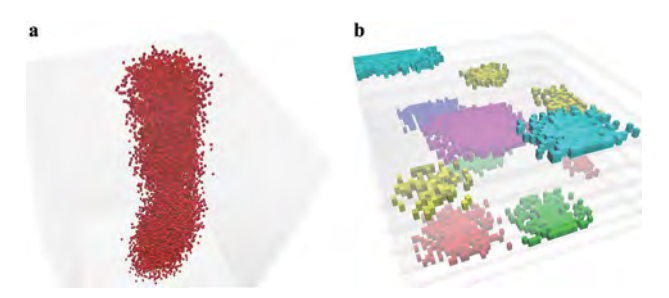


Fig. 3 3D visualization of carbon clusters within BN layers. (a) In the case of low reactor pressure, carbon clusters appear in an organized manner and thus a large three-dimensional carbon pillar-shaped grain is formed. (b) In the case of high reactor pressure, carbon clusters present in the different BN layers are uncorrelated and appear in a chaotic way - carbon clusters have been marked with different colours for each layer.

between them. It can therefore be concluded that formation of carbon grains is indeed different in 3D mode and selfterminated mode.

In the case of 3D growth, carbon clusters appear in an organized manner. They continue through the whole van der Waals structure eventually forming three-dimensional pillarshaped carbon grains - this means that the carbon clusters in one BN layer have to be effective nucleation sites for the next BN layer. They reproduce themselves in successive BN layers, which means that formation of the next carbon cluster above the one beneath it has to be energetically favourable. This mode is characterised by low reactor pressure and thus one may assume that the diffusion length of carbon, boron and nitrogen species is relatively long, larger than the separation between carbon clusters. Therefore, the most energetically favourable nucleation site can be always decorated with carbon and boron species. Apparently, an ordered system of carbon clusters within van der Waals layers has to have lower energy than a chaotic system. SIMS maps show that eventually a large threedimensional carbon grain is formed, as shown in Fig. 3a.

The situation is significantly different for growth under high reactor pressure (Fig. 3b), which leads to self-terminated mode. Carbon clusters present in the different BN layers are

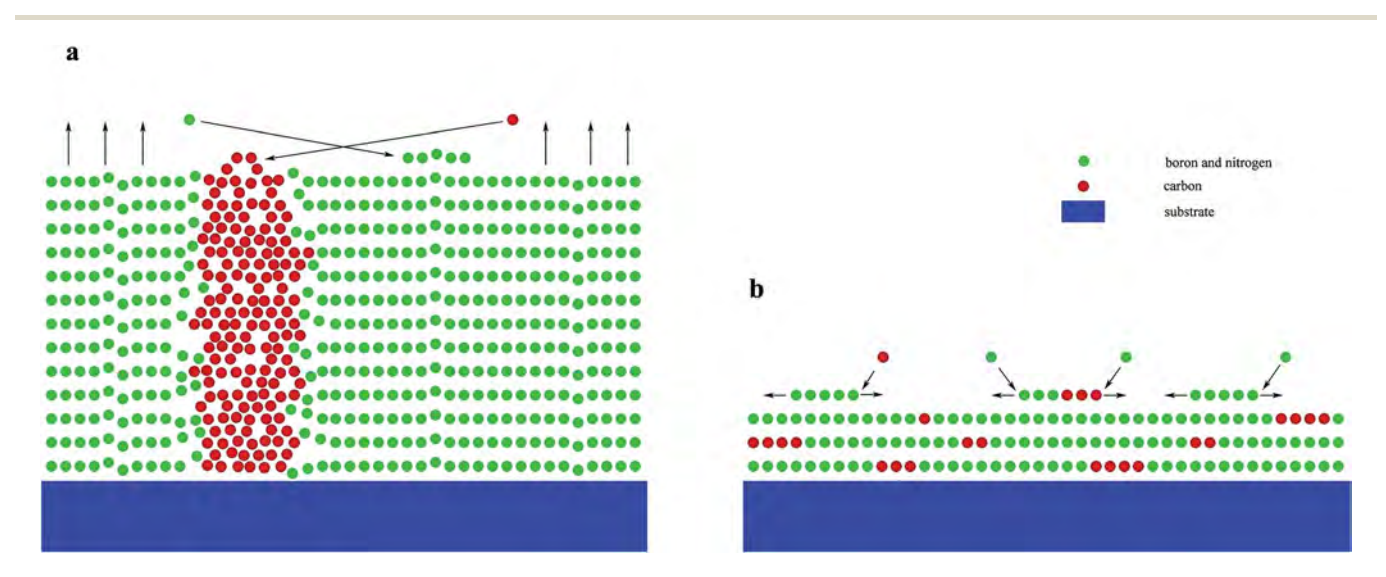


Fig. 4 Schematic illustration of the formation of carbon grains in BN films. (a) For low reactor pressure, the diffusion length is high and thus each species can migrate to a favourable location and replicate the layer beneath. (b) For high reactor pressure, the diffusion length is limited and each atom is incorporated into the film in the vicinity of the region where the reaction between TEB and NH₃ takes place. The distribution of carbon clusters is chaotic and there is no correlation between subsequent layers.

JAAS Paper

uncorrelated and appear in a chaotic way, contrary to what is observed in the case of 3D growth mode. Under high reactor pressure, a sufficiently high concentration of $\mathrm{NH_3}$ species on the surface of the BN layer may limit the diffusion of carbon and boron species. This will lead to a limited region for effective nucleation sites, the carbon and boron species having to choose a nucleation site in the vicinity of the region where the reaction between TEB and $\mathrm{NH_3}$ takes place.

It should be emphasized that the number of layers detected in each sample corresponds very well to the thickness of the BN film, namely 68 layers: \sim 22 nm and 6 layers: \sim 1.8 nm for samples grown under low and high reactor pressure respectively. This confirms that the established SIMS measurement procedure does indeed reach atomic depth resolution.

4 Conclusions

One of the main results of this work is the demonstration of SIMS as a useful technique for the investigation of 2D van der Waals materials. SIMS with atomic depth resolution has allowed the analysis of the composition and contamination content layer by layer. The detection of carbon clusters within successive layers has allowed us to study carbon grain formation in both 3D mode and self-terminated mode. The differences observed between the growth modes seem to depend on the diffusion length of the carbon and boron species.

For low reactor pressure the diffusion length of the carbon and boron species is sufficiently long to find the most energetically convenient nucleation sites. These sites are connected with carbon clusters being in the lower BN layer. Nucleation sites will be reproduced from one layer to the next leading to carbon inclusions in the form of 3D carbon grains as shown in Fig. 3a and schematically in Fig. 4a. For high reactor pressure, due to the limited diffusion length of the carbon and boron species, there is no correlation between carbon grains in consecutive layers as shown in Fig. 3b and schematically in Fig. 4b.

Conflicts of interest

There are no conflicts to declare.

Acknowledgements

This work was supported by the European Union's Horizon 2020 research and innovation programme under grant agreement No 785219.

References

- 1 K. S. Novoselov, A. Mishchenko, A. Carvalho and A. H. Castro Neto, *Science*, 2016, 353, aac9439.
- 2 C. Dean, A. Young, I. Meric, L. Wang, S. Sorgenfrei, K. Watanabe, T. Taniguchi, P. Kim, K. Shepard and J. Hone, *Nat. Nanotechnol.*, 2010, 5, 3209.
- 3 K. K. Kim, A. Hsu, X. Jia, S. M. Kim, Y. Shi, M. Dresselhaus, T. Palacios and J. Kong, *ACS Nano*, 2012, **6**, 8583–8590.

4 T. Taniguchi, T. Sato, W. Utsumi, T. Kikegawa and O. Shimomura, *Diamond Relat. Mater.*, 1997, **6**, 1806–1815.

- 5 W. Gannett, W. Regan, K. Watanabe, T. Taniguchi, M. F. Crommie and A. Zettl, Appl. Phys. Lett., 2011, 98, 242105
- 6 J. Li, R. Dahal, S. Majety, J. Lin and H. Jiang, Nucl. Instrum. Methods Phys. Res., Sect. A, 2011, 654, 417–420.
- 7 M. Chubarov, H. Pedersen, H. HÃűgberg, J. Jensen and A. Henry, *Cryst. Growth Des.*, 2012, 12, 3215–3220.
- 8 T. Doan, S. Majety, S. Grenadier, J. Li, J. Lin and H. Jiang, Nucl. Instrum. Methods Phys. Res., Sect. A, 2015, 783, 121-127.
- 9 S. K. Jang, J. Yuon, Y. J. Song and S. Lee, *Sci. Rep.*, 2016, 6, 30449.
- 10 H. J. Kim, S. Choi, D. Yoo, J.-H. Ryou, R. D. Dupuis, R. F. Dalmau, P. Lu and Z. Sitar, *Appl. Phys. Lett.*, 2008, 93, 022103.
- 11 S. Majety, J. Li, X. K. Cao, R. Dahal, B. N. Pantha, J. Y. Lin and H. X. Jiang, *Appl. Phys. Lett.*, 2012, **100**, 061121.
- 12 X. Yang, S. Nitta, K. Nagamatsu, S.-Y. Bae, H.-J. Lee, Y. Liu, M. Pristovsek, Y. Honda and H. Amano, *J. Cryst. Growth*, 2018, 482, 1–8.
- 13 Q. S. Paduano, M. Snure, J. Bondy and T. W. Zens, *Appl. Phys. Express*, 2014, 7, 071004.
- 14 M. Snure, Q. Paduano, M. Hamilton, J. Shoaf and J. M. Mann, *Thin Solid Films*, 2014, 571, 51–55.
- 15 M. Snure, Q. Paduano and A. Kiefer, *J. Cryst. Growth*, 2016, 436, 16–22.
- 16 Q. Paduano, M. Snure, D. Weyburne, A. Kiefer, G. Siegel and J. Hu, J. Cryst. Growth, 2016, 449, 148–155.
- 17 A. Rice, A. Allerman, M. Crawford, T. Beechem, T. Ohta, C. Spataru, J. Figiel and M. Smith, *J. Cryst. Growth*, 2018, 485, 90–95.
- 18 P. Caban, D. Teklińska, P. Michałowski, J. Gaca, M. Wójcik, J. Grzonka, P. Ciepielewski, M. Możdżonek and J. Baranowski, J. Cryst. Growth, 2018, 498, 71–76.
- 19 CAMECA, Genneviliers, CAMECA SC-Ultra, User's Guide, 2005.
- 20 D. Kouzminov, A. Merkulov, E. Arevalo and H. J. Grossmann, *Surf. Interface Anal.*, 2013, **45**, 345–347.
- 21 A. Merkulov, Surf. Interface Anal., 2013, 45, 90-92.
- 22 C. A. Andersen and J. R. Hinthorne, *Science*, 1972, **175**, 853–860.
- 23 A. Benninghoven, Surf. Sci., 1975, 53, 596-625.
- 24 A. Benninghoven, F. G. Rudenauer and H. W. Werner, Secondary ion mass spectrometry: basic concepts, instrumental aspects, applications and trends, John Wiley & Sons, New York, 1987.
- 25 H. W. Werner, Surf. Sci., 1975, 47, 301-323.
- 26 H. Liebl, J. Vac. Sci. Technol., A, 1975, 12, 385.
- 27 H. Liebl, J. Appl. Phys., 1967, 38, 5277-5283.
- 28 K. Wittmaack, Appl. Phys. Lett., 1976, 29, 552.
- 29 B. Y. Ber, Y. A. Kudriavtsev, A. V. Merkulov, S. V. Novikov, D. E. Lacklison, J. W. Orton, T. S. Cheng and C. T. Foxon, Semicond. Sci. Technol., 1998, 13, 71–74.
- 30 C. Y. Chiou, C. C. Wang, Y. C. Ling and C. I. Chiang, *Appl. Surf. Sci.*, 2003, **203–204**, 482–485.

Paper JAAS

31 M. Emziane, K. Durose, D. P. Halliday, A. Bosio and N. Romeo, *J. Appl. Phys.*, 2006, **100**, 013513.

- 32 T. Matsunaga, S. Yoshikawa and K. Tsukamoto, *Surf. Sci.*, 2002, 515, 390–402.
- 33 H. Gnaser, Surf. Interface Anal., 1997, 25, 737-740.
- 34 P. Michałowski, W. Kaszub, A. Merkulov and W. Strupiński, *Appl. Phys. Lett.*, 2016, **109**, 011904.
- 35 P. P. Michałowski, W. Kaszub, I. Pasternak and W. Strupinski, *Sci. Rep.*, 2017, 7, 7479.
- 36 P. P. Michałowski, I. Pasternak and W. Strupinski, *Nanotechnology*, 2018, **29**, 015702.
- 37 I. Grzonka, J. Pasternak, P. P. Michałowski, V. Kolkovsky and W. Strupinski, *Appl. Surf. Sci.*, 2018, 447, 582–586.
- 38 P. P. Michałowski, I. Pasternak, P. Ciepielewski, F. Guinea and W. Strupinski, *Nanotechnology*, 2018, **29**, 305302.
- 39 L. Ci, L. Song, C. Jin, D. Jariwala, D. Wu, Y. Li, A. Srivastava, Z. Wang, K. Storr, L. Balicas, F. Liu and P. Ajayan, *Nat. Mater.*, 2010, **9**, 430–435.

ChemComm



COMMUNICATION



Cite this: Chem. Commun., 2019, 55, 11539

Received 19th June 2019, Accepted 30th August 2019

DOI: 10.1039/c9cc04707g

rsc.li/chemcomm

Three dimensional localization of unintentional oxygen impurities in gallium nitride†

Paweł Piotr Michałowski, 📵* Sebastian Złotnik 📵 and Mariusz Rudziński

Further development of gallium nitride (GaN) based optoelectronic devices requires in-depth understanding of the defects present in GaN grown on a sapphire substrate. In this work, we present three dimensional secondary ion mass spectrometry (SIMS) detection of oxygen. Distribution of these impurities is not homogeneous and the vast majority of oxygen atoms are agglomerated along pillar-shaped structures. Defect-selective etching and scanning electron microscopy imaging complement SIMS results and reveal that oxygen is predominantly present along the cores of screw and mixed dislocations, which proves their high tendency to be decorated by oxygen. A negligible amount of oxygen can be found within the bulk of the material and along the edge dislocations.

The III-nitrides are well-known materials for various optoelectronic and power electronic applications, such as light emitting diodes (LEDs) or high power transistors. ^{1,2} Ideally, a native bulk GaN substrate would be the most appropriate for GaN-based structures but this technology is still developing. Currently, the most popular commercial substrate is sapphire, a $\alpha\text{-Al}_2O_3$ phase possessing a hexagonal unit cell with a lattice mismatch to GaN as high as \sim 16%. Although sapphire is the most common substrate for GaN-based heterostructures, due to its relatively low cost production a large lattice mismatch, as well as difference in the thermal expansion coefficients, leads to high threading dislocation density (TDD) of $10^8\text{-}10^{10}~\text{cm}^{-2}$ in epitaxially grown GaN-based structures. ^{3,4} These TDs have a strong influence on the electrical properties (leakage current) of GaN-based devices. ⁵

However, it was stated that TDs scarcely affect the internal quantum efficiency as long as the TDD is lower than $\sim 2 \times 10^{10}~\text{cm}^{-2}.^6$ However, it has to be taken into account that dislocations in semiconductors by themselves form an electronic subsystem. Additionally, the TDs in GaN-based epilayers provide diffusion paths for impurity incorporation, substantially affecting the electrical and optical properties. From a technological point of

Lukasiewicz Research Network-Institute of Electronic Materials Technology, Wólczynska 133, 01-919 Warsaw, Poland. E-mail: pawel.michalowski@itme.edu.pl † Electronic supplementary information (ESI) available. See DOI: 10.1039/c9cc04707g

view it is an important aspect since it is known that GaN epitaxial layers grown on sapphire by metalorganic vapor phase epitaxy (MOVPE) are characterized by unintentional n-type conductivity, normally with carrier densities $>10^{16}~{\rm cm}^{-3}$, due to residual impurities, such as oxygen, hydrogen or carbon, originating from metalorganic precursors and carrier gases.¹⁰

Therefore, an assessment of defects plays a key role for heterostructure growth. One of the most effective methods revealing a broad range of defects is defect-selective etching (DSE).¹¹ The most routine mode of selective etching of semiconductors, in particular GaN-based compounds is classical chemical with the use of molten salts, *e.g.*, KOH and its eutectic with NaOH with modifiers, in order to reveal the etch pit density (EPD) of dislocations. However, DSE can be exclusively used to distinguish different types of dislocations (edge, mixed and screw)¹² or evaluate interfaces and EPD depending on the growth method and doping level. Until now, it was not possible to study with direct methods the impurities decorating the dislocations. Here, secondary ion mass spectrometry (SIMS) is implemented to analyse the planar and in depth distribution of one of the most common unintentional impurities – oxygen – in MOVPE-grown GaN epilayers.

Unintentionally doped $\sim\!1.5~\mu m$ -thick GaN epitaxial structures were grown on a (0001)-oriented sapphire substrate by an AIX 200/4 RF-S low-pressure MOVPE reactor; details of epitaxial growth of GaN are described in the ESI.† The GaN surface layer was wet etched with a molten eutectic mixture of KOH–NaOH with 10% of MgO (E + M) at 450 °C for 3 min. Scanning electron microscopy (SEM) observations by using a Hitachi SU8230 Cold-FEG high resolution microscope equipped with a semi-in-lens type objective lens using an SE detector were conducted to evaluate the surface morphology of DSE treated GaN structures. The diameter of the etch pits was measured by drawing a circle that touches the hexagon at the vertexes, and the detailed protocol is discussed in the ESI.†

All SIMS depth profiles were performed employing the CAMECA SC Ultra instrument under ultra-high vacuum (UHV), usually of 4×10^{-10} mbar. Cs⁺ primary beam rastered over $50\times 50~\mu m^2$ (the analysis area was limited to $20\times 20~\mu m^2$) and negative

ChemComm Communication

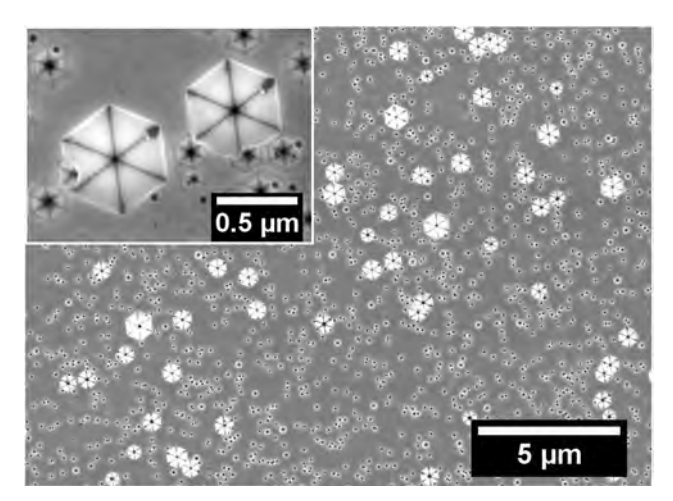


Fig. 1 SEM micrographs of the etch pits revealed on the GaN surface using E + M etch at 450 °C for 3 min. The inset depicts a magnified micrograph with revealed hexagonal pits generated on dislocation cores; the two biggest pits, >500 nm, represent TDs with the screw component of the Burgers vector.

ion detection mode was used in the experiments. The intensity of the primary beam was 5-60 nA and the impact energy was 13 keV.

Wet etching was used to accurately determine EPD in as-grown wurtzite-type GaN epitaxial layers. Fig. 1 depicts SEM micrographs of the etch pits formed due to etching in molten E + M on the GaN epilayer; the inset shows a magnified micrograph with revealed hexagonal pits generated on dislocation cores and the two biggest pits, >500 nm, represent TDs with the screw component of the Burgers vector. The size of the pits can be attributed to distinct types of dislocations: (i) screw and mixed ones appear as large pits, and (ii) edge dislocations as small pits; the difference is associated with etch rate differences due to the distinct magnitude of Burgers vectors. 13 The size of these etch pits was determined and Fig. 2 presents the distribution of the diameter of the etch pits.

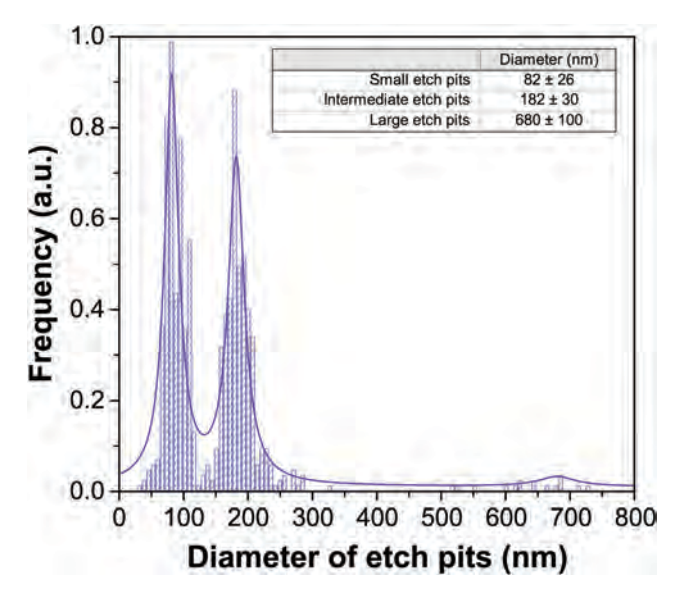


Fig. 2 Normalized frequency of diameter of the corresponding etch pits: (i) small: 82 \pm 26 nm, (ii) intermediate: 182 \pm 30 nm, and large: 670 \pm 100 nm.

The obtained data show clear bimodal distribution with two maxima at 82 ± 26 and 182 ± 30 nm, and the third broad one at 670 ± 100 nm. The large etch pits correspond to screw and mix type dislocations and their fraction is around 1% of all EPD. The total EPD was counted from several SEM micrographs and is in the order of $\sim 1.1 \times 10^9$ cm⁻².

Besides DSE, other destructive and non-destructive techniques were implemented for dislocation analysis, e.g., X-ray topography, ¹⁴ transmission electron microscopy (TEM),15 scanning tunneling microscopy (STM), 16 cathodoluminescence (CL), 9 photoluminescence (PL), 17 Raman spectroscopy, 18 atom probe tomography, 19 among others. Although these methods offer detailed dislocation examination (even three-dimensional mapping) with high resolution, a compositional distribution of relevant technological impurities (mainly oxygen) is scarcely reported, mostly due to not enough detection limits (sensitivity) of the aforementioned methods. SIMS on the other hand, is known for its excellent detection limits useful in dopant and contamination analysis. We have previously demonstrated its usefulness for GaN/AlGaN material showing how oxygen contamination influences the diffusion of Mg dopant.²⁰ In this work we have used the technique to study the lateral distribution of oxygen which is predicted to decorate dislocations in GaN materials - it is a common consensus that it decorates screw and mixed dislocations21-24 and while frequently communicated, simulations and calculations^{8,25-28} predict that a direct empirical proof requires sophisticated methodology, such as electron energy loss spectroscopy (EELS).^{22,23}

However, SIMS analysis of vacuum contaminant species – in this case oxygen - is always challenging because of residual gases present in the analysis chamber. Peres et al.29 have established a procedure to estimate a background level of contaminant species which can be subtracted from a result to obtain a realistic concentration of the measured species. Briefly, the intensity of the measured signal depends on the actual concentration of a measured species and vacuum background contribution (VBC) and the latter term is inversely proportional to the primary beam density. By performing several experiments with varying beam densities, an interpolated result for infinite beam density (and thus vacuum background contribution equals zero) can be obtained, which is the actual concentration of the measured species. In this way vacuum background contribution can be determined for each primary beam density.

In this case, however, the situation is more complicated as the lateral distribution of elements is required. To present the result clearly we have chosen a cuboid with a base diameter of $5 \times 5 \,\mu\text{m}^2$ and height in the range of 100–1100 nm from the surface of the sample - the region close to the surface has been intentionally omitted as some residual contamination can be present there. This cuboid consists of $90 \times 90 \times 595$ voxels (depth resolution is much better than lateral) and a voxel is blue or transparent if an oxygen count is or is not registered at the specific position, respectively. Fig. 3A presents raw data - as it can be seen, a lot of oxygen counts have been registered and it may seem that the distribution is very uniform. However, about 95% of these voxels can be attributed to the VBC. But since the VBC is related to a flux of contaminating atoms from the vacuum adsorbed onto the

ChemComm Communication

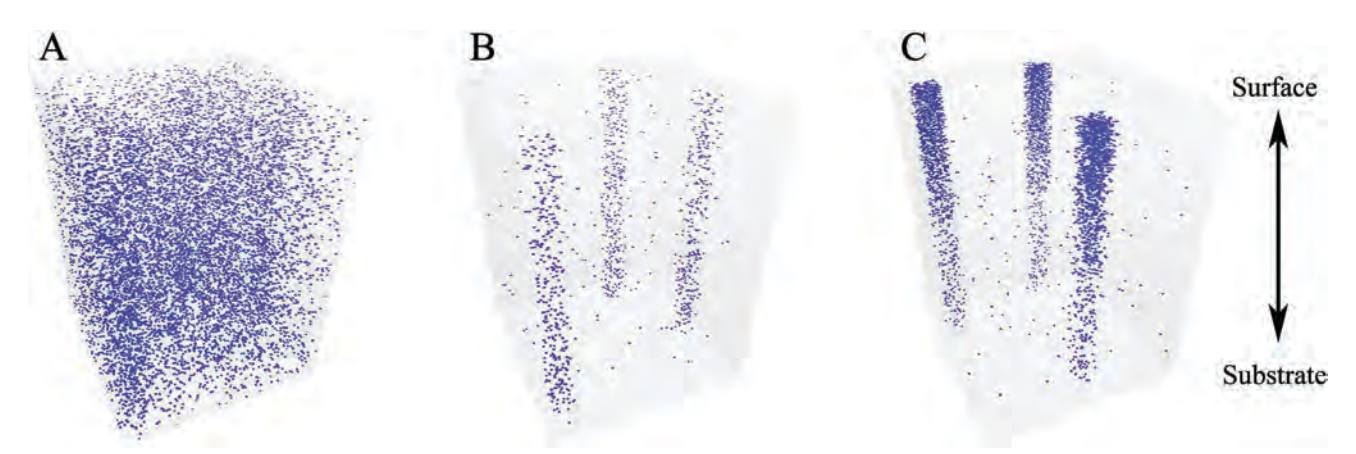


Fig. 3 3D view of oxygen counts in a small $5 \times 5 \times 1 \mu m^3$ cuboid (for better visibility, the z-scale is elongated). Part A: raw data, Part B: background contribution subtracted. Part C: similar result for a sample after wet etching. The result shows that oxygen agglomerates along the pillar-shaped structures.

analyzing area, it can be assumed that each point of the sample has the same probability to adsorb these atoms. It should be therefore possible to subtract the VBC from the raw data by elimination of 95% of randomly chosen voxels. Part B shows the same region but with reduced background. The majority of oxygen is agglomerated along the three pillar-shaped structures. It can be noted that some other counts are also present. It is, however, not possible to determine whether these are actual contaminating atoms found within the bulk of the material or the result of a reduction procedure error: at some points, the reduction procedure may subtract a contribution where oxygen has been indeed agglomerated, whereas at the other position, it will leave a background count unaffected and thus some artificial counts may still be present while some real counts may be reduced. This minor inaccuracy does not impede a final conclusion: a substantial part of oxygen atoms are localized in pillar-shaped structures. The result is in line with the expectations as a vast majority of the dislocations are perpendicular to the surface³⁰ and thus the position of the dislocation's core is the same through the depth of the sample. Part C shows the result for a sample after wet etching. It can be immediately seen that the process has introduced more oxygen into the system and a clear indication of oxygen diffusion from the surface of the sample can be seen. Nevertheless oxygen is still mostly agglomerated along the pillar-shaped structures. Based on multiple experiments it can be estimated that the oxygen concentration is 9×10^{16} atm cm⁻³ and 1.4×10^{17} atm cm⁻³ for a sample before and after wet etching, respectively. 82 \pm 3% (88 \pm 3% after a wet etching) of oxygen atoms are agglomerated along the pillar-shaped structures.

3D images can be converted into a planar view (counts from each depth are integrated) and compared to the position of different dislocations. Fig. 4 presents the distribution of oxygen (blue pixels) obtained from a sample after wet etching projected on an SEM image. It can be immediately noted that oxygen is present only at the center of the largest pits. In most cases, a clear rectangular shape of blue pixels can be noted. It is not surprising as the dislocation core is much smaller than the size of the primary beam and thus the secondary ion image inherits the shape of the primary beam. It is, however, important to

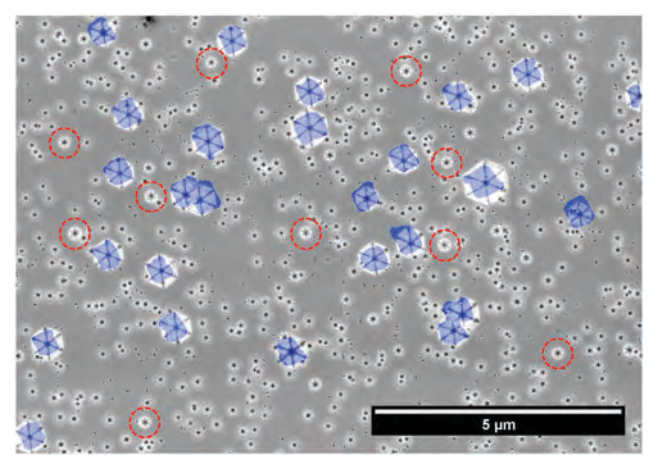


Fig. 4 Lateral distribution of oxygen secondary ions (blue pixels) projected on a SEM micrograph. Despite SIMS related artifacts (poor lateral resolution determined by the size of the primary beam) one can observe a clear correlation between the position of the largest pits and oxygen. Red circles show a few examples of mixed/screw dislocations that are not decorated with oxygen.

emphasize that each of these rectangles is tilted at the same angle (roughly 30 counter-clockwise) which apparently corresponds to the difference in how the sample was mounted during SEM and SIMS measurements. It can be therefore concluded that oxygen has been found at the center of the largest pits and its broader, rectangular-shaped distribution is a SIMS artifact. However, it should be noted that the combined density of screw and mixed dislocations is much higher than that of the density of oxygen rich columns. Red circles on Fig. 4 show a few examples of mixed/screw dislocations that are not decorated with oxygen. It is therefore not possible to determine which type has a stronger tendency to be decorated with oxygen. Perhaps the effect can be correlated with the core structure (open/closed). Cherns et al. use TEM to show that for each type of dislocation the core structure can be open or closed depending on the growth method and on the presence of dopants and impurities.³¹ Given that both SIMS and TEM are destructive methods, it is not possible to use both techniques on the same etch pit and prove this hypothesis.

ChemComm Communication

Generally, diffusion of atoms in a crystalline lattice is strongly accelerated by defects, namely by dislocations, 32 and the mechanism is known as pipe diffusion. It originates from the disordered core region that lowers the activation energy for diffusion, and dislocation lines act as fast paths for diffusing atoms. It was demonstrated that in GaN mobile oxygen adatoms present during growth segregate and accumulate at surface pits, mainly of the open core of screw dislocations, and are not observed in the bulk.22 Indeed, recent experimental studies of oxygen diffusion in GaN were reported demonstrating that oxygen concentration was found to be significantly higher in macro defects, i.e., pinholes, and its bulk diffusion is rather low.^{33,34} These reported data collaborate well with our SIMS results. On the other hand, high resolution local studies of AlGaN/GaN strained superlattices suggested a local segregation (nanometric regions) of light atoms (Mg or Al) in Cottrell atmosphere around the dislocation core as the possible origin of enhanced diffuse scattering of electrons during observations.³⁵ However, our data cannot confirm or exclude such scenario due to limited lateral resolution of SIMS. However, for the further optimization of this material, the positive and negative roles of impurity-decorated defects need to be explored.

Unintentional oxygen impurities in epitaxially grown GaN on a foreign substrate are successfully determined by SIMS and complemented with DSE and SEM. The lateral distribution of oxygen demonstrates that some screw and/or mixed dislocations might be considered as steady-sources of oxygen. Its presence, regardless of the overall concentration, is strongly defectdependent, giving insight into the electrical and optical properties of the GaN-based structures. Therefore, such oxygen-decorated dislocations acting as local nonradiative recombination centres are responsible for n-type conductivity in unintentionally doped GaN epilayers.

This work was partially supported by the National Science Centre (NCN) within SONATA14 2018/31/D/ST5/00399 and OPUS10 2015/19/B/ST7/02163 projects.

Conflicts of interest

There are no conflicts to declare.

Notes and references

- 1 G. Li, W. Wang, W. Yang, Y. Lin, H. Wang, Z. Lin and S. Zhou, Rep. Prog. Phys., 2016, 79, 056501.
- 2 H. Amano, Y. Baines, E. Beam, M. Borga, T. Bouchet, P. R. Chalker, M. Charles, K. J. Chen, N. Chowdhury, R. Chu, C. D. Santi, M. M. D. Souza, S. Decoutere, L. D. Cioccio, B. Eckardt, T. Egawa, P. Fay, J. J. Freedsman, L. Guido, O. Haeberlen, G. Haynes, T. Heckel, D. Hemakumara, P. Houston, J. Hu, M. Hua, Q. Huang, A. Huang, S. Jiang, H. Kawai, D. Kinzer, M. Kuball, A. Kumar, K. B. Lee, X. Li, D. Marcon, M. Maerz, R. McCarthy, G. Meneghesso, M. Meneghini,
 - E. Morvan, A. Nakajima, E. M. S. Narayanan, S. Oliver, T. Palacios,
 - D. Piedra, M. Plissonnier, R. Reddy, M. Sun, I. Thayne, A. Torres, N. Trivellin, V. Unni, M. J. Uren, M. V. Hove, D. J. Wallis, J. Wang,

- J. Xie, S. Yagi, S. Yang, C. Youtsey, R. Yu, E. Zanoni, S. Zeltner and Y. Zhang, J. Phys. D: Appl. Phys., 2018, 51, 163001.
- 3 H.-C. K. J. Huang and S.-C. Shen, Nitride Semiconductor Light-Emitting Diodes (LEDs), Woodhead Publishing, Sawston, 2014.
- 4 L. A. L. E. R. Dobrovinskaya and V. Pishchik, Sapphire: Material, Manufacturing, Applications, Springer US, New York, 2009.
- 5 M. M. Bajo, H. Sun, M. J. Uren and M. Kuball, Appl. Phys. Lett., 2014, **104**, 223506.
- 6 S. Ichikawa, M. Funato and Y. Kawakami, Phys. Rev. Appl., 2018, 10, 064027.
- 7 M. Albrecht, J. L. Weyher, B. Lucznik, I. Grzegory and S. Porowski, Appl. Phys. Lett., 2008, 92, 231909.
- 8 B. V. Petukhov and P. A. Klyuchnik, Crystallogr. Rep., 2012, 57, 388-392.
- 9 J. Wang, Y. Oshima, Y. Cho, Y. Shi and T. Sekiguchi, Superlattices Microstruct., 2016, 99, 77-82.
- 10 A. Ishibashi, H. Takeishi, M. Mannoh, Y. Yabuuchi and Y. Ban, J. Electron. Mater., 1996, 25, 799-803.
- 11 J. L. Weyher, Cryst. Res. Technol., 2012, 47, 333-340.
- 12 J. Weyher, S. Lazar, L. Macht, Z. Liliental-Weber, R. Molnar, S. Müller, V. Sivel, G. Nowak and I. Grzegory, J. Cryst. Growth, 2007, 305, 384-392.
- 13 J. Weyher, Superlattices Microstruct., 2006, 40, 279-288.
- 14 S. Sintonen, M. Rudziński, S. Suihkonen, H. Jussila, M. Knetzger, E. Meissner, A. Danilewsky, T. O. Tuomi and H. Lipsanen, J. Appl. Phys., 2014, 116, 083504.
- 15 Z. Liliental-Weber, Jpn. J. Appl. Phys., 2014, 53, 100205.
- 16 P. Ebert, L. Ivanova, S. Borisova, H. Eisele, A. Laubsch and M. Dähne, Appl. Phys. Lett., 2009, 94, 062104.
- 17 T. Tanikawa, K. Ohnishi, M. Kanoh, T. Mukai and T. Matsuoka, Appl. Phys. Exp., 2018, 11, 031004.
- 18 N. Kokubo, Y. Tsunooka, F. Fujie, J. Ohara, S. Onda, H. Yamada, M. Shimizu, S. Harada, M. Tagawa and T. Ujihara, Appl. Phys. Exp., 2018, 11, 111001.
- 19 S. Usami, N. Mayama, K. Toda, A. Tanaka, M. Deki, S. Nitta, Y. Honda and H. Amano, Appl. Phys. Lett., 2019, 114, 232105.
- 20 P. Michałowski, S. Złotnik, J. Sitek, K. Rosiński and M. Rudziński, Phys. Chem. Chem. Phys., 2018, 20, 13890-13895.
- 21 I. Arslan and N. D. Browning, Phys. Rev. Lett., 2003, 91, 165501.
- 22 M. E. Hawkridge and D. Cherns, Appl. Phys. Lett., 2005, 87, 221903.
- 23 I. Arslan, A. Bleloch, E. A. Stach, S. Ogut and N. D. Browning, *Philos.* Mag., 2006, 86, 4727-4746.
- 24 S. Hautakangas, V. Ranki, I. Makkonen, M. Puska, K. Saarinen, L. Liszkay, D. Seghier, H. Gislason, J. J. A. Freitas, R. Henry, X. Xu and D. Look, Phys. B, 2006, 376-377, 424-427.
- 25 R. Jones, J. Elsner, M. Haugk, R. Gutierrez, T. Frauenheim, M. I. Heggie, S. Oeberg and P. R. Briddon, Phys. Status Solidi A, 1999, 171, 167-173.
- 26 J. Elsner, R. Jones, M. I. Heggie, P. K. Sitch, M. Haugk, T. Frauenheim, S. Öberg and P. R. Briddon, Phys. Rev. B: Condens. Matter Mater. Phys., 1998, 58, 12571-12574.
- 27 M. Tapajna, U. K. Mishra and M. Kuball, Appl. Phys. Lett., 2010, 97, 023503.
- 28 J. E. Northrup, Phys. Rev. B: Condens. Matter Mater. Phys., 2006, 73, 115304.
- 29 P. Peres, A. Merkulov, S. Y. Choi, F. Desse and M. Schuhmacher, Surf. Interface Anal., 2013, 45, 437-440.
- 30 M. A. Moram, C. S. Ghedia, D. V. S. Rao, J. S. Barnard, Y. Zhang, M. J. Kappers and C. J. Humphreys, J. Appl. Phys., 2009, 106, 073513.
- 31 D. Cherns and M. E. Hawkridge, J. Mater. Sci., 2006, 41, 2685-2690.
- 32 M. Legros, G. Dehm, E. Arzt and T. J. Balk, Science, 2008, 319, 1646-1649.
- 33 R. Jakiela, E. Dumiszewska, P. Caban, A. Stonert, A. Turos and A. Barcz, Phys. Status Solidi C, 2011, 8, 1513-1515.
- 34 B. Sadovyi, A. Nikolenko, J. Weyher, I. Grzegory, I. Dziecielewski, M. Sarzynski, V. Strelchuk, B. Tsykaniuk, O. Belyaev, I. Petrusha, V. Turkevich, V. Kapustianyk, M. Albrecht and S. Porowski, J. Cryst. Growth, 2016, 449, 35-42.
- 35 H. L. Tsai, T. Y. Wang, J. R. Yang, C. C. Chuo, J. T. Hsu, M. ÄNeh and M. Shiojiri, J. Appl. Phys., 2007, 101, 023521.

JAAS



PAPER



Cite this: *J. Anal. At. Spectrom.*, 2019, **34**, 1718

Received 4th April 2019 Accepted 18th June 2019

DOI: 10.1039/c9ja00122k

rsc.li/jaas

Indium concentration fluctuations in InGaN/GaN quantum wells

Paweł Piotr Michałowski, ** Ewa Grzanka, ** Szymon Grzanka, ** Artur Lachowski, ** Grzegorz Staszczak, ** Jerzy Plesiewicz, ** Mike Leszczyński ** and Andrzej Turos**

InGaN/GaN quantum wells grown by Metal Organic Chemical Vapor Phase Epitaxy (MOVPE) were initially studied by optical measurements and X-ray diffraction measurements. The comparison of these two techniques indicated that indium is not distributed homogeneously, which was confirmed by transmission electron microscopy in the nanometer scale. The experimental results of Secondary Ion Mass Spectrometry (SIMS) measurements showed that this analytic method can provide specific information on In spatial distributions not accessible by other methods. SIMS data revealed that In fluctuations occur only in the lower part of 2 nm thick InGaN quantum wells, whereas the QW composition is quite uniform in the upper parts. From the experimental data, one may estimate a SIMS depth resolution of about 0.2 nm and of about 1 μ m in lateral directions.

1 Introduction

The most important applications of nitride semiconductors are blue laser diodes and LEDs¹ which illuminate a luminophor giving white light. Such LEDs have wall-plug efficiencies more than 10 times higher than incandescent bulbs which should enable the world to save 10% (now it is already 1.5%) electric energy. The second huge market of nitride-based devices are blue and green laser diodes (LDs)² used in Blu-ray recorders and players, in white lighting, RGB projectors, underwater and "last mile" telecommunication, and in quantum technologies, in medicine, industry and many others.

In these LEDs and LDs, the most important part is InGaN quantum wells (QWs) in which photons are generated by recombination of holes and electrons. InGaN QWs are typically grown on GaN substrates (either bulk or templates grown on sapphire). Large lattice mismatch of InGaN and GaN (about 10% between InN and GaN) and low growth temperature necessary for the InGaN deposition result in non-uniform QW widths, as well as non-uniform indium distribution.

Indium concentration fluctuations in InGaN have been studied by a number of laboratories³⁻⁹ showing how these fluctuations depend on the growth conditions. In our previous studies, ^{10,11} we have proven that In-incorporation depends on misorientation of the substrate with respect to the (001) direction. As the structural quality of InGaN is never perfect and local

misorientations vary in space, one always deals with In-fluctuations. The scale and microstructure of these fluctuations are by no means easy to determine in spite of the different analytical methods used in such studies. These methods are:

- (1) Photoluminescence (PL). Through examination of the PL peak position *versus* temperature (0–300 K) one can observe the so-called S-shape¹² which is a qualitative indication of the Influctuations. Moreover, by a comparison of the PL peak position and the average In-content measured using X-ray diffraction one can detect In-fluctuations, as the photon emission is usually from the areas of the highest In-content.
- (2) Cathodoluminescence (CL). This is a similar method to PL, but using CL one can additionally construct topographs with about 100 nm resolution visualizing the In-fluctuations.
- (3) X-ray Diffraction (XRD). There are two ways of tracing Influctuations using this method: by measuring the InGaN peak intensity¹³ and by measuring the diffuse scattering.¹⁴
- (4) Transmission Electron Microscopy (TEM). This is the most direct way of measuring the In-fluctuations in the nanometer scale. Techniques such as atom-probe microscopy, high angle annular dark field scanning electron microscopy (HAADF STEM),¹⁵ or high resolution transmission electron microscopy, sometimes combined with the digital analysis of lattice images (HRTEM DALI), can be used.¹⁶

In order to construct a microscopic model of In-fluctuations in InGaN QWs, one should use all methods described above, as every one of them is sensitive to different spatial scales and none of them provide all information needed.

In this paper, we show that ultra-shallow depth profiling combined with lateral imaging provided by modern Secondary Ion Mass Spectrometry (SIMS) allows supplementary information about the three dimensional distribution of indium

^aLukasiewicz Research Network, Institute of Electronic Materials Technology, Wólczyńska 133, 01-919 Warsaw, Poland. E-mail: pawel.michalowski@itme.edu.pl ^bInstitute of High Pressure Physics, Polish Academy of Sciences, Sokolowska 29/37, 01-142, Warsaw, Poland

^cTopGaN Ltd., Sokolowska 29/37, 01-142, Warsaw, Poland

^dNational Centre for Nuclear Research, Soltana 7, 05-400 Otwock, Poland

Paper JAAS

concentration in InGaN QWs to be obtained. While the technique is widely used to determine the elemental composition of a sample, ^{17–22} measurements of ultra-thin layers require subnanometer depth resolution. In our previous studies we have already presented such superior resolution for 2D materials, ^{23–30} superlattices ³¹ and quantum wells. ³²

2 Experimental

2.1 Sample preparation

The sample consisted of 5 InGaN quantum wells grown using a home-made 2-inch MOVPE vertical reactor. The growth conditions were: 720 °C, 500 mbar, TEGa flow of 200 sccm, TMIn flow of 400 sccm. The growth rate of QWs was 3.6 nm min⁻¹. The order number of each QW correlates with the growth sequence.

2.2 X-ray diffraction

A high resolution X-ray diffraction method was used for structural sample characterization. Measurements were performed with an Empyrean (Malvern Panalytical) X-ray diffractometer operating with Cu K α 1 radiation, equipped with a hybrid 2bounce monochromator and a threefold Ge(220) analyzer.

2.3 Photoluminescence

The PL measurements were performed at T=13 K. PL was excited by the 320 nm line of a DPSS laser with a power density of about 5 W cm⁻². The emission from the samples was collected in backscattering geometry and dispersed using a SPEX500 spectrometer and detected with a charge coupled device camera (CCD).

2.4 Transmission electron microscopy

The transmission electron microscopy and scanning transmission microscopy (STEM) studies were performed on FEI microscopes – Tecnai G20 and Titan Cubed 80-300.

2.5 Secondary ion mass spectrometry

In this work all SIMS measurements were performed employing a CAMECA SC Ultra instrument under ultra-high vacuum (UHV), usually of 4×10^{-10} mbar. Sufficient depth resolution was obtained for negative ion detection mode by using a low impact energy of 100 eV for a Cs⁺ primary beam rastered over $250 \times 250 \,\mu\text{m}^2$. The analysis area was limited to $200 \times 200 \,\mu\text{m}^2$. The SC Ultra tool is able to achieve such low impact energies due to the EXLIE (EXtra Low Impact Energy) technology, in the case of which a primary floating column concept is used.33 In this notion, contrary to standard SIMS tools, the primary column has a "floating voltage" instead of the grounded voltage level between the space at any two lenses inside the column and thus primary ions are slowed down at the end of the column maintaining favorable conditions for ion acceleration and beam stability. The ion beam on the sample in the SC Ultra tool has a square shape and due to the "variable rectangular shape concept" forms a homogeneous spot. The primary beam at a working point in the SC Ultra is formed by two stencils – well-shaped apertures. While the first one is used to choose the most intense and homogeneous part of the ion beam, the second one changes the size of the spot. These innovations allow one to use the low impact energy of primary ions with high sensitivity for all elements measured, high depth resolution (below 1 nm), and high dynamic range with a low sputter rate. 34,35

3 Results and discussion

Fig. 1 shows the XRD scan of the (002) reflection with the simulation for a perfect epitaxial structure: InGaN QWs with an average In content of 9% and a thickness of 2 nm; GaN barrier thickness of 7 nm. Simulations were performed using Epitaxy software (Malvern Panalytical) and are in good agreement with the measured pattern. However, we were not able to detect Influctuations because of two reasons: (i) the InGaN zeroth-order overlaps the GaN peak and we could not precisely examine the peak height,¹³ and (ii) the theory relating the diffuse scattering to In-fluctuations that has been proposed by us¹⁴ so far is validated only for thick InGaN layers.

Fig. 2 shows the PL data obtained at temperatures of 15–450 K. At room temperature, we observe a peak at 492 nm that corresponds to an In-content of about 20%. Compared to XRD data which show an average In concentration of 9%, it is evident that the sample should contain indium fluctuations as the PL emission usually takes place from areas of the smallest bandgap (the largest In concentration). The PL peak is rather broad: the FWHM (Full Width at Half Maximum) is 42 nm, two times broader than that for typical samples emitting at that wavelength.

Low temperature data show that the PL peaks consist of two peaks: e1 at about 420 nm and e2 at about 480 nm (we performed deconvolution using Gaussian-shape peaks) corresponding to In concentrations of about 11% and 19%, respectively. At the right-hand side of Fig. 2, it is shown how the

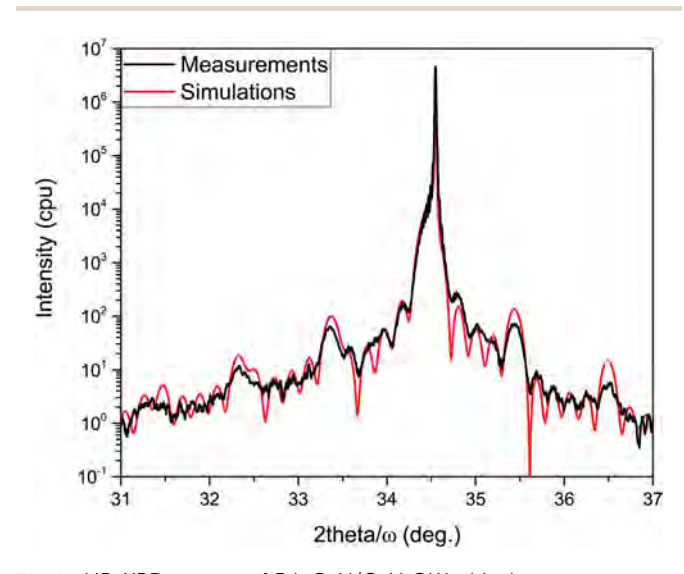


Fig. 1 HR-XRD pattern of 5 InGaN/GaN QWs, black – measurement and red – simulation.

JAAS Paper

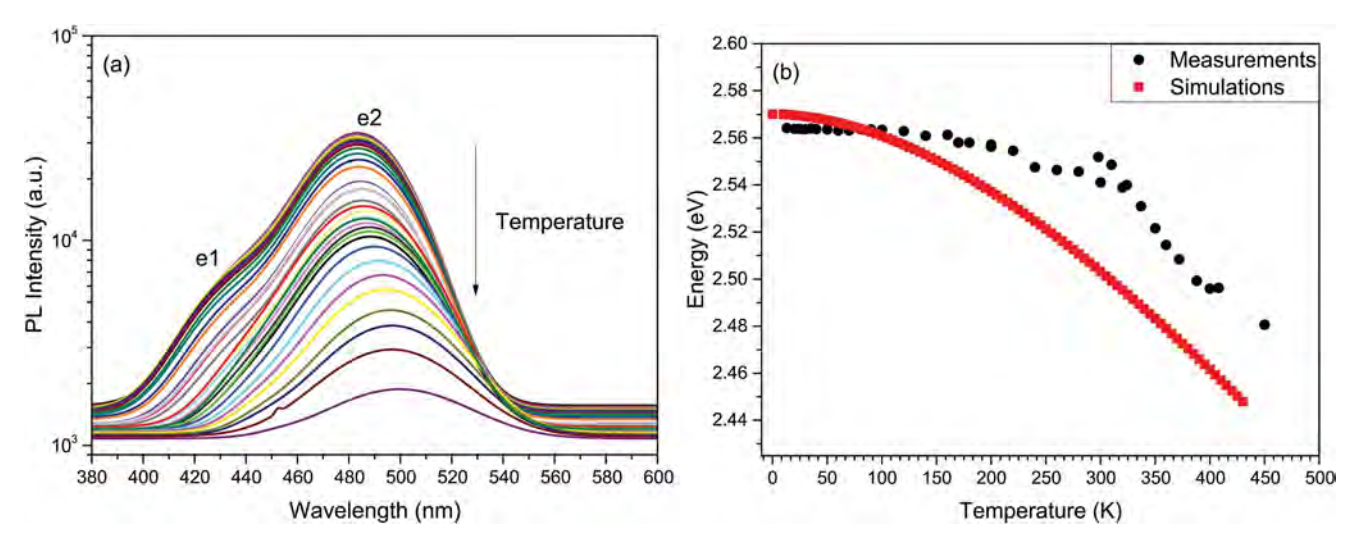


Fig. 2 Temperature dependence of photoluminescence PL(T): (a) spectra measured at temperatures ranging from 13 K up to 450 K reveal clear evidence of "two phases" with low and high In concentrations and as a consequence it emits at 415 nm and 490 nm wavelengths, and (b) temperature dependence of emitted energy maxima showing large localization.

position of the e2 peak changes with temperature. Comparing the dependence of the energy gap *versus* temperature, one may conclude that the sample contains energy-band gap spatial variations which disappear at temperatures as high as 300 K. Although based on the PL data one can deduce that In fluctuations are present, it is impossible to devise a microscopic model of such fluctuations. Such a model in the nanoscale is possible using TEM – the topograph is shown in Fig. 3.

Different contrast for the first, second, *etc.* quantum wells is due to sample preparation. In the topograph, the undulations seen are not caused by variation of the QW thickness (which is 2 nm in accordance with the XRD data) but by variation of In concentration. The numerical analysis of this topograph indicates that these variations can explain the PL data (peaks e1 and e2). TEM topographs provide information on In-fluctuations in the nanometer scale. However, such fluctuations can be also present in a much larger scale and to prove this we have used SIMS.

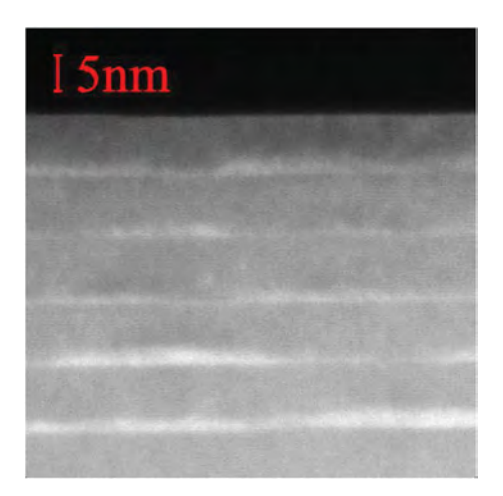


Fig. 3 TEM topograph of 5 InGaN/GaN QWs.

A sufficiently low primary ion impact energy provides good enough depth resolution to precisely profile the InGaN/GaN quantum well/barrier structure as presented in Fig. 4. InGaN and GaN materials have different etching rates and thus the profile is not depth calibrated to avoid stretching and compressing of signals which significantly reduces the clearness of the presented data. A normalized In signal (black line) reveals that the first and the last quantum wells have a slightly different composition than the other ones: they contain 5% and 20% less indium, respectively. These discrepancies, however, cannot explain the unexpected luminescence behavior of the sample

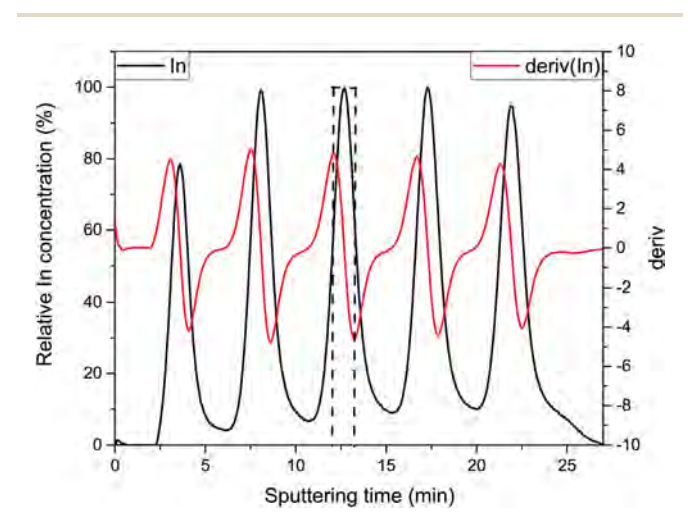


Fig. 4 Depth profile of the InGaN/GaN quantum well/barrier structure. Due to SIMS related artifacts the shape of the indium signal (black line) is Gaussian and not rectangular as it should be in an ideal situation. The analysis of a derivative of the In signal (red line) allows to define the beginning and the end of the quantum well to be defined – at the local extrema. A dashed line shows the region selected for lateral analysis. Note: an erosion during the SIMS analysis occurs in the opposite direction to the growth process and thus the first well is the last one measured (about 22 min of the sputtering time).

Paper JAAS

(cf. Fig. 2) and thus lateral imaging has to be performed to estimate In fluctuations within the quantum well.

This task, however, is far from being trivial. Due to the mixing effect, non-effective sputtering and changing of the ionization probability the shape of the indium signal is Gaussian and not rectangular as it should be in an ideal situation. It is therefore essential to define a part of the depth profile which should be used for lateral analysis. Although this choice is mostly arbitrary it is essential to assure the same definition for the whole experiment. It is therefore useful to analyze a derivative of the In signal (red line in Fig. 4). The local extrema are a good choice because they correspond to locations where the signal starts to stabilize and thus SIMS related artifacts are minimized. It is still necessary to perform point-topoint normalization of the In signal to reproduce the rectangular shape of the quantum well as shown in Fig. 4 by a dashed line. In this way no less than 66% of the central part of the quantum well can be analyzed laterally with minimized artifacts.

This approach has proven to be effective. Fig. 5A and B present the lateral distribution of In at the top part (closest to the surface) and at the bottom part (closest to the substrate) of the analyzed part of the middle quantum well, respectively. It is apparent that while the top part seems to be homogeneous a clear In fluctuation can be detected at the bottom of the analyzed part of the quantum well. Similar pictures have been taken for the remaining quantum wells. It should be emphasized that this result is particularly important as a proof that SIMS-related artifacts have been minimized: if the top part contained In fluctuation while the bottom one was homogeneous it would be possible that the mixing effect caused homogenization of the image. In this case, however, it is the first part that is homogeneous and deeper fluctuations occur. It is very improbable that SIMS could have caused such artifacts and therefore it can be concluded that SIMS is capable of monitoring In fluctuations within InGaN quantum wells.

Even though this is an important achievement the quality of the obtained pictures is not satisfactory. Moreover, simple noise reduction using Fourier transform does produce significant improvement. This is not surprising because each of these pictures represents a lateral distribution of In in a slice of the quantum well with a thickness of a fraction of one nanometer and thus there is not enough data to improve the signal-to-noise ratio. Usually SIMS lateral imaging is averaged over some depth and thus a better contrast can be achieved. In this case, however, such an approach cannot be applied as the whole quantum well is only 2 nm thick. It has been therefore concluded that to increase the contrast it is better to present the result as a ZX cross-sectional view with an In signal averaged over 20 µm in the Y direction. Red dashed lines in Fig. 5 show a slice of the image that has been used to average the signal and to produce a cross-sectional view. We have tested many possibilities and while most of them significantly increased signal-tonoise ratios for further analysis we have chosen the boundaries shown in Fig. 5 because they provide the best quality crosssectional view which is presented in Fig. 6.

One can note that this approach significantly increases the signal contrast. It becomes apparent that the top part of the quantum well contains In fluctuations as well, which is not visible in standard XY imaging (Fig. 5A). For such an averaged image it is not easy to determine lateral/depth resolutions, and only some estimations can be performed: the lateral resolution is predominantly influenced by the size of the primary beam which is about 1 $\mu m \times 1~\mu m$. For the depth resolution a good indication is a change in the root mean square (RMS) roughness of the crater after the analysis. For this experiment this change has been found to be about 0.2 nm.

Concentration calibration has been performed based on analysis of several thick InGaN samples with a known concentration. Analysis of the cross-sectional view reveals that there are three distinct regions in the quantum well:

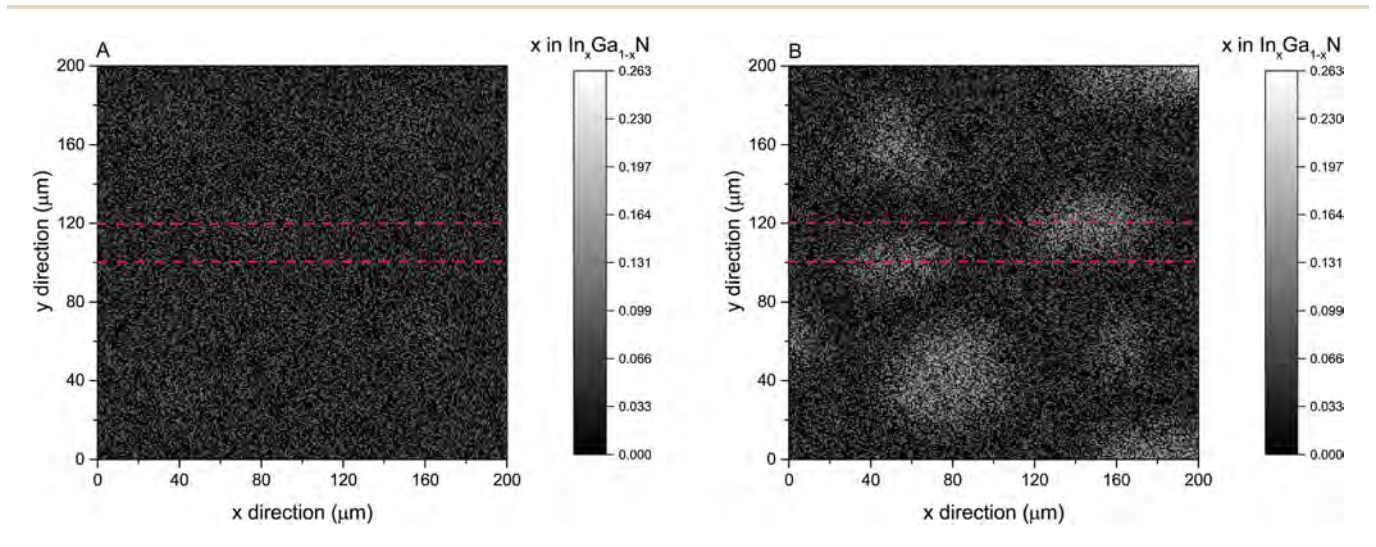


Fig. 5 Lateral distribution of In at the top (part A) and at the bottom (part B) of the analyzed part of the middle quantum well. Even though the signal-to-noise ratio is rather poor In segregation at the bottom of the quantum well is apparent. Dashed lines present a region which has been used for the cross-sectional view.

JAAS Paper

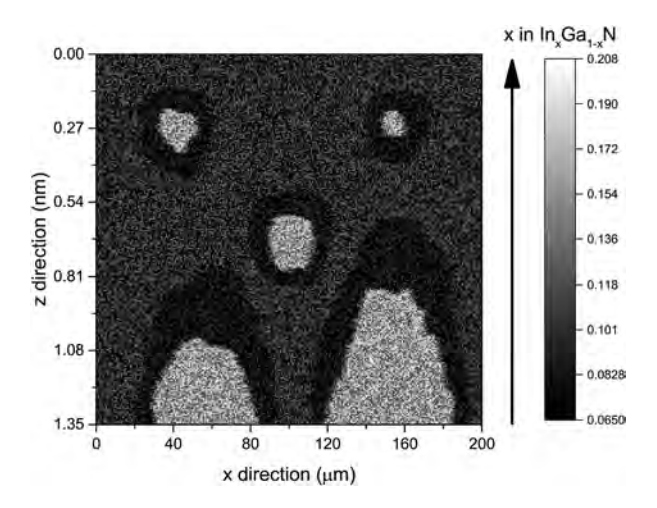


Fig. 6 Cross-sectional view of In distribution in a InGaN QW. Pronounced In concentration fluctuation can be observed. Inenriched regions are surrounded by In-depleted regions, which reflect In segregation. Indium segregation occurs predominantly in lateral directions as the total z-scale is about 1.35 nm while the x-scale is 200 μ m. The arrow indicates the QW growth direction.

- (1) Most of the quantum well is homogeneous with an average In content in the range of 9–11%.
- (2) In-enriched regions with an average In content in the range of 17–20%.
- (3) In-depleted regions with an average In content in the range of 6–8%.

The SIMS results are in a very good agreement with other data. An average indium content measured using XRD is 9%. However, this value was obtained from simulations for perfect InGaN QWs without any indium fluctuations. In the case of the sample examined with large In fluctuations, we may expect the average indium content to be slightly higher (10-11%), because the InGaN peak is weaker than for the perfect QWs. In the case of PL, we attributed the peaks to an In content of 19% and 11%. However, the PL position depends not only on indium content in InGaN QWs, but also on their thickness (blue shift). Therefore, for very thin areas of the QWs, we may expect the indium content to be higher than 19%. One must be also aware of the fact that the luminescence occurs from the areas of the smallest band gaps (largest indium content); however, this depends strongly on the length-scales of the fluctuations and diffusion lengths of holes and electrons created by laser photons used for PL stimulation.

4 Conclusions

Indium concentration fluctuations in InGaN/GaN QWs have been detected by means of different complementary techniques. Some of them give either only qualitative information (PL), or are not very sensitive to In-fluctuations (XRD), or give information at different length-scales (TEM). We have shown that modern SIMS is a very powerful tool for the study of Influctuations in InGaN quantum wells which allows a much larger area ($200 \times 200 \ \mu m^2$) to be tested. Even though the depth

resolution is determined by the size of the primary beam and can be estimated to be about 1 μm it is possible to achieve a very good depth resolution (0.2 nm) which allows very precise imaging. While XRD measurements suggest that the average In concentration is about 9%, SIMS analysis reveals regions with lower and much higher indium contents (6% and 20% respectively). Such an accuracy may prove to be valuable for further development of growth and processing procedures of InGaN quantum wells.

Conflicts of interest

There are no conflicts to declare.

Acknowledgements

The first author was supported by the National Science Centre within the SONATA14 2018/31/D/ST5/00399 project. The authors from the Institute of High Pressure Physics thank the TEAM/2016-3/26 project carried out within the TEAM programme of the Foundation for Polish Science co-financed by the European Union under the European Regional Development Fund and the grant no. 2015/17/B/ST5/02835 of the Polish National Science Centre.

References

- 1 J. Cho, J. H. Park, J. K. Kim and E. F. Schubert, *Laser Photonics Rev.*, 2017, **11**, 1600147.
- 2 J. J. Wierer Jr, J. Y. Tsao and D. S. Sizov, *Laser Photonics Rev.*, 2013, 7, 963–993.
- 3 S. Y. Karpov, *Photonics Res.*, 2017, 5, A7-A12.
- 4 N. Duxbury, U. Bangert, P. Dawson, E. J. Thrush, W. Van der Stricht, K. Jacobs and I. Moerman, *Appl. Phys. Lett.*, 2000, **76**, 1600–1602.
- 5 Z. Deng, Y. Jiang, W. Wang, L. Cheng, W. Li, W. Lu, H. Jia, W. Liu, J. Zhou and H. Chen, *Sci. Rep.*, 2014, 4, 6734.
- 6 J. Takatsu, B. Mitchell, A. Koizumi, S. Yamanaka, M. Matsuda, T. Gregorkiewicz, T. Kojima and Y. Fujiwara, J. Cryst. Growth, 2017, 468, 831–834.
- 7 M. K. Horton, S. Rhode, S.-L. Sahonta, M. J. Kappers, S. J. Haigh, T. J. Pennycook, C. J. Humphreys, R. O. Dusane and M. A. Moram, *Nano Lett.*, 2015, 15, 923–930.
- 8 K. Pantzas, G. Patriarche, D. Troadec, M. Kociak, N. Cherkashin, M. Hytch, J. Barjon, C. Tanguy, T. Rivera, S. Suresh and A. Ougazzaden, *J. Appl. Phys.*, 2015, **117**, 055705.
- 9 M. Auf der Maur, A. Pecchia, G. Penazzi, W. Rodrigues and A. Di Carlo, *Phys. Rev. Lett.*, 2016, **116**, 027401.
- 10 M. Sarzynski, M. Leszczynski, M. Krysko, J. Z. Domagala, R. Czernecki and T. Suski, *Cryst. Res. Technol.*, 2012, 47, 321–328.
- 11 M. Leszczynski, R. Czernecki, S. Krukowski, M. Krysko, G. Targowski, P. Prystawko, J. Plesiewicz, P. Perlin and T. Suski, J. Cryst. Growth, 2011, 318, 496–499.

Paper JAAS

- 12 Y.-H. Cho, G. H. Gainer, A. J. Fischer, J. J. Song, S. Keller, U. K. Mishra and S. P. DenBaars, *Appl. Phys. Lett.*, 1998, 73, 1370–1372.
- 13 M. Krysko, E. Grzanka, J. Domagala and M. Leszczynski, *Cryst. Res. Technol.*, 2015, **50**, 759–763.
- 14 V. Holý, M. Kryško and M. Leszczyński, *J. Appl. Crystallogr.*, 2018, 51, 969–981.
- 15 T. Mehrtens, M. Schowalter, D. Tytko, P. Choi, D. Raabe, L. Hoffmann, H. JÃűnen, U. Rossow, A. Hangleiter and A. Rosenauer, Appl. Phys. Lett., 2013, 102, 132112.
- 16 V. Potin, E. Hahn, A. Rosenauer, D. Gerthsen, B. Kuhn, F. Scholz, A. Dussaigne, B. Damilano and N. Grandjean, J. Cryst. Growth, 2004, 262, 145–150.
- 17 C. A. Andersen and J. R. Hinthorne, *Science*, 1972, 175, 853–860
- 18 A. Benninghoven, Surf. Sci., 1975, 53, 596-625.
- 19 A. Benninghoven, F. G. Rudenauer and H. W. Werner, Secondary ion mass spectrometry: basic concepts, instrumental aspects, applications and trends, John Wiley & Sons, New York, 1987.
- 20 H. W. Werner, Surf. Sci., 1975, 47, 301-323.
- 21 H. Liebl, J. Vac. Sci. Technol., A, 1975, 12, 385.
- 22 H. Liebl, J. Appl. Phys., 1967, 38, 5277-5283.
- 23 P. P. Michałowski, W. Kaszub, A. Merkulov and W. Strupinski, *Appl. Phys. Lett.*, 2016, **109**, 011904.
- 24 P. P. Michałowski, W. Kaszub, I. Pasternak and W. Strupinski, *Sci. Rep.*, 2017, 7, 7479.

- 25 P. P. Michałowski, I. Pasternak and W. Strupinski, *Nanotechnology*, 2018, **29**, 015702.
- 26 P. P. Michałowski, I. Pasternak, P. Ciepielewski, F. Guinea and W. Strupinski, *Nanotechnology*, 2018, **29**, 305302.
- 27 J. Grzonka, I. Pasternak, P. P. Michałowski, V. Kolkovsky and W. Strupinski, *Appl. Surf. Sci.*, 2018, 447, 582.
- 28 P. A. Caban, D. Teklinska, P. P. Michalowski, J. Gaca, M. Wojcik, J. Grzonka, P. Ciepielewski, M. Mozdzonek and J. M. Baranowski, J. Cryst. Growth, 2018, 498, 71.
- 29 P. P. Michałowski, P. Caban and J. Baranowski, *J. Anal. At. Spectrom.*, 2019, 34, 848–853.
- 30 P. P. Michałowski, P. Knyps, P. Ciepielewski, P. Caban, E. Dumiszewska and J. Baranowski, *Phys. Chem. Chem. Phys.*, 2019, 21, 8837–8842.
- 31 P. Michałowski, P. Gutowski, D. Pierścińska, K. Pierściński, M. Bugajski and W. Strupiński, *Nanoscale*, 2017, **9**, 17571–17575.
- 32 P. Michałowski, S. Złotnik, J. Sitek, K. Rosiński and M. Rudziński, *Phys. Chem. Chem. Phys.*, 2018, **20**, 13890–13895.
- 33 CAMECA, CAMECA SC-Ultra, User's Guide, Genneviliers, 2005.
- 34 D. Kouzminov, A. Merkulov, E. Arevalo and H. J. Grossmann, *Surf. Interface Anal.*, 2013, **45**, 345–347.
- 35 A. Merkulov, Surf. Interface Anal., 2013, 45, 90-92.

JAAS



COMMUNICATION



Cite this: *J. Anal. At. Spectrom.*, 2019, **34**, 1954

Received 28th June 2019 Accepted 2nd September 2019

DOI: 10.1039/c9ja00223e

rsc.li/jaas

Probing a chemical state during ultra low impact energy secondary ion mass spectrometry depth profiling

Paweł Piotr Michałowski **

A procedure to probe a chemical state during ultra low impact energy secondary ion mass spectrometry depth profiling is presented. For impact energies in the range of 90–150 eV the sputtering process is significantly different from a standard SIMS experiment (impact energy of 1 keV and above): each primary ion carries so little energy that breaking of strong covalent bonds is inefficient. Thus, formation of polyatomic ions is enhanced but only if atoms which are part of these ions have been bonded and not only located in a vicinity to each other. This can be used to obtain qualitative information about the types of bonds present in a sample. Annealed titanium and indium films deposited on silicon dioxide have been compared. The procedure reveals formation of oxides but in the case of titanium a clear indication of silicide formation can also be seen. The procedure is therefore beneficial for analysis of phenomena occurring at the nanoscale.

Ultra low impact energy secondary ion mass spectrometry (SIMS) depth profiling allows us to reach subnanometer depth resolution. Some previous studies present such a superior resolution for 2D materials. However, typical dynamic SIMS measurements are used to determine the elemental composition of a sample with little or no information about its chemical state. Time-of-flight SIMS is commonly used to quantitatively analyse and identify organic molecules, even depth profiling of organic films is possible but with relatively poor depth resolution (8–12 nm). This work shows that for ultra low impact energies it is possible to obtain qualitative information about chemical bonds present in inorganic samples while still maintaining subnanometer depth resolution.

SIMS measurements were performed employing the CAMECA SC Ultra instrument under ultra-high vacuum (UHV), usually of 4×10^{-10} mbar or in an oxygen flooded environment (the pressure in the chamber can be changed within a range of 4×10^{-10} to 1×10^{-6} mbar). Negative ion detection mode for two

Eukasiewicz Research Network-Institute of Electronic Materials Technology, Wólczyńska 133, 01-919 Warsaw, Poland. E-mail: pawel.michalowski@itme.edu.pl

different impact energies was used: 100 eV and 1000 eV. Cs^+ primary beam was rastered over $250 \times 250 \ \mu\text{m}^2$ and the analysis area was limited to $200 \times 200 \ \mu\text{m}^2$.

It has been experimentally noted that the sputtering process is significantly different while using ultra low impact energy (in the range of 90-150 eV). In typical SIMS experiments (impact energy 500 eV and above) signals coming from monoatomic ions usually have the highest intensity while for cluster ions signals are typically at least an order of magnitude less intense. Fig. 1A (black bars) presents the normalized intensities of Si⁻, SiO⁻, Si₂O⁻ and SiO₂⁻ for 1 keV impact energy (the results are very similar for higher energies as well) for a silicon dioxide sample. As it can be seen the intensity of Si⁻ signal constitutes 85% of all registered counts. The second most intense signal -SiO is almost 10 times weaker. The situation, however, is much different for ultra low impact energies. Red bars represent similar experiments but performed with an impact energy of 100 eV. The normalized intensity of Si⁻ ion drops to about 50% and the intensity of polyatomic ions significantly increases.

The interpretation of these observations is not easy. As the intensity of secondary ion signals depends on ionization probability and partial sputter yield (number of species emitted per primary ion) it is hard to predicate whether ultra low impact energy bombardment changes the ionization probability or/and partial sputter yield. To verify it additional experiments have been devised: instead of SiO2 pure silicon sample has been used (see Fig. 1B). Obviously in this case only Si ions have been registered (black and red bars for 1000 eV and 100 eV, respectively). In the next step oxygen flooding has been introduced.12 In such a case polyatomic ions have been registered (black and red bars with blue lines for 1000 eV and 100 eV, respectively) but no significant difference between impact energies has been observed. Even changing the flooding pressure (and thus amount of oxygen present at the sample surface) has little impact on normalized intensities - they are almost identical for both, standard and ultra low impact energies. This experiment alone, however, can prove nothing as oxygen flooding does influence negative ionization probability. Therefore the oxygen

Communication JAAS

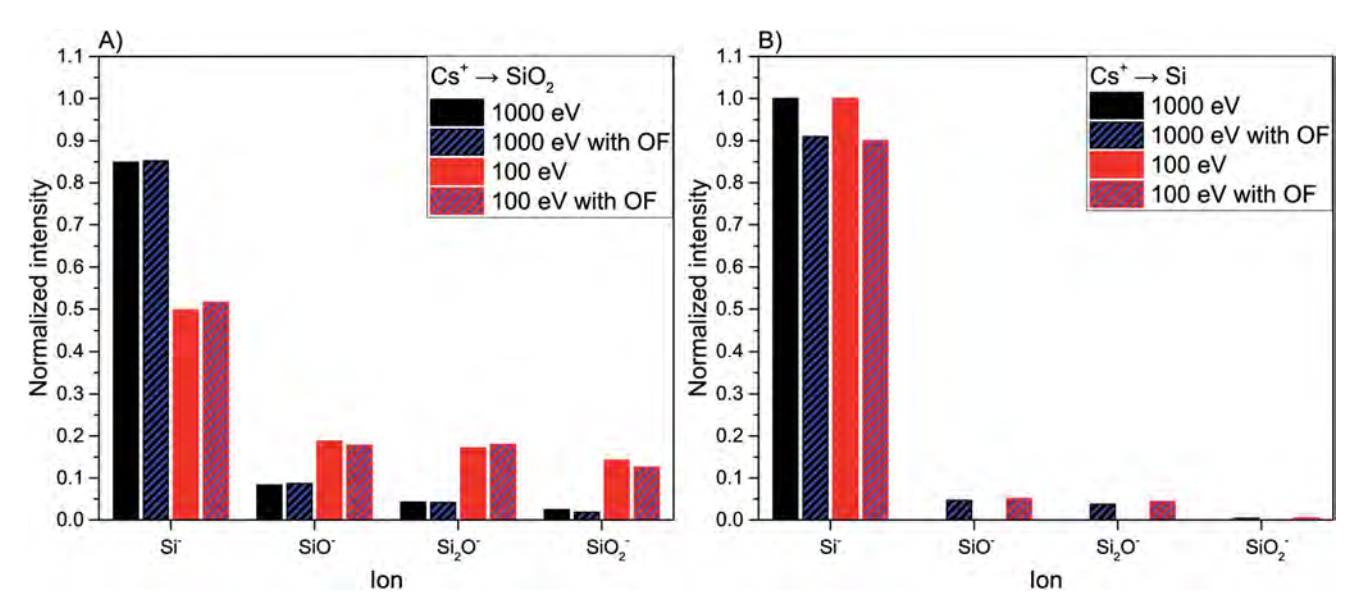


Fig. 1 Relative intensities of four ions are compared. (A) Experiments on silicon dioxide. For 1000 eV impact energy (black bars) the intensity of Si⁻ signal is by far the highest while for 100 eV impact energy (red bars) polyatomic ions are of much higher intensity. Oxygen flooding (OF) has no significant influence on the experiment (bars with blue lines). (B) Experiments on silicon. Without oxygen flooding (black and red bars for 1000 eV and 100 eV impact energy, respectively) only Si⁻ signal is registered. As expected, oxygen containing ions are only registered with oxygen flooding (bars with blue lines) but there is no difference between experiments with different impact energies and the intensity of Si⁻ signal is by far the highest.

flooding experiment has also been repeated for standard and ultra low impact energies for silicon dioxide sample (Fig. 1A black and red bars with blue lines for 1000 eV and 100 eV, respectively) but the results have not been different than previous experiments without oxygen flooding.

If ultra low impact energy was to change the ionization probability of polyatomic species then the experiment with oxygen flooded silicon would have shown enhanced formation of these ions. It is not the case and therefore it can be concluded that ultra low impact energy bombardment most probably has a significant impact on the partial sputter yield. This conclusion is consistent with this logic: for a standard SIMS experiment both the intensity of the beam and the impact energy of primary ions are high enough to effectively fragment the sputtered matter and thus monoatomic species are most abundant. For the ultra low impact energy experiment, even if the intensity of the beam is the same, the total number of sputtered species is significantly lower. It is not surprising as each primary ion has little energy to transfer to atoms of the bombarded sample. In such a case breaking all bonds (especially covalent) is far from effective and thus a probability to sputter larger species is higher. The experiment with oxygen flooding confirms it as in this case oxygen and silicon atoms are only brought nearer to each other, no/few bonds are created. Thus, there is no difference between standard and ultra low impact experiments. For silicon dioxide sample strong bonds between oxygen and silicon do exist and thus the emission of species containing several of these atoms is more probable for ultra low impact energy experiments. It should be emphasized that such experiments provide only very general qualitative information. It is not possible to determine the exact oxidation state, just a suggestion that a strong bond between particular atoms exists in the sample.

The usefulness of this method has been verified on 50 nm thick titanium film evaporated on silicon dioxide and annealed at 350 °C for ten minutes – see Fig. 2. If only standard ions were registered (Ti⁻, O⁻, Si⁻) only a very general remark about silicon and oxygen diffusion into Ti films would be possible to make. Including TiSi⁻ and TiO⁻ signals, however, provides additional information. Close to the interface between silicon dioxide and titanium film (depth 48–50 nm) only TiSi⁻ is of relatively high intensity whereas only a few counts for TiO⁻ are registered, even

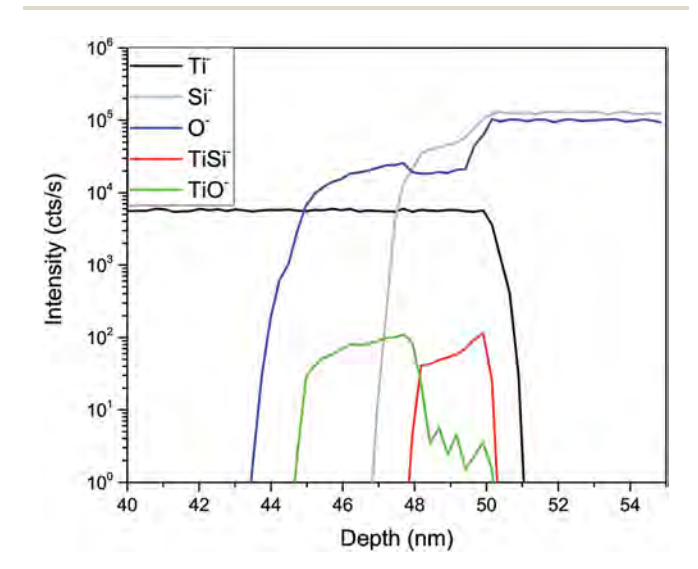


Fig. 2 Depth profile of annealed titanium film on silicon dioxide. The presence of TiSi⁻ and TiO⁻ allows us to precisely localize titanium silicide and titanium oxide.

JAAS Communication

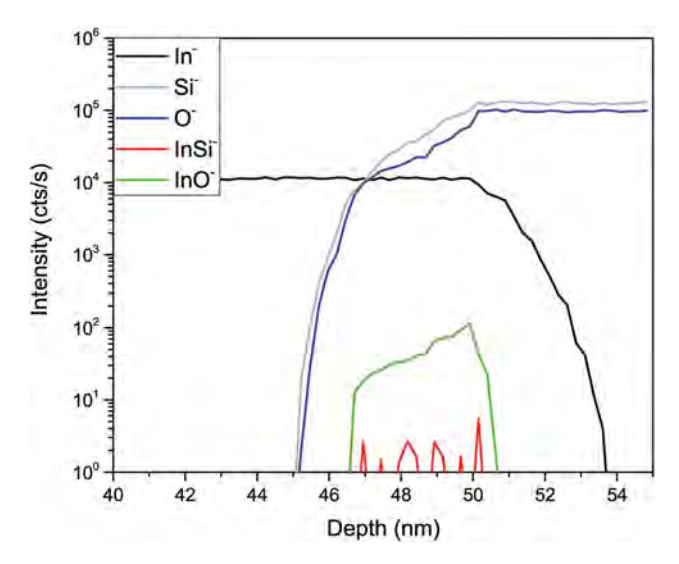


Fig. 3 Depth profile of annealed indium film on silicon dioxide. The presence of indium oxide is confirmed whereas no silicide can be detected.

though there are clearly a lot of oxygen and titanium atoms available. However, further away from the interface (depth 45–48 nm) the intensity of TiO⁻ signal is significantly higher. This experiment therefore suggests that thermal treatment leads to formation of titanium silicides at the interface and titanium oxide farther away. A similar behaviour occurring on a much larger scale has been confirmed by Auger electron spectroscopy.¹³ If indium is used instead of titanium (see Fig. 3) no silicide formation can be observed even though a clear diffusion of silicon can be seen – only indium oxide formation can be confirmed. This result further authenticates the proposed procedure as indium does not react with silicon.

The proposed procedure to probe the chemical state of titanium/indium thin films during ultra low impact energy experiments clearly cannot replace well established techniques like Auger electron spectroscopy, ^{13–16} X-ray photoelectron spectroscopy, ^{17–20} and Raman spectroscopy. ^{21–24} However, the depth resolution of these methods is limited and thus very small changes that have occurred during low temperature annealing cannot be resolved. SIMS experiments with ultra low impact energy are already known for subnanometer depth resolution and adding a few additional polyatomic signals does not impede the measurement. Additional qualitative information can be beneficial to characterize phenomena occurring at the nanoscale.

Conflicts of interest

There are no conflicts to declare.

Acknowledgements

This work was supported by the National Science Centre (NCN) within SONATA14 2018/31/D/ST5/00399 projects.

Notes and references

- 1 P. P. Michałowski, W. Kaszub, A. Merkulov and W. Strupinski, *Appl. Phys. Lett.*, 2016, **109**, 011904.
- 2 P. P. Michałowski, W. Kaszub, I. Pasternak and W. Strupinski, *Sci. Rep.*, 2017, 7, 7479.
- 3 P. P. Michałowski, I. Pasternak and W. Strupinski, *Nanotechnology*, 2018, **29**, 015702.
- 4 P. P. Michałowski, I. Pasternak, P. Ciepielewski, F. Guinea and W. Strupinski, *Nanotechnology*, 2018, **29**, 305302.
- 5 J. Grzonka, I. Pasternak, P. P. Michałowski, V. Kolkovsky and W. Strupinski, *Appl. Surf. Sci.*, 2018, 447, 582.
- 6 P. A. Caban, D. Teklinska, P. P. Michalowski, J. Gaca, M. Wojcik, J. Grzonka, P. Ciepielewski, M. Mozdzonek and J. M. Baranowski, *J. Cryst. Growth*, 2018, 498, 71.
- 7 P. P. Michałowski, P. Caban and J. Baranowski, *J. Anal. At. Spectrom.*, 2019, 34, 848–853.
- 8 P. P. Michałowski, P. Knyps, P. Ciepielewski, P. Caban, E. Dumiszewska and J. Baranowski, *Phys. Chem. Chem. Phys.*, 2019, **21**, 8837–8842.
- 9 J. Brison, S. Muramoto and D. G. Castner, J. Phys. Chem. C, 2010, 114, 5565–5573.
- 10 R. Havelund, M. P. Seah and I. S. Gilmore, J. Phys. Chem. B, 2016, 120, 2604–2611.
- 11 K. Nakano, T. Shibamori and K. Tajima, *ACS Omega*, 2018, 3, 1522–1528.
- 12 Y. Kudriatsev, A. Villegas, S. Gallardo, G. Ramirez, R. Asomoza and V. Mishurnuy, *Appl. Surf. Sci.*, 2008, **254**, 4961–4964.
- 13 L. J. Brillson, M. L. Slade, H. W. Richter, H. VanderPlas and R. T. Fulks, *J. Vac. Sci. Technol.*, A, 1986, 4, 993–997.
- 14 J. K. N. Sharma, B. R. Chakraborty and S. M. Shivaprasad, *J. Vac. Sci. Technol.*, A, 1988, 6, 3120–3124.
- 15 Z. Tass, G. Horvath and V. Josepovits, *Surf. Sci.*, 1995, 331–333, 272–276.
- 16 J. Ong and L. Lucas, Biomaterials, 1998, 19, 455-464.
- 17 P. Tam, Y. Cao and L. Nyborg, Surf. Sci., 2012, 606, 329-336.
- 18 P. Osiceanu, Appl. Surf. Sci., 2006, 253, 381-384.
- 19 C. E. Marino, P. A. Nascente, S. R. Biaggio, R. C. Rocha-Filho and N. Bocchi, *Thin Solid Films*, 2004, **468**, 109–112.
- 20 U. Diebold and T. E. Madey, *Surf. Sci. Spectra*, 1996, **4**, 227–231.
- 21 R. J. Nemanich, R. W. Fiordalice and H. Jeon, *IEEE J. Quantum Electron.*, 1989, **25**, 997–1002.
- 22 E. Lim, G. Karunasiri, S. Chua, Z. Shen, H. Wong, K. Pey, K. Lee and L. Chan, *Microelectron. Eng.*, 1998, 43–44, 611–617.
- 23 U. Balachandran and N. Eror, J. Solid State Chem., 1982, 42, 276–282.
- 24 E. Ekoi, A. Gowen, R. Dorrepaal and D. Dowling, *Results Phys.*, 2019, 12, 1574–1585.

JAAS



COMMUNICATION



Cite this: *J. Anal. At. Spectrom.*, 2020, **35**, 1047

Received 18th March 2020 Accepted 12th May 2020

DOI: 10.1039/d0ja00107d

rsc.li/jaas

Titanium pre-sputtering for an enhanced secondary ion mass spectrometry analysis of atmospheric gas elements

Paweł Piotr Michałowski **

Pre-sputtering before secondary ion mass spectrometry measurement is a well known technique to increase the detection limits of atmospheric gas elements: during a prolonged primary ion bombardment of a clean target a layer on the sample surface and the immersion lens is formed which decreases the re-implantation process of light elements and, as a consequence, improves the detection limits. Float zone silicon is the most commonly used target for the pre-sputtering process. In this work a metallic titanium block is considered as a suitable replacement of the pre-sputtering target. When compared to the silicon target the gettering properties of titanium allow one to reach better detection limits of hydrogen and oxygen whereas no significant improvement is observed for carbon and nitrogen. However, the optimal conditions are reached much faster for the Ti target which makes it a better choice, especially for ultra low energy measurements where standard detection limits of light elements are poor.

Improvement of the secondary ion mass spectrometry (SIMS) detection limits of atmospheric gas elements is an important topic for the global SIMS community1-9 and, more generally, for the semiconductor industry. The detection of these light elements is typically limited by a presence of residual gas present in the analysis chamber-thus the detection limit of atmospheric elements is usually defined as a background level registered during the profiling of a clean substrate. It is generally accepted that the best detection limits are achieved by reducing the pressure in the analysis chamber and increasing the sputter rate by increasing the primary beam density and decreasing the raster size - in this way a contribution of parasitic counts originating from residual gas present in the analysis chamber can be minimized.3,5 However, this also results in a severe degradation of the depth resolution and thus such approach cannot be applied to ultra thin films. Thus, Miwa et al.7 proposed additional improvement - pre-sputtering. In

Lukasiewicz Research Network-Institute of Electronic Materials Technology, Wólczyńska 133, 01-919 Warsaw, Poland. E-mail: pawel.michalowski@itme.edu.pl

this procedure, prior to the actual measurement, a clean target is sputtered for a long time with a dense and high energetic primary beam. Atoms sputtered from the target form a clean layer on the immersion lens (thickness in the range of several hundreds nanometers) and the sample surface (thickness in the range of several nanometers) which decreases the reimplantation process of light elements and, as a consequence, improves the detection limits. This approach has been optimized for measurements for which the sputtering rate was about 2 nm s⁻¹. However, nowadays much thinner materials (including 2D materials) are analyzed with SIMS and thus the benefit of the pre-sputtering may not be sufficient anymore. It should be noted that the pre-sputtering process is typically performed on any clean substrate (Miwa et al. used gallium arsenide substrate and float zone (FZ) silicon is commonly used nowadays). In this work a different pre-sputtering target, namely a metallic titanium block, is considered. This material not only provides a cover for the sample surface and the immersion lens but also can absorb water vapor and hydrogen even at room temperature.10 Thus the detection limit of oxygen and hydrogen can be further increased when compared to a standard pre-sputtering procedure.

All SIMS measurements were performed employing the CAMECA SC Ultra instrument. Cs^+ primary beam with impact energies of 13 keV and 100 eV and intensities of 50 nA and 5 nA were used for the pre-sputtering and measurements with subnanometer depth resolution, respectively. $^1H^-$, $^{12}C^-$, $^{28}Si^{14}N^-$ and $^{16}O^-$ species were measured to estimate hydrogen, carbon, nitrogen and oxygen detection limits, respectively. Three types of measurements were performed: with two different presputtering targets (titanium and FZ silicon) and without presputtering as a reference.

The type of the pre-sputtering target has a significant influence on the vacuum in the analysis chamber. As shown on Fig. 1 the initial value for both measurements has been 2.9×10^{-10} mbar. At the beginning of the silicon pre-sputtering the vacuum conditions slightly deteriorate (5.6 \times 10 $^{-10}$ mbar) and after ten minutes stabilizes at around 4×10^{-10} mbar which is a typical

JAAS Communication

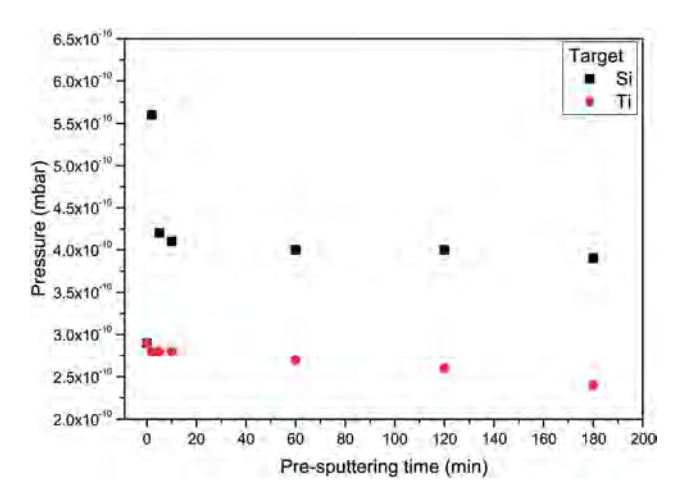


Fig. 1 Pressure in the analysis chamber during the pre-sputtering for Si and Ti targets. For Ti target the vacuum is slightly enhanced while for Si it deteriorates but after a while stabilizes at a reasonable level.

value for this tool. For titanium target no vacuum deterioration has been observed and the reading even dropped to 2.5×10^{-10} mbar after three hours. While the difference is relatively small this observation confirms that titanium has indeed absorbed some residual gases from the analysis chamber.

Fig. 2 compares depth profiles of silicon implanted with carbon and oxygen (parts A and B, respectively) for three types of measurements using the high energetic beam. It can be immediately noted that the detection limit of both, carbon and oxygen is the worse for the measurement without presputtering: 2.03×10^{17} atoms per cm³ and 2.41×10^{17} atoms per cm³, respectively. The type of the pre-sputtering target has no significant influence on the detection limit of carbon, as it has been found to be 5.02×10^{16} atoms per cm³ and 5.16×10^{16}

atoms per cm³ for Si and Ti targets, respectively. One can, however, observe an enhanced detection limit of oxygen for Ti target – 4.61×10^{16} atoms per cm³ while it is 1.07×10^{17} atoms per cm³ for Si target. Further experiments have revealed that the pre-sputtering of the Ti target improves the detection limit not only of oxygen but even more so of hydrogen. No significant difference has been observed for carbon and nitrogen. This is not surprising as titanium at room temperature may absorb hydrogen, water vapor and methane and only at elevated temperatures titanium absorbs oxygen, nitrogen and carbon dioxide¹⁰ which is a more common residual gas in the analysis chamber than methane.

Table 1 summarizes the background levels of light elements in silicon substrate for high impact energy measurements without and with both types of pre-sputtering targets. It can be noted that detection limits are worse than reported by Miwa et al.7 CAMECA SC Ultra instrument is not ideal for detection of light elements as its analysis chamber is about three times bigger when compared to other SIMS instruments manufactured by CAMECA and the primary beam is formed by projecting the Gaussian-shaped beam on a pair of square stencils which increases the uniformity but limits the maximum current.11 Thus, the contribution of parasitic counts originating from residual gas present in the analysis chamber cannot be efficiently minimized. Uncertainties of background levels determination are given for depth profiling mode (as presented on Fig. 2). However, high impact energy measurement are usually used for semi-bulk analysis where signals are integrated for a long time and uncertainties become much smaller and are in general of little concern.

The most important application of the proposed method is the analysis with sub-nanometer depth resolution. In this case the primary ion energy is reduced to very low values (100 eV) and thus the background contribution is considerable and, as

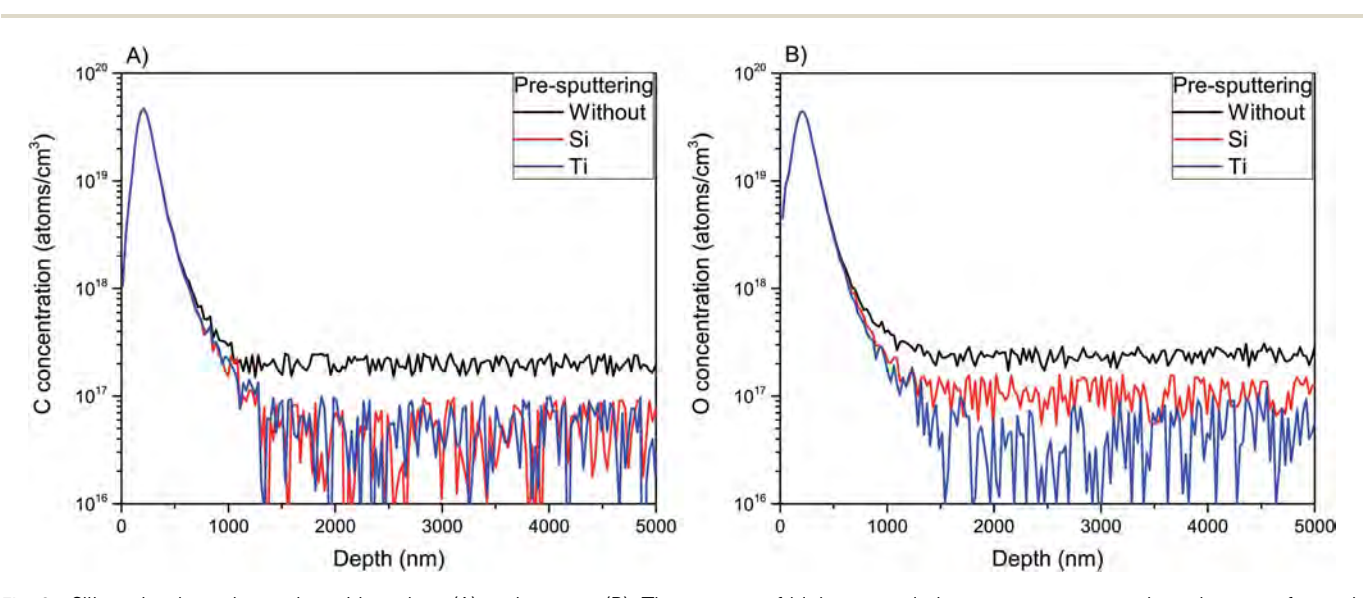


Fig. 2 Silicon implanted samples with carbon (A) and oxygen (B). Three types of high energetic beam measurements have been performed: without and with pre-sputtering (Si and Ti targets). Pre-sputtering enhances the detection limit of light elements but while for carbon the result is similar for both targets, oxygen detection limit is superior for Ti target. All profiles are limited to the part of the original Si substrate – no Si/Ti covering layer is shown.

Communication JAAS

Table 1 Background levels of light elements in silicon substrate for measurements with high impact energy. Results are presented for measurements without and with pre-sputtering for silicon and titanium targets. All values are presented in atoms per cm³

Element/target	Without	Si	Ti
Hydrogen Carbon Nitrogen Oxygen	$egin{array}{l} (1.40\pm0.28) imes10^{18} \ (2.03\pm0.28) imes10^{17} \ (8.43\pm2.43) imes10^{15} \ (2.41\pm0.30) imes10^{17} \end{array}$	$egin{array}{l} (8.45\pm2.94) imes10^{17} \ (5.02\pm2.79) imes10^{16} \ (3.21\pm2.51) imes10^{15} \ (1.07\pm0.31) imes10^{17} \end{array}$	$egin{array}{l} (4.99\pm3.2) imes10^{17} \ (5.16\pm2.75) imes10^{16} \ (3.18\pm2.49) imes10^{15} \ (4.61\pm3.56) imes10^{16} \end{array}$

a consequence, detection limits of light elements are much worse. Fig. 3 compares depth profiles of silicon implanted with carbon and oxygen (parts A and B, respectively) for low energetic beam measurements. It can be immediately noted that without pre-sputtering the quality of measurements is significantly reduced. Thus, pre-sputtering is essential to obtain acceptable sensitivity for measurements with extreme depth resolution. Similarly to high energy measurements titanium pre-sputtering is particularly important for the analysis of hydrogen and oxygen. Even though for carbon and nitrogen the results are similar to silicon pre-sputtering there is an additional benefit of using the Ti target: it takes only about twenty hours of pre-sputtering to reach optimal conditions for all light elements while fifty for the Si target.

Table 2 summarizes the background levels of light elements in silicon substrate for low impact energy measurements without and with both types of pre-sputtering targets. As expected, background levels are even worse for low energetic measurements – for such measurements the sputtering rate is much lower and thus the contribution of parasitic counts originating from residual gas present in the analysis chamber is significant. It should be, however, noted that Miwa *et al.*⁷ performed measurements with a sputtering rate of two nanometers per second whereas low impact energy measurements

presented in this work were performed with a sputtering rate of less than half a nanometer per minute. For such conditions there are eleven data points per one nanometer, the depth resolution for oxygen profiling is about 0.8 nm per decade (calculated for a profile after Ti pre-sputtering shown on Fig. 3B) and combining it with the detection limit of 8.45×10^{16} atoms per cm³ enables very precise characterization of ultra-thin films. However, in this case the uncertainty of the background level determination is an important factor to consider: if the concentration of atmospheric element in the sample is close to the background level a longer integration time is required to reduce uncertainty. Unfortunately, for longer integration times the number of data point per one nanometer will decrease and thus a proper characterization of particularly thin films may not be possible.

Furthermore, low energetic beam measurements can also be applied to 2D materials characterization. In such a case, however, the situation is non-trivial as introduction of the sample of interest and the pre-sputtering target on the same sample holder will result in covering of the 2D layer with Si/Ti which may damage or even destroy it. In some cases it can still be acceptable: when hydrogen intercalation process of graphene layers grown on various substrates was considered 12,13 the sample was covered with chromium layer anyway so

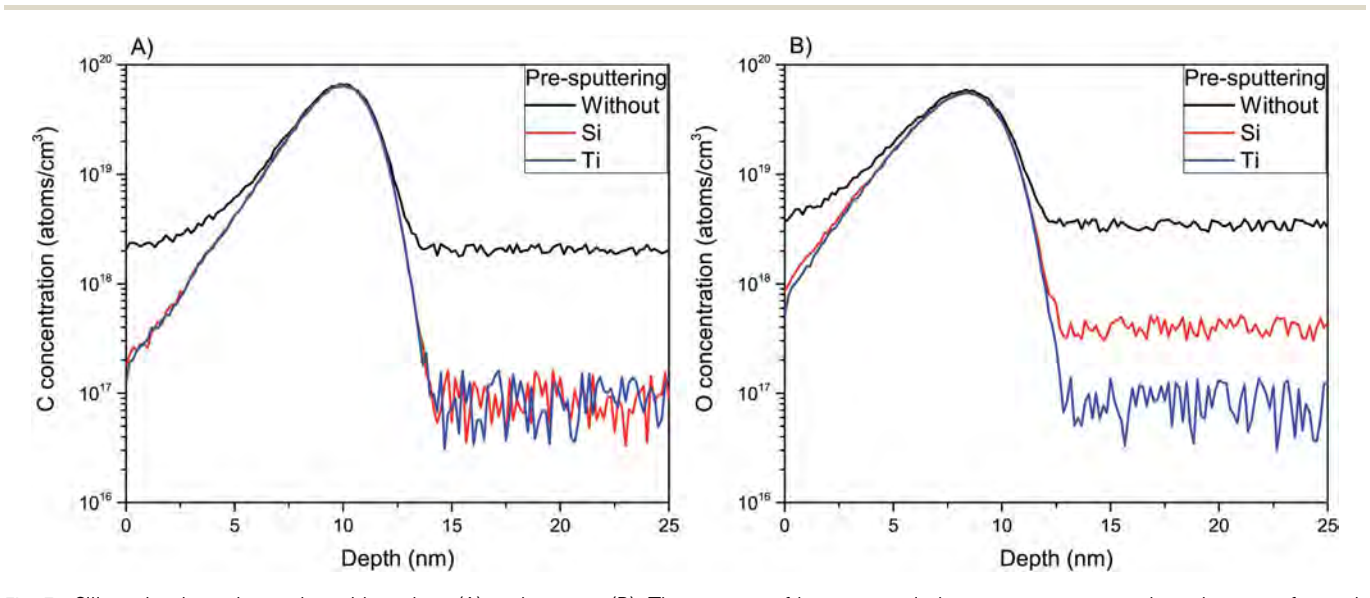


Fig. 3 Silicon implanted samples with carbon (A) and oxygen (B). Three types of low energetic beam measurements have been performed: without and with pre-sputtering (Si and Ti targets). Without pre-sputtering poor detection limits significantly reduce the quality of measurements. Similarly to high energetic beam measurements the type of the pre-sputting target has a significant/little impact on oxygen/carbon detection limits, respectively. All profiles are limited to the part of the original Si substrate – no Si/Ti covering layer is shown.

JAAS Communication

Table 2 Background levels of light elements in silicon substrate for measurements with low impact energies. Results are presented for measurements without and with pre-sputtering for silicon and titanium targets. All values are presented in atoms per cm³

Element/target	Without	Si	Ti
Hydrogen Carbon Nitrogen Oxygen	$egin{array}{l} (9.22\pm0.84) imes10^{18} \ (2.04\pm0.13) imes10^{18} \ (2.76\pm0.29) imes10^{17} \ (3.43\pm0.27) imes10^{18} \end{array}$	$egin{array}{l} (4.04\pm0.63) imes10^{18} \ (9.71\pm3.36) imes10^{16} \ (1.01\pm0.34) imes10^{16} \ (4.05\pm0.60) imes10^{17} \end{array}$	$\begin{array}{l} (9.04 \pm 5.42) \times 10^{17} \\ (9.65 \pm 3.60) \times 10^{16} \\ (1.02 \pm 0.32) \times 10^{16} \\ (8.45 \pm 3.34) \times 10^{16} \end{array}$

deposition of titanium during the pre-sputtering was not an issue. Similarly, for molybdenum sulfide sample¹⁴ it was the oxygen out-diffusion from a substrate that was considered and thus some damages of MoS₂ was acceptable.

However, in other cases, namely when residual contamination within graphene,15,16 and hexagonal boron nitride17-19 was considered such an approach was unacceptable. In such and similar situations it is better to mount the sample of interest and the pre-sputtering target on two separate sample holders and put them both into the load lock. The pre-sputtering target should be moved to the analysis chamber first and after the pre-sputtering interchanged with the holder containing the sample of interest. In this way a clean layer of Si/Ti will be formed on the immersion lens which will enhance detection limits of light elements whereas the surface of the sample of interest will remain intact. Unfortunately movement of sample holders between the analysis chamber and the load lock usually deteriorates vacuum conditions and thus it can be expected that the benefit of Ti pre-sputtering will be at least partially reduced. It is not possible to precisely estimate how big is the difference as the deterioration of vacuum conditions depends on a cleanliness of a sample holder and it cannot be reproduced.

It can be therefore concluded that titanium is a better presputtering target than FZ silicon or other clean substrates, especially for a detection of hydrogen and oxygen. It is particularly important for low energetic measurements with subnanometer depth resolution where typical detection limits of light elements are poor. It should be, however, emphasized that using this approach leads to titanium contamination of the secondary column and thus the detection limit of Ti may become worse for other measurements.

Conflicts of interest

There are no conflicts to declare.

Acknowledgements

This work was supported by the National Science Centre (NCN) within SONATA14 2018/31/D/ST5/00399 projects.

Notes and references

- 1 C. W. Magee and E. M. Botnick, *J. Vac. Sci. Technol.*, 1981, 19, 47.
- 2 K. Wittmaack, Nucl. Instrum. Methods Phys. Res., 1983, 218, 327.
- 3 J. Kobayashi, M. Nakajima and K. Ishida, *J. Vac. Sci. Technol.*, 1988, **6**, 86.
- 4 M. Meuris, W. Vandervorst and G. Borghs, *J. Vac. Sci. Technol.*, 1989, 7, 1663.
- 5 M. Gauneau, R. Chaplain, A. Rupert, M. Salvi and B. Descouts, *J. Vac. Sci. Technol.*, A, 1990, 8, 4039–4045.
- 6 H. Yamazaki, J. Vac. Sci. Technol., A, 1997, 15, 2542-2547.
- 7 S. Miwa, I. Nomachi and H. Kitajima, *Appl. Surf. Sci.*, 2006, **252**, 7247–7251.
- 8 P. Peres, A. Merkulov, F. Desse and M. Schuhmacher, *Surf. Interface Anal.*, 2011, 43, 643–645.
- 9 R. Jakiela, A. Barcz, J. Sarnecki and G. Celler, *Surf. Interface Anal.*, 2018, **50**, 729–733.
- 10 K. Pałka, R. Pokrowiecki and M. Krzywicka, in *Titanium for Consumer Applications*, ed. F. Froes, M. Qian and M. Niinomi, Elsevier, 2019, pp. 27–75.
- 11 CAMECA, Genneviliers, CAMECA SC-Ultra, User's Guide, 2005.
- 12 P. P. Michałowski, W. Kaszub, A. Merkulov and W. Strupinski, *Appl. Phys. Lett.*, 2016, **109**, 011904.
- 13 J. Grzonka, I. Pasternak, P. P. Michałowski, V. Kolkovsky and W. Strupinski, *Appl. Surf. Sci.*, 2018, **447**, 582.
- 14 P. P. Michałowski, P. Knyps, P. Ciepielewski, P. Caban, E. Dumiszewska and J. Baranowski, *Phys. Chem. Chem. Phys.*, 2019, 21, 8837–8842.
- 15 P. P. Michałowski, I. Pasternak and W. Strupinski, *Nanotechnology*, 2018, **29**, 015702.
- 16 P. P. Michałowski, I. Pasternak, P. Ciepielewski, F. Guinea and W. Strupinski, *Nanotechnology*, 2018, 29, 305302.
- 17 P. A. Caban, D. Teklinska, P. P. Michalowski, J. Gaca, M. Wojcik, J. Grzonka, P. Ciepielewski, M. Mozdzonek and J. M. Baranowski, J. Cryst. Growth, 2018, 498, 71.
- 18 P. P. Michałowski, P. Caban and J. Baranowski, *J. Anal. At. Spectrom.*, 2019, **34**, 848–853.
- 19 P. A. Caban, P. P. Michałowski, I. Wlasny, J. Gaca, M. Wojcik, P. Ciepielewski, D. Teklinska and J. Baranowski, *J. Alloys Compd.*, 2020, 815, 152364.

Video Article

3D Depth Profile Reconstruction of Segregated Impurities using Secondary Ion Mass Spectrometry

Paweł Piotr Michałowski¹, Sebastian Zlotnik¹, Iwona Jóźwik¹, Adrianna Chamryga¹, Mariusz Rudziński¹

¹Łukasiewicz Research Network-Institute of Electronic Materials Technology

Correspondence to: Paweł Piotr Michałowski at Pawel.Michalowski@itme.edu.pl

URL: https://www.jove.com/video/61065

DOI: doi:10.3791/61065

Keywords: Chemistry, Issue 158, secondary ion mass spectrometry, gallium nitride, defect selective etching, dislocation, impurity, oxygen

Date Published: 4/29/2020

Citation: Michałowski, P.P., Zlotnik, S., Jóźwik, I., Chamryga, A., Rudziński, M. 3D Depth Profile Reconstruction of Segregated Impurities using Secondary Ion Mass Spectrometry. *J. Vis. Exp.* (158), e61065, doi:10.3791/61065 (2020).

Abstract

The presented protocol combines excellent detection limits (1 ppm to 1 ppb) using secondary ion mass spectrometry (SIMS) with reasonable spatial resolution (~1 µm). Furthermore, it describes how to obtain realistic three-dimensional (3D) distributions of segregated impurities/ dopants in solid state materials. Direct 3D depth profile reconstruction is often difficult to achieve due to SIMS-related measurement artifacts. Presented here is a method to identify and solve this challenge. Three major issues are discussed, including the i) nonuniformity of the detector being compensated by flat-field correction; ii) vacuum background contribution (parasitic oxygen counts from residual gases present in the analysis chamber) being estimated and subtracted; and iii) performance of all steps within a stable timespan of the primary ion source. Wet chemical etching is used to reveal the position and types of dislocation in a material, then the SIMS result is superimposed on images obtained via scanning electron microscopy (SEM). Thus, the position of agglomerated impurities can be related to the position of certain defects. The method is fast and does not require sophisticated sample preparation stage; however, it requires a high-quality, stable ion source, and the entire measurement must be performed quickly to avoid deterioration of the primary beam parameters.

Introduction

Secondary ion mass spectrometry (SIMS) is a well-known technique used for contamination monitoring with excellent detection limits ^{1,2,3,4,5,6}. Vacuum background contribution can be problematic for light elements (e.g., hydrogen, carbon, nitrogen, oxygen), which may be present in the form of residual gases in a measurement chamber. Peres et al. previously established a technique to estimate background contribution; thus, a realistic concentration of contaminating atoms can be determined ⁷.

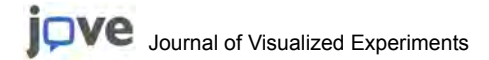
In many materials, the distribution of contaminating atoms is not uniform. The case of gallium nitride (GaN) is particularly interesting, as it is predicted that oxygen mainly decorates screw and mixed dislocations^{8,9,10,11}. Considering that most analytical methods lack sensitivity or spatial resolution to detect low concentration contaminating atoms, it is essential to develop a SIMS measurement procedure that is capable of 3D localization of segregated impurities¹².

While many SIMS spectrometers are equipped with position sensitive detectors, a direct three-dimensional (3D) reconstruction of a depth profile is insufficient to obtain realistic distribution of oxygen atoms in a GaN sample. Imperfection of the detector may distort the image and prevent researchers from obtaining a realistic distribution of contaminating atoms. However, a large problem is vacuum background contribution, as usually >90% of registered oxygen counts originate from residual gases present in the analysis chamber. Presented here is a method to identify and adequately solve each of these challenges.

Nonuniformity of the detector can be tested on a blank silicon wafer. Even a long integration time can lead to the observation of some secondary ion image nonuniformity, due to varying sensitivity of each channel in a microchannel plate detector. Therefore, flat-field correction is needed to obtain high-quality images of 3D distributions of segregated atoms.

Vacuum background contribution is related to a flux of contaminating atoms from the vacuum adsorbed onto the analyzing area. Considering that the process is dynamic (i.e., the sample surface is constantly sputtered by the primary beam), it can be assumed that each point of the analyzed area has the same probability to adsorb these oxygen atoms. Furthermore, they are almost immediately sputtered and do not have enough time to segregate. Therefore, a statistical approach is the most efficient. Random elimination of 90% (or more) of oxygen counts should reveal regions where oxygen is agglomerated.

It should be noted that the stability of the primary beam is crucial for this type of experiment. After some time, the intensity and homogeneity of the beam deteriorates, which reduces the quality of the image. It is therefore essential to estimate a timespan of stable operation of the beam and perform all experiments before the beam becomes unstable. The protocol can be easily used for other materials and detected elements at which nonuniform distribution is expected. It is particularly interesting to combine this with wet chemical etching, which reveals the positions and types of dislocation. Thus, the position of agglomerated impurities can be correlated to the position of defects.



Protocol

1. Defect selective etching

1. Solid etchant preparation

- Prepare eutectic mixture of strong bases of potassium hydroxide (KOH) and sodium hydroxide (NaOH), together with magnesium oxide (MgO), by dissolving and mixing the composing alkali hydroxides and metal oxide in distilled water. Keep stoichiometric quantities of 53.6/37.3/9.1 at % of NaOH, KOH, and MgO, respectively¹³. MgO addition increases the etchant viscosity such that it remains on the Ga-polar surface and does not flow over the edges to the N-polar surface^{13,14}. All chemicals used should be practical grade quality.
- 2. Heat the mixture in a flask on a hot plate to 200 °C and agitate by magnetic stirring for 1 h (above the melting point of the KOH-NaOH eutectic point).
- 3. Cool the mixture to ~100 °C by reducing the temperature of a hot plate to completely evaporate the remaining liquid. This step depends on flask size and water volume, so it may require several minutes up to 1 h.
- 4. Transfer the solid etchant (denoted as E+M) into a dried bottle, avoiding exposure to moisture. CAUTION: KOH and NaOH may cause skin irritation and eye damage. Work with gloves and goggles. The protocol can also be paused here.

2. Defect selective etching

- 1. Prepare a clean GaN surface for the analysis. GaN that is epitaxially grown on sapphire is used in the following steps 12.
- 2. Place the GaN sample on a hot plate heated to ~450 °C. Place the thermocouple near the sample to precisely read the real temperature.
- 3. Place a piece of solid E+M etchant on top of the GaN and leave for 3 min.
- 4. Take the sample from the hot plate and place in a beaker with hot HCl for 3-5 min to eliminate remaining E+M.
- 5. Remove the sample from HCl and insert in a beaker with deionized (DI) water and ultrasonic bath for 5-10 min.
- Dry the sample by N₂ blowing.
 CAUTION: HCl may cause skin irritation and eye damage. Work with gloves and goggles. Avoid getting burnt. The protocol can also be paused here.

2. Scanning electron microscopy (SEM) observation

- 1. Mark the sample (e.g., with an L-shaped scratch using a diamond pen cutter).
- 2. Mount the sample on a metal stub dedicated to the SEM model to be used, using a conductive adhesive (i.e., double-sided carbon conductive tape or a similar material). Use gloves during sample preparation and transfer to avoid grease contamination from hands.
- 3. Add a piece of the tape from step 2.2 to connect the sample surface with a metal stub to prevent charge buildup on the specimen surface. Alternatively, a sputtered coating with conductive material (~10 nm thick) can be applied to prevent charging effects.
- Acquire at least three high-resolution SEM micrographs (ideally, a minimum of five) of a top view of the sample. Each image should display
 an area of at least 25 x 25 μm. Avoid taking images from the surface regions with macroscopic surface defects. Figure 1 presents a typical
 result.
- Note the exact position of each picture with a respect to the L-shaped marker. NOTE: The protocol can be paused here.

3. Secondary ion mass spectrometry measurements

1. Tool calibration

- Calibrate the SIMS equipment using negative polarity, Cs primary ions with 7-13 keV impact energy. Align the secondary and primary beams. Keep the beam as small as possible (at least 1 μm in diameter), as the lateral resolution is predetermined by the size of the heam
- 2. Prepare five-seven settings for beams with various ion current density. For simplicity, keep the size of the beam intact, and change the beam current. Measure the beam current and size of the beam¹⁵. In the following steps, beam currents of 5 nA, 10 nA, 15 nA, 20 nA, 30 nA, and 50 nA and a spot size of 1 µm are used.
- 3. Use a 50 x 50 µm raster size and 35 x 35 µm analysis area for the following steps. Choose 256 x 256 pixels for spatial resolution. If not specified otherwise, use a standard integration time for each signal (typically 1-2 s).

2. Primary source stability

- 1. Choose a setting with a moderate beam current (15-20 nA).
- Obtain series of images using ³⁰Si₂⁻ secondary ion for a blank silicon wafer. For each image, integrate the signal for 5-10 min.
- 3. Perform pixel-to-pixel comparisons of all images with the first image. If >5% of pixels show a >5% difference from the first image, this indicates that the beam became unstable. Note the timespan of the beam stability.

3. Measurement

NOTE: The following steps are performed within a stable timespan of the beam.

 Follow the procedure described by Peres et al. to estimate the background level of oxygen contamination in the measurement chamber⁷. For each measurement, there is no need to obtain the absolute values of oxygen concentration, as the intensity ratio of ¹⁶O⁻ and ⁶⁹Ga⁻ signals is sufficient.

- Use beam settings prepared in step 3.1.2. Perform at least five measurements for each beam setting. Obtain a depth profile using ¹⁶O⁻ secondary ion, reach a ~200 nm depth, and measure the intensity of ⁶⁹Ga⁻ secondary ion by integrating the signal for 10-15 s. Do not perform this in regions where SEM images have been obtained.
- 3. Plot the intensity ratio of ¹⁶O and ⁶⁹Ga signals as a function of the inversed primary current density (there is no need to calculate absolute values). A good linear fit is expected (here, R² = 0.997). Estimate the vacuum background contribution as shown in **Figure 2**.
- Choose an intense beam (30 nA) for the following steps. Obtain an image that will be used for flat-field correction. Use a ³⁰Si₂-secondary ion for a blank silicon wafer. Integrate the signal for 5-10 min. Figure 3 presents a typical result.
- 5. Perform depth profile measurements in the same regions where SEM images were aquired. Using a ¹⁶O secondary ion, integrate the signal for 3-5 s for each data point.

NOTE: The protocol can be paused here.

4. Data treatment

- 1. Reconstruct a 3D image from a depth profile.
- 2. Perform flat-field correction: pixel-to-pixel normalize each ¹⁶O ion image using a reference image obtained in step 3.3.4. **Figure 4A** presents raw data and **Figure 4B** presents the image after the flat-field correction.
- 3. Estimate vacuum background contribution from a plot obtained in step 3.3.2. There is no need to calculate absolute values; however, note the specific percentage of total counts that can be attributed to vacuum background contribution. A value between 90-95% is typical for such an experiment.
- Subtract the vacuum background contribution: randomly eliminate 90-95% of the registered ¹⁶O⁻ counts. Figure 4C presents a typical result for a single plane.
- 5. Plot the remaining counts as a 3D image. Figure 5 presents a typical result.
- 6. Integrate signals from all data points and superimpose the 2D image on the previously obtained SEM image using any image editor software with layer support. Treat the SEM image as background. A layer containing SIMS results should only contain actual counts as colored pixels (delete the white regions in between). Add ~30% of transparency to this layer. **Figure 6** presents a typical result

Representative Results

Very clear pillar-shaped structures should be observed in the 3D image. More oxygen should be agglomerated in a region closer to the surface, since the etching process introduces more oxygen that can diffuse through the sample. **Figure 7** presents a 3D image of raw data and an animation of how the reduction procedure reveals the final result. **Figure 4C** also presents a typical result for a single plane.

The SIMS image superimposed on the SEM image reveals that oxygen is agglomerated along cores of largest etch pits. These can be attributed to mixed/screw dislocations ¹⁵. It should be noted that if the core is smaller than the size of a primary beam, the secondary image will inherit the size and shape of the primary beam. In suboptimal experiments, a random distribution of oxygen counts can be seen (**Figure 8**). **Figure 9** presents a situation in which the beam becomes unstable during the experiment. Specifically, the quality is high for a region so close to the surface, but it gradually deteriorates during the experiment.

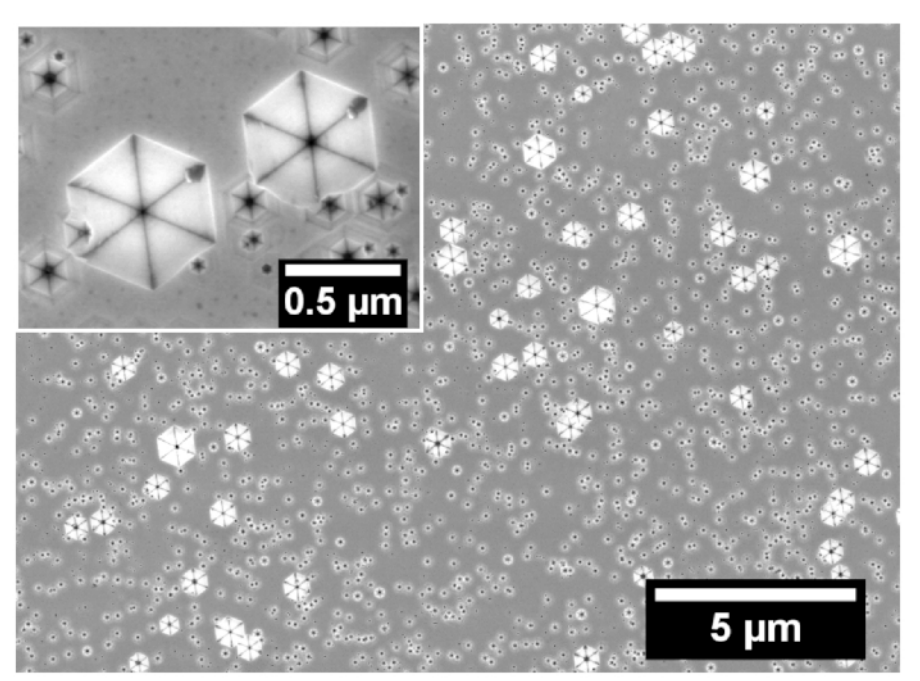


Figure 1: SEM micrographs of etch pits revealed on GaN surface using E+M etch. The etching parameters were set at 450 °C for 3 min. The inset depicts a magnified micrograph with revealed hexagonal pits generated on dislocation cores. The two biggest pits (>500 nm) represent dislocations with screw component of the Burgers vector. This figure has been reproduced with permission ¹². Please click here to view a larger version of this figure.

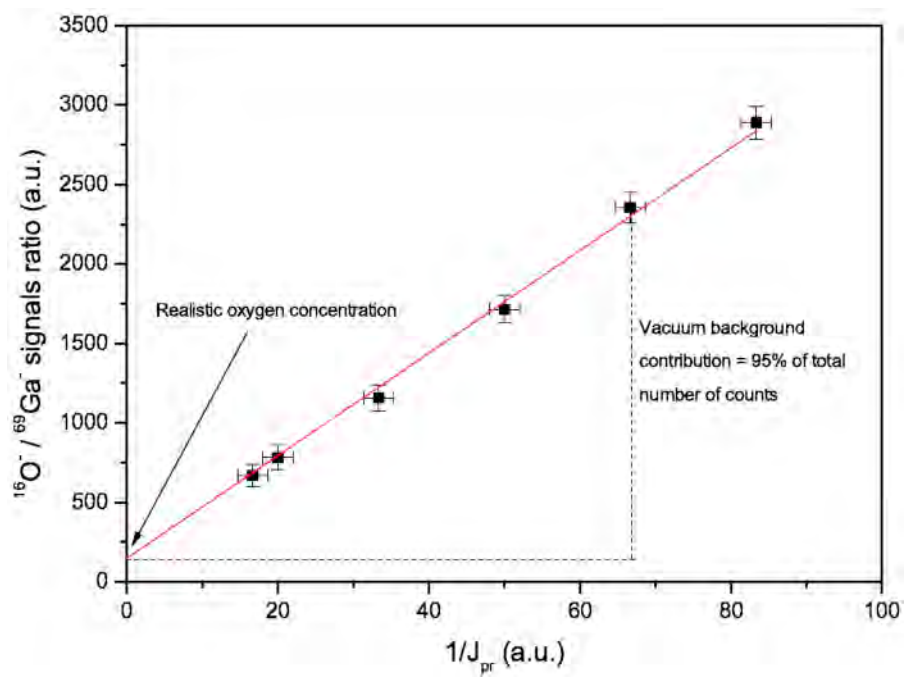


Figure 2: Average O- concentration vs. inverse primary current. Vacuum background contribution can be estimated from the plot. Error bars represent the standard deviation of each data set (five measurements). Please click here to view a larger version of this figure.

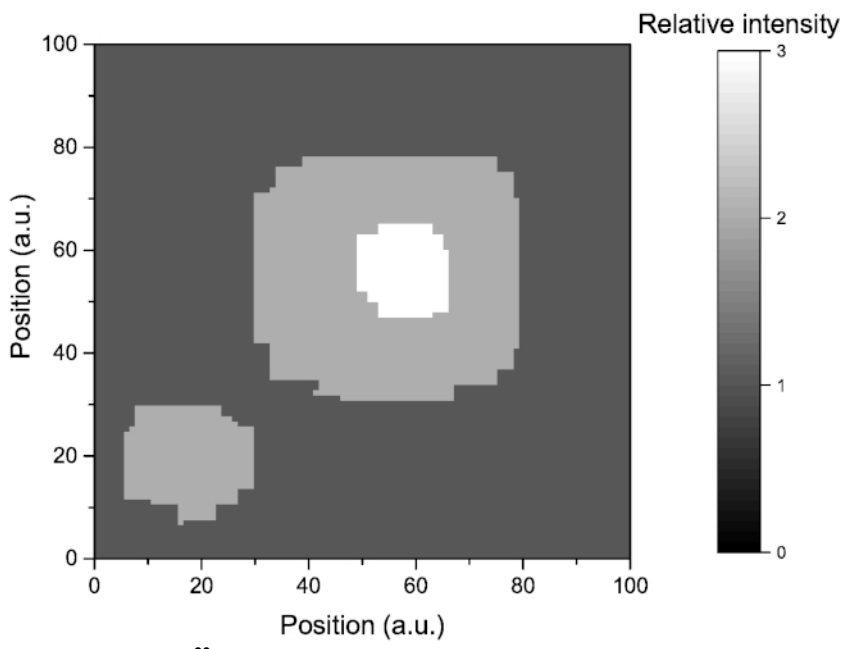


Figure 3: A typical ³⁰Si₂ secondary ion image for a blank silicon wafer. Intensity differences are caused by nonuniformity of the detector. Please click here to view a larger version of this figure.

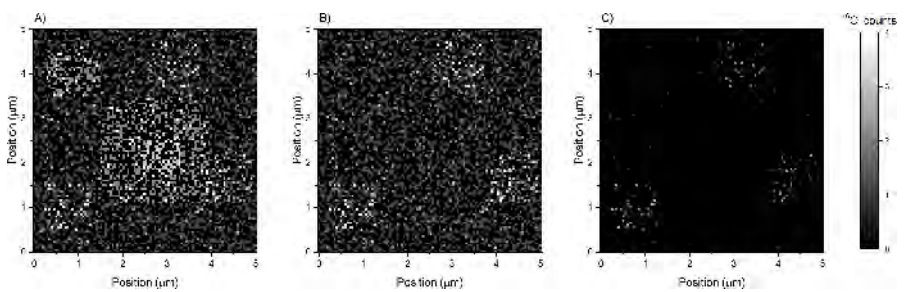


Figure 4: Typical plane view of oxygen counts distribution measured in 3D mode. Shown are images (A) from raw data, (B) after flat-field correction, and (C) after subtraction of vacuum background contribution. This figure has been adapted with permission ¹². Please click here to view a larger version of this figure.

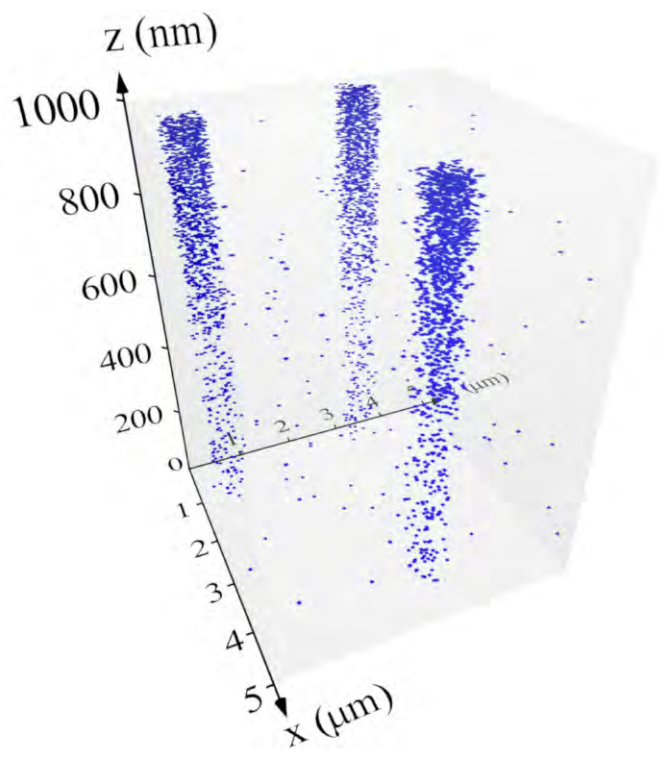


Figure 5: 3D view of oxygen counts in a 5 μ m x 5 μ m x 1 μ m cuboid. For better visibility, the z-scale is elongated. See Supplemental Figure 1 for animation. This figure has been adapted with permission 12. Please click here to view a larger version of this figure.

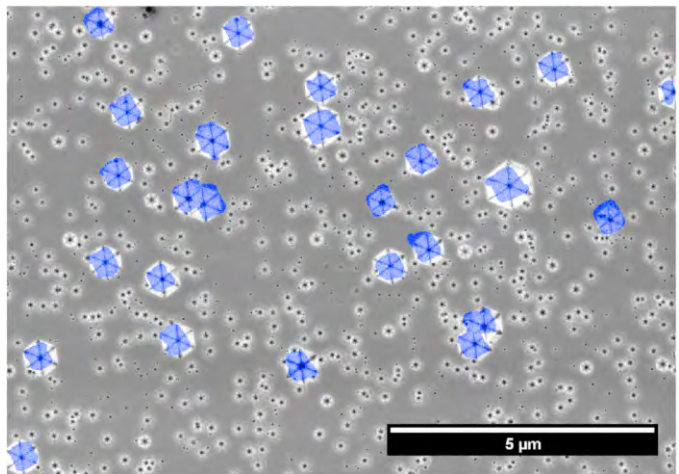


Figure 6: Lateral distribution of oxygen secondary ions (blue pixels) projected on SEM micrograph. Despite SIMS-related artifacts (lateral resolution determined by size of the primary beam), a clear correlation between the positions of largest pits and oxygen are observed. This figure has been adapted with permission 12. Please click here to view a larger version of this figure.

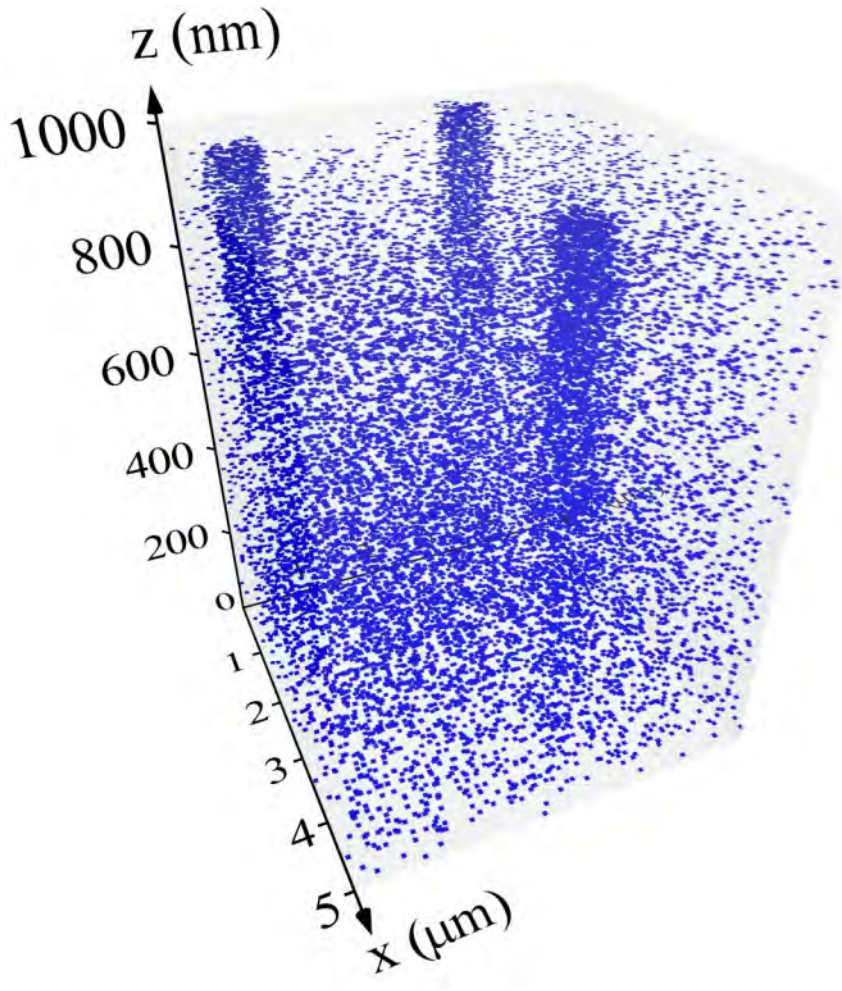


Figure 7: Animation showing how the reduction procedure is performed. At the beginning of the procedure, all counts are present, then for each layer, 90% of counts are randomly eliminated. Please click here to download this animation.

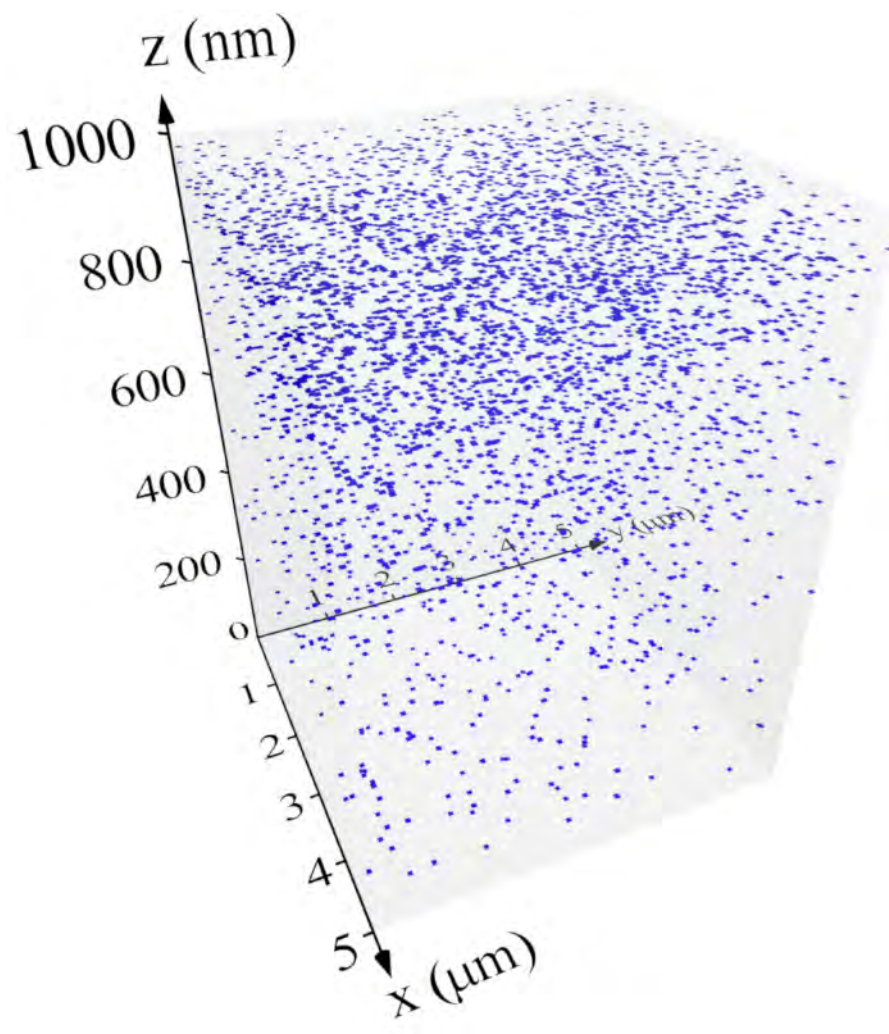


Figure 8: Random distribution of oxygen counts in suboptimal experiment. Please click here to view a larger version of this figure.

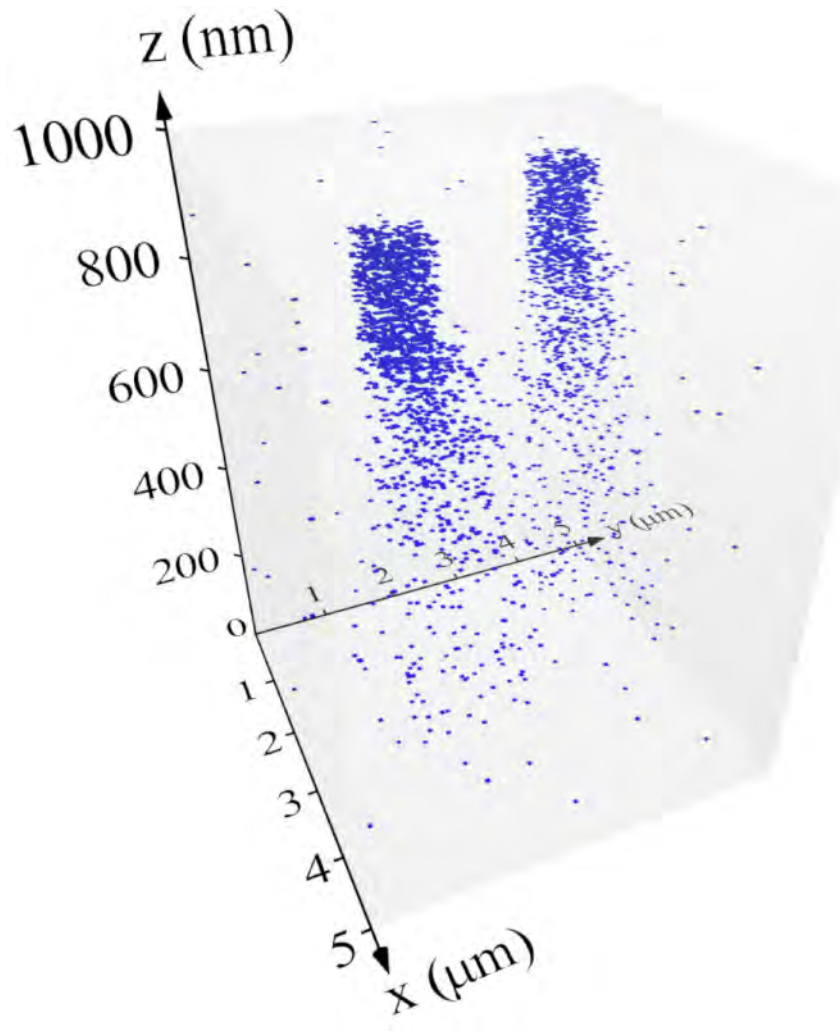


Figure 9: Experiment performed with an unstable beam. The quality deceases with sputtering depth. Please click here to view a larger version of this figure.

Supplemental Figure 1. Please click here to download this figure.

Discussion

Issues of nonuniformity of the detector and vacuum background contribution are easy to solve by flat-field correction and subtraction of parasitic counts, respectively. The subtraction procedure is not perfect, as it may subtract a contribution where oxygen has been agglomerated. In contrast, at the other position, it will leave the background count unaffected; thus, some artificial counts may still be present while some real counts are reduced. Nevertheless, it is efficient and sensitive enough to provide acceptable results.

The primary beam instability is the most problematic, as deterioration of the primary beam parameters will blur the secondary ion image; thus, no reliable information about the sample can be obtained. Section 3.2 in the protocol is particularly important. For instance, for a well-aligned beam, the first $^{30}\text{Si}_2^{-1}$ secondary ion image reflects nonuniformity of the detector, but after some time, the image will start to change. This is caused by deterioration of primary beam parameters (i.e., primary current loss, defocusing, position drift, etc.). It is therefore important to estimate the timespan of beam stability. It is advised to start the experiment 2-3 h after initialization of the beam, as it is typically more stable.

If the experiment is performed within a stable timespan of the beam and the result is still not satisfactory, it is advised to consider the quality of the primary beam. For a small primary beam, it is more challenging to confirm sufficient quality by observing a secondary ion image only. It is therefore advised to perform atomic force microscopy roughness tests at the crater bottom after sputtering ~1 µm of a very flat material (i.e., a blank silicon wafer). If the root mean squared roughness is above 1 nm, then further optimization of the primary beam is required.

The size of the beam limits the lateral resolution of this method. SIMS can image features that are smaller than the beam size, but the secondary ion image will inherit the shape and size of the primary ion beam. If a distance between two features is smaller than the size of the beam, the secondary ion image will blur them together. Despite these issues, the method allows users to obtain a realistic 3D distribution of impurities/ dopants in solid state samples. Furthermore, any spatial segregation of atoms can be correlated to the position of defects and interfaces.

For GaN-based structures (i.e., oxygen-decorated), dislocations acting as local nonradiative recombination centers are responsible for n-type conductivity. For other materials any inhomogeneity of the dopant/contaminating atoms distribution may have major impacts on the performance of a device. Thus, the protocol is particularly useful for failure analysis and optimization of growth and processing procedures.

Disclosures

The authors have nothing to disclose.

Acknowledgments

This work was partially supported by the National Science Centre (NCN) within SONATA14 2018/31/D/ST5/00399 and OPUS10 2015/19/B/ST7/02163 projects.

References

- Wittmaack, K. High-sensitivity depth profiling of arsenic and phosphorus in silicon by means of SIMS. Applied Physics Letters. 29, 552 (1976).
- 2. Ber, B. Y. et al. Secondary ion mass spectroscopy investigations of magnesium and carbon doped gallium nitride films grown by molecular beam epitaxy. Semiconductor Science and Technology. 13, 71-74 (1998).
- Chiou, C. Y., Wang, C. C., Ling, Y. C., Chiang, C. I. Secondary ion mass spectrometry analysis of In-doped p-type GaN films. Applied Surface Science. 203 - 204, 482-485 (2003).
- 4. Emziane, M., Durose, K., Halliday, D. P., Bosio, A. Romeo, N. In situ oxygen incorporation and related issues in CdTe/CdS photovoltaic devices. *Journal of Applied Physics*. **100**, 013513 (2006).
- Matsunaga, T., Yoshikawa, S., Tsukamoto, K. Secondary ion yields of C, Si, Ge and Cs surface density and concentration in SIMS. Surface Science. 515, 390-402 (2002).
- 6. Gnaser, H. SIMS detection in the 10¹² atoms cm⁻³ range. Surface and Interface Analysis. **25**, 737-740 (1997).
- Peres, P., Merkulov, A., Choi, S. Y., Desse, F., Schuhmacher, M. Characterization of LED materials using dynamic SIMS. Surface and Interface Analysis. 45, 437-440 (2013).
- 8. Arslan, I., Browning, N. D. Role of Oxygen at Screw Dislocations in GaN. Physical Review Letters. 91, 165501 (2003).
- 9. Hawkridge, M. E., Cherns, D. Oxygen segregation to dislocations in GaN. Applied Physics Letters. 87, 221903 (2005).
- 10. Arslan, I., Bleloch, A., Stach, E. A., Ogut, S., Browning, N. D. Using EELS to observe composition and electronic structure variations at dislocation cores in GaN. *Philosophical Magazine*. **86**, 4727-4746 (2006).
- 11. Hautakangas, S. et al. Gallium and nitrogen vacancies in GaN: Impurity decoration effects. *Physica B: Condensed Matter.* **376-377**, 424-427 (2006).
- 12. Michałowski, P. P., Złotnik, S., Rudziński, M. Three dimensional localization of unintentional oxygen impurities in gallium nitride. *Chemical Communications*. **55**, 11539 (2019).
- 13. Kamler, G., Weyher, J. L., Grzegory, I., Jezierska, E., Wosiński, T. Defect-selective etching of GaN in a modified molten bases system. *Journal of Crystal Growth.* **246**, 21-24 (2002).
- 14. Zhuang, D., Edgar, J. H., Strojek, B., Chaudhuri, J., Rek, Z. Defect-selective etching of bulk AlN single crystals in molten KOH/NaOH eutectic alloy. *Journal of Crystal Growth.* **262**, 89-94 (2004).
- 15. CAMECA SC-Ultra, User's Guide, CAMECA. Genneviliers, (2005).
- 16. Weyher, J. v. L. et al. Orthodox etching of HVPE-grown GaN. Journal of Crystal Growth. 305, 384-392 (2007).



Contents lists available at ScienceDirect

Measurement

journal homepage: www.elsevier.com/locate/measurement





Defect-mediated sputtering process of boron nitride during high incident angle low-energy ion bombardment

Paweł Piotr Michałowski ^{a,*}, Dawid Maciążek ^b, Zbigniew Postawa ^b, Piotr A. Caban ^a, Sylwia Kozdra ^a, Adrianna Wójcik ^{a,c}, Jacek M. Baranowski ^a

- ^a Łukasiewicz Research Network Institute of Microelectronics and Photonics, Aleja Lotników 32/46, 02-668 Warsaw, Poland
- b Smoluchowski Institute of Physics, Jagiellonian University, Łojasiewicza 11, 30-348 Kraków, Poland
- ^c Faculty of Physics, Warsaw University, Pasteura 5, 02-093 Warsaw, Poland

ARTICLE INFO

Keywords: Secondary ion mass spectrometry Molecular dynamics Sputtering Boron nitride 2D materials

ABSTRACT

Further development of hexagonal boron nitride (hBN) towards electronic devices requires the application of precise analytical techniques. High incident angle ($>65^{\circ}$) secondary ion mass spectrometry has been recently developed, and allows to reach atomic depth. However, the procedure has been optimized experimentally, and thus computer simulations are needed to validate and comprehend the experiment. It is revealed that a sample without any defects cannot be sputtered in such conditions — all ions are reflected from the surface. Only defects, particularly vacancies, can act as erosion centers. After prolong bombardment (dose in the range of 10^{17} ions cm $^{-2}$), the number of defects and their sizes are sufficiently large that rapid removal of a top-most hBN layer can be observed. Computer simulations and additional experiments reveal that the sputtering process is defect-mediated and anisotropic — significantly more prominent along the incident direction.

1. Introduction

Two dimensional (2D) materials and their potential application into electronic devices are studied worldwide. One of the most promising representatives of this group is hexagonal boron nitride (hBN) with $\rm sp^2$ -hybridized atomic sheets of boron and nitrogen. Its structure is very similar to graphene, with a relatively low lattice mismatch (1.7% lattice mismatch), and high thermal conductivity. The major difference is a wide band gap of hBN, and thus, it can be potentially integrated with other 2D materials as a substrate and dielectric [1].

Before mass production and commercialization, the basic properties of 2D materials have to be examined. A variety of experimental methods are widely used to investigate the properties and quality of the hexagonal boron nitride samples: Raman spectroscopy is a useful tool for quick determination of the structural properties and quality of h-BN. The shift of the Raman peaks to higher and lower frequencies may give information about compressive and tensile stress, respectively [2]. Furthermore, Raman scattering can be used to determine the volume fraction of h-BN in the BN films [3]. Ultra-low Frequency Raman spectroscopy allows for the estimation of the number of layers in ultra-thin hBN [4,5]. Optical properties of the boron nitride have been studied experimentally, e.g., by means of Photoluminescence [6–8]. Useful information on an hBN structure such as distances between layers, average grain size, strain, crystal plane alignment can be delivered by

X-ray diffraction investigations [9,10]. Additional support in structural characterization can be also obtained by scanning transmission electron microscopy images, which give a direct indication of the phase and quality of the structure [11,12]. Moreover, an inspection of the sample at the atomic scale can reveal the presence of structural defects [12,13]. Scanning electron microscopy and atomic force microscopy (AFM) are frequently used to investigate the morphology of the hBN samples [11,14]. Particularly, AFM has been widely employed to probe surface topography of hBN, e.g., to get quantitative information about the height of the characteristic wrinkles [15].

In our previous secondary ion mass spectrometry (SIMS) experiments on graphene [16–18], we have shown that measurements of 2D materials are non-trivial, and their presence can affect the ionization probability. We have also used SIMS to study the quality of hBN layers and the formation of carbon precipitation during the growth process of thin and smooth BN layers grown in a self-terminated growth mode [19–21]. We have described a measurement procedure that allowed us to reach atomic depth resolution [21]. First, the top layer is measured in a static SIMS regime. The total primary ion dose is sufficiently low, and less than 1% of the surface is damaged during the measurement. Then the sample is bombarded with a short pulse of primary ions at high incident angles. This ensures that weak van der Waals bonds are

E-mail address: pawel.michalowski@imif.lukasiewicz.gov.pl (P.P. Michałowski).

^{*} Corresponding author.

P.P. Michałowski et al. Measurement 179 (2021) 109487

preferentially broken, and the top layer is sputtered, and the second layer is exposed for a static SIMS analysis. The repetition of these steps allows a precise characterization of each layer individually. This procedure, however, has been optimized experimentally, and a detailed description of the underlying physical processes responsible for such behavior during high incident angle ion bombardment are still unclear.

The impact of the incident angle was intensively studied in 70 s and 80 s by Wittmaack [22-26] and Magee [27-29]. The final conclusion was that incident angle in the range of 40° – 60° ensured high secondary ion yield and good depth resolution for most materials. Thus nowadays most instruments have fixed ion columns without a possibility to directly manipulate the incident angle and, as a consequence, its impact is seldom considered in recent studies. In most publications containing SIMS results the incident angle is not even reported. Recently Schiffmann [30] has presented a study for a broad range of incident angles (a sample can be tilted between 0° and 90° around the axis) and come to a conclusion that optimal value is 45° and 55° for carbon-based and nitride materials, respectively, which is in line with aforementioned studies by Wittmaack and Magee. However, the most prominent exceptions are proceedings of International Conferences on Secondary Ion Mass Spectrometry where authors regularly discuss this parameter [31-41]. Kataoka et al. [33] notice formation of ripples at the crater bottom during high incident angle bombardment. Merkulov et al. [41] discussed extra low impact energy SIMS procedures with varying incident angles, however, only the change of the impact energy is directly considered. Iida et al. [35] shows a particularly interesting study for C₆₀⁺ primary beam. The conclusion is that the highest incident angle (76°) is the most suitable for molecular depth profiling because sputter induced damage of polymers is significantly reduced.

Computer simulation are not limited by instruments' design and thus the influence of the incident angle is often considered [42–46]. Thus in this work molecular dynamics computer simulations combined with experimental measurements are used to study in detail the sputtering process of boron nitride during high incident angle low-energy ion bombardment. In this way, it is possible to obtain valuable knowledge about the interaction of primary ions with hBN layers but also indirectly about properties of the hexagonal boron nitride itself.

2. Experimental setup

2.1. Sample preparation

Boron nitride films were grown in the self-terminated growth mode investigated by Paduano et al. [47,48] and exact growth parameters are presented in our previous studies [19,21]. Argon was used as a carrier gas and thickness of BN sample was about 1.8 nm which corresponds to 6 layers.

2.2. Secondary ion mass spectrometry

SIMS measurements were performed employing the CAMECA SC Ultra instrument and the details about measurement procedure are presented in our previous study [21]. The most important changes, when compared to standard SIMS experiments, were the ultra low impact energy of 100 eV and a high incident angle $(65-77^{\circ})$ for a Cs⁺ primary beam and negative secondary ion polarity. No significant differences has been observed for various angles and thus the same value as in our previous study has been chosen (69°) for the following experiments.

2.3. Computer simulations

A detailed description of the molecular dynamics computer simulations used to model cluster bombardment can be found elsewhere [49].

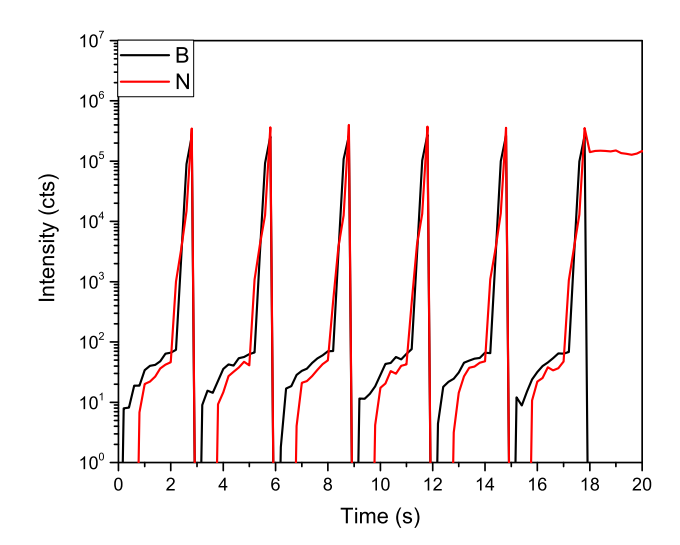


Fig. 1. A depth profile showing B and N signal for ultra low impact energy and high incident angle cesium bombardment. In the beginning, the intensity of both signals is very low. At one point, they rapidly increase and shortly thereafter vanish. The number of such cycles corresponds to the number of hBN layers, which indicates that each hBN layer is sputtered independently. The figure is available in csv format in Supplementary Materials.

Briefly, the motion of particles is determined by integrating the Hamilton equations of motion. The forces between boron and nitrogen atoms in the hexagonal Boron Nitride (h-BN) layer are described by BN-ExTeP potential [50]. The Lennard-Jones potential describes the interlayer interactions. These potential parameters are fitted, so the relaxed sample has 3.33 Å interlayer distance, and interlayer binding energy per atom is equal to 85.9 meV [51]. Interactions involving cesium projectile (Cs-Cs, Cs-B, Cs-N) are described by the ZBL potential [52]. All simulations are performed with the large-scale atomic/molecular massively parallel simulator code (LAMMPS) [53].

The simulated sample consisted of 5 layers of h-BN in the AA' stacking mode [51] with a size 135 Å \times 104 Å \times 17 Å. Periodic boundary conditions are used in the lateral directions, with the bottommost layer fixed in place. A thermal bath is applied to the second and third layers from the bottom to keep the system at $T=300~\rm K$. The sputtering process is modeled as a series of sequential impacts, where each impact consisted of 3 steps. In step one, the Cs atom is created above the sample surface at a randomly selected position with a velocity vector corresponding to the beam parameters used in the experiment (kinetic energy 100 eV, impact angle 69°). In the next step, the evolution of the system is simulated for 10 ps. During this phase, sputtering, atom redistribution, and the chemical effects are taking place. In the final step, the additional thermal bath is applied to all layers to remove residual stress before the next impact.

3. Results and discussion

In our previous work [21], high incident angle bombardment was used only for removal of subsequent hBN layers, and the detector was switched off because it was difficult to optimize the extraction of secondary ions in such non-trivial conditions. Since then, we have, however, overcome this problem (by finely tuning the extraction parameters) and thus we have been able to create full depth profiles during the high incident angle bombardment — see Fig. 1. As it can be immediately seen, the result is periodic and consists of six almost identical parts corresponding to six layers of hBN. For samples with a bigger number of layers the result is analogous. At the end of a profile, the B signal vanishes, whereas the N signal reaches a constant value (the substrate was nitridated before the growth process). However, contrary to a typical SIMS result, both signals change a lot during the sputtering process of hBN layers:

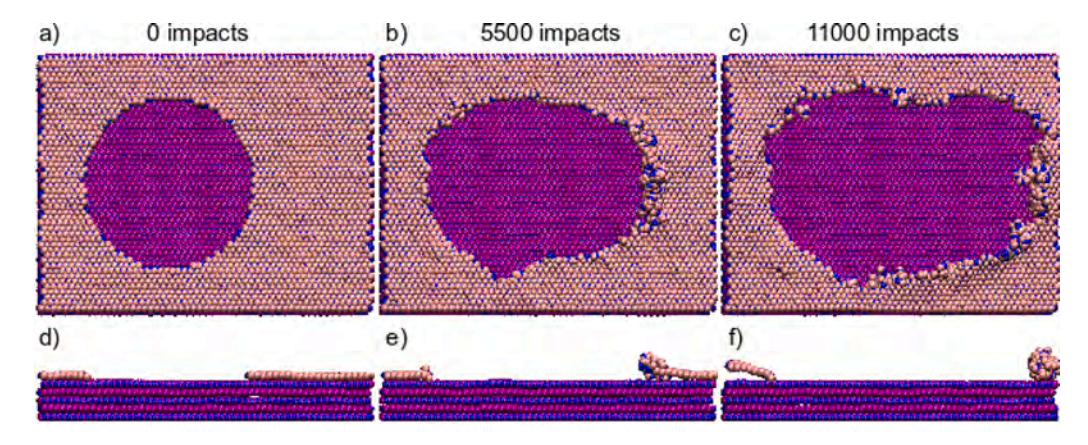


Fig. 2. Visualization of the evolution of the h-BN sample with initial circular defect undergoing continuous bombardment with different doses: (a,d) 0 ions cm⁻², (b, (e) 3.9×10^{15} ions cm⁻², (c, (f) 7.8×10^{15} ions cm⁻². The system top view is shown in panels (a-c), while panels (d-f) present the cross-sectional view. Nitrogen atoms are represented as blue spheres, and boron atoms are represented as pink (topmost layer) and violet $(2th-5th \ layer)$ spheres. A movie showing evolution of this system can be found in Supplementary Materials. (For interpretation of the references to color in this figure legend, the reader is referred to the web version of this article.)

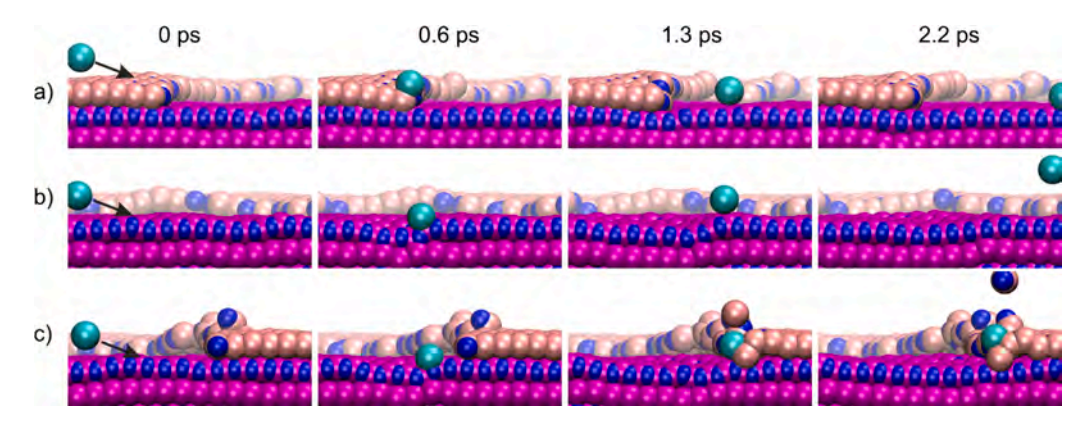


Fig. 3. Temporal evolution of the BN surface bombarded by 100 eV Cs projectile at 69° angle of incidence for impacts occurring on (a) the topmost layer near the defect edge, b the locally undamaged part of the exposed portion of the second layer far from the defect edge, and (c) the exposed second layer near the defect edge. The atom coloring scheme is the same as in Fig. 2. Movies showing these impacts can be found in Supplementary Materials.

- at the beginning, only a minimal number of boron counts can be registered;
- · after some time, nitrogen counts can also be registered;
- both signals steadily increase over about two seconds, but their intensities remain very low (less than one hundred counts);
- at one point, both signals start to increase rapidly, reaching more
 than three orders of magnitude higher values within less than half
 a second (it may seem that the nitrogen signal increases faster but
 there is only a single data point difference which originates from
 the fact that secondary ions are measured sequentially);
- · both signals drop to zero even more rapidly.

The fact that the boron signal is the first to be registered is easy to explain. Cesium is used as primary ions. The electronegativity difference between cesium and nitrogen is 2.25, whereas 1.25 between cesium and boron. Electronegativity is a concept that describes the tendency of an atom to attract a shared pair of electrons towards itself. The more significant is the electronegativity difference, the greater is the tendency to attract electrons by an atom of a given element, even at the expense of another. Furthermore, the atomic radius of boron (87 pm) is bigger than of nitrogen (56 pm), and, thus, much larger cesium (298 pm) may preferentially sputter a boron atom and take its place in the hBN lattice. However, such simple consideration cannot explain why at some point both, signals increase rapidly and vanish entirely in a split second.

It is also important to emphasize that the quality of the profile presented on Fig. 1 does not deteriorate even for much thicker samples

(more than 60 layers of hBN) — each and every periodic feature is of the same quality. It suggests that each layer is sputtered individually and there is no atomic redistribution between neighboring layers.

To gain better insight, we have performed computer simulations for two systems of multi-layer hBN. The first system is a pristine sample without any defects. After 7000 impacts (dose 5×10^{15} ions cm $^{-2}$), not a single defect is created in the sample. All impacting projectiles are reflected from the surface without introducing any permanent surface modification. This is in line with work of Iida et al. [35] where it has been presented that for high incident angle bombardment the sputter induced damage is significantly reduced.

For the second system, we have introduced a circular defect with a radius of 50 Å to the topmost layer (see Fig. 2a). The evolution of the system undergoing 11 000 impacts (dose equal to 7.8×10^{15} ions cm $^{-2}$) is shown in Fig. 2 and corresponding Animation. In this case, projectiles are bombarding the surface from left to right. It is evident that this time, the geometry of the topmost layer is modified by projectile impacts. The defect evolution of this layer displays a strong anisotropy of erosion on the defect right-hand side. Additionally, continuous bombardment does not alter the geometry of the second layer. This result corresponds very well to study of Kataoka et al. [33] where formation of ripples during high incident angle bombardment has been reported.

Before exploring the kinematics of individual cases of a projectile impact, we should mention the factors that will limit the effectiveness of energy transfer between the projectile and individual surface atoms. The first factor is the large mass difference between the projectile atom and the substrate atoms. Even in the most favorable case of a central

P.P. Michałowski et al. Measurement 179 (2021) 109487

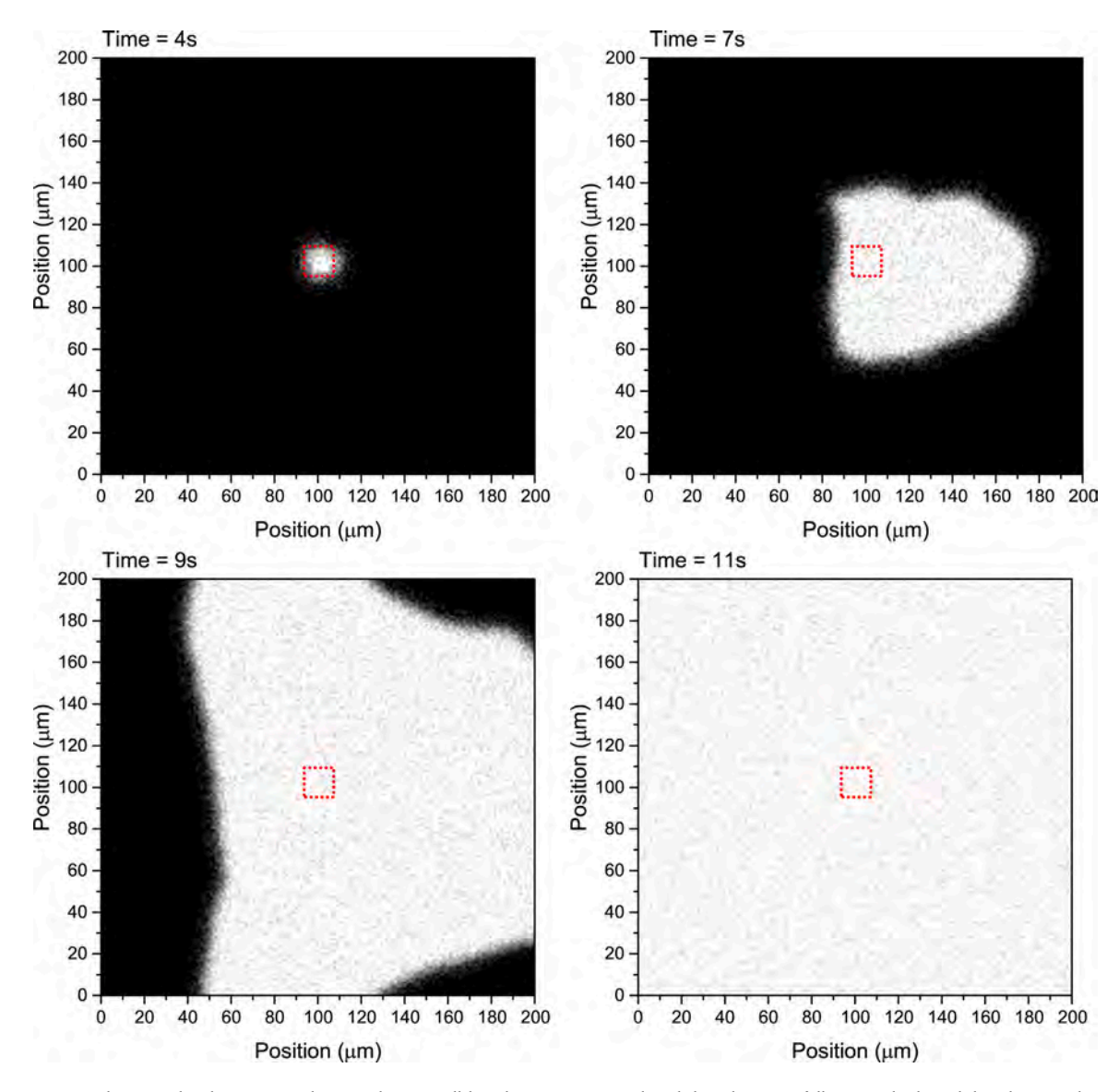


Fig. 4. Aluminum secondary ions distribution maps show at what time all hBN layers are sputtered, and the substrate is fully exposed. The red dotted square shows the location of the pre-bombardment area. For this region, the substrate is exposed after four seconds. The rest of the sputtering process is asymmetrical: layers at the right side are sputtered faster, which corresponds to the direction of primary ions incidence: from left to right. Four selected frames are presented. Full animation of these data (one frame per second) can be found in Supplementary Materials.

two-body collision, only around 26 eV and 34 eV of kinetic energy would be transferred to the boron or nitrogen atoms, respectively. The second factor is related to the many-body nature of interactions. The projectile impacts at the surface at a high angle of incidence. As a result, it will never transfer its energy to one atom but share it among several atoms. To explain erosion anisotropy, we consider three different cases of the impact location. In the first case, impact occurs on the topmost layer near the defect edge, as shown in Fig. 3a and corresponding Animation. The projectile arrives at a high incidence angle. It agitates several atoms losing its kinetic energy before hitting the atom located at the edge. The atoms on the left also shield this atom, so the collision usually occurs with a large impact parameter, limiting the efficiency of energy transfer. Furthermore, a part of the velocity gained by this atom is directed towards the second layer and shared with atoms located in deeper layers. As a result, the energy of the impacted atoms is not sufficient to let this atom to eject, and such an impact results in a minimal chance of sputtering. In the second case, the impact occurs on the undamaged part of the topmost layer or the exposed portion of the second layer far from the defect edge. The latter case is visualized in Fig. 3b and corresponding Animation. Due to a high angle of incidence,

normal component of projectile velocity is low, and the projectile slides over the perfect surface distorting its geometrical structure only temporarily. No sputtering or defect formation occurs in both these situations, as observed in simulations performed on the pristine sample. In the third case, illustrated in Fig. 3c and corresponding Animation, the impact occurs on the exposed second layer near the defect edge. The initial behavior of the projectile is the same as the impact on the perfect flat surface. The projectile only temporarily distorts the surface, sliding over it. However, in this case, it collides with the first layer atom located at the edge of a defect on its way out. The transmitted momentum is directed upwards. The collision can be central, and the energy transfer is efficient. The atom is forced to eject. This scenario can only occur for projectiles impacting the surface within a specific distance of approximately 6 Å between the projectile impact point and the ejected atom initial location. If the distance is larger than this specific distance, the scenario is described in Fig. 3b. Finally, it should be noted that our simulations do not show how the initial defects are created. We believe that this could be linked to possible beam imperfections (particularly presence of ions with lower incident angles) or thermodynamical processes of statistical nature, which occur at the time scale we cannot model.

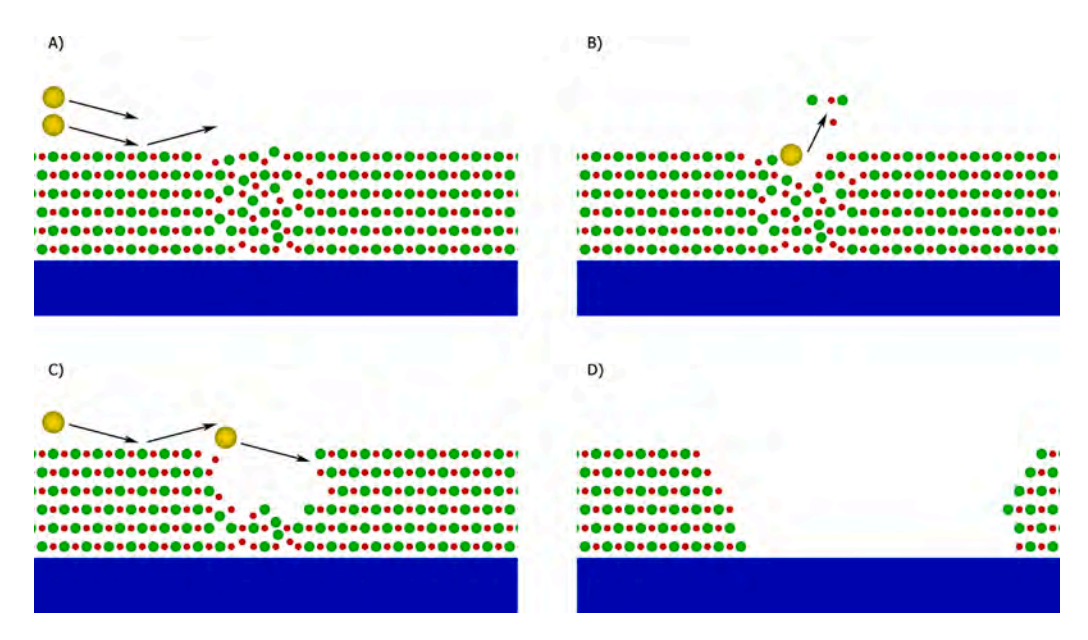


Fig. 5. Schematic visualization of a high incident angle cesium ions bombardment of a pre-defected sample. For such conditions, most primary ions bounce off the surface (part A). Those projectiles which hit a pre-bombarded defected area, cause the sputtering of hBN layers (part B). The further sputtering process is asymmetrical. Ions still bounce off the surface at one side, whereas collision at effectively lower incident angle at the other side (part C) causes that this side is sputtered much faster (part D). For a pre-defected sample, the layer-by-layer nature of the sputtering process is no longer preserved.

To verify these conclusions, we have devised an additional experiment: a high energy beam (13 keV) with a standard incident angle (40°) and a very low density (the total dose below 10^{12} atoms cm $^{-2}$) has been used to pre-bombard a very small area (15 × 15 microns). For such a low dose, it is not possible to sputter many atoms, but such a high impact energy ensures that a lot of defects have been created in this area. Then high incident angle beam has been used, but instead of boron or nitrogen, we have decided to measure ion images of aluminum signal (lateral distribution). This element is not present in hBN layers, and thus no signal is expected at the beginning of the experiment. However, after the removal of all hBN layers, the sapphire is exposed, and the Al signal can be registered.

The result presented in Fig. 4 is indeed very interesting. As expected, no Al signal is observed at the beginning of the experiment. But just after four seconds, the substrate in the region pre-bombarded by a high energy beam is fully exposed (without pre-bombardment, it takes eighteen seconds to fully remove six hBN layers). Other regions are exposed with time but, similarly to computer simulations, in a very asymmetrical manner: material located to the right of the prebombarded area is sputtered much faster than to the left. This is not surprising as this corresponds to the direction of primary ions incidence: from left to right. Therefore primary ions can sputter this part of a sample much easier because the effective collision angle is much lower. This is schematically shown in Fig. 5. It should be also emphasized that the substrate is fully exposed everywhere just after eleven seconds — seven seconds faster than for a case without prebombardment. This is not surprising as the introduction of defects to all six layers causes the layer-by-layer nature of the sputtering process to be no longer preserved. A simultaneous sputtering of several hBN layers is naturally a faster process.

4. Conclusions

The Molecular dynamics computer simulations are combined with the experimental measurements to delineate the processes leading to layer-by-layer sputtering of hexagonal boron nitride with low-energy high incidence angle bombardment with cesium projectiles. It has been found that for such non-trivial bombardment conditions the evolution of the sputtering process is strongly affected by the presence of defects, particularly vacancies. It should be emphasized that computer simulations are in excellent agreement with experiments, and they both reveal anisotropic nature of the sputtering process — it is significantly more prominent along the incident direction. Such an effect has not been observed for standard SIMS experiments with moderate/low incident angles.

These results finally allow to explain the shape of the depth profile presented in Fig. 1. Every realistic sample contains some vacancies and other defects, and while they may not be as big as it has been assumed in computer simulations, these defects act as erosion centers — in the initial state of the ion bombardment, these defects become bigger, and thus more and more atoms are sputtered (a steady increase of boron and nitrogen signals). After some time, the number and the size of these defects are large enough that the whole layer can be sputtered very quickly (a very rapid increase of both signals). Then a fresh layer is exposed, and thus the entire process starts again (signals drop to zero).

CRediT authorship contribution statement

Paweł Piotr Michałowski: Conceptualization, Methodology, Validation, Formal analysis, Investigation, Writing - original draft, Writing - review & editing, Visualization, Funding acquisition. Dawid Maciążek: Software, Validation, Formal analysis, Data curation. Zbigniew Postawa: Software, Validation, Formal analysis, Data curation, Writing - review & editing, Funding acquisition. Piotr A. Caban: Formal analysis, Resources, Investigation. Sylwia Kozdra: Formal analysis, Visualization. Adrianna Wójcik: Formal analysis, Visualization. Jacek M. Baranowski: Formal analysis, Writing - review & editing.

Declaration of competing interest

The authors declare that they have no known competing financial interests or personal relationships that could have appeared to influence the work reported in this paper.

Acknowledgments

This work was supported by the Polish National Science Centre within SONATA 14 2018/31/D/ST5/00399 and OPUS 17 2019/33/B/ST4/01778 projects. MD simulations were performed at the PLGrid Infrastructure.

P.P. Michałowski et al. Measurement 179 (2021) 109487

Appendix A. Supplementary data

Supplementary material related to this article can be found online at https://doi.org/10.1016/j.measurement.2021.109487.

References

- [1] C. Dean, A. Young, I. Meric, L. Wang, S. Sorgenfrei, K. Watanabe, T. Taniguchi, P. Kim, K. Shepard, J. Hone, Boron nitride substrates for high-quality graphene electronics, Nature Nanotechnol. 5 (2010) 3209.
- [2] Y. Kobayashi, T. Akasaka, Hexagonal BN epitaxial growth on (0001) sapphire substrate by MOVPE, J. Cryst. Growth 310 (23) (2008) 5044–5047.
- [3] S. Reich, A.C. Ferrari, R. Arenal, A. Loiseau, I. Bello, J. Robertson, Resonant Raman scattering in cubic and hexagonal boron nitride, Phys. Rev. B 71 (2005) 205201
- [4] I. Stenger, L. Schué, M. Boukhicha, B. Berini, B. Plaçais, A. Loiseau, J. Barjon, Low frequency Raman spectroscopy of few-atomic-layer thick hBN crystals, 2d Mater. 4 (3) (2017) 031003.
- [5] L. Schué, I. Stenger, F. Fossard, A. Loiseau, J. Barjon, Characterization methods dedicated to nanometer-thick hBN layers, 2d Mater. 4 (1) (2016) 015028.
- [6] M.G. Silly, P. Jaffrennou, J. Barjon, J.-S. Lauret, F. Ducastelle, A. Loiseau, E. Obraztsova, B. Attal-Tretout, E. Rosencher, Luminescence properties of hexagonal boron nitride: Cathodoluminescence and photoluminescence spectroscopy measurements, Phys. Rev. B 75 (2007) 085205.
- [7] J. Wu, W.-Q. Han, W. Walukiewicz, J.W. Ager, W. Shan, E.E. Haller, A. Zettl, Raman Spectroscopy and time-resolved photoluminescence of BN and bxcynz nanotubes, Nano Lett. 4 (4) (2004) 647–650.
- [8] K. Watanabe, T. Taniguchi, H. Kanda, Direct-bandgap properties and evidence for ultraviolet lasing of hexagonal boron nitride single crystal, Nature Mater. 3 (6) (2004) 404–409.
- [9] B. Matović, J. Luković, M. Nikolić, B. Babić, N. Stanković, B. Jokić, B. Jelenković, Synthesis and characterization of nanocrystaline hexagonal boron nitride powders: XRD and luminescence properties, Ceram. Int. 42 (15) (2016) 16655–16658.
- [10] M. Öz, N.K. Saritekın, Ç. Bozkurt, G. Yildirim, Synthesis of highly ordered hBN in presence of group i/IIA carbonates by solid state reaction, Cryst. Res. Tech. 51 (6) (2016) 380–392.
- [11] X. Li, S. Sundaram, Y. El Gmili, T. Ayari, R. Puybaret, G. Patriarche, P.L. Voss, J.P. Salvestrini, A. Ougazzaden, Large-area two-dimensional layered hexagonal boron nitride grown on sapphire by metalorganic vapor phase epitaxy, Cryst. Growth Des. 16 (6) (2016) 3409–3415.
- [12] M.L. Odlyzko, K.A. Mkhoyan, Identifying hexagonal boron nitride monolayers by transmission electron microscopy, Microsc. Microanal. 18 (3) (2012) 558–567.
- [13] N.L. McDougall, J.G. Partridge, R.J. Nicholls, S.P. Russo, D.G. McCulloch, Influence of point defects on the near edge structure of hexagonal boron nitride, Phys. Rev. B 96 (2017) 144106.
- [14] K.P. Sharma, S. Sharma, A. Khaniya Sharma, B. Paudel Jaisi, G. Kalita, M. Tanemura, Edge controlled growth of hexagonal boron nitride crystals on copper foil by atmospheric pressure chemical vapor deposition, CrystEngComm 20 (2018) 550–555.
- [15] D. Chugh, J. Wong-Leung, L. Li, M. Lysevych, H.H. Tan, C. Jagadish, Flow modulation epitaxy of hexagonal boron nitride, 2d Mater. 5 (4) (2018) 045018.
- [16] P.P. Michałowski, W. Kaszub, I. Pasternak, W. Strupinski, Graphene enhanced secondary ion mass spectrometry (GESIMS), Sci. Rep. 7 (2017) 7479.
- [17] P.P. Michałowski, I. Pasternak, W. Strupinski, Contamination-free ge-based graphene as revealed by graphene enhanced secondary ion mass spectrometry (GESIMS), Nanotechnology 29 (2018) 015702.
- [18] P.P. Michałowski, I. Pasternak, P. Ciepielewski, F. Guinea, W. Strupinski, Formation of a highly doped ultra-thin amorphous carbon layer by ion bombardment of graphene, Nanotechnology 29 (2018) 305302.
- [19] P. Caban, D. Teklińska, P. Michałowski, J. Gaca, M. Wójcik, J. Grzonka, P. Ciepielewski, M. Możdżonek, J. Baranowski, The role of hydrogen in carbon incorporation and surface roughness of MOCVD-grown thin boron nitride, J. Cryst. Growth 498 (2018) 71–76.
- [20] P. Caban, P. Michalowski, I. Wlasny, J. Gaca, M. Wojcik, P. Ciepielewski, D. Teklinska, J. Baranowski, Carbon incorporation in boron nitride grown by MOCVD under N2 flow, J. Alloys Compd. 815 (2020) 152364.
- [21] P.P. Michałowski, P. Caban, J. Baranowski, Secondary ion mass spectrometry investigation of carbon grain formation in boron nitride epitaxial layers with atomic depth resolution, J. Anal. Atom. Spectrom. 34 (2019) 848–853.
- [22] K. Wittmaack, Secondary ion yield variations due to cesium implantation in silicon, Surf. Sci. 126 (1) (1983) 573–580.
- [23] K. Wittmaack, Impact-energy dependence of atomic mixing and selective sputtering of light impurities in cesium-bombarded silicon, Nucl. Instrum. Methods Phys. Res. B 209–210 (1983) 191–195.
- [24] K. Wittmaack, The effect of the angle of incidence on secondary ion yields of oxygen-bombarded solids, Nucl. Instrum. Methods Phys. Res. B 218 (1) (1983) 307–311.

[25] K. Wittmaack, Beam-induced broadening effects in sputter depth profiling, Vacuum 34 (1) (1984) 119–137.

- [26] K. Wittmaack, Influence of the impact angle on the depth resolution and the sensitivity in SIMS depth profiling using a cesium ion beam, J. Vac. Sci. Technol. A 3 (3) (1985) 1350-1354.
- [27] C.W. Magee, W.L. Harrington, R.E. Honig, Secondary ion quadrupole mass spectrometer for depth profiling—design and performance evaluation, Rev. Sci. Instrum. 49 (4) (1978) 477–485.
- [28] C.W. Magee, S.A. Cohen, D.E. Voss, D.K. Brice, Depth distributions of low energy deuterium implanted into silicon as determined by sims, Nucl. Instrum. Methods 168 (1) (1980) 383–387.
- [29] C.W. Magee, R.E. Honig, Depth profiling by SIMS—depth resolution, dynamic range and sensitivity, Surf. Interface Anal. 4 (2) (1982) 35–41.
- [30] K.I. Schiffmann, SIMS Depth profile analysis of tribological coatings on curved surfaces: Influence of ion impact angle and take-off angle on ion yield and on the quantitative analysis of chemical composition, Surf. Interface Anal. 51 (7) (2019) 703–711.
- [31] M. Bersani, D. Giubertoni, M. Barozzi, E. Elacob, L. Vanzetti, M. Anderle, P. Lazzeri, B. Crivelli, F. Zanderigo, D-SIMS and tof-SIMS quantitative depth profiles comparison on ultra thin oxynitrides, Appl. Surf. Sci. 203–204 (2003) 281–284.
- [32] Y. Homma, A. Takano, Y. Higashi, Oxygen-ion-induced ripple formation on silicon: evidence for phase separation and tentative model, Appl. Surf. Sci. 203–204 (2003) 35–38.
- [33] Y. Kataoka, K. Yamazaki, M. Shigeno, Y. Tada, K. Wittmaack, Surface roughening of silicon under ultra-low-energy cesium bombardment, Appl. Surf. Sci. 203–204 (2003) 43–47.
- [34] A. Villegas, Y. Kudriavtsev, A. Godines, R. Asomoza, Work function change caused by alkali ion sputtering, Appl. Surf. Sci. 203–204 (2003) 94–97.
- [35] S.-i. Iida, T. Miyayama, N. Sanada, M. Suzuki, G.L. Fisher, S.R. Bryan, Optimizing C60 incidence angle for polymer depth profiling by tof-SIMS, Surf. Interface Anal. 43 (1–2) (2011) 214–216.
- [36] A. Merkulov, P. Peres, D.J. Larson, M. Schuhmacher, Quantitative low energy depth profiling of sige laterally nonuniform structures, J. Vac. Sci. Technol. B 36 (3) (2018) 03F121.
- [37] Y. Mazel, E. Nolot, J.-P. Barnes, M. Charles, R. Bouveyron, M. Mrad, A. Tempez, S. Legendre, Multitechnique elemental depth profiling of inalgan and inaln films, J. Vac. Sci. Technol. B 36 (3) (2018) 03F119.
- [38] M.K.I. Senevirathna, M. Vernon, G.A. Cooke, G.B. Cross, A. Kozhanov, M.D. Williams, Analysis of useful ion yield for si in gan by secondary ion mass spectrometry, J. Vac. Sci. Technol. B 38 (4) (2020) 044002.
- [39] M.K.I. Senevirathna, M.D. Williams, G.A. Cooke, A. Kozhanov, M. Vernon, G.B. Cross, Analysis of useful ion yield for the Mg dopant in gan by quadrupole—SIMS, J. Vac. Sci. Technol. B 38 (3) (2020) 034015.
- [40] N. Nishida, M. Sakurai, D. Kato, H.A. Sakaue, Observation of light and secondary ion emissions from surfaces irradiated with highly charged ions, J. Vac. Sci. Technol. B 38 (4) (2020) 044006.
- [41] A. Merkulov, P. Peres, K. Soulard, D.J. Larson, K. Sivaramakrishnan, Improvement of extra low impact energy SIMS data reduction algorithm for process control, J. Vac. Sci. Technol. B 38 (5) (2020) 053201.
- [42] B. Weidtmann, S. Hanke, A. Duvenbeck, A. Wucher, Influence of the polar angle of incidence on secondary ion formation in self-sputtering of silver, Surf. Interface Anal. 43 (1–2) (2011) 24–27.
- [43] L. Rzeznik, R. Paruch, B.J. Garrison, Z. Postawa, Sputtering of a coarse-grained benzene and ag(111) crystals by large ar clusters – effect of impact angle and cohesive energy, Surf. Interface Anal. 45 (1) (2013) 27–30.
- [44] M. Golunski, Z. Postawa, Effect of kinetic energy and impact angle on carbon ejection from a free-standing graphene bombarded by kilo-electron-volt C60, J. Vac. Sci. Technol. B 36 (3) (2018) 03F112.
- [45] M. Kański, Z. Postawa, Effect of the impact angle on the kinetic energy and angular distributions of β-carotene sputtered by 15 kev ar2000 projectiles, Anal. Chem. 91 (14) (2019) 9161–9167.
- [46] M. Gołuński, S. Hrabar, Z. Postawa, Mechanisms of molecular emission from phenylalanine monolayer deposited on free-standing graphene bombarded by C60 projectiles, Appl. Surf. Sci. 539 (2021) 148259.
- [47] Q.S. Paduano, M. Snure, J. Bondy, T.W.C. Zens, Self-terminating growth in hexagonal boron nitride by metal organic chemical vapor deposition, Appl. Phys. Express 7 (7) (2014) 071004.
- [48] Q. Paduano, M. Snure, D. Weyburne, A. Kiefer, G. Siegel, J. Hu, Metalorganic chemical vapor deposition of few-layer sp2 bonded boron nitride films, J. Cryst. Growth 449 (2016) 148–155.
- [49] B.J. Garrison, Z. Postawa, Computational view of surface based organic mass spectrometry, Mass Spectrom. Rev. 27 (4) (2008) 289–315.
- [50] J.H. Los, J.M.H. Kroes, K. Albe, R.M. Gordillo, M.I. Katsnelson, A. Fasolino, Extended tersoff potential for boron nitride: Energetics and elastic properties of pristine and defective h-BN, Phys. Rev. B 96 (2017) 184108.
- [51] O. Hod, Graphite and hexagonal boron-nitride have the same interlayer distance. Why?, J. Chem. Theory Comput. 8 (4) (2012) 1360–1369.
- [52] J.F. Ziegler, J.P. Biersack, The stopping and range of ions in matter, in: D.A. Bromley (Ed.), Treatise on Heavy-Ion Science: Volume 6: Astrophysics, Chemistry, and Condensed Matter, Springer US, Boston, MA, 1985, pp. 93–129.
- [53] S. Plimpton, Fast parallel algorithms for short-range molecular dynamics, J. Comput. Phys. 117 (1) (1995) 1–19.

dr Wawrzyniec Kaszub

Sieć Badawcza Łukasiewicz Instytut Mikroelektroniki i Fotoniki al. Lotników 32/46 02-668 Warszawa wawrzyniec kaszub@imif.lukasiewicz.gov.pl

OŚWIADCZENIE

Oświadczam, że w pracy:

Secondary ion mass spectroscopy depth profiling of hydrogen-intercalated graphene on SiC Paweł Piotr Michałowski, Wawrzyniec Kaszub, Alexandre Merkulov and Włodek Strupiński Applied Physics Letters 109, 011904 (2016)

Mój udział polegał na przygotowaniu próbek do pomiarów SIMS i dyskusji

Manymec Karub (podpis)

Leuven, 01.09.2021

Alexandre Merkulov, PhD

IMEC Remisebosweg 1 3001 Leuven Belgium

Alex.Merkulov@imec.be

STATEMENT

I hereby confirm that in the article

Secondary ion mass spectroscopy depth profiling of hydrogen-intercalated graphene on SiC Paweł Piotr Michałowski, Wawrzyniec Kaszub, Alexandre Merkulov and Włodek Strupiński Applied Physics Letters 109, 011904 (2016)

My contribution was related to expertise in extreme low impact energy SIMS experiment

(signature)

dr hab. inż. Włodzimierz Strupiński

Politechnika Warszawska Wydział Fizyki ul. Koszykowa 75 00-662 Warszawa włodek.strupinski@pw.edu.pl

OŚWIADCZENIE

Oświadczam, że w pracy:

Secondary ion mass spectroscopy depth profiling of hydrogen-intercalated graphene on SiC Paweł Piotr Michałowski, Wawrzyniec Kaszub, Alexandre Merkulov and Włodek Strupiński Applied Physics Letters 109, 011904 (2016)

Mój udział polegał na koordynacji prac i dyskusji wyników

dr Wawrzyniec Kaszub

Sieć Badawcza Łukasiewicz Instytut Mikroelektroniki i Fotoniki al. Lotników 32/46 02-668 Warszawa wawrzyniec.kaszub@imif.lukasiewicz.gov.pl

OŚWIADCZENIE

Oświadczam, że w pracy:

Graphene Enhanced Secondary Ion Mass Spectrometry (GESIMS)

Paweł Piotr Michałowski, Wawrzyniec Kaszub, Iwona Pasternak and Włodek Strupiński
Scientific Reports 7, 7479 (2017)

Mój udział polegał na przygotowaniu próbek do pomiarów SIMS i dyskusji wyników

Nauryme Ranus (podpis)

dr Iwona Pasternak

Politechnika Warszawska Wydział Fizyki ul. Koszykowa 75 00-662 Warszawa iwona.pasternak@pw.edu.pl

OŚWIADCZENIE

Oświadczam, że w pracy:

Graphene Enhanced Secondary Ion Mass Spectrometry (GESIMS)
Paweł Piotr Michałowski, Wawrzyniec Kaszub, Iwona Pasternak and Włodek Strupiński
Scientific Reports 7, 7479 (2017)

Mój udział polegał na wzroście CVD i transferze grafenu i dyskusji wyników

dr hab. inż. Włodzimierz Strupiński

Politechnika Warszawska Wydział Fizyki ul. Koszykowa 75 00-662 Warszawa włodek.strupinski@pw.edu.pl

OŚWIADCZENIE

Oświadczam, że w pracy:

Graphene Enhanced Secondary Ion Mass Spectrometry (GESIMS) Paweł Piotr Michałowski, Wawrzyniec Kaszub, Iwona Pasternak and Włodek Strupiński Scientific Reports 7, 7479 (2017)

Mój udział polegał na koordynacji prac i dyskusji wyników

dr inż. Piotr Gutowski

Instytut Technologii Elektronowej Zakład Fotoniki aleja Lotników 32/46 02-668 Warszawa gutowski@ite.waw.pl

OSWIADCZENIE

Oświadczam, że w pracy:

Characterization of the superlattice region of a quantum cascade laser by secondary ion mass spectrometry

Paweł Piotr Michałowski, Piotr Gutowski, Dorota Pierścińska, Kamil Pierściński, Maciej Bugajski

Nanoscale 9, 17571 (2017)

Mój udział polegał na wytworzeniu struktury lasera metodą MBE oraz dyskusji wyników.

Prot. Gatowiki

dr inż. Dorota Pierścińska

Instytut Technologii Elektronowej Zakład Fotoniki aleja Lotników 32/46 02-668 Warszawa dorota pierscinska@ite.waw.pl

OŚWIADCZENIE

Oświadczam, że w pracy:

Characterization of the superlattice region of a quantum cascade laser by secondary ion mass spectrometry

Paweł Piotr Michałowski, Piotr Gutowski, Dorota Pierścińska, Kamil Pierściński, Maciej Bugajski

Nanoscale 9, 17571 (2017)

Mój udział polegał na wstępnej charakteryzacji struktury lasera, dyskusji wyników.

glesciuls (podpis)

dr inż. Kamil Pierściński

Instytut Technologii Elektronowej Zakład Fotoniki aleja Lotników 32/46 02-668 Warszawa pierscin@ite.waw pl

OŚWIADCZENIE

Oświadczam, że w pracy:

Characterization of the superlattice region of a quantum cascade laser by secondary ion mass spectrometry

Paweł Piotr Michałowski, Piotr Gutowski, Dorota Pierścińska, Kamil Pierściński, Maciej Bugajski

Nanoscale 9, 17571 (2017)

Mój udział polegał na zaprojektowaniu struktury lasera kaskadowego oraz dyskusji wyników.

Stoull Prescial

prof. dr hab. Maciej Bugajski

Instytut Technologii Elektronowej Zakład Fotoniki aleja Lotników 32/46 02-668 Warszawa bugajski@ite.waw.pl

OSWIADCZENIE

Oświadczam, że w pracy:

Characterization of the superlattice region of a quantum cascade laser by secondary ion mass spectrometry

Paweł Piotr Michałowski, Piotr Gutowski, Dorota Pierścińska, Kamil Pierściński, Maciej Bugajski

Nanoscale 9, 17571 (2017)

Mój udział polegał na koordynacji prac, dyskusji wyników i przygotowaniu manuskryptu

dr hab. inż. Włodzimierz Strupiński

Politechnika Warszawska Wydział Fizyki ul. Koszykowa 75 00-662 Warszawa włodek.strupinski@pw.edu.pl

OŚWIADCZENIE

Oświadczam, że w pracy:

Characterization of the superlattice region of a quantum cascade laser by secondary ion mass spectrometry

Paweł Piotr Michałowski, Piotr Gutowski, Dorota Pierścińska, Kamil Pierściński, Maciej Bugajski

Nanoscale 9, 17571 (2017)

Mój udział polegał na koordynacji prac i dyskusji wyników

dr Iwona Pasternak

Politechnika Warszawska Wydział Fizyki ul. Koszykowa 75 00-662 Warszawa iwona.pasternak@pw.edu.pl

OŚWIADCZENIE

Oświadczam, że w pracy:

Contamination-free Ge-based graphene as revealed by graphene enhanced secondary ion mass spectrometry (GESIMS)

Paweł Piotr Michałowski, Iwona Pasternak and Włodek Strupiński

Nanotechnology 29, 015702 (2018)

Mój udział polegał na wzroście CVD i transferze grafenu i dyskusji wyników

dr hab. inż. Włodzimierz Strupiński

Politechnika Warszawska Wydział Fizyki ul. Koszykowa 75 00-662 Warszawa włodek.strupinski@pw.edu.pl

OŚWIADCZENIE

Oświadczam, że w pracy:

Contamination-free Ge-based graphene as revealed by graphene enhanced secondary ion mass spectrometry (GESIMS)

Paweł Piotr Michałowski, Iwona Pasternak and Włodek Strupiński

Nanotechnology 29, 015702 (2018)

Mój udział polegał na koordynacji prac i dyskusji wyników

dr Iwona Pasternak

Politechnika Warszawska Wydział Fizyki ul. Koszykowa 75 00-662 Warszawa iwona.pasternak@pw.edu.pl

OŚWIADCZENIE

Oświadczam, że w pracy:

Formation of a highly doped ultrathin amorphous carbon layer by ion bombardment of graphene

Paweł Piotr Michałowski, Iwona Pasternak, Paweł Ciepielewski, Francisco Guinea and Włodek Strupiński

Nanotechnology 29, 305302 (2018)

Mój udział polegał na wzroście CVD i transferze grafenu i dyskusji wyników

dr Paweł Ciepielewski

Sieć Badawcza Łukasiewicz Instytut Mikroelektroniki i Fotoniki al. Lotników 32/46 02-668 Warszawa pawel.ciepielewski@imif.lukasiewicz.gov.pl

OŚWIADCZENIE

Oświadczam, że w pracy:

Formation of a highly doped ultrathin amorphous carbon layer by ion bombardment of graphene

Paweł Piotr Michałowski, Iwona Pasternak, Paweł Ciepielewski, Francisco Guinea and Włodek Strupiński

Nanotechnology 29, 305302 (2018)

Mój udział polegał na wykonaniu pomiarów Ramanowskich i dyskusji wyników

P. Ceiceen

Prof. Francisco Guinea

IMDEA C/ Faraday 9 28049 MADRID Spain

paco.guinea@imdea.org

STATEMENT

I hereby confirm that in the article

Formation of a highly doped ultrathin amorphous carbon layer by ion bombardment of graphene

Paweł Piotr Michałowski, Iwona Pasternak, Paweł Ciepielewski, Francisco Guinea and Włodek Strupiński

Nanotechnology 29, 305302 (2018)

My contribution was related to discussing a mechanism of interaction of ions with graphene.

...Francisco Guinea......(signature)

dr hab. inż. Włodzimierz Strupiński

Politechnika Warszawska Wydział Fizyki ul. Koszykowa 75 00-662 Warszawa włodek.strupinski@pw.edu.pl

OŚWIADCZENIE

Oświadczam, że w pracy:

Formation of a highly doped ultrathin amorphous carbon layer by ion bombardment of graphene

Paweł Piotr Michałowski, Iwona Pasternak, Paweł Ciepielewski, Francisco Guinea and Włodek Strupiński

Nanotechnology 29, 305302 (2018)

Mój udział polegał na koordynacji prac i dyskusji wyników

dr Jarosław Gaca

Sieć Badawcza Łukasiewicz Instytut Mikroelektroniki i Fotoniki al. Lotników 32/46 02-668 Warszawa jaroslaw.gaca@imif.lukasiewicz.gov.pl

OŚWIADCZENIE

Oświadczam, że w pracy:

Oxygen out-diffusion and compositional changes in zinc oxide during ytterbium ions bombardment
Paweł Piotr Michałowski, Jarosław Gaca, Marek Wójcik, and Andrzej Turos
Nanotechnology 29, 425710 (2018)

Mój udział polegał na wykonaniu pomiarów rentgenowskich i dyskusji wyników

dr Marek Wójcik

dezyderat8993@wp.pl

OŚWIADCZENIE

Oświadczam, że w pracy:

Oxygen out-diffusion and compositional changes in zinc oxide during ytterbium ions bombardment

Paweł Piotr Michałowski, Jarosław Gaca, Marek Wójcik, and Andrzej Turos

Nanotechnology 29, 425710 (2018)

Mój udział polegał na wykonaniu pomiarów rentgenowskich i dyskusji wyników

Harel Wy and (podpis)

prof. dr hab. inż. Andrzej Turos

Sieć Badawcza Łukasiewicz Instytut Mikroelektroniki i Fotoniki al. Lotników 32/46 02-668 Warszawa andrzej.turos@imif.lukasiewicz.gov.pl

OŚWIADCZENIE

Oświadczam, że w pracy:

Oxygen out-diffusion and compositional changes in zinc oxide during ytterbium ions bombardment
Paweł Piotr Michałowski, Jarosław Gaca, Marek Wójcik, and Andrzej Turos
Nanotechnology 29, 425710 (2018)

Mój udział polegał na koordynacji prac i dyskusji wyników

dr Wawrzyniec Kaszub

Sieć Badawcza Łukasiewicz Instytut Mikroelektroniki i Fotoniki al. Lotników 32/46 02-668 Warszawa wawrzyniec kaszub@imif lukasiewicz.gov.pl

OŚWIADCZENIE

Oświadczam, że w pracy:

A-Crater-within-a-Crater Approach for Secondary Ion Mass Spectrometry Evaluation of the Quality of Interfaces of Multilayer Devices
Paweł Piotr Michałowski, Wawrzyniec Kaszub, Piotr Knyps, Krzysztof Rosiński, Beata Stańczyk, Krystyna Przyborowska and Ewa Dumiszewska
ACS Applied Materials & Interfaces 10, 37694–37698 (2018)

Mój udział polegał na koordynacji prac związanych z wytworzeniem ogniw słonecznych i dyskusji wyników

Manonymec Karul

mgr inż. Piotr Knyps

SEMICON Sp. z o.o. Zwoleńska 43/43a 04-761 Warszawa pknyps@semicon.com.pl

OŚWIADCZENIE

Oświadczam, że w pracy:

A-Crater-within-a-Crater Approach for Secondary Ion Mass Spectrometry Evaluation of the Quality of Interfaces of Multilayer Devices
Paweł Piotr Michałowski, Wawrzyniec Kaszub, Piotr Knyps, Krzysztof Rosiński, Beata Stańczyk, Krystyna Przyborowska and Ewa Dumiszewska
ACS Applied Materials & Interfaces 10, 37694–37698 (2018)

Mój udział polegał na processingu ogniw słonecznych oraz pomiarach ich sprawności

Pllnyps (podpis) mgrBeata Stańczyk

Sieć Badawcza Łukasiewicz Instytut Mikroelektroniki i Fotoniki al. Lotników 32/46 02-668 Warszawa beata.stanczyk a imif.lukasiewicz.gov.pl

OŚWIADCZENIE

Oświadczam, że w pracy:

A-Crater-within-a-Crater Approach for Secondary Ion MassSpectrometry Evaluation of the Quality of Interfaces of MultilayerDevices
Paweł Piotr Michałowski, Wawrzyniec Kaszub, Piotr Knyps, Krzysztof Rosiński, Beata Stańczyk, Krystyna Przyborowska and Ewa Dumiszewska
ACS Applied Materials & Interfaces 10, 37694–37698 (2018)

Mój udział polegał na processingu ogniw słonecznych

beata Stanosyk

mgrKrystyna Przyborowska

Sieć Badawcza Łukasiewicz Instytut Mikroelektroniki i Fotoniki al. Lotników 32/46 02-668 Warszawa krystyna.przyborowska@imif.lukasiewicz.gov.pl

OŚWIADCZENIE

Oświadczam, że w pracy:

All Crater-within-a-Crater Approach for Secondary Ion MassSpectrometry Evaluation of the Quality of Interfaces of MultilayerDevices

Paweł Piotr Michałowski, Wawrzyniec Kaszub, Piotr Knyps, Krzysztof Rosiński, Beata Stańczyk, Krystyna Przyborowska and Ewa Dumiszewska

ACS Applied Materials & Interfaces 10, 37694–37698 (2018)

Mój udział polegał na processingu ogniw słonecznych

19. Pay bowks lee

dr inż. Ewa Dumiszewska

Sieć Badawcza Łukasiewicz Instytut Mikroelektroniki i Fotoniki al. Lotników 32/46 02-668 Warszawa ewa.dumiszewska@imif.lukasiewicz.gov.pl

OŚWIADCZENIE

Oświadczam, że w pracy:

A-Crater-within-a-Crater Approach for Secondary Ion Mass Spectrometry Evaluation of the Quality of Interfaces of Multilayer Devices
Paweł Piotr Michałowski, Wawrzyniec Kaszub, Piotr Knyps, Krzysztof Rosiński, Beata Stańczyk, Krystyna Przyborowska and Ewa Dumiszewska ACS Applied Materials & Interfaces 10, 37694–37698 (2018)

Mój udział polegał na wytwarzaniu struktur epitaksjalnych ogniw słonecznych i dyskusji wyników

Ena Dinsunska (podpis)

mgr inż. Piotr Knyps

SEMICON Sp. z o.o. Zwoleńska 43/43a 04-761 Warszawa pknyps@semicon.com.pl

OŚWIADCZENIE

Oświadczam, że w pracy:

Destructive role of oxygen in growth of molybdenum disulfide determined by secondary ion mass spectrometry

Paweł Piotr Michałowski, Piotr Knyps, Paweł Ciepielewski, Piotr Caban, Ewa Dumiszewska and Jacek Baranowski

Physical Chemistry Chemical Physics, 21:8837–8842 (2019)

Mój udział polegał na wytwarzaniu próbek do pomiarów

Plyg5 (podpis) dr Paweł Ciepielewski

Sieć Badawcza Łukasiewicz Instytut Mikroelektroniki i Fotoniki al. Lotników 32/46 02-668 Warszawa pawel.ciepielewski@imif.lukasiewicz.gov.pl

OŚWIADCZENIE

Oświadczam, że w pracy:

Destructive role of oxygen in growth of molybdenum disulfide determined by secondary ion mass spectrometry

Paweł Piotr Michałowski, Piotr Knyps, Paweł Ciepielewski, Piotr Caban, Ewa Dumiszewska and Jacek Baranowski

Physical Chemistry Chemical Physics, 21:8837–8842 (2019)

Mój udział polegał na wykonaniu pomiarów Ramanowskich i dyskusji wyników

P. Ceceles (podpis)

dr Piotr Caban

Sieć Badawcza Łukasiewicz Instytut Mikroelektroniki i Fotoniki al. Lotników 32/46 02-668 Warszawa piotr.caban@imif.lukasiewicz.gov.pl

OŚWIADCZENIE

Oświadczam, że w pracy:

Destructive role of oxygen in growth of molybdenum disulfide determined by secondary ion mass spectrometry

Paweł Piotr Michałowski, Piotr Knyps, Paweł Ciepielewski, Piotr Caban, Ewa Dumiszewska and Jacek Baranowski

Physical Chemistry Chemical Physics, 21:8837–8842 (2019)

Mój udział polegał na opracowaniu technologii wytwarzania próbek, przygotowaniu próbek, dyskusji wyników.

dr inż. Ewa Dumiszewska

Sieć Badawcza Łukasiewicz Instytut Mikroelektroniki i Fotoniki al. Lotników 32/46 02-668 Warszawa ewa.dumiszewska@imif.lukasiewicz.gov.pl

OŚWIADCZENIE

Oświadczam, że w pracy:

Destructive role of oxygen in growth of molybdenum disulfide determined by secondary ion mass spectrometry

Paweł Piotr Michałowski, Piotr Knyps, Paweł Ciepielewski, Piotr Caban, Ewa Dumiszewska and Jacek Baranowski

Physical Chemistry Chemical Physics, 21:8837–8842 (2019)

Mój udział polegał na opracowaniu technologii wytwarzania próbek

Ene Dunisienske (podpis)

prof. dr hab. Jacek Baranowski

Sieć Badawcza Łukasiewicz Instytut Mikroelektroniki i Fotoniki al. Lotników 32/46 02-668 Warszawa jacek.baranowski@imif.lukasiewicz.gov.pl

OŚWIADCZENIE

Oświadczam, że w pracy:

Destructiverole of oxygen in growth of molybdenum disulfide determined by secondary ion massspectrometry

Paweł Piotr Michałowski, Piotr Knyps, Paweł Ciepielewski, Piotr Caban, Ewa Dumiszewska and Jacek Baranowski

PhysicalChemistryChemicalPhysics, 21:8837–8842 (2019)

Mój udział polegał nadyskusji i interpretacji wyników

mgr inż. Piotr Knyps

SEMICON Sp. z o.o. Zwoleńska 43/43a 04-761 Warszawa pknyps@semicon.com.pl

OŚWIADCZENIE

Oświadczam, że w pracy:

Growth of highly oriented MoS2 via an intercalation process in the graphene/SiC(0001) system

Paweł Piotr Michałowski, Piotr Knyps, Paweł Ciepielewski, Piotr Caban, Ewa Dumiszewska, Grzegorz Kowalski, Mateusz Tokarczyk and Jacek Baranowski

Physical Chemistry Chemical Physics, 21: 20641–20646 (2019)

Mój udział polegał na processingu ogniw słonecznych oraz pomiarach ich sprawności.

P Wryps (podpis) dr Paweł Ciepielewski

Sieć Badawcza Łukasiewicz Instytut Mikroelektroniki i Fotoniki al. Lotników 32/46 02-668 Warszawa pawel.ciepielewski@imif.lukasiewicz.gov.pl

OŚWIADCZENIE

Oświadczam, że w pracy:

Growth of highly oriented MoS2 via an intercalation process in the graphene/SiC(0001) system

Paweł Piotr Michałowski, Piotr Knyps, Paweł Ciepielewski, Piotr Caban, Ewa Dumiszewska, Grzegorz Kowalski, Mateusz Tokarczyk and Jacek Baranowski

Physical Chemistry Chemical Physics, 21: 20641–20646 (2019)

Mój udział polegał na wykonaniu pomiarów Ramanowskich i dyskusji wyników

dr Piotr Caban

Sieć Badawcza Łukasiewicz Instytut Mikroelektroniki i Fotoniki al. Lotników 32/46 02-668 Warszawa piotr.caban@imif.lukasiewicz.gov.pl

OŚWIADCZENIE

Oświadczam, że w pracy:

Growth of highly oriented MoS2 via an intercalation process in the graphene/SiC(0001) system

Paweł Piotr Michałowski, Piotr Knyps, Paweł Ciepielewski, Piotr Caban, Ewa Dumiszewska, Grzegorz Kowalski, Mateusz Tokarczyk and Jacek Baranowski

Physical Chemistry Chemical Physics, 21: 20641–20646 (2019)

Mój udział polegał na opracowaniu technologii wytwarzania próbek, przygotowaniu próbek, dyskusji wyników.

dr inż. Ewa Dumiszewska

Sieć Badawcza Łukasiewicz Instytut Mikroelektroniki i Fotoniki al. Lotników 32/46 02-668 Warszawa ewa.dumiszewska@imif.lukasiewicz.gov.pl

OŚWIADCZENIE

Oświadczam, że w pracy:

Growth of highly oriented MoS2 via an intercalation process in the graphene/SiC(0001) system

Paweł Piotr Michałowski, Piotr Knyps, Paweł Ciepielewski, Piotr Caban, Ewa Dumiszewska, Grzegorz Kowalski, Mateusz Tokarczyk and Jacek Baranowski

Physical Chemistry Chemical Physics, 21: 20641-20646 (2019)

Mój udział polegał na opracowaniu technologii wytwarzania próbek

Euro Dimbreugla (podpis) dr hab. Grzegorz Kowalski

Wydział Fizyki Uniwersytetu Warszawskiego Ludwika Pasteura 5 02-093Warszawa Grzegorz.Kowalski@fuw.edu.pl

OŚWIADCZENIE

Oświadczam, że w pracy:

Growth of highly oriented MoS2 via an intercalation process in the graphene/SiC(0001) system

Paweł Piotr Michałowski, Piotr Knyps, Paweł Ciepielewski, Piotr Caban, Ewa Dumiszewska, Grzegorz Kowalski, Mateusz Tokarczyk and Jacek Baranowski

Physical Chemistry Chemical Physics, 21: 20641–20646 (2019)

Mój udział polegał na wykonaniu pomiarów rentgenowskich i dyskusji wyników

dr Mateusz Tokarczyk

Wydział Fizyki Uniwersytetu Warszawskiego Ludwika Pasteura 5 02-093 Warszawa mateusz.tokarczyk@fuw.edu.pl

OŚWIADCZENIE

Oświadczam, że w pracy:

Growth of highly oriented MoS2 via an intercalation process in the graphene/SiC(0001) system

Paweł Piotr Michałowski, Piotr Knyps, Paweł Ciepielewski, Piotr Caban, Ewa Dumiszewska, Grzegorz Kowalski, Mateusz Tokarczyk and Jacek Baranowski

Physical Chemistry Chemical Physics, 21: 20641–20646 (2019)

Mój udział polegał na wykonaniu pomiarów rentgenowskich i dyskusji wyników

Mateusz Thonsryk
(podpis)

prof. dr hab. Jacek Baranowski

Sieć Badawcza Łukasiewicz Instytut Mikroelektroniki i Fotoniki al. Lotników 32/46 02-668 Warszawa jacek.baranowski@imif.lukasiewicz.gov.pl

OŚWIADCZENIE

Oświadczam, że w pracy:

Growth of highly oriented MoS2via an intercalation processin the graphene/SiC(0001) system

Paweł Piotr Michałowski, Piotr Knyps, Paweł Ciepielewski, Piotr Caban, Ewa Dumiszewska, Grzegorz Kowalski, Mateusz Tokarczyk and Jacek Baranowski

PhysicalChemistryChemicalPhysics, 21:20641–20646 (2019)

Mój udział polegał nadyskusji i interpretacji wyników

dr Piotr Caban

Sieć Badawcza Łukasiewicz Instytut Mikroelektroniki i Fotoniki al. Lotników 32/46 02-668 Warszawa piotr.caban@imif.lukasiewicz.gov.pl

OŚWIADCZENIE

Oświadczam, że w pracy:

Secondary ion mass spectrometry investigation of carbon grain formation in boron nitride epitaxial layers with atomic depth resolution

Paweł Piotr Michałowski, Piotr Caban and Jacek Baranowski

Journal of Analytical Atomic Spectrometry, 34:848-853 (2019)

Mój udział polegał na opracowaniu technologii wytwarzania próbek, wytwarzaniu próbek, dyskusji wyników.

(nodnis)

prof. dr hab. Jacek Baranowski

Sieć Badawcza Łukasiewicz Instytut Mikroelektroniki i Fotoniki al. Lotników 32/46 02-668 Warszawa jacek.baranowski@imif.lukasiewicz.gov.pl

OŚWIADCZENIE

Oświadczam, że w pracy:

Secondary ion mass spectrometry investigation of carbon grain formation in boron nitride epitaxial layers with atomic depth resolution

Paweł Piotr Michałowski, Piotr Caban and Jacek Baranowski

Journal of Analytical Atomic Spectrometry, 34:848-853 (2019)

Mój udział polegał nadyskusji i interpretacji wyników

7/3 --- (podpis)

dr Sebastian Złotnik

Wydział Nowych Technologii i Chemii Wojskowej Akademii Technicznej ul. gen. Sylwestra Kaliskiego 2 00-908 Warszawa sebastian.zlotnik@wat.edu.pl

OŚWIADCZENIE

Oświadczam, że w pracy:

Three dimensional localization of unintentional oxygen impurities in gallium nitride Paweł Piotr Michałowski, Sebastian Złotnik and Mariusz Rudziński Chemical Communications, 55:11539–11542 (2019)

Mój udział polegał na wytwarzaniu oraz trawieniu próbek, analizie dyslokacji, wykonaniu obrazowania SEM, dyskusji wyników i przygotowanie manuskryptu

Gelestien Totale

dr inż. Mariusz Rudziński

mariusz.rudzinski@gmail.com

OŚWIADCZENIE

Oświadczam, że w pracy:

Three dimensional localization of unintentional oxygen impurities in gallium nitride Paweł Piotr Michałowski, Sebastian Złotnik and Mariusz Rudziński Chemical Communications, 55:11539–11542 (2019)

Mój udział polegał na koordynacji prac, opracowaniu teoretycznych założeń artykułu, opracowaniu technologii wzrostu materiałów i ich wykonanie metodą MOCVD oraz dyskusji i interpretacji wyników.

(podpis)

Harin Rudriski

mgr. Ewa Grzanka

Instytut Wysokich Ciśnień Polskiej Akademii Nauk Sokołowska 29/37 01-142 Warszawa elesk@unipress.waw.pl

OŚWIADCZENIE

Oświadczam, że w pracy:

Indium concentration fluctuations in InGaN/GaN quantum wells Paweł Piotr Michałowski, Ewa Grzanka, Szymon Grzanka, Artur Lachowski, Grzegorz Staszczak, Jerzy Plesiewicz, Mike Leszczyński and Andrzej Turos

Journal of Analytical Atomic Spectrometry, 34:1718–1723 (2019)

Mój udział polegał na wykonaniu i interpretacji pomiarów rentgenowskich.

Ewa mento

dr Szymon Grzanka

Instytut Wysokich Ciśnień Polskiej Akademii Nauk Sokołowska 29/37 01-142 Warszawa szgrzanka@unipress.waw.pl

OŚWIADCZENIE

Oświadczam, że w pracy:

Indium concentration fluctuations in InGaN/GaN quantum wells Paweł Piotr Michałowski, Ewa Grzanka, Szymon Grzanka, Artur Lachowski, Grzegorz Staszczak, Jerzy Plesiewicz, Mike Leszczyński and Andrzej Turos

Journal of Analytical Atomic Spectrometry, 34:1718–1723 (2019)

Mój udział polegał na wykonaniu pomiarów fotoluminescencyjnych.

(podpis)

Symon

mgr inż. Artur Lachowski

Instytut Wysokich Ciśnień Polskiej Akademii Nauk Sokołowska 29/37 01-142 Warszawa artur@unipress.waw.pl

OŚWIADCZENIE

Oświadczam, że w pracy:

Indium concentration fluctuations in InGaN/GaN quantum wells Paweł Piotr Michałowski, Ewa Grzanka, Szymon Grzanka, Artur Lachowski, Grzegorz Staszczak, Jerzy Plesiewicz, Mike Leszczyński and Andrzej Turos

Journal of Analytical Atomic Spectrometry, 34:1718–1723 (2019)

Mój udział polegał na wykonaniu próbek do badań i wykonaniu pomiarów TEM.

(podpis)

Artur Lachawsli

dr Grzegorz Staszczak

Instytut Wysokich Ciśnień Polskiej Akademii Nauk Sokołowska 29/37 01-142 Warszawa staszczak@unipress.waw.pl

OŚWIADCZENIE

Oświadczam, że w pracy:

Indium concentration fluctuations in InGaN/GaN quantum wells Paweł Piotr Michałowski, Ewa Grzanka, Szymon Grzanka, Artur Lachowski, Grzegorz Staszczak, Jerzy Plesiewicz, Mike Leszczyński and Andrzej Turos

Journal of Analytical Atomic Spectrometry, 34:1718–1723 (2019)

Mój udział polegał na wykonaniu pomiarów fotoluminescencyjnych.

Slagent Green
(podpis)

mgr Jerzy Plesiewicz

Top-GaN sp. z o.o. Solec 24/90 00-403 Warszawa

OŚWIADCZENIE

Oświadczam, że w pracy:

Indium concentration fluctuations in InGaN/GaN quantum wells Paweł Piotr Michałowski, Ewa Grzanka, Szymon Grzanka, Artur Lachowski, Grzegorz Staszczak, Jerzy Plesiewicz, Mike Leszczyński and Andrzej Turos

Journal of Analytical Atomic Spectrometry, 34:1718–1723 (2019)

Mój udział polegał na wykonaniu próbek do badań.

Jerry Plantevous (podpis) prof. Mike Leszczyński

Instytut Wysokich Ciśnień Polskiej Akademii Nauk Sokołowska 29/37 01-142 Warszawa mike@unipress.waw.pl

OŚWIADCZENIE

Oświadczam, że w pracy:

Indium concentration fluctuations in InGaN/GaN quantum wells Paweł Piotr Michałowski, Ewa Grzanka, Szymon Grzanka, Artur Lachowski, Grzegorz Staszczak, Jerzy Plesiewicz, Mike Leszczyński and Andrzej Turos

Journal of Analytical Atomic Spectrometry, 34:1718–1723 (2019)

Mój udział polegał na koordynacji prac i dyskusji wyników

prof. dr hab. inż. Andrzej Turos

Sieć Badawcza Łukasiewicz Instytut Mikroelektroniki i Fotoniki al. Lotników 32/46 02-668 Warszawa andrzej.turos@imif.lukasiewicz.gov.pl

OŚWIADCZENIE

Oświadczam, że w pracy:

Indium concentration fluctuations in InGaN/GaN quantum wells Paweł Piotr Michałowski, Ewa Grzanka, Szymon Grzanka, Artur Lachowski, Grzegorz Staszczak, Jerzy Plesiewicz, Mike Leszczyński and Andrzej Turos

Journal of Analytical Atomic Spectrometry, 34:1718–1723 (2019)

Mój udział polegał na koordynacji prac i dyskusji wyników

dr Sebastian Złotnik

Wydział Nowych Technologii i Chemii Wojskowej Akademii Technicznej ul. gen. Sylwestra Kaliskiego 2 00-908 Warszawa sebastian.zlotnik@wat.edu.pl

OŚWIADCZENIE

Oświadczam, że w pracy:

3D Depth Profile Reconstruction of Segregated Impurities using Secondary Ion Mass Spectrometry

Paweł Piotr Michałowski, Sebastian Złotnik, Iwona Jóźwik, Adrianna Chamryga and Mariusz Rudziński

Journal of Visualized Experiments, 158:e61065 (2020)

Mój udział polegał na wytwarzaniu oraz trawieniu próbek, analizie dyslokacji, dyskusji wyników i przygotowanie manuskryptu

Gelsestian Italine (podpis)

dr Iwona Jóźwik

Sieć Badawcza Łukasiewicz Instytut Mikroelektroniki i Fotoniki al. Lotników 32/46 02-668 Warszawa iwona.jozwik@imif.lukasiewicz.gov.pl

OŚWIADCZENIE

Oświadczam, że w pracy:

3D Depth Profile Reconstruction of Segregated Impurities using Secondary Ion Mass Spectrometry

Paweł Piotr Michałowski, Sebastian Złotnik, Iwona Jóźwik, Adrianna Chamryga and Mariusz Rudziński

Journal of Visualized Experiments, 158:e61065 (2020)

Mój udział polegał na wykonaniu obrazowania SEM

U- Yozhul (podpis) inż. Adrianna Chamryga

Sieć Badawcza Łukasiewicz Instytut Mikroelektroniki i Fotoniki al. Lotników 32/46 02-668 Warszawa adrianna.chamryga@imif.lukasiewicz.gov.pl

OŚWIADCZENIE

Oświadczam, że w pracy:

3D Depth Profile Reconstruction of Segregated Impurities using Secondary Ion Mass Spectrometry

Paweł Piotr Michałowski, Sebastian Złotnik, Iwona Jóźwik, Adrianna Chamryga and Mariusz Rudziński

Journal of Visualized Experiments, 158:e61065 (2020)

Mój udział polegał na wykonaniu pomiarów AFM

tdreama Chamrepa.

dr inż. Mariusz Rudziński

mariusz.rudzinski@gmail.com

OŚWIADCZENIE

Oświadczam, że w pracy:

3D Depth Profile Reconstruction of Segregated Impurities using Secondary Ion Mass Spectrometry

Paweł Piotr Michałowski, Sebastian Złotnik, Iwona Jóźwik, Adrianna Chamryga and Mariusz Rudziński

Journal of Visualized Experiments, 158:e61065 (2020)

Mój udział polegał na koordynacji prac, opracowaniu teoretycznych założeń artykułu, opracowaniu technologii wzrostu materiałów i ich wykonanie metodą MOCVD oraz dyskusji i interpretacji wyników.

Mariner Rudninski

dr Dawid Maciążek

dawid.maciazek@gmail.com

OŚWIADCZENIE

Oświadczam, że w pracy:

Defect-mediated sputtering process of boron nitride during high incident angle low-energy ion bombardment

Paweł Piotr Michałowski, Dawid Maciążek, Zbigniew Postawa, Piotr A. Caban, Sylwia Kozdra, Adrianna Wójcik, Jacek M. Baranowski

Measurement, 179:109487 (2021)

Mój udział polegał na wykonaniu symulacji komputerowych

David Maciozal

Kraków, 01.09.2021



Instytut Fizyki

im.

Mariana Smoluchowskiego

ul. prof. Łojasiewicza 11

PL 30-348 Kraków

OŚWIADCZENIE

Oświadczam, że w pracy:

Defect-mediated sputtering process of boron nitride during high incident angle low-energy ion bombardment

Paweł Piotr Michałowski, Dawid Maciążek, Zbigniew Postawa, Piotr A. Caban, Sylwia Kozdra, Adrianna Wójcik, Jacek M. Baranowski

Measurement, 179:109487 (2021)

Mój udział polegał na wykonaniu symulacji komputerowych i przygotowaniu manuskryptu

Thym Postova

Prof. dr hab. Zbigniew Postawa

tel. +48(12) 664-4626

email:

zbigniew.postawa@uj.edu.pl

dr Piotr Caban

Sieć Badawcza Łukasiewicz Instytut Mikroelektroniki i Fotoniki al. Lotników 32/46 02-668 Warszawa piotr.caban@imif.lukasiewicz.gov.pl

OŚWIADCZENIE

Oświadczam, że w pracy:

Defect-mediated sputtering process of boron nitride during high incident angle low-energy ion bombardment

Paweł Piotr Michałowski, Dawid Maciążek, Zbigniew Postawa, Piotr A. Caban, Sylwia Kozdra, Adrianna Wójcik, Jacek M. Baranowski

Measurement, 179:109487 (2021)

Mój udział polegał na opracowaniu technologii wytwarzania próbek, wytwarzaniu próbek, dyskusji wyników.

dr inż. Sylwia Kozdra

Sieć Badawcza Łukasiewicz Instytut Mikroelektroniki i Fotoniki al. Lotników 32/46 02-668 Warszawa piotr.caban@imif.lukasiewicz.gov.pl

OŚWIADCZENIE

Oświadczam, że w pracy:

Defect-mediated sputtering process of boron nitride during high incident angle low-energy ion bombardment

Paweł Piotr Michałowski, Dawid Maciążek, Zbigniew Postawa, Piotr A. Caban, Sylwia Kozdra, Adrianna Wójcik, Jacek M. Baranowski

Measurement, 179:109487 (2021)

Mój udział polegał na analizie reaktywności pierwiastków azotu i boru z jonami cezu

Syluma Kozolva (podpis) mgr Adrianna Wójcik

Sieć Badawcza Łukasiewicz Instytut Mikroelektroniki i Fotoniki al. Lotników 32/46 02-668 Warszawa piotr.caban@imif.lukasiewicz.gov.pl

OŚWIADCZENIE

Oświadczam, że w pracy:

Defect-mediated sputtering process of boron nitride during high incident angle low-energy ion bombardment

Paweł Piotr Michałowski, Dawid Maciążek, Zbigniew Postawa, Piotr A. Caban, Sylwia Kozdra, Adrianna Wójcik, Jacek M. Baranowski

Measurement, 179:109487 (2021)

Mój udział polegał na uczestnictwie w omawianiu wyników oraz analizie literatury

Adnorna Wojak (podpis) prof. dr hab. Jacek Baranowski

Sieć Badawcza Łukasiewicz Instytut Mikroelektroniki i Fotoniki al. Lotników 32/46 02-668 Warszawa jacek.baranowski@imif.lukasiewicz.gov.pl

OŚWIADCZENIE

Oświadczam, że w pracy:

Defect-mediated sputtering process of boron nitride during high incidentangle low-energy ion bombardment

Paweł Piotr Michałowski, DawidMaciążek, ZbigniewPostawa, Piotr A. Caban, SylwiaKozdra, Adrianna Wójcik, Jacek M. Baranowski

Measurement, 179:109487 (2021)

Mój udział polegał nadyskusji i interpretacji wyników